TECHNISCHE UNIVERSITÄT MÜNCHEN

LEHRSTUHL FÜR TECHNISCHE PHYSIK E19
INTERFACES AND ENERGY CONVERSION

ADVANCED MATERIALS FOR REDOX FLOW BATTERIES

JOCHEN FRIEDL

Vollständiger Abdruck der von der Fakultät für Physik der
Technischen Universität München
zur Erlangung des akademischen Grades eines
Doktors der Naturwissenschaften (Dr. rer. nat.)
genehmigten Dissertation.

Vorsitzender:	Univ.-Prof. Dr. Alessio Zaccone
Prüfer der Dissertation:	1. Univ.-Prof. Dr. Ulrich Stimming
	2. Univ.-Prof. Aliaksandr Bandarenka, Ph.D.
	3. Univ.-Prof. Dr. Christina Roth Freie Universität Berlin (nur schriftliche Beurteilung)

Die Dissertation wurde am 12.01.2015 bei der Technischen Universität München eingereicht und durch die Fakultät für Physik am 16.03.2015 angenommen.

Table of Contents

Chapter 1
Introduction

At the moment mankind is facing two major limitations in conjunction with the use of energy: *Climate* and *resources*.
Regarding the *climate* of our planet, the International Energy Agency (IEA) calculated that in order to limit the rise in global temperature to *2* ℃ (with a probability of *80 %*), all energy related CO_2 emissions in the year 2050 have to be half of what was emitted in 2009 [1–3]. In the year 2009, a total of *20043 TWh* of electrical energy were produced globally [4]. Coal contributed to more than *40 %* of that mix, with gas and oil adding another *25 %*. The remaining electricity was mostly generated by nuclear (*15 %*) and hydro (*17 %*) power plants. Failure to significantly reduce emissions could result in scenarios with a global rise in temperature of up to *6* ℃ which would certainly have a major impact on life as we know it now.
Regarding the boundary *resources* the situation seems less grim. Steven Chu, Nobel prize laureate and former United States Secretary of Energy (2009 – 2013), and Arun Majundar estimate that the ability of mankind to "… find and extract fossil fuels continues to improve, and economically recoverable reservoirs around the world are likely to keep pace with the rising demands for decades." [5,6]. This means that, while the large scale oil import of many countries leads to significant challenges related to balance-of-trade and national-security, there does not seem to be a fundamental limit to petroleum-derived liquid fuels for transportation and industry. But "the Stone Age came to an end not for lack of stones and the oil age will end, but not for a lack of oil." [5].

To reach the set climate goal, electricity generation has to transition to affordable and environmentally sustainable means in conjunction with electrification of the vehicle powertrain. While the generation of electricity from renewables such as wind and solar is already at cost parity in areas with relatively high energy costs (> $US\$ 200\ MWh^{-1}$), the full economic benefit of them can only be realized if these intermittent sources are integrated into transmission, load response and storage of electricity [6].

The exact requirements for large-scale grid storage are durability for large numbers of charge/discharge cycles as well as long calendar life, high round-trip efficiency, rapid response to changes in load or input and reasonable capital cost [7]. Redox flow batteries (RFBs) are one of the few options that could fulfil above requirements and store large amounts of electrical energy relatively cheaply and efficiently [8]. Distinct advantages of RFBs comprise independent scalability of energy- and power-content and long cycle life, as the electrodes do not undergo physical changes as opposed to batteries using intercalation or conversion reactions.

The most mature RFB system is the All-Vanadium RFB (VRB) pioneered by M. Skyllas-Kazacos [9–11]. Four oxidation states of vanadium are employed for cell operation which has the benefit that cross-over of species through the membrane does not lead to a chemical contamination and the charge can be rebalanced electrically. However, the VRB suffers from low energy- and power-density (for details see section 2.9).

Similar to fuel cells, the slow charge transfer kinetics, specifically of the high-potential half-cell, limit the obtainable currents and therefore power-density [12].
To remedy this shortcoming, considerable efforts have been put into catalyzing the electron transfer [9,13,14]. Mostly carbon nanomaterials such as carbon nanotubes (CNTs) or graphene were employed for this endeavor and those novel materials were in general regarded superior to classic carbonaceous electrode materials. While it was shown that the surface structure and electronic properties of carbon is highly intricate and that these properties have a strong influence on their electrochemical and electrocatalytic behavior, it is not a priori clear why the properties of carbon nanomaterials should differ vastly from other carbonaceous materials [15–17]. In the following, some of these studies that especially target the vanadium related redox-reactions are briefly described.

Zhu et al. employed a composite of CNTs and graphite as electrode material and stated that graphite improves kinetics whereas CNTs increase currents due to their high electronic conductivity [18].
The performance of functionalized carbon fibers for the V^{2+}/V^{3+} and VO^{2+}/VO_2^+ redox reactions was investigated with cyclic voltammetry (CV), electrochemical impedance spectroscopy (EIS) and charge-discharge tests by Yue et al. [19]. The authors described a mechanism in which $-OH$ groups seem to increase the kinetics for both reactions.
Employing similar techniques, Li et al. tested multi-walled carbon nanotubes (MWCNTs) with different degrees of functionalization as electrode material [20]. It was concluded that especially carboxylic-groups show superior activity towards the VO^{2+}/VO_2^+ redox reaction.
Gao et al. tested the influence of Fenton's reagent (H_2O_2 mixed with Fe^{2+} in acid) treatment on the activity of graphite felt as high potential electrode in VRBs [21]. Using CVs and non-normalized EIS they declared higher electrochemical activity of hydroxilated fibers.
A faster electron transfer rate towards the VO^{2+}/VO_2^+ redox reaction for thermally reduced graphene from graphite oxides than from graphene oxide was found and attributed to "enhanced restoration of the 2D graphitic structure of the platelets, leading to higher electrical conductivity of the material, and also to the presence of a large amount of reactive edges." [22]. Again, CVs were employed as electrochemical method.
A composite of graphite-graphite oxide (GO) was prepared and investigated for VRB applications by Li et al. and even schematics for a catalytic mechanics were presented [23]. It was stated that because of "oxygen functional groups on the basal planes and sheet edges of the GO materials, more reactive ions can be adsorbed onto the electrode surface, the

electron transfer and oxygen transfer processes can also be catalyzed and become more faster (sic!) on the composite electrode than on the graphite electrode.”. CVs and non-normalized EIS were used as electrochemical methods to deduct the catalytic mechanism. There is a multitude of similar studies and a recent review gives an overview about the application of carbon materials in RFBs [13].

As it will be detailed in chapter 4, it is complicated to extract reliable kinetic information from high-surface area, porous electrodes as commonly employed for VRBs. On the one hand, normalization is difficult, as the true electrochemically active surface area is typically unknown. On the other hand, popular experimental techniques that employ potential ramps yield an apparent kinetic effect for porous electrode structures that overestimates the true electrode kinetics [14,24]. To make things more complicated, addition or removal of surface functional groups changes the hydrophilicity of the electrode, drastically altering the wetting behavior and therefore the electrochemical active surface area. The catalytic effects found in the studies detailed above might have been only an apparent phenomenon and especially the contribution of electrode morphology should be scrutinized.
An effort to revisit the electrocatalysis of the VO^{2+}/VO_2^+ redox reaction is performed in chapter 5.

Before going into details and considering the relatively complicated VO^{2+}/VO_2^+ redox reaction, in that reaction electron transfer is coupled to two chemical reactions [25], the Fe^{2+}/Fe^{3+} redox reaction was analyzed. It was employed as a model system to find reliable techniques for determining charge transfer kinetics in chapter 4. Different electrochemical techniques are investigated regarding their suitability on flat model electrodes and porous MWCNT electrodes. It will be concluded that both potential step (PS) and EIS measurements are suitable for the determination of the exchange current on flat and porous electrodes. Normalization to recalculate the exchange current to a more comparable exchange current density can be performed via the double layer capacitance. Additionally, single and double current steps, cyclic and linear voltammetry are tested.

Building on the obtained findings, the electron transfer on MWCNT with various degrees of functionalization is tested for the VO^{2+}/VO_2^+ and the Fe^{2+}/Fe^{3+} redox reaction in chapter 5. A novel evaluation method is introduced that employs the fact that both the double layer capacitance and the charge transfer resistance can be obtained from a single EIS measurement and that both observables contain the true electrochemically active surface area. As the latter also contains kinetic information, a slight mathematical rearrangement eliminates the unknown surface area and yields the desired, normalized information. Using this simple method we were the first group to show that the VO^{2+}/VO_2^+ redox reaction is actually hindered by the presence of surface functional groups, not catalyzed [14]. The accuracy of this statement was later supported by other groups [26,27].
However, this result also suggests that a large number of previous studies claiming superior

activity on carbon nanomaterials should be revisited and the contribution of electrode hydrophilicity and electrode geometry should be especially considered [18–20,22,23,28].

Chapter 5 shows that the VO^{2+}/VO_2^+ redox reaction cannot easily be catalyzed on carbon electrodes, which ultimately means that the VRB is likely to remain a low-power density device. Therefore, it is logical to follow a novel approach to circumvent the shortcomings of the VRB, low energy- and power density, altogether.

There have been several approaches to design a novel RFB with characteristics superior to the VRB.
In the Sandia National Laboratory of the United States room temperature ionic liquids (RTILs) were developed which contain copper, manganese or zinc cations as redox center [29]. At least one these metal-based RTILs, the one containing Mn^{2+}, showed facile redox-kinetics on a glassy carbon electrode. Idea was that redox-active RTILs could reach very high concentrations of redox-centers, as the electrolyte itself carries them. This could lead to a RFB with a very high energy density. The authors stated that high viscosity, low conductivity and reversible electrochemistry still pose challenges that need to be tackled.
In order to minimize capital cost for large-scale energy storage, the group of M.J. Aziz suggested to employ organic *9,10-anthraquinone-2,7-disuplhonic acid (AQDS)* as redox couple for the low potential half-cell and Br_2/Br^- in the high potential half-cell to form a metal free aqueous RFB [30]. In their study the authors contrast costs of $US\$ \ 81 \ (kW\,h)^{-1}$ for active redox-species in the VRB with $US\$ \ 21 \ (kW\,h)^{-1}$ for *AQDS* and $US\$ \ 6 \ (kW\,h)^{-1}$ for bromine. Indeed it was shown that the overall capital costs of VRBs are very sensitive to vanadium costs and that the electrolyte contributes considerably (*37 %*) to a *1000 kW/12 MWh* system [31]. In addition to low costs, the *AQDS* redox couple exhibits fast kinetics with a determined rate constant $k_0 = 7.2 \ 10^{-3} \ cm \ s^{-1}$ which should enable high power density. However, at the moment low solubility and low cell-potential limit the energy density of this metal-free approach [30]. A similar cell chemistry, also tailored towards capital cost reduction, was presented by Yang et al. [32]. The proposed organic RFB employs quinones in both half-cells.
Dispersed Lithium-ion battery anode and cathode material form anolyte and catholyte in the semi-solid lithium RFB proposed by Duduta et al. [33]. More specifically, a suspension of *26 vol%* $LiCoO_2$ in $LiPF_6$ and alkyl carbonate blend functions as catholyte and *25 vol%* $Li_4T_5O_{12}$ in $LiPF_6$ and dimethyl carbonate represents the anolyte. Achieved coulombic efficiencies were relatively low (*73 %* in the first cycle), but the authors were confident to improve that with capacity matching. Reached concentrations of redox-molecule were high, with $10.2 \ mol \ L^{-1}$ for $LiCoO_2$ and $2.3 \ mol \ L^{-1}$ for $Li_4T_5O_{12}$ [33]. This could pave the way to a high energy density RFB, as the authors reported a value of $397 \ Wh \ L^{-1}$. Replacing $LiCoO_2$ with $LiNi_{0.5}Mn_{1.5}O_4$ led to a higher cell voltage and an even higher volumetric energy density of $615 \ Wh \ L^{-1}$.
Another approach using typical Li-ion battery materials was published by Huang et al. from

the National University of Singapore [34]. The energy storage materials are solid $LiFePO_4$ (cathode material) and $Li_4T_5O_{12}$ (anode material) and those lithium-oxides are oxidized and reduced by redox-mediator liquid that is circulated through tanks and power converter. A proof-of concept cell was built in which the glass ceramic membrane showed high resistivity and poor chemical and mechanical stability. However, if this issue could be overcome the authors estimate a *6 - 12* times improved energy density over state of the art VRB.

A novel approach was first proposed by our group [35] and later also reported by researchers from the Sandia National Laboratory [36]. It was suggested to employ polyoxometalates (POMs) as new, nanosized electron shuttles for RFBs. POMs are distinguished from more common extended metal-oxide networks by their solubility [37]. These molecules have three properties that make them very suitable for energy applications. First, they can easily be modified which allows for engineering of their properties [38,39]. Second, they can undergo multiple electron transfer which increases the number of electrons transferred per molecule and therefore the energy density of a future POM RFB [40]. Third, as their hydrodynamic radius is fairly large (some Angstroms), fundamental Marcus theory predicts facile electron transfer which entails a high power-density for future POM RFBs [41].
Pratt et al. utilized the three electron V^{4+}/V^{5+} –redox reaction of the $[SiV_3W_9O_{40}]^{7-}$ polyoxoanion as catholyte, and reduction of three of the W^{VI}-ions of the tungsten framework of same molecule as anolyte [36].
The two tri-Manganese substituted Keggin polyoxoanions employed by us have the advantage of shuttling six electrons per molecule instead of three which could double the energy density at the same concentration [42].

Chapter 6 is a detailed electrochemical study of $[Mn^{II}_3(H_2O)_3(OH)_3SiW_9]^{7-}$ and $[Mn^{III}_3(H_2O)_3(OH)_3SiW_9]^{4-}$. Besides asserting the fact that the molecules transfer six electrons at suitably high potential with fast kinetics, also the reaction mechanism was intensively investigated [39,42]. It was the first study that showed that the initial oxidation state has an effect on the redox behavior, which was explained in the framework of Born solvation energy.

Chapter 2 provides the required theoretical background while chapter 3 details the experimental procedures.

As the three chapters presenting results deal with quite different topics, summaries and conclusions are placed after each single chapter to keep the presentation concise.

After the experimental results of this work are presented, chapter 7 discusses how physical parameters, like the kinetics of an electron transfer, influence macroscopic, economic properties of RFBs. For a base case RFB (*1000 kW / 12 MWh*) capital costs will be estimated for the VRB and for a novel All-POM RFB.

Lastly, an outlook assesses what the direction of future research should be in order to realize RFBs with higher power- and energy density.

Chapter 2
Fundamentals

2.1 Potentials, Fermi levels in electrolytes and the absolute scale of redox potentials

In order to establish a robust basis to treat electrochemistry from a physical point of view and also to enable comparison of physical chemistry to other fields of physics, like solid state and semiconductor physics, the term *potential* has to be accurately introduced [43]. This section will closely follow the argumentation of the seminal publication by Heinz Gerischer and Walter Ekardt that derived the Fermi Energy E_F in electrolytes [44].

The location of E_F in a metal is shown in Fig. 2.1. This value can be directly measured in metals and semiconductors by photoelectron emission into vacuum [45]. In this experiment the minimum (photon-) energy required to extract one electron from the attractive forces of the bulk by passing the interface that is free of excess charges is determined. Due to a relaxation process, however, a dipole barrier will normally exist at the interface that contributes an additional electrostatic potential energy difference. Therefore, the workfunction W is commonly split into two parts, one for the dipole layer contribution χ and the other is equivalent to the chemical potential μ_e of the electrons in the bulk [46]. As reference potential usually the average electrostatic potential energy of an electron in the conduction band formed by the overlapping potentials of the nuclei is defined: $V_i(-\infty)$ (compare Fig. 2.1). Far from the interface the energy of an electron is given by $V_i(+\infty)$ and its difference to the vacuum level is a result of the dipole layer at the boundary; this deviation from the vacuum level is given by $e\,\varphi(\mathrm{z})$, in which $\varphi(z)$ is the Galvani potential. In absence of excess charges at the interface χ is defined as:

$$\chi = \varphi(-\infty) - \varphi(+\infty) \tag{2.1}$$

On the other hand, the chemical potential μ_e is given by:

$$\mu_e = E_F - V_i(+\infty) \tag{2.2}$$

Therefore, the E_F in a metal can be expressed as:

$$E_F = -W = \mu_e + e\chi \equiv \overline{\mu_e} \tag{2.3}$$

The Fermi energy is equivalent to the electrochemical potential $\overline{\mu_e}$.

In a redox electrolyte, an electrolyte that contains a redox-couple, $E_{F,El}$ has a different expression [44]:

$$E_{F,El} = \mu_{red} - \mu_{ox} + e\,\chi_s = -I + S_{red} - S_{ox} + e\,\chi_s \tag{2.4}$$

In this equation μ_{red} and μ_{ox} are the chemical potentials of the reduced (red) and oxidized (ox) species in solution and χ_s is the surface potential of the electrolyte. This is equivalent to an expression containing the ionization energy I and the free energies of solvation for reduced (S_{red}) and oxidized (S_{ox}) molecules. S_{red} and S_{ox} also contain the interaction with components of the solution, like ligand attachment and solvation shell formation.

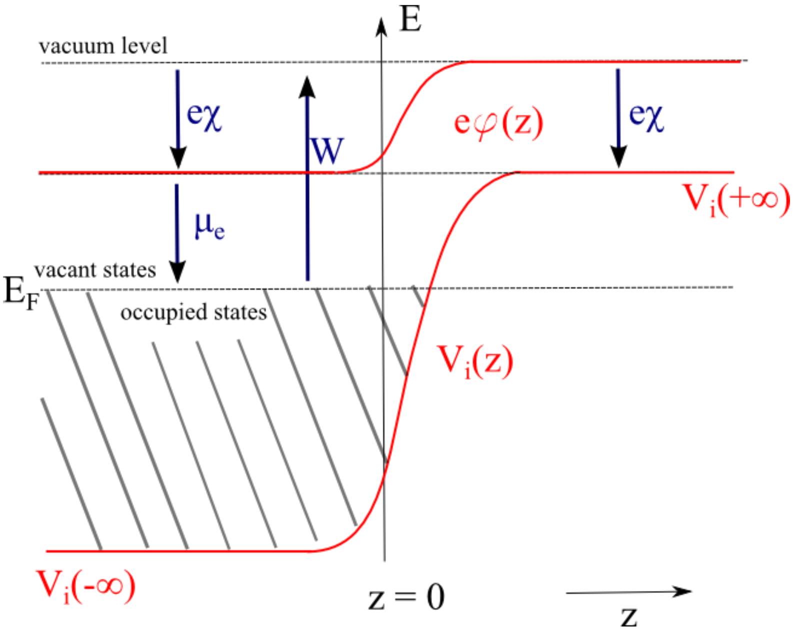

Figure 2.1 *- Electronic energies at the metal/vacuum interface in absence of excess surface charge. The graph is adapted from* [44].

This influence of the free energies of solvation on $E_{F,El}$ can be seen in two examples, as the system properties manifest themselves in a shift in the equilibrium potential U_0. Exchanging the ligands of the ferric/ferrous redox-couple from aquo-groups $(Fe(H_2O)_6)^{2+/3+}$ to cyano-groups $(Fe(CN)_6)^{4-/3-}$ shifts U_0 from *+0.771 V vs.* Normal Hydrogen Electrode (NHE) to *0.361 V vs.* NHE [47]. In an electrolyte that contains sulfate ions and $(Fe(H_2O)_6)^{2+/3+}$ U_0 is decreased by *-0.08 V* to *0.69 V vs.* NHE [48].

These observations state that E_F of a metal and $E_{F,El}$ of a redox-electrolyte are different and that therefore the electrons in these phases possess different potential energies. Once brought into contact, however, a current will flow until $\overline{\mu_e}$ is constant across the interface. As soon as equilibrium is reached the resulting potential difference across the interface is the Volta potential difference ΔU:

$$\Delta U = U_2 - U_1 = (W_2 - W_1)/q \tag{2.5}$$

From here Gerischer and Ekardt propose a method to determine the $E_{F,El}$ on an absolute scale of redox potentials relative to a reference point, which is the vacuum above the electrolyte solution [43,44]. In a series of articles S. Trasatti scrutinized this absolute scale of redox potentials and gave a value for the electron work function of the Standard Hydrogen Electrode (SHE) of ~ *4.7 - 4.8 eV* on mercury electrodes [43,49,50].

2.2 Electrochemical double layer

It was stated in the previous section that immersion of a metal into an electrolyte will lead to a (Volta) potential difference ΔU across the interface because of the different electronic potential energies. As a result, charges accumulate at the interface so that $\overline{\mu_e}$ is constant across this boundary and an electrochemical double layer (ECDL) will form. H. L. F von Helmholtz realized as early as 1853 that this electrode-electrolyte interphase can be modelled as a parallel plate capacitor [51]. The metal electrode can be seen as one plate while the ions in the solution form the counter-charge. A differential capacitance C_H is obtained which is inversely proportional to the distance between the two virtual plates *z* and directly proportional to the dielectric constant ε_r, the permittivity of free space ε_0 and the electrochemical active surface area (ECSA) *A*:

$$C_H = \frac{d\,Q}{d\,(\Delta U)} = \frac{\varepsilon_r\,\varepsilon_0\,A}{z} \tag{2.6}$$

This innermost region of charge carrier accumulation within the electrolyte is called Helmholtz plane (HP) which is shown in Fig. 2.2.

A. Gouy extended the concept of the Helmholtz double layer upon realizing that the thermal motion of ions would destroy the rigid HP [52]. Also, the accumulation of charges in the ECDL would cause an osmotic pressure as the concentration of ions is lower in the bulk of the electrolyte. L. Chapman suggested that the osmotic pressure is in equilibrium with the electrostatic force [53].

The charge density $\varrho(z)$ is related to the potential difference $\Delta\varphi = \varphi(z) - \varphi(0)$ between interface and distance *z* by:

$$\varrho(z) = \mathrm{F} \sum_j c_j\, n_j \exp\left(-\frac{n_j F}{R\,T}\,\Delta\varphi\right) \tag{2.7}$$

where F is the Faraday constant, c_j the concentration of species *j*, n_j the valence of ions *j*, *R* the gas constant and *T* the absolute temperature. The Poisson equation gives the relation between the charge density and the Laplace operator applied to $\varphi(z)$. Combination of eq. 2.7 with the Poisson equation for arguments of the exponent << 1 (Taylor series of exponential function) yields [54]:

$$\nabla^2 \varphi = \frac{4\,\pi F^2}{\varepsilon_r \varepsilon_0 RT} \sum_j n_j^2 c_j \Delta\varphi = \xi^2 \Delta\varphi \tag{2.8}$$

For a one-dimensional geometry ($\partial^2\,\varphi/\partial x^2\ = \partial^2\,\varphi/\partial y^2\ = 0$) eq. 2.8 can be expressed as:

$$\Delta\varphi = -\frac{4\,\pi}{\varepsilon_r\,\varepsilon_0\,\chi} Q_e \exp(-\chi\,z) \tag{2.9}$$

with excess charge Q_e in the electrolyte.

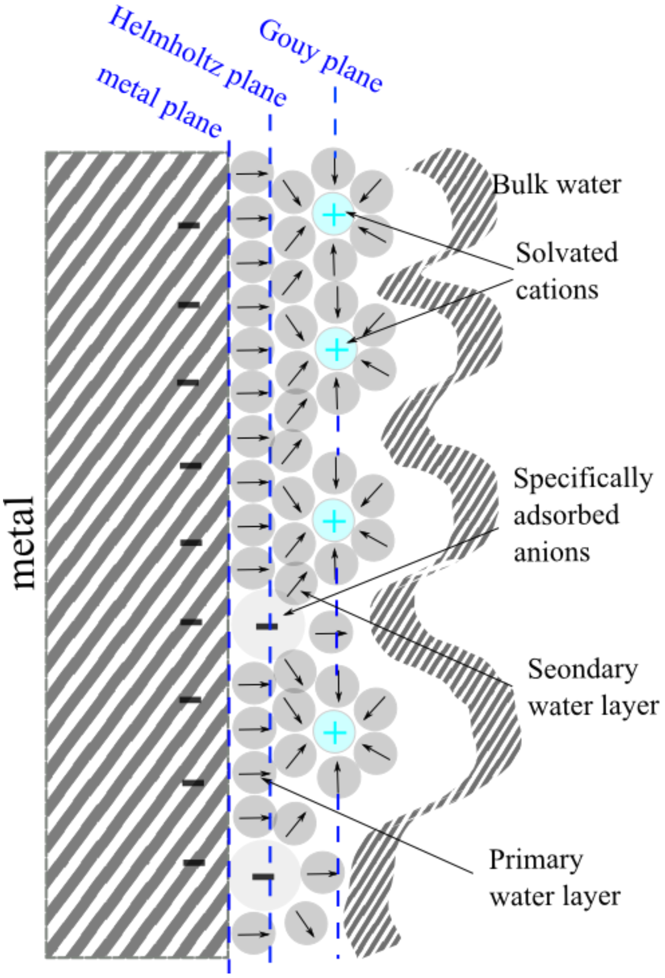

***Figure 2.2** – Model of the electrochemical double layer. The graph is adapted from* [55].

Equation 2.9 suggests that the potential drops exponentially from the interface to the electrolyte with a characteristic, inverse length ξ that was introduced in eq. 2.8. The Debye length λ_D is $1/\xi$ and is defined as the thickness of the polarized layer of ions adjacent to a charged surface [56]. The capacitance of the diffuse double layer C_d is given as:

$$C_d = -\frac{\varepsilon_r\, \varepsilon_0}{4\,\pi} \lambda_D^{-1} \tag{2.10}$$

which strongly depends on the electrolyte concentration c_j.

O. Stern introduced the finite size of ions and particles of the solvent to double layer theory [57]. Furthermore, he divided the charges into a part corresponding to the HP and another one which is similar to the diffuse double layer of Gouy-Chapman. Only in the HP the particles were modelled as non-point charges, as remarked by V. Freise [58]. This is important because the charges in the electrolyte can approach the counter charges in the solid phase only to a smallest possible distance that is given by the radius of the hydrated ions (several Angstroms) [54]. A representation of these ideas is given in Fig. 2.2. The primary water layer and specifically adsorbed anions form the HP, secondary water layer and solvated cations are present in the Gouy plane. The corresponding electronic energy levels at the electrode-solution interface within the ECDL are shown in Fig. 2.3.

The capacitance of the HP C_H and the diffuse capacitance C_d are in series and therefore the total capacitance of the ECDL C_{DL} is given by [59]:

$$\frac{1}{C_{DL}} = \frac{1}{C_H} + \frac{1}{C_d} \tag{2.11}$$

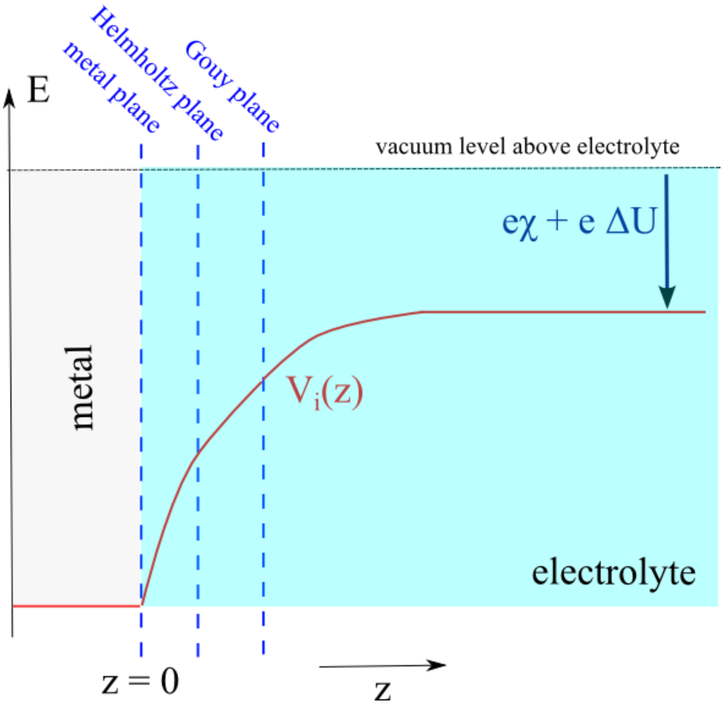

***Figure 2.3** – Electronic energies at an electrochemical double layer as shown in Fig. 2.2*

While the Guy-Chapman-Stern model explains experimental results quite well, in its derivation some approximations were made that were subjected to many studies later on

[54,60,61]. One simplification was the independence of the dielectric constant on the spatial coordinate when applying the Poisson Equation (eq. 2.8). However, it is important to note that ε_r for small distances z from the metal surface is much smaller than in bulk due to distortions caused by the massive electric field experienced there [55,62,63]. This complication should only affect C_H as for this effect of dielectric saturation to occur very high electric fields are required.

Another approach was to model the electrolyte as an ensemble of N particles with finite size interacting with the charged electrode within the potential of neighboring particles [64].

The topic of double layer theory is still part of scientific discussion. For example, a recent set of publications by the group of A. Kornyshev dealt with the formation of the ECDL in ionic liquids (ILs) [65,66]. The authors argue that the classical electrochemical theories do not hold for ILs as they cannot be treated with dilute-solution approximation. They propose the application of density functional theory (DFT) and statistical mechanics and their equations approach the classical expressions of Gouy-Chapman theory when the volume of liquid excluded by the ions is taken to be zero.

2.3 Standard and equilibrium potentials

A difference in E_F of two phases prior to contact leads to transport of charged particles once the two phases are in contact with each other [54]. Once the equilibrium potential U_0 is reached, the reaction apparently stops. However, only the net current equals zero, the forward and reverse reaction rates compensate each other. The current of either forward or reverse reaction is the exchange current I_0 which is a measure for the kinetics of a redox reaction. Normalizing I_0 by concentration of redox species and electrode area gives the fundamental electron transfer constant k_0 [67]:

$$k_0 = \frac{I_0}{n\,F\,A\,c} \tag{2.12}$$

where n is the number of transferred electrons per molecule, the electrode reaction valence. Equation 2.12 holds for the case of equal concentrations of oxidized and reduced species. Another common expression is the exchange current density j_0 which is the exchange current normalized by the ECSA A.

If the Gibbs free energy change ΔG^0 is known U_0 can be calculated thermodynamically, as the change in ΔG for the conversion of one Mole is given as:

$$\Delta G^0 = -\,n\,F\,U_0 \tag{2.13}$$

The derivation of above formula is based on Faraday's law and requires that the reaction proceeds at an infinitesimal small current, so that the cell potential ΔU does not deviate notably from U_0.

For a multicomponent system U_0 is given by the sum of chemical potentials times the stoichiometric factors ν_j:

$$U_0 = \frac{1}{n\,F}\sum_j \nu_j \mu_j \tag{2.14}$$

U_0 does also depend on temperature, pressure and concentrations c_j (or rather activities a_j) of components S_j. The dependence on a_j is given by one of the most important equations of electrochemistry, the Nernst equation [54]. This relation is derived by substituting the activity dependence of the chemical potential:

$$\mu_j = \bar{\mu}_j + RT \ln a_j \tag{2.15}$$

into eq. 2.14:

$$U_0 = U^{\theta} + \frac{R\,T}{n\,F} \sum_j \nu_j \ln a_j \tag{2.16}$$

The characteristic standard potential U^{θ} is a tabulated value and can be found in the literature for a multitude of different redox reactions [47].

As it is not convenient to measure electrode potentials on an absolute scale, the method discussed in 2.1 to relate it to the vacuum energy is not practical, they are experimentally measured against a reference electrode that exhibits a well-known, reproducible U_0. An example for such a reaction is the SHE, which was suggested as reference electrode by W. Nernst [54]. The electrode consists of a platinized sheet immersed in an acid with hydrogen ion activity $a_{H^+} = 1\ mol\,L^{-1}$ ($pH = 0$) and hydrogen gas is supplied to the acid at *1 bar* pressure. Its U_0 is defined as *0 V* on the SHE potential scale. The reaction that establishes the potential is:

$$2\,H^+(aq) + 2\,e^- \leftrightharpoons H_2 \tag{2.17}$$

Throughout this work NHE will be used as reference scale. While SHE is a theoretical construct, NHE can be actually measured by immersing a *Pt* electrode in an electrolyte of above given properties. However, the H^+ will interact with other ions and therefore their activity will be roughly *0.8*, shifting $U_{0,NHE}$ from *0 V vs. SHE* [68].

2.4 Charge transfer reactions

If a current flows through an electrode its potential U differs from U_0. This difference in potential called overpotential:

$$\eta = (U - U_0) \tag{2.18}$$

A positive overpotential is always correlated to a positive (anodic) current, a negative overpotential to a negative (cathodic) current (see Fig. 2.4). According to Bonhoeffer, Gerischer and Vetter there are four different kinds of overpotential [54]:

- Charge-transfer overpotential. Only the charge transfer reaction for the transport of charge carriers through the ECDL is hindered;
- Reaction overpotential. There is a coupled chemical reaction (independent of potential) that is hindered and impedes the current flow;
- Crystallization overpotential. The incorporation or removal of ions into or from a crystal lattice is hindered;
- Diffusion overvoltage. The diffusion of reacting species to the electrode is slow and therefore hinders the reaction to proceed.

The first description of charge-transfer overpotential was published by J.A.V. Butler and T. Erdey-Gruz and M. Volmer for the cathodic evolution of hydrogen from protons [69–71].

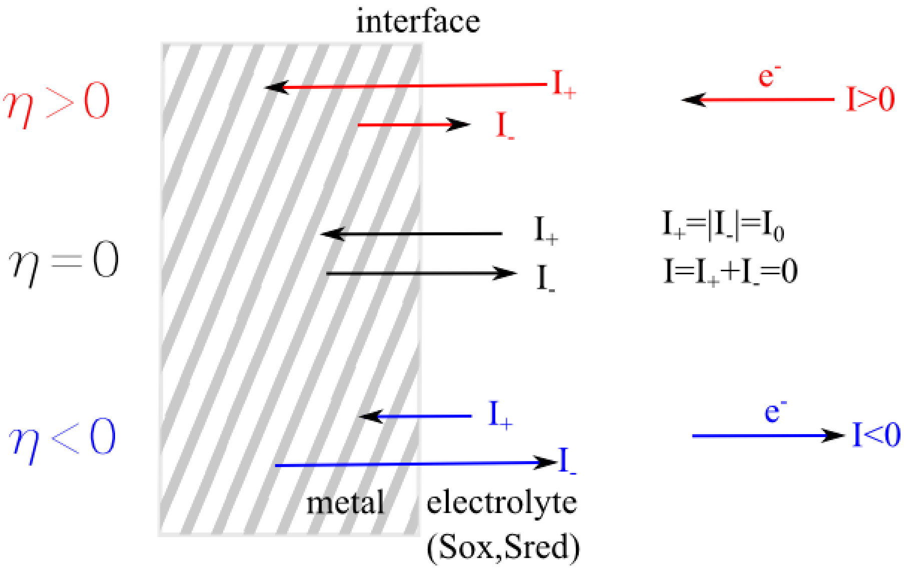

Figure 2.4 *- Schematic of the currents at a redox electrode in dependence on the overpotential* η*. The metal is immersed in an electrolyte containing redox species* S_{ox} *and* S_{red}*. The graph is adapted from* [54].

In Fig. 2.4 the magnitude and directions of currents in dependence on the applied overpotential η at a redox electrode are schematically presented. Regardless of η, electrons are exchanged (donated and accepted) by the metal with the redox species S_{ox} and S_{red} in the electrolyte. Thereby the oxidized species S_{ox} is reduced and the reduced species S_{red} is oxidized:

$$S_{ox} + e^- \leftrightharpoons S_{red} \tag{2.19}$$

The anodic partial current I_+ and the cathodic partial current I_- add up to the total current I which equals zero in the case of $\eta = 0$.

Charge-transfer reactions at redox electrodes were quantum mechanically treated by Gurney, Gerischer, Levich and Dogonadze [72–74]. Just like the theory by R.A. Marcus, their work was based on the Franck-Condon principle [41,75]. The Franck-Condon principle approximates that an electronic transition occurs without change in position of the nuclei, that the transition is vertical on a scale of nuclear reaction coordinates [76].

For a redox reaction to occur a redox-species has to go from the local minimum of Gibbs free energy of the reduced state to the local minimum of the oxidized state or vice versa. In the classical treatment this transition is coupled to overcoming either the anodic or the cathodic activation energy E_a [54]. A quantum mechanical treatment, however, allows for tunneling of a particle with mass m and energy E_0 through a (rectangular) energy barrier with probability P:

$$\mathrm{P} \approx \exp\left(-\frac{4\pi a}{h}\sqrt{2\,m\,(E_a - E_0)}\right) \qquad (2.20)$$

here h is the Planck constant and E_a and a are height and width of the energy barrier. As the electron mass is tiny ($m_e = 9.1\ 10^{-28}\ g$), the electron has a significant probability of tunneling through an energy barrier at room temperature (e.g. $E_a = 1\ eV$, $a = 0.5\ nm$, $m = m_e$, $E_0 = k_BT$ ➔ $\mathrm{P} = 6\ 10^{-3}$). On the other hand, quasi-thermodynamic transfer over the potential barrier given by Boltzman-function ($\mathrm{P} = exp(-E_a/k_BT)$) for the same parameters yields a probability of only $\mathrm{P} = 5\ 10^{-12}$ [54].

During oxidation of a species in the electrolyte an electron transfers from an occupied state in the electrolyte to an unoccupied state in the metal, the opposite holds for a reduction process.

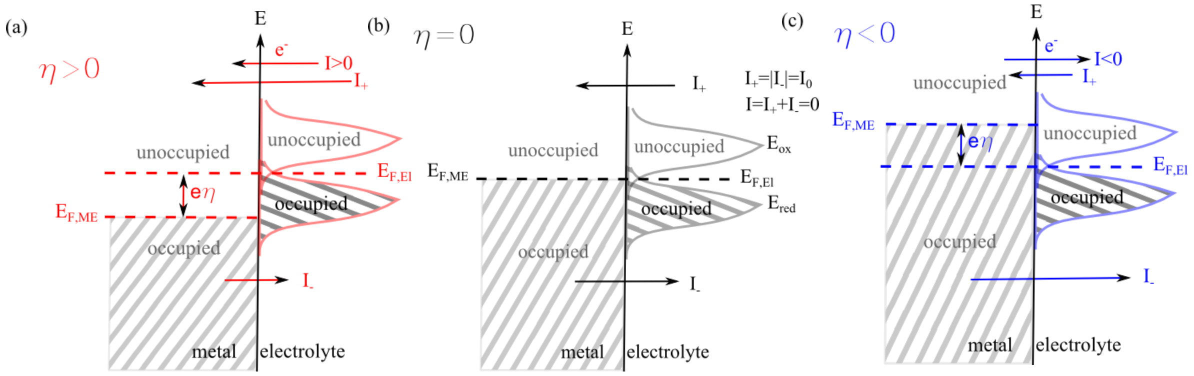

***Figure 2.5** - Schematic representation of energy levels during the course of a redox charge-transfer reaction by the quantum mechanical tunneling effect with currents in the case for **(a)** anodic, **(b)** no and **(c)** cathodic overpotential. The shown energy states in the electrolyte are proportional to the concentration of species S_{ox} and S_{red}. The graph is adapted from* [54].

Fig. 2.5 shows a quantum mechanical picture of charge-transfer redox reactions. In Fig. 2.5a an anodic overpotential is applied to the metal (electrode), therefore electrons from the occupied state in the electrolyte can tunnel into unoccupied states in the electrode, oxidizing the electrolyte which results in a net positive current. The opposite case is shown in Fig. 2.5c, a negative overpotential is applied and electrons tunnel from the metal (electrode) into unoccupied states of the electrolyte. Fig. 2.5b was treated in the previous section; when $E_{F,Me} = E_{F,El}$ the redox system has reached its equilibrium potential and no net current flows.

The electronic states in the metal follow the band model and are the product of density of states (DOS) and Fermi distribution function, the details can be found in condensed matter physics textbooks [77].

Within an electrolyte that contains a dissolved redox system the occupied states are formed by molecules S_{red} and the unoccupied states are represented by oxidized molecules S_{ox}. The energy levels of S_{red} and S_{ox} are broadened due to interactions with the solvent (e.g. there are several spatial distances between the atoms of the solvation shell that possess the same energy level). The density of states within the electrolyte *(DOS_{El})* has a two maxima at E_{red} and E_{ox} (compare Fig. 2.5b) [74]. These maxima are functions of the concentration c_{red} and c_{ox} respectively [54]. Furthermore, the Fermi distribution is valid and $E_{F,El}$ depends on the ratio of c_{red}/c_{ox}.

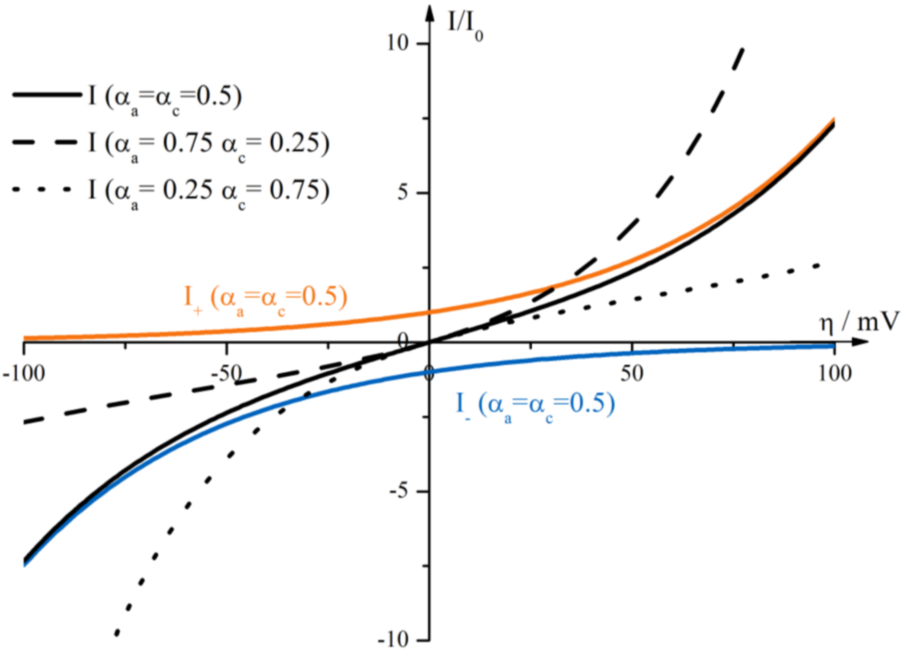

Figure 2.6 *- Calculated values for eq. 2.21 in units of current normalized by exchange current* I/I_0*. While* $n = 1$ *and* $T = 300$ *K were kept constant, the transfer coefficients* α_a *and* α_c *were varied according to the information given in the graph.*

Applications of a semiconductor as electrode instead of a metal complicates the situation as the electrons are only located within the conduction band and the band gap has to be taken into account [54,77,78].

The equation that gives the current I in dependence of an applied overpotential η is the Butler-Volmer equation, derived by T. Erdey-Gruz and M. Volmer [54]:

$$I = I_0[\exp\left(\frac{\alpha_a n\,F}{R\,T}\eta\right) - \exp\left(-\frac{\alpha_c n\,F}{R\,T}\eta\right)] \qquad (2.21)$$

where α_a is the anodic and α_c the cathodic transfer coefficient which give the symmetry of the potential barrier. As proven by Horiuti and Polanyi, eq. 2.21 can be derived both from a classical and a quantum mechanical approach [79].
Examples for trajectories calculated from eq. 2.21 can be seen in Fig. 2.6. As stated in Fig. 2.4 and Fig. 2.5, the total current I is the sum of anodic I_+ and cathodic I_- current.

Using the Taylor expansion eq. 2.21 can be simplified to (small overpotentials):

$$I = I_0\,\frac{(\alpha_a + \alpha_c)\,n\,F}{R\,T}\eta \qquad (2.22)$$

This then immediately leads to the model of a charge-transfer resistance R_{CT} that is inversely proportional to I_0:

$$R_{CT} = \frac{\eta}{I} = \frac{RT}{I_0\,(\alpha_a + \alpha_c)\,n\,F} = \frac{RT}{j_0\,A\,(\alpha_a + \alpha_c)\,n\,F} \qquad (2.23)$$

For high positive (negative) overpotentials only the anodic (cathodic) branch of eq. 2.21 has to be considered to obtain a suitable approximation:

$$I = I_0\exp\left(\frac{\alpha_a nF}{RT}\eta\right) \text{ and } I = -I_0\exp\left(-\frac{\alpha_c nF}{RT}\eta\right) \qquad (2.24)$$

The question what can be considered as a small or high overpotential is tightly connected to the problem what relative error is acceptable. Table 2.1 gives relative errors for the two approximations (eq. 2.22 and eq. 2.24) in dependence of different overpotentials:

	$\lvert\eta\rvert = 10\,mV$	$\lvert\eta\rvert = 25\,mV$	$\lvert\eta\rvert = 50\,mV$	$\lvert\eta\rvert = 100\,mV$	$\lvert\eta\rvert = 200\,mV$
Rel. error linear approx.	*± 0.0067*	*± 0.0410*	*± 0.15*	*± 0.45*	*± 0.86*
Relative error exp. approx.	*± 2.0*	*± 0.58*	*± 0.15*	*± 0.018*	*± 0.00032*

Table 2.1 *- Listed are calculated relative errors for the linear approximation which is the quotient of eq. 2.22 and eq. 2.21 as well as for the exponential approximation which is the quotient of eq. 2.24 and eq. 2.21. A one electron reaction at room temperature was assumed with a symmetric energy barrier* $\alpha_a = \alpha_c = 0.5$.

From this table it is obvious that each approximation holds well for its designated range of overpotentials.

Experimental studies of electrode processes involve determining the rate(s) k_0 at which one or more charge transfer steps proceed across the electrode-solution interface [80]. In most scenarios this is done by controlling either potential or current and measuring the other observable to determine I_0, n, α_a and α_c via eq. 2.21**.** Electrochemical methods following this general approach will be described in the next section.

Determining the k_0 (from I_0 via eq. 2.12) together with an understanding of the reaction mechanism is pivotal for electrocatalytic studies. On the one hand, there are large differences in electron transfer rate found for a given reaction depending on electrode composition and its structure [81]. For example k_0 of the hydrogen evolution reaction (HER) (eq. 2.14) varies by ten orders of magnitude depending on the metal electrode material [82]. On the other hand, different products may be obtained on different electrodes in the same redox electrolyte. The anodic oxidation of ethylene (C_2H_4), for example, produces mostly aldehydes and acetone on Au electrodes while CO_2 is the main product on Pt electrodes [83]. Anderson and Eyring differentiate between three possible electrocatalytic effects of the electrode [80]:

- The free energy of activation is determined by the interaction between electrode and activated complex;
- The concentration of adsorbed reactants or intermediates is determined by the interaction of them with the electrode. Also the number of available surface sites is given by the electrode;
- Potential dependent specific adsorption of solvent or electrolyte onto the electrode is a material property of the electrode material.

The situation becomes more intricate when the electrode consists of nanoparticles on substrate. Structural effects such as the size of the nanoparticles [84–86], their dispersion [87,88] and the influence of the substrate material [89–93] have to be considered [81].

2.5 Electrochemical methods

While the Butler-Volmer equation (eq. 2.21) is relatively simple from a mathematical viewpoint, its application to experimental, electrochemical systems is complicated by a number of effects. In the terminology used by Vetter the intricacy stems from the fact that the charge-transfer overpotentials has to be separated from the other, possible overpotentials (reaction, crystallization, diffusion) [54].

Consistent with above declaration but rephrased, Yeager and Kuta state that to obtain kinetic information not only the heterogeneous charge transfer but also possible chemical reactions and the transport of reactants need to be investigated and their influence separated from pure electrochemical kinetics [94].

While the diffusion limitation obscures kinetics at longer measurement times, the charging of the ECDL shrouds the initial phase of electrochemical experiments by contributing a non-faradaic current (I_{NF}) to the faradaic current (I_F) of the electron-transfer reaction.

Therefore, this section is dedicated to presenting electrochemical methods to determine k_0 with their intrinsic advantages and limitations. This part follows the chapter "Techniques for the Study of Electrode Processes" in "Physical Chemistry – an advanced treatise" written by Ernest Yeager and Jaroslav Kuta [94].

Electrochemical methods generally work by perturbing the electrode-electrolyte system from its equilibrium state and measuring the steady-state or non-steady-state response [94]. While Yeager and Kuta listed seven such perturbations, only displacement of the electrode potential from U_0 and passage of a current are considered here.

For all the non-steady state methods the current associated with charging the ECDL contributes to the external current:

$$I_{NF} = \frac{dQ_e}{dt} = C_{DL}\frac{dU}{dt} \tag{2.25}$$

It was shown by Paul Delahay that the straight-forward separation $I_F = I - I_{NF}$ is not always justified as the equations for the faradic current I_F, the continuity of fluxes and the total (external) current I form an interdependent set of equations [95–97]. To avoid complications, in order to make the current contributions separable, Yeager and Kuta suggest to use a high concentration of supporting electrolyte (0.1 M or higher) as well as only investigate systems that do not adsorb specifically [94]. The reasoning behind this is that the changes of excess surface species $d\Gamma_{Ox}/dt$ of S_{Ox} and $d\Gamma_{Red}/dt$ of S_{Red} are then negligible compared to the mass-transport fluxes which decouples the formerly interdependent equations [98].

2.5.1 Electrode potential steps

Electrode Potential Steps (PSs) are a method that perturbs the electrode potential from U_0 or some other resting potential relative to a fixed reference potential and measures the current (therefore it is also called Chronoamperometry) [99].

When a PS is applied the electrode potential is not at the described potential for the very first time segment, ~10^{-5} s after the jump, because the ability of the potentiostat to apply current is limited [94]. After charging of the ECDL a decreasing current is observed. It diminishes as a concentration gradient develops at the electrode surface. The time-dependence of I_F during a PS experiment was investigated by a number of authors in the early 1950s and yields [100]:

$$I_F = I_0\left(\exp\left[\frac{\alpha_a\, n\, F}{R\, T}\eta\right] - \exp\left[-\frac{\alpha_c\, n\, F}{R\, T}\eta\right]\right) * \left(\exp[\lambda^2 t]\mathrm{erfc}[\lambda\sqrt{t}]\right) \tag{2.26}$$

where η is equal to the potential jump. The second part containing λ gives the time dependence with:

$$\lambda = \frac{I_0}{nF}\left(\frac{1}{c_O^*\sqrt{D_{Ox}}}\exp\left[\frac{\alpha_a nF}{RT}\eta\right] + \frac{1}{c_R^*\sqrt{D_{Red}}}\exp\left[\frac{\alpha_c nF}{RT}\eta\right]\right) \tag{2.27}$$

where D_{Ox} and D_{Red} are the diffusion coefficients of the redox species. Comparison with eq. 2.21 indicates that the I_F given in eq. 2.26 is equivalent to the current predicted by the Butler-Volmer equation with an added part correcting for diffusion and time dependence.

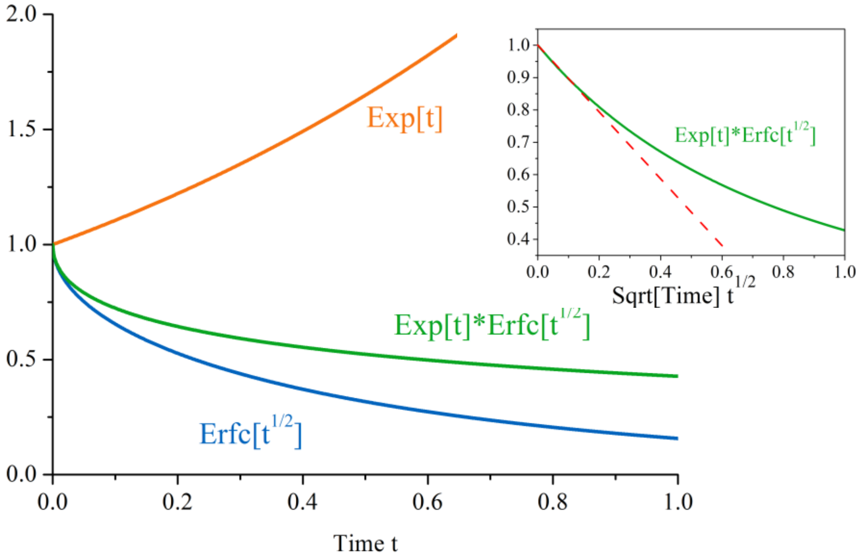

Figure 2.7 *- Calculated values for the functions from eq. 2.26 for $\lambda = 1$. The inset shows the square-root of time as abscissa. For small t the function can be approximated by a straight line (dashed red line) which allows for extrapolating to $I_F(t=0)$.*

As the error function is not very common, Fig. 2.7 gives the two functions responsible for the time dependence and their product for values of the independent variable from 0 to 1. For short times an approximation can be applied:

$$\left(\exp[\lambda^2 t]\mathrm{erfc}[\lambda\sqrt{t}]\right) \cong 1 - 2\lambda\sqrt{\frac{t}{\pi}} \qquad \text{for } \lambda\sqrt{t} \ll 1 \tag{2.28}$$

For short times a plot of I_F vs. $\sqrt{t}$ can be extrapolated back to yield the desired value of *I(t=0s)*. Unfortunately, within the initial phase of the PS the ECDL charging takes place and also the potential of the working electrode is not stable, as discussed earlier. Therefore, assuming a fast potentiostat, a concentrated supporting electrolyte (~ *1 M*) and a advantageously placed Luggin capillary for the reference electrode, Yeager and Kuta gave the fastest measurable $k_{0,max}$ [94]:

$$k_{0,max} \leq 2.5\ (D/\tau_{pot})^{1/2} \tag{2.29}$$

as a function of diffusion constant D and potentiostat response time τ_{pot}. For $\tau_{pot} = 50\ 10^{-6}\ s$ and $D = 10^{-6}\ cm^2\ s^{-1}$ the fastest measurable redox-reactions have a rate of $k_{0,max} = 0.35\ cm\ s^{-1}$.

Faster rates can be measured if the charging current of the ECDL is empirically determined and taken into account for the analysis [101]. An example for the presence of faradaic and non-faradaic current during a PS is shown in Fig. 2.8. The experiment shows a PS from a potential at which no electrochemical reaction is taking place to a potential at which O_2 is reduced at a graphitized carbon black electrode. If there is no O_2 present, if the used electrolyte is thoroughly purged by inert Ar, a PS leads to the orange curve in which the current is purely non-faradaic; it stems from the charging of the ECDL and it decays exponentially. The blue curve was recorded in an electrolyte that was flushed with O_2 prior to measurement for two hours at $0.015\ ml\ min^{-1}$. This curve is composed of both I_{NF} and I_F, the faradaic current reducing O_2 to $O^-_{2,ads}$ can clearly be seen and it gives a contribution throughout the measurement time. Subtracting the orange curve from the blue curve yields I_F. Therefore, recording a PS in an inert electrolyte is a way to experimentally determine the non-faradaic contribution to enhance PS measurements.

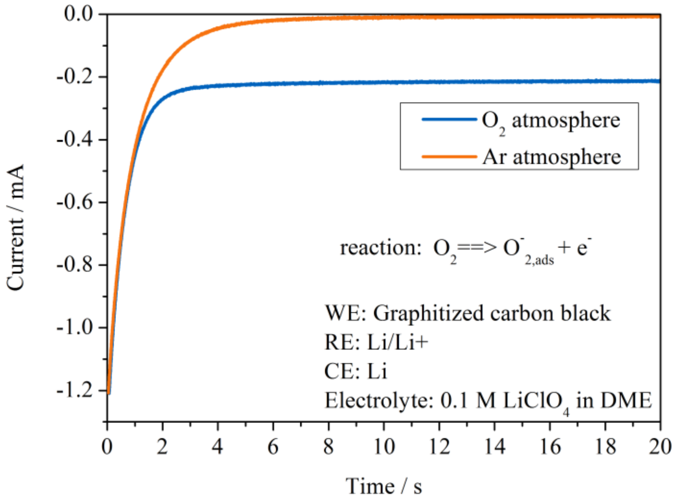

***Figure 2.8** - Experimental results for a PS experiment. The supporting electrolyte was 0.1 M $LiClO_4$ in 1,2-dimethoxy ethane (DME), electrodes are given in the graph. While both curves show non-faradaic current, only the transient taken in O_2-atmosphere has a non-zero faradaic contribution.*

2.5.2 Single and double current pulse(s)

For a single current pulse (SCP) a rectangular current pulse is passed through the working electrode and the resulting change in potential is recorded over time (Chronopotentiometry). A review of this method was written by Milan Paunovic [102].

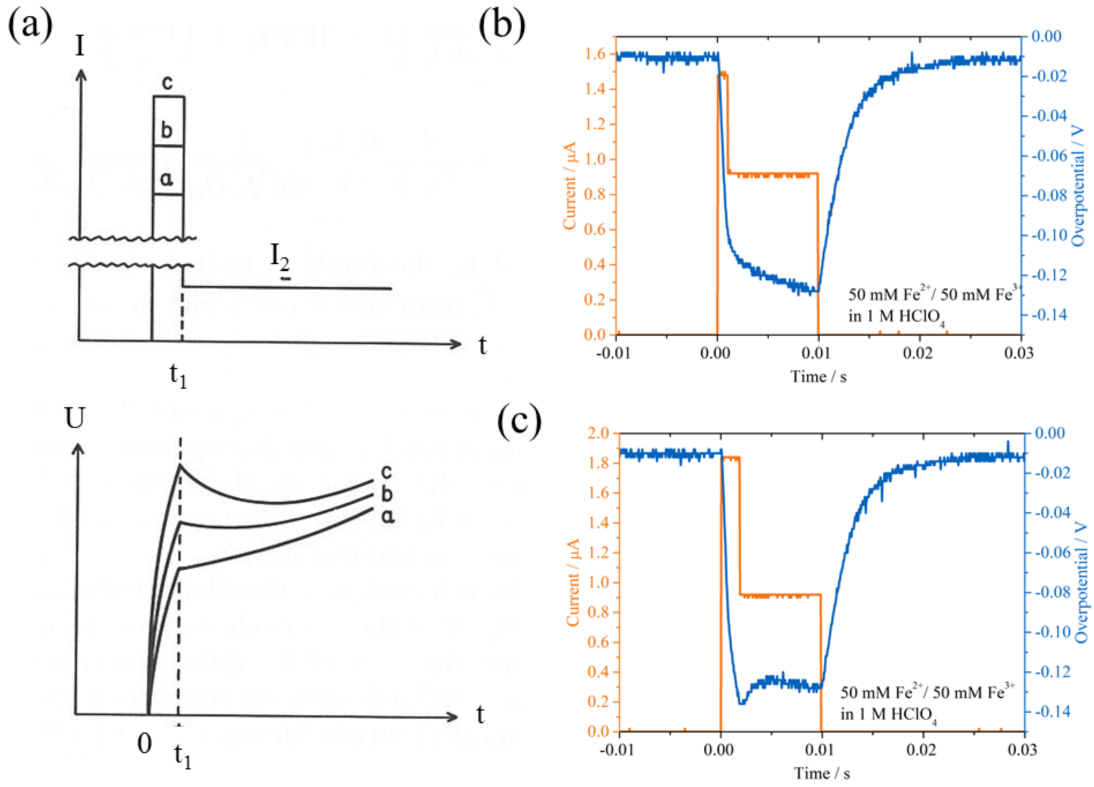

Figure 2.9* - (a)** *Schematics of the double current pulse technique. At time t_1 the first pulse ends and the second pulse commences. While currents c and b overcharge the ECDL, current a transfers the correct amount so that all non-faradaic currents subside at t_1. The graph is adapted from* [94]. *Exemplary curves of* ***(b) *under- and* ***(c)*** *over- charging the ECDL. The measurements were performed in the electrolyte given in the graph with a home-made galvanostat coupled to a function generator and an oscilloscope.*

While SCPs are generally very similar to PSs, the technique also suffers from non-faradaic current charging the ECDL, its η vs. t behavior is more complicated than I vs. t for the latter method:

$$\eta = -\frac{R\,T}{n\,F}\left[\frac{1}{I_0} + \frac{2\,L}{n\,F}\sqrt{\frac{t}{\pi}} - R\,T\left(\frac{L}{n\,F}\right)^2 C_{DL}\right] I \tag{2.30}$$

And:

$$L = \frac{1}{c^*_{Ox}\sqrt{D_{Ox}}} + \frac{1}{c^*_{Red}\sqrt{D_{Red}}} \qquad (2.31)$$

The additional intricacy stems from the fact that the changes in concentration of redox-species at the interface are smaller than one would anticipate because the measured current is partly non-faradaic, a contribution given by the third term in the brackets of eq. 2.30 [94]. Paul Delahay has estimated that $k_{0,max}$ measurable with SCP is ~ 0.2 cm s^{-1}.

The fundamental limitation of the SCP method for the study of very fast electrode processes is a result of ECDL charging currents. This problem that can be remedied by the double current pulse method (DCP) presented by Gerischer and Krause [103]. The method is schematically shown in Fig. 2.9a. A first, short current pulse serves to rapidly inject the required charges to charge the ECDL. Immediately afterwards a second current pulse is applied that is of the current of interest. The transferred charge in the first pulse should be adjusted in a way that the overpotential curve starts flat, $(d\eta/dt) = 0$. Fig. 2.9b is an example of a measurement in which the first pulse was insufficient to charge the ECDL. On the other hand, in Fig. 2.9c too much charge was transferred and the first pulse overcompensated the ECDL.

It was proposed that at the end of the first pulse the potential corresponds to the activation overpotential and that the concentration polarization (compare SCP) can be neglected [103]. Other authors disagreed [104] and the upper limit for $k_{0,max}$ was estimated to $0.5\ cm\ s^{-1}$ [105].

2.5.3 Linear and cyclic voltammetry

Linear voltammetry is a method that scans the potential at a certain rate. If there is one sweep between an initial potential and a final potential then the method is called linear voltammetry (LV). When the potential is continuously cycled between two vertex potentials it is called cyclic voltammetry (CV). In this work CVs are used to obtain first, semi-qualitative insights into an electrode-electrolyte system. With CVs it is possible to locate U_0 of a redox reaction, to approximately check for the reversibility of a reaction, to recognize adsorption –desorption processes and whether multiple reaction steps are involved [94]. The complete theoretical analysis in order to obtain kinetic information, is complex and electrode surfaces that deviate from ideal, flat geometry might lead to apparent electrocatalytic effects [14,24]. Theoretically, with potential scan-rates of several thousand volts per second, LS can be used to measure $k_{0,max}$ as high as $0.5\ cm\ s^{-1}$ [106]. One of the obvious challenges of such an effort, however, is the increase in non-faradaic contributions with faster scan-rates $\frac{dU}{dt}$:

$$I = C_{DL}\frac{dU}{dt} + I_F \tag{2.32}$$

2.5.4 Electrochemical impedance spectroscopy

As seen in eq. 2.23, the activity of an electrode can be expressed as an inverse resistance R_{CT}. This resistance related to the charge transfer plus the double layer capacitance C_{DL} in parallel combined with an ohmic resistance R_{Ohm} in series form an equivalent circuit that represents the polarization of an electrode that is slightly perturbed from equilibrium.

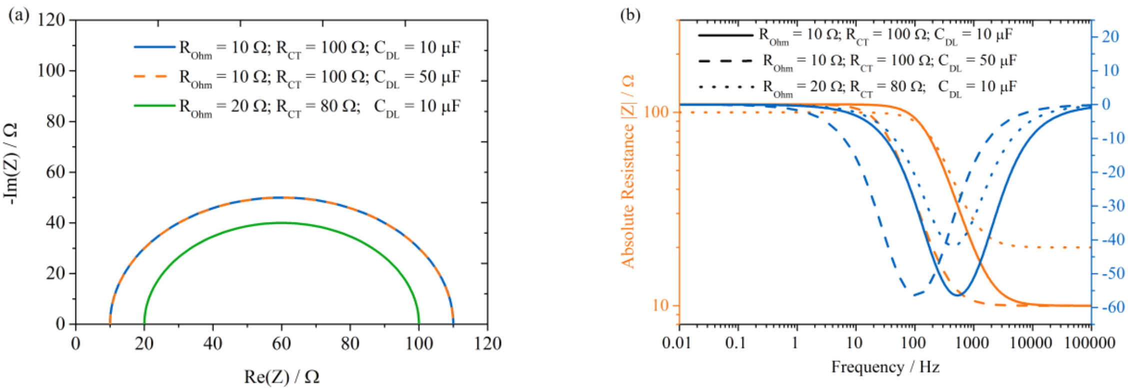

Figure 2.10 *- For this graph the response of three equivalent circuits to a sine-wave with amplitude 10 mV and frequencies from 10^{-2} Hz to 10^{5} Hz was simulated. The simulation parameters are given in the graphs.* ***(a)*** *Nyquist- and* ***(b)*** *Bode-representation.*

The fundamental concept of electrochemical impedance spectroscopy (EIS) is that the complex resistance Z of a parallel combination of a resistor and a capacitor is frequency dependent [107]:

$$Z = \frac{R}{1+i\,2\pi\,f\,R\,C} \tag{2.33}$$

with frequency of the sine-wave perturbation f and imaginary number i ($i = \sqrt{-1}$). Therefore, the expression for Z for the impedance associated with a single electrochemical reaction on a flat surface can be expressed as:

$$Z = R_{Ohm} + \frac{R_{CT}}{1 + i\,2\pi\,f\,R_{CT}\,C_{DL}} \tag{2.34}$$

This expression is plotted in Fig. 2.10. For high frequencies ($f \sim 10^5$ Hz) the quotient is zero and therefore $Z = R_{Ohm}$. From a physical perspective a viable explanation is that at high frequencies C_{DL} is shorted and R_{CT} is bypassed, as not enough charges are transferred for the capacitor to become fully charged and therefore blocking. At low frequencies ($f \sim 1$ Hz)

$Z \approx R_{Ohm} + R_{CT}$ and therefore R_{CT} is given by the width of the semicircle in Fig. 2.10a. For intermediate frequencies there is an imaginary contribution to Z.

The representation of $-Im(Z)$ vs. $Re(Z)$ plotted in Fig 2.10a is called a Nyquist-plot, while Fig 2.10b shows a Bode-plot. In the latter the logarithm to the base ten of the absolute resistance Z and the phase angle φ ($\varphi = tan^{-1}(Re(z)/Im(z))$) are plotted as ordinates. The abscissa is the frequency of the perturbing sine-wave.

The two representations are complimentary. While the Nyquist-plot is an excellent tool to obtain R_{Ohm} and R_{CT}, it is insensitive to C_{DL}. In Fig. 2.10a the blue curve and the dashed orange curve overlap, although the latter is calculated for a capacitance that is five times higher than the former. The Bode-plot on the other hand is able to resolve the three curves. However, this representation is also busier and less intuitive due to the double-logarithmic scale. In this work values for R_{Ohm}, R_{CT} and C_{DL} are obtained by fitting experimental curves to equivalent circuits.

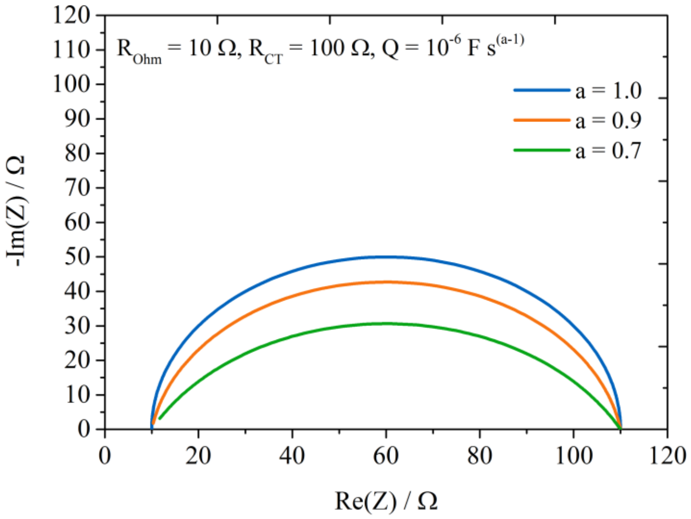

Figure 2.11 *- Nyquist plot of the response of three equivalent circuits to a sine-wave with amplitude 10 mV and frequencies from* 10^{-2} *Hz to* 10^{5} *Hz. The equivalent circuit contains a constant phase element (CPE) instead of a double layer capacitance.*

Nyquist plots are a suitable tool to identify depressed semi-circles as shown in Fig. 2.11 (the orange and the green curve are depressed). Depressed semicircles can be modelled employing a constant phase element (CPE) instead of C_{DL}. This reflects the heterogeneity of an electrode. As impedance data for a redox-reaction often reveals a frequency-dispersion that cannot be described by simple circuit elements, this "capacitance dispersion" CPE is introduced [108]. The relationship between effective C_{DL}^{eff} and CPE with parameters σ was proposed by Hsu and Mansfeld [109]:

$$C_{DL}^{eff} = CPE\ (2\pi f_{max})^{\sigma-1} \tag{2.35}$$

where f_{max} is the frequency at which φ has its extreme value in the Bode-plot and σ is a value between 0 and 1.

In order for EIS to be applicable two requirements have to be met. First, the redox-species in solution have to be in equilibrium, ideally $c_{ox} = c_{red}$ and the resting potential $U_{OCV} = U_0$. Second, the capacitance dispersion should be as small as possible. Flat, non-porous electrodes are advantageous [14]. If those conditions are met, EIS is a fast and reliable way to determine I_0 via R_{CT}.

2.6 Spectroscopic methods

In this work spectroscopic methods are used to support and complement the electrochemical techniques. Electrochemical methods are able to provide thermodynamic and kinetic insights into a range of processes driven by electron transfer. However, electrochemistry supplies only limited and indirect information on chemical composition of electrode and electrolyte or structural changes accompanying redox events [110]. Thermogravimetric analysis coupled to mass-spectroscopy (TGA-MS), scanning electron microscopy (SEM), Fourier-transform infrared spectroscopy (FTIR) and Raman spectroscopy were employed to establish a detailed picture of carbon working electrodes. Ultraviolet-visible light spectroscopy (UV-Vis) was used to investigate the molecular identity of ions in solution before and after bulk electrolysis.

2.6.1 Thermogravimetric analysis coupled to mass-spectroscopy

Thermogravimetric analysis (TGA) is a technique in which the weight and hence the mass of a sample is measured as a function of temperature [111]. It is possible to determine the nature of gases as they evolve during TGA with a mass-spectroscopy (MS); a connection of a TGA with a MS leads to the coupled method TGA-MS. TGA-MS is suitable to determine the following material properties [111]:

- Purity of crystalline non-polymers;
- Temperature stability;
- Oxidation stability;
- Chemical composition;
- Content of physisorbed water.

In this work TGA-MS in inert atmosphere was employed to determine the nature of surface functional groups on carbon materials and also their relative amount. In an oxygen atmosphere the method was used to obtain the oxidation stability of carbon materials which reflects the quality of their crystal structure.

Desorption range / °C	**Functional group**	**Detectable gas**	**References**
100 – 150	physisorbed water	H_2O	[112]
> 300	Phenols	H_2O	[112–115]
300 – 400	Carboxylic	CO_2	[112–115]
500 – 625	Anhydride	CO, CO_2	[112–115]
600 - 750	Lactone	CO_2	[112–115]
> 600	phenol, carbonyl, quinone	CO	[112–115]

***Table 2.2** - Literature values for desorption temperatures and evolved gasses for surface functional groups on carbon materials in inert atmosphere. The table is adapted from* [116].

The TGA setup consists of a furnace with a (compensation) balance. The balance is purged with protective gas (*Ar*) to limit the ingress of corrosive decomposition products. A blank measurement with an empty crucible is performed prior to every set of experiments to correct for buoyancy effects. This is necessary as the density of gas changes with variations in temperature and without corrections the sample would show an increase in mass during heating [111].

Results of a TGA measurement are typically displayed as mass vs. temperature. Changes in mass occur when the sample loses material due to a number of possible reactions with the surrounding atmosphere. If there is oxygen present in the measurement chamber organic samples can be decomposed by oxidation with O_2. Should the measurement chamber be flushed with inert gases, such as *Ar* or N_2, the sample can be prone to thermal decomposition.

MS is a good addition to TGA as it enables analysis of evolved gases. Through a capillary gaseous products are transported from the furnace chamber of the TGA to the ultra-high vacuum (UHV, $1.3\ 10^{-6}$ *mbar*) of the MS. There the molecules are ionized and electromagnetically separated according to the mass over charge (*m/q*) ratio. Then the number of detected ions over *m/q* at respective temperatures is recorded.

The interpretation of both TGA and MS data is done by comparison with literature values. Table 2.2 lists desorption temperatures and the detectable gas(es) for various molecules or surface functional groups that can be attached to carbons in inert atmosphere [116]:

The chemical composition of a number of surface functional groups that can be present on carbon is given in Fig. 2.12.

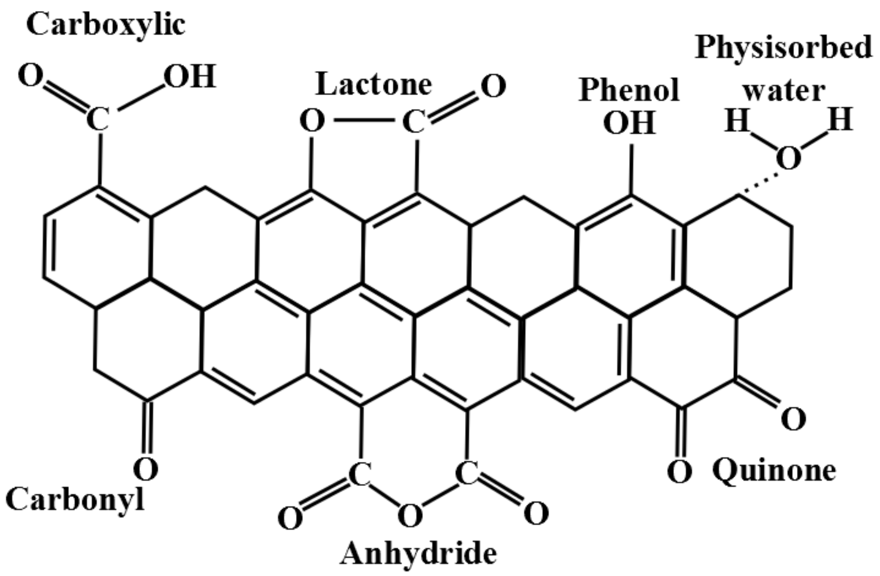

Figure 2.12 *– Selected surface groups on carbon.*

2.6.2 Scanning electron microscopy

In this thesis micrographs obtained with a SEM were used to obtain qualitative insights into the structure of glassy carbon electrodes decorated with MWCNTs. A detailed description of SEM instrumentation and how to interpret obtained images is beyond the scope of this work and can be found in several textbooks [117,118].

At the core of the SEM is an electron beam that is accelerated by some thousand volts and collimated by a system of electromagnetic lenses [119]. When the electrons hit the sample they will be partially slowed down, scattered, diffracted or reflected. Also, emission of secondary electrons (SEs) takes place. If the electron beam is scanned across the sample the number of transmitted, reflected or released electrons contains the necessary information to obtain the structure of the sample.

The method employed in this work to generate micrographs, and also the most commonly used detection mode, is SE imaging. The method is surface-sensitive, typically penetrating not deeper into the sample than 10 nm, and the SEs are normally ejected from the innermost K-shell. SE SEM images contain topographic information as the brightness of each scanned spot depends on how many SEs reach the detector. As a result, regions that a further away from the detector will appear darker in the micrograph [117,118].

2.6.3 Vibrational spectroscopy

Vibrations in molecules or crystals are caused either by absorption of photons (UV, Vis, IR-spectroscopy) or by scattering of photons (Raman spectroscopy) or electrons (electron energy loss spectroscopy) or neutrons (inelastic neutron scattering) [118].
The methods that operate based on absorption and scattering of photons were employed in this study and will therefore be briefly presented here. Again, the reader is referenced to textbooks for further details [77,117,118]. When the vibrations are caused by interaction of chemical bonds with an electromagnetic wave (photons or electrons), the excitation has to fulfil strict selection rules.

2.6.3.1 Fourier transform infrared spectroscopy

Many molecules have their fingerprint absorption lines in the infrared (IR) spectral range [120]. In FTIR spectroscopy an IR light source emits light onto the sample and a blank reference. A mirror system controls the interference of the two beams of light and after detection the software converts the interferogram to a plot of absorption over wavenumber [117].
In this work FTIR was employed to assert what kind of functional groups (compare Fig. 2.10) were attached to carbon material. Wavenumbers from $\tilde{\nu} = 4000\ cm^{-1}$ ($\lambda = 2.5\ \mu m$) to $\tilde{\nu} = 400\ cm^{-1}$ ($\lambda = 25.0\ \mu m$) were scanned. Within this range a number of bonds that are present in surface functional groups absorb the IR-light; these are given in Table 2.3:

Wavenumber / cm^{-1}	**Bond**	**Functional group(s)**	**Reference**
3440	O-H	Hydroxyl	[19,112,121]
2850-3000	$C\text{-}H_n$	Aliphatic	[112,121,122]
1710-1755	R-C=O	Lactone, Carboxylic, Anhydride	[19,112,121,123]
1633		Adsorbed water	[19,112]
1580	C=O, C=C	Carbonyl, Quinone	[112,121,123]
1170	C-OH, R-C=O	Phenol, Lactone, Carboxylic, Anhydride	[112,113,121]

Table 2.3 *- Literature values of wavenumbers at which certain chemical bonds absorb IR – light and functional groups that contain those bonds* [116].

The wavenumbers (and therefore the absorbed energies $E = hc\tilde{\nu}$, with speed of light c) are not sharp for a certain kind of bond because there are interactions between the different dipoles and also between dipole and substrate that broaden the possible stretching frequencies [118]. For example, the wavenumber of absorption of carbon monoxide (*C-O* stretching) adsorbed on pure *Pd* increases from 2070 to 2095 cm^{-1} with increasing *CO*-coverage due to intra-molecule interaction [124].

2.6.3.2 Raman spectroscopy

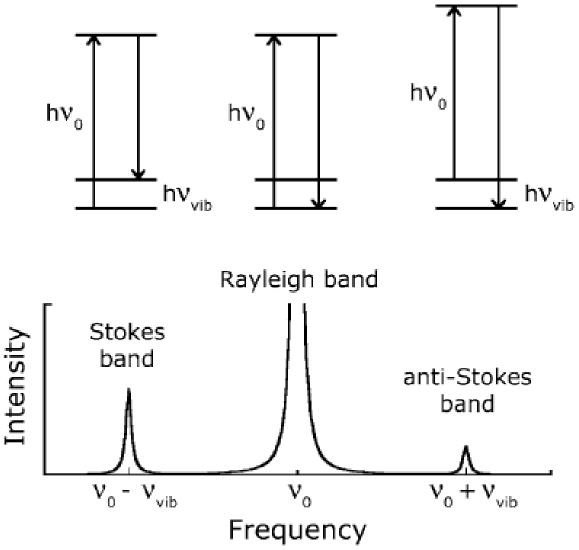

Figure 2.13 *- Monochromatic light (frequency* ν_0*) is scattered by a sample according to the Raman effect. Elastic scattering leads to no energy loss of the photon, incident and scattered photons have the same frequency* ν_0*. If the photon is inelastically scattered and excites (de-excites) the sample molecule it loses (gains) energy equal to* $h\,\nu_{vib}$ *and the Stokes (anti-Stokes) band is formed. Graph taken from* [118].

Raman spectroscopy is based on inelastic scattering of photons [118]. As schematically presented in Fig. 2.13, monochromatic light with frequency ν_0 is shown onto the sample. The majority of the incident photons undergo elastic Rayleigh scattering, they form the Rayleigh band. The representation in Fig. 2.13 indicates that the sample molecule is excited into an unstable, virtual state $h\,\nu_0$ and immediately decays back into the ground state. Should the molecule decay from the excited state into the first vibrational state with energy $h\,\nu_{vib}$ the photon loses the corresponding energy and the Stokes band is formed at frequency $(\nu_0 - \nu_{vib})$. The reverse process, that the photon excites the molecule to a state with energy $h(\nu_0 + \nu_{vib})$ and the molecule then relaxes back to the ground state, is also possible which gives rise the anti-Stokes band. The intensity of this peak at frequency $(\nu_0 + \nu_{vib})$ is typically small [118].

In this study Raman spectroscopy was employed to determine the degree of disorder in carbon samples. It is a sensitive tool to detect distortions in the translational symmetry of graphite [125,126]. Single crystals of graphite show one single line at *1575* cm^{-1}, which is dubbed the G-band. For other forms of carbon, like vitreous (glassy) carbon or charcoal, another peak can be detected at *1355* cm^{-1}, the so-called D-band. The D-band becomes more pronounced when the crystallite sizes are smaller or when there are more boundaries between larger crystallites. This is, according to Tuinstra and Koenig, caused by a breakdown in k-selection rule within the Brillouin zone of graphite [126]. The Raman signal was fitted and the ration of D-band and G-band intensities (I_D/I_G) was used to estimate the amount of defects in the graphitic structure.

2.6.3.3 Ultraviolet-visible light spectroscopy

In UV-Vis light absorption spectroscopy the attenuation of a beam of light is measured after it passes through a sample [117]. The wavelengths typically considered UV range from $\lambda = 200\ nm$ to $\lambda = 400\ nm$ and the visible spectrum stretches from $\lambda = 400\ nm$ to $\lambda = 750\ nm$. Absorbance and absorber concentration are linearly dependent which makes UV-Vis spectroscopy attractive for quantitative measurements.

Attenuation of the beam of light can stem from absorption, scattering, reflection or interference. For an accurate characterization it is important to ensure that the only cause of attenuation is absorbance of the analyte. The general formula describing the absorbance *Abs* is the Beer-Lambert law:

$$Abs = \varepsilon\ b\ c \tag{2.36}$$

with wavelength-dependent molar absorptivity coefficient ε, path length b and concentration c. The absorption of photons is caused by excitation of electrons from the ground-state within molecules in solution.

2.7 Carbons

The application of carbon as electrodes began as early as 1800, when Sir Humphrey Davy used a graphite electrode for studies on electric arcs [127]. Electrodes made from carbon have four benign characteristics [15]:

- Low cost;
- Wide potential window;
- Relatively inert electrochemistry;
- Electrocatalytic activity for a variety of redox-reactions.

Graphite, diamond and fullerenes are some of the well-known allotropes of carbon. In graphite, all carbon atoms are sp^2 hybridized and stacks of ideally infinite sheets of “graphene” form the crystal. Graphite can serve as a unique host lattice for the intercalation of various atomic of molecular species [128]. Intercalation is a solid state reaction which requires chemical bonding anisotropy of one of the reactants.

Diamond, on the other hand, contains only sp^3 hybridized carbon atoms. It has to be doped in order to provide sufficient electronic conductivity for electrode applications [92].

Carbon nanotubes are the most common fullerene used as electrode material. For single wall carbon nanotubes (SWCNTs) one sheet of graphene is rolled up which forms tubes of varying thickness, length and termination.

In the following carbon materials which were employed as electrode in this work are described.

Highly oriented pyrolytic graphite (HOPG) is a very ordered three-dimensional graphite material [15]. It is created by high-temperature decomposition of gaseous hydrocarbons followed by pressing at high temperature and high pressure. Characteristic for HOPG are in-plane crystallite sizes exceeding 1 μm [15]. Furthermore it is “turbostratic”, its crystallites are aligned along their c-axis but they are rotationally disordered. Electronically HOPG is considered to be a semi-metal with a DOS that is about $0.8\ \%$ of the DOS of Au (0.0022 $states\ atom^{-1}\ eV^{-1}$) [129]. This low DOS has an influence on the electrochemical activity, as it manifests itself in the low specific C_{DL} of basal plane HOPG, $c_{DL} < 2\ 10^{-6}\ F\ cm^{-2}$ in aqueous electrolytes [130]. Also, literature data suggests that the basal planes of HOPG exhibit only a low electrochemical activity towards certain model redox-couples, supposedly also an effect of the low DOS:

An example for such a model system is the redox couple $Fe(CN)_6^{3-}/Fe(CN)_6^{4-}$ that is often employed to probe carbon electrodes, despite the fact that the catalytic interaction is not clear [131,132]. However, a well-established fact is that this redox reaction is not an ideal outer-sphere reaction and that it depends both on interactions with cations in solution and on the surface chemistry [133–135]. Therefore, Robert McCreery uses the phenomenological term “surface sensitive” to describe $Fe(CN)_6^{3-}/Fe(CN)_6^{4-}$ [15]. Another typical model redox-couple is $Ru(NH_3)_6^{2+}/\ Ru(NH_3)_6^{3+}$. It is the archetype for a “surface insensitive”, purely outer-sphere, electron transfer.

When measuring k_0 for $Fe(CN)_6^{3-}/Fe(CN)_6^{4-}$ on HOPG basal plane (in $1\ M\ KCl$) a very low value $k_0 < 10^{-7}\ cm\ s^{-1}$ was determined [130]. Similarly, basal planes (in $1\ M\ KCl$) show a low activity for the $Ru(NH_3)_6^{2+}/\ Ru(NH_3)_6^{3+}$ redox reaction with $k_0 = 0.0014\ cm\ s^{-1}$ [136]. Considering the system, this value is very low compared to the typical values determined on metal electrodes, $k_0 \approx 1$ cm s^{-1} [137,138].

Due to the tremendous variety of carbon surface bonds and functional groups (compare Fig. 2.12), carbon materials have a significant more complex surface structure than metals [15]. As electrochemistry deals with interfacial phenomena the nature of the carbon surface is of importance. The HOPG basal plane, however, is atomically ordered and smooth and does not react with air at room-temperature. As defects are hard to avoid, however, the basal plain electrode will certainly be interspersed with defects such as step edges and grain boundaries [139]. This “edge plane”, in contrast to the basal plane, is rough, partly sp^3 hybridized and unsaturated, dangling bonds interact with oxygen and water to form various oxygen containing groups. This increases the DOS of the edge plane HOPG and this phase is characterized by $c_{DL} = 60\ 10^{-6}\ F\ cm^{-2}$ and $k_0 \approx 0.1$ cm s^{-1} for $Fe(CN)_6^{3-}/Fe(CN)_6^{4-}$ (in $1\ M$

KCl) [15,136]. Fig. 2.14 shows an AFM micrograph of a freshly prepared HOPG surface. The large basal planes interrupted by step edges can clearly be seen.
On a similar note there is currently a discussion in the community regarding the electrochemical activity of graphene, as model system for graphite [140–142]. The questions, whether films of graphene are more active than defects and if multiple layers are more active than monolayers are being disputed.

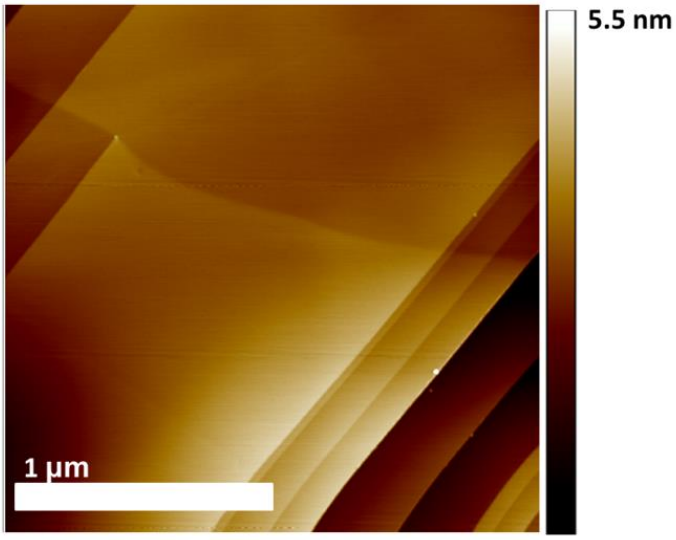

Figure 2.14 *- AFM micrograph of freshly cleaved HOPG.*

Another form of graphite which is important for electrochemistry is glassy carbon (GC) [15]. It is created by pyrolysis of thermosetting resins such as phenol, furan and polphenylene [127]. Its highly disordered structure is formed by branched and twisted ribbons of graphitic planes and although it contains many voids (density of GC is $60\ \%$ of the density of HOPG) it is impermeable to liquids and gases. The randomness results in uncertainty regarding the microstructure [139]. The c_{DL} is given as $(24 – 36)\ 10^{-6}\ F\ cm^{-2}$ and its activity for the surface sensitive $Fe(CN)_6^{3-}/Fe(CN)_6^{4-}$ ranges from $k_0 = (0.5 \pm 0.2)\ cm\ s^{-1}$ to $(0.005 \pm 0.003)\ cm\ s^{-1}$ (in $1\ M\ KCl$) depending on the method of pretreatment [15,143]. It was said that cleanliness of the surface is a major factor contributing to the facility of electron transfer [143]. Methods for carbon electrode surface pretreatment, cleaning and activation can be found in the literature [15,110].

CNTs are available in two main forms, either SWCNTs or multiple graphene sheets wrapped around each other forming MWCNTs [144]. CNTs possess unusual properties such as high aspect ratio, high conductivity, thermal stability and flexibility. The DOS of CNTs is similar to one-dimensional graphene. The confinement in one dimension yields an energy-dependence that decays like $\mathrm{DOS}(E) \propto E^{-1/2}$ according to solid-state physics textbooks [77]. In addition, the SWCNT DOS shows distinct van Hove singularities that stem from size-quantization of the electronic wavefunction around the circumference of the SWCNT [145]. Smaller radii lead to a larger distance between the energy levels of adjacent van Hofe singularities. An energy diagram showing the DOS of a semiconducting SWCNT and the overlap of electronic states redox-couple in solution and electrode is given in Fig. 2.15.

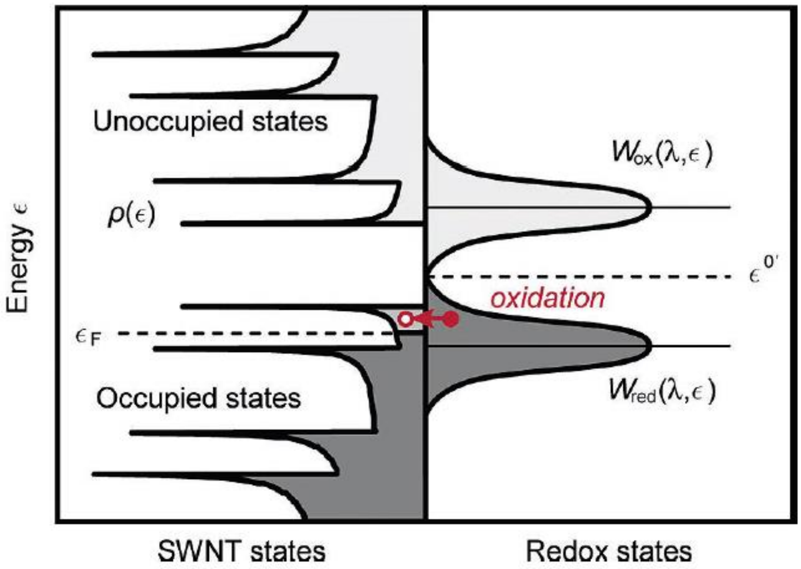

Figure 2.15 *- Overlap of DOS of a semiconducting SWCNT with energy states of a redox-couple in solution. Dark shaded states are filled with electrons. The graph is taken from* [145].

It was argued that due to the intricate electronic structure of SWCNTs Butler-Volmer kinetics do not hold and instead a model called Gerischer-Marcus model of electron transfer should be applied to consider the distribution of electronic energy states in both electrode and electrolyte [67,145,146]. However, direct correlation between the DOS and SWCNT electrocatalytic activity is complicated by the fact that the tubes typically exhibit an ensemble of sizes and diameters which leads to a dispersed effective DOS [15]. Chapter 5 of this work is concerned with the determining electron transfer kinetics on MWCNTs for two redox-reactions.

2.8 Polyoxometalates

Polyoxometalates (POMs) are the polyoxoanions of early transition elements, mostly vanadium, molybdenum and tungsten [147]. The first POM was reported in 1933 by Keggin [148,149]. It was the heteropolyacid $H_3[PW_{12}O_{40}]\ 6\ H_2O$ and this heteropolytungstate forms the archetype of the class of Keggin-ions. Since 1933, many heteropolytungstates or -molybdates were found with more than 70 different possible heteroelements and effective charges from *-3* to *-12* [147]. POMs form a unique class of

inorganic molecules that exhibit astonishing molecular and electronic structural versatility [148,150,151]. They can be described as nanoscale metal-oxide systems with a length scale from $1 - 5\ nm$ [152].
Polyoxoanions are built-up by linked MO_n polyhedra (with $n = 4 - 6$) and two principal groups are known. One group contains silicates or oxoanions of neighboring main-group elements (B, Si, Ge, P, As, Sb, S, Se, Te, I) and form polymeric structures based on linked MO_4 tetrahedra. The second group, POMs, are predominantly characterized by MO_6 octahedra with short ("terminal") $M{=}O$ bonds which tend to result in discrete structures [147]. Their low surface charge density results in extensive solution chemistry in both aqueous and non-aqueous media. On the surface of the POM anions both terminal ($M{=}O$) as well as bridging (M-O-M) oxygen atoms are present and DFT data and experimental evidence suggest that the bridging oxygen atoms carry a greater negative charge and are often protonated [153].

The formation of POMs is commonly described as self-assembly, although the exact mechanism is not well understood [154,155]. As POMs offer the prospect of materials with designed functionality there was and still is a large drive in the community to elucidate the assembly mechanism in order to make a more controlled and predictable synthesis of novel molecules possible. Quantum mechanical calculations [156,157] are combined with single crystal X-ray diffraction [158], MS [159] or nuclear magnetic resonance (NMR) [160] spectroscopy to explain the nucleation mechanism.

For electrochemistry POMs are interesting because of three properties, besides their solubility. First, they can undergo multiple redox-reactions per molecule. For example, the Keggin-ion $[PMo_{12}O_{40}]^{3-}$ was reported to be able to take up 24 electrons, reducing all the Mo-ions from oxidation state VI to IV in the process [40]. Both anions, $[PMo_{12}O_{40}]^{3-}$ and the reduced $[PMo_{12}O_{40}]^{27-}$ are shown in Fig. 2.16. Second, from a structural analysis a low reorganization energy and therefore high values of k_0 can be expected for POMs in general. The outer-shell reorganization energy λ_{out} for a one-electron transfer is usually treated on the basis of the dielectric continuum model, by the Born energy of solvation [146,161,162]:

$$\lambda_{out} = \frac{e^2}{8\,\pi\,\varepsilon_0\,k_B\,T}\left(\frac{1}{a} - \frac{1}{R_e}\right)\left(\frac{1}{\varepsilon_{op}} - \frac{1}{\varepsilon_s}\right) \tag{2.37}$$

with the effective radius of the reactant a, the distance of the molecule to its image in the metal surface R_e and the optical ($\varepsilon_{op} = 4.74$) and static ($\varepsilon_s = 11.58$) dielectric constants. Inserting the radius from Fig. 2.16a and assuming $R_e = 3a$ yields a very low $\lambda_{out} = 59.6\ meV$.
The inner reorganization energy $\lambda_{in}$is associated with the internal coordinates like changes in the metal-ligand bond distances [162]:

$$\lambda_{in} = 0.5 \sum_i f_i(\Delta d/2)^2 \tag{2.38}$$

with the change in distance Δd and force constants f_i. While we do not know the force constants, comparison of Fig. 2.16a and Fig. 2.16b shows that even the addition of 24 electrons does not lead to a large alteration in Δd for $[PMo_{12}O_{40}]^{3-/27-}$.
According to Marcus theory, the total reorganization energy $\lambda = \lambda_{in} + \lambda_{out}$ determines the rate of electron transfer reactions as [41]:

$$\Delta G^* = \frac{\lambda}{4}\left(1 + \frac{\Delta G^0}{\lambda}\right) \approx \frac{\lambda}{4} \tag{2.39}$$

and:

$$k_0 = A\, exp(-\Delta G^*/k_B T) \tag{2.40}$$

with Gibbs standard reaction energy ΔG^0, free energy barrier ΔG^* and a pre-exponential factor A that contains a nuclear frequency factor, the electronic transmission coefficients and the nuclear tunneling factor [162]. Typical values for A are on the order of $5\ 10^4\ cm\ s^{-1}$ [163].

From these equations it can be seen that especially the large effective radius a of POMs is responsible for a small λ_{out} and therefore a large k_0.

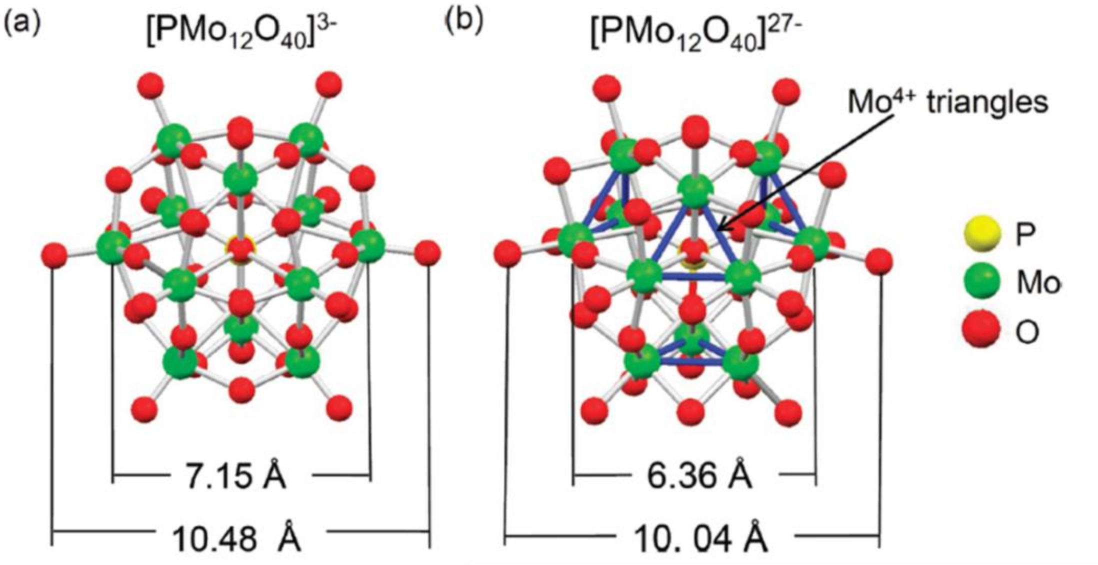

Figure 2.16 *- Molecular structure of* ***(a)*** *$[PMoO_{40}]^{3-}$ and* ***(b)*** *$[PMoO_{40}]^{27-}$ determined from X-ray absorption fine structure studies. The graph is adapted from* [40].

Third advantageous property is the ease with which the structure of POMs can be modified to exert desirable electrochemical properties. This will be demonstrated in chapter 6 when the evolution of electrochemical properties from $[SiW_{12}O_{40}]^{4-}$ to $[Mn^{II}_3SiW_9O_{34}]^{7-}$ via $[SiW_{11}O_{39}]^{8-}$ and $[SiW_9O_{34}]^{10-}$ is shown.

POMs containing lanthanides or metals often feature paramagnetic properties which were reviewed recently [164]. Again, the benefit of POM chemistry is that ions can be deliberately embedded in various POM frameworks and that these additions modify the physical behavior of the created molecule. R.E.P Winpenny states that molecular magnets, such as *V*-containing POM cage molecules could be employed to process information in quantum computers [165].

2.9 Redox Flow Batteries

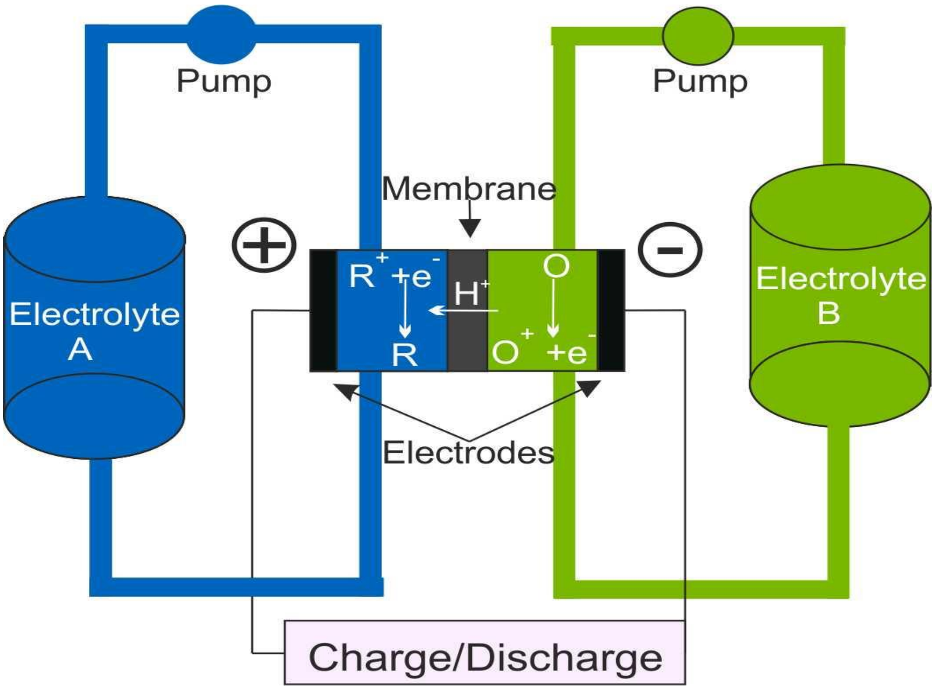

Figure 2.17 *- Schematic representation of a redox flow battery with two external tanks that contain electrolytes A and B. The electrochemical reactions take place in the power converter that consists of two electrodes and an ion exchange membrane.*

RFBs are energy storage devices that store energy in liquid electrolytes; they are typically classified by the active species that shuttle electrons [8,12,166]. They comprise two external tanks, a power converter as well as the required periphery (pumps, heat exchangers, pipes) to ensure its operation. In discharge mode an anolyte is transported from the tank to the power converter where it is oxidized to generate electrons which flow through an external circuit. The discharged electrolyte is pumped back into its tank. Simultaneously, a catholyte flows from tank to power converter and back to the tank. During its residence time in the power converter it is reduced. Cross-over of ions, typically protons, through an ion-exchange membrane in the power converter ensures charge neutrality.

The general reactions related to charge and discharge are (forward reaction gives charging):

$$\mathrm{R}^{n+} + xe^- \rightleftarrows R^{(n-x)+} \quad and \quad O^{m+} \rightleftarrows \ O^{(m+y)+} + ye^- \tag{2.41}$$

with species in anolyte *R* and species in catholyte *O* and $n > x$, $m > y$. A schematic representation of a RFB is shown in Fig. 2.17.

The specific capacity (normalized to volume) q stored in the electrolyte is given as:

$$q = c\, n\, F \tag{2.42}$$

As with every other battery, the volumetric energy density ϵ is the product of specific capacity times the potential difference of the two half-cells:

$$\epsilon = \frac{1}{2} q\, \Delta U \tag{2.43}$$

The factor ½ enters the equation because two electrolytes are required for a working battery.

Species	**U_0 vs. NHE / V**	**k_0 / cm s^{-1}**	**c / mol L^{-1}**
Fe^{2+}/Fe^{3+}	0.71 in 1 M $HClO_4$ * 0.69 in 1 M H_2SO_4 *,[14]	1.2 10^{-5} on Au(111) in H_2SO_4 purified from Cl^- [12] 4.1 10^{-4} on Pt * 4.7 10^{-5} on GC *	0.8 in NaAC [167] 1.25 in 2.3 M HCl [168]
Cr^{2+}/Cr^{3+}	-0.41 in 1 M $HClO_4$ [12]	2 10^{-4} on Hg [12] ~ 2 10^{-5} on CF with Au cat. [169]	1.0 in 2 M HCl [169]
V^{2+}/V^{3+}	-0.26 in 1 M H_2SO_4 [12] -0.25 in 1 M H_2SO_4 *,[14]	4 10^{-3} on Hg [12] 1.7 10^{-5} on GC [170] 5.5 10^{-4} on PG [171]	2.3 in 6 M HCl [172] 2.0 in 2 M H_2SO_4 [173]
VO^{2+}/VO_2^+	1.05 in 1 M H_2SO_4 *,[12,14]	3 10^{-7} on GC [25] 2.8 10^{-6} on GC [171] 2 10^{-6} on MWCNT *,[14]	2.3 in 6 M HCl [172] 1.6 in 2 M H_2SO_4 [173]
Br_2/Br^-	~ 1.05 in 1 M HCl [174]	5.8 10^{-4} on GC [12]	2.5 NaBr in 1 M HCl [174]

Table 2.4 *Fundamental constants for some redox-couples employed in RFBs. Abbreviations: * - this work, CF - Carbon felt, NaAC – sodium acetate, cat. – catalyst, PG- pyrolitic graphite.*

From eq. 2.43 it can immediately be seen that RFBs in general will not achieve the energy density of solid-state batteries, like the lead-acid or Li-ion batteries. Typical concentrations of solved redox-species are on the order of *1 mol* L^{-1} which corresponds to 10^{20} *atoms* cm^{-3}.

Solid phase is characterized by a much higher density of ions, on the order of *10^{23} atoms cm^{-3}* [77]. For state-of the art batteries not every ion contributes the battery capacity, as electrodes from metallic lithium are not feasible from a safety point of view, but the ratio is high with one Li^+ stored for every six *C* atoms [175]. Therefore, the (volumetric) energy density of liquid electrolytes will always be smaller than of solid electrodes.
The power density of a RFB is intimately tied to the rate at which electrons can be transferred to and from the electrodes. Therefore it is proportional to I_0 and therefore to k_0 and ECSA *A* (compare eq. 2.12).

	Cr^{2+}/Cr^{3+}	**V^{2+}/V^{3+}**
Fe^{2+}/Fe^{3+}	$\Delta U = 1.18\,V$ $\epsilon = 15.8\text{ Wh }L^{-1}$ $j_0 = 4.5\;10^{-3} A\;cm^2$	$\Delta U = 1.02V$ $\epsilon = 17.1\text{ Wh }L^{-1}$ $j_0 = 5.7\;10^{-3} A\;cm^2$
VO^{2+}/VO_2^+	$\Delta U = 1.46\,V$ $\epsilon = 19.6\text{ Wh }L^{-1}$ $j_0 = 2.7\;10^{-3} A\;cm^2$	$\Delta U = 1.31\,V$ $\epsilon = 40.4\text{ Wh }L^{-1}$ / $28.1\text{ Wh }L^{-1}$ $j_0 = 0.62\;10^{-3} A\;cm^2$ / $0.43\;10^{-3} A\;cm^2$
Br_2/Br^-	$\Delta U = 1.46\,V$ $\epsilon = 19.6\text{ Wh }L^{-1}$ $j_0 = 2.4\;10^{-3} A\;cm^2$	$\Delta U = 1.31\,V$ $\epsilon = 40.4\text{ Wh }L^{-1}$ $j_0 = 3.7\;10^{-3} A\;cm^2$

***Table 2.5** Comparison of different half-cell combinations from Table 2.4. ΔU is calculated as the difference in U_0, ϵ according to eq. 2.43 and j_0 according to eq. 2.12. For k_0 the lowest value on carbon electrodes was selected, the smaller concentration of the two half-cells determined the overall concentration. For the all-Vanadium system the commercial concentration of 1.6 mol L^{-1} is given in addition to the value for the concentrations achieved in laboratories (2.5 mol L^{-1}).*

In Table 2.4 a number of possible redox couples are analyzed in terms of critical electrochemical and chemical parameters. With these, theoretical exchange current densities and energy densities can be calculated which is shown in Table 2.5. Besides the listed couples quite a few other chemistries were investigated, for details the reader is referred to current reviews [8,12]. Of the possible combinations listed in Table 2.5 only three are of scientific or commercial interest.

The iron/chromium couple started the development of modern RFBs [12]. The NASA developed a 1 kW/13 kWh system for storage of electricity generated by a photovoltaic array. One of the issues with the system is the sluggish Cr^{2+}/Cr^{3+} redox couple that requires a catalyst on carbon electrodes. Another shortcoming is the relatively low open-circuit potential. Crossover of iron-ions to the chromium half-cell and vice versa leads to irreversible chemical contamination.

The all-vanadium RFB (V^{2+}/V^{3+}, VO^{2+}/VO_2^+) (VRB) has the obvious advantage that crossover of ions through the membrane does not lead to a chemical contamination and that therefore the whole system can be electrochemically rebalanced. Recent advances in supporting electrolyte research, addition of stabilizers [176] or mixed acid systems [172] enable solution that are capable of dissolving *2.3 M* vanadium with excellent thermal stability [173]. The commercial systems that are being distributed at the moment work with a *V*-ion concentration of *1.6 M*. This reduces the energy density to $28.1\ Wh\ L^{-1}$ as given in Table 2.5.

The significantly larger issue with the VRB is the sluggish electron transfer reaction of the VO^{2+}/VO_2^+ half-cell. It was estimated that the minimum practical current density for a RFB is $j_0^{geo} = 50$ mA cm^{-2} (normalized to geometric electrode area) [12]. If that target is not reached the cell will suffer from low electrical efficiency. In order for the VRB to reach that specification the ECSA of the electrode has to be 116 times larger than the geometrical surface area (for the commercial concentration of *1.6 M*). However, increased porosity of the electrode might lead to problems like a pressure drop in the power converter.

Gattrell investigated the VO^{2+}/VO_2^+ redox-reaction in detail and concluded that it is a multi-step electron transfer coupled to a chemical reaction [25]. There is a plethora of studies on electrocatalytic effects accelerating the reaction mostly on high surface area carbon materials [20,21,23,177,178]. However, none of these studies performed a proper normalization to *ECSA* and the validity of employed electrochemical methods, mostly CVs, are dubious for that application [24]. In this work we propose that the electron transfer reaction cannot be catalyzed by surface functional groups and we suggest a new method to determine charge transfer kinetics on porous electrodes (see chapter 5).

As the presence of halide ions can increase the solubility of vanadium ions, and to avoid the kinetically problematic VO^{2+}/VO_2^+ couple, the V^{2+}/V^{3+} - Br_2/Br^- RFB was devised [174]. However the problem of the system is the concern of toxic bromine-vapor emission during operation [12].

Chapter 3

Materials and methods

3.1 Chemicals

Chemicals	**Formula**	**Provider**	**Purity**
Sulfuric Acid	H_2SO_4	Sigma Aldrich	Suprapur
Perchloric Acid	$HClO_4$	Merck	Suprapur
Phosphoric Acid	H_3PO_4	Sigma Aldrich	*99.99 %*
Acetic Acid	CH_3COOH	Sigma Aldrich	*≥ 99.99 %*
Citric Acid	$C_6H_8O_7$	Sigma Aldrich	*≥ 99.5 %*
Vanadium(V) Pentoxide	V_2O_5	Sigma Aldrich	*99.99 %*
Vanadyl(IV) Sulfate Hydrate	$VOSO_4 \; x \; H_2O$	Sigma Aldrich	*≥ 99.99 %*
Vanadium(III) Chloride	VCl_3	Sigma Aldrich	*97 %*
Vanadium(II) Chloride	VCl_2	Sigma Aldrich	*85 %*
Iron(III) Chloride Hexahydrate	$FeCl_3 \; 6 \; H_2O$	Sigma Aldrich	*≥ 99 %*
Iron(II) Chloride Tetrahydrate	$FeCl_2 \; 4 \; H_2O$	Sigma Aldrich	*≥ 99 %*
Lithium Sulfate	Li_2SO_4	Sigma Aldrich	*≥ 99.99 %*
Potassium Sulfate	K_2SO_4	Sigma Aldrich	*≥ 99.0 %*
Potassium Chloride	KCl	Sigma Aldrich	*≥ 99.0 %*
Potassium Bromide grade	KBr	Alfa Aesar	FTIR
Sodium Acetate Trihydrate	$NaCH_3COO \; 3 \; H_2O$	Sigma Aldrich	*99 %*
Lithium Citrate Hydrate	$Li_3C_6H_5O_7 \; x \; H_2O$	Sigma Aldrich	*99.0 %*
Sodium Citrate Dihydrate	$Na_3C_6H_5O_7 \; 2 \; H_2O$	Sigma Aldrich	≥ 99.0 %
Sodium Phosphate Dihydrate	$Na_2HPO_4 \; 2 \; H_2O$	Sigma Aldrich	*99 %*
Sodium Phosphate Heptahydrate	$NaH_2PO_4 \; 7 \; H_2O$	Sigma Aldrich	*≥ 99.99 %*
Acetone	C_3H_6O	Sigma Aldrich	p.a.
Hexane	C_6H_{14}	Sigma Aldrich	*95 %*
Dimethylformamide	C_3H_7NO	Sigma Aldrich	*> 99.8 %*
Isopropanol	C_3H_8OH	Sigma Aldrich	*≥ 99.7 %*
Agar for microbiology		Sigma Aldrich	
NC3100 MWCNT		Nanocyl	*≥ 95 %*
Glassy Carbon Electrode		ALS Co.	
Highly order pyrolytic graphite		VEECO	ZYH
Electrode Polishing Kit		ALS Co.	

Argon	*Ar*	National Oxygen	*99.99 %*
Oxygen	O_2	National Oxygen	*99.99 %*
DI-water	H_2O	ELGA	*18.2 MΩ, 3 ppm* TOC

Table 3.1 *- List of chemicals and other consumables.*

Noble metal wires used in the experiments were either *Au* with a diameter of *0.5 mm* or *Pt* with a diameter of *0.25 mm*. They were purchased from Carl Schäfer GmbH & Co. KG with a purity of *99.9 %.* The noble metal wires were cleaned in sulfuric acid before each experiment.

The GC electrodes employed were isolated in polyether ether ketone (PEEK) with an exposed GC disk of *1.6 mm* in diameters or were GC rods with a diameter of *5 mm*. Before each measurement the facets were polished with grit papers with successively smaller grain sizes (P800, P2400, P4000) followed by polishing with an alumina slurry (*50 nm* particles) and a silica slurry (*7 nm* particles) on polishing cloth [14]. Between polishing steps the electrode was rinsed with DI-water.

The NC 3100 MWCNTs from Nanocyl were selected because the excel in terms of purity, size distribution and crystallinity [179].

The POMs were synthesized in the group of Prof. Ulrich Kortz at the Jacob's University, Bremen, Germany. Detailed information on the synthesis process as well as on the characterization by single crystal X-ray diffraction, nuclear magnetic resonance can be found in these publications: [39,180,181].

3.2 Electrochemical setup

3.2.1 Electrochemical glass cell

For this work two types of glass cell were employed. The LV, CV, PS, SCP, DCP and EIS measurements were performed in a custom built, double-jacketed glass cell which is schematically shown in Fig. 3.1a. The lower part of the cell that holds the electrolyte of interest is enclosed by a second compartment that can be flushed by temperated water, thus allowing for temperature control. In the upper part are ports for working electrode (WE) holder, reference electrode (RE) holder, counter electrode (CE) holder as well as for Ar gas inlet and outlet.

The RE electrode holder comprises a second compartment and a Luggin capillary that is placed in an advantageous position close to the working electrode (for a detailed discussion on ideal location see [94]). Commercial Mercury/Mercourus Sulfate ($Hg|Hg_2SO_4$, MSE) electrodes were used as RE. Supporting electrolytes were either *1 M* H_2SO_4 (*0.674 V vs.* NHE) or *0.6 M* K_2SO_4 (*0.640 V vs.* NHE) depending on the electrolyte in the main

compartment [14,182]. All potentials are given recalculated to NHE.
The CE was a gold wire that was coiled up to achieve high surface area. It was melted in a glass grinding.
Ar gas inlet and outlet were connected to eliminate residual O_2 in the cell and the electrolyte was thoroughly purged for *20* minutes prior to experiments. Any outgoing gas passed through a water-filled bubble counter that prevented diffusion of laboratory atmosphere back into the cell.

The second type of custom built glass cell is shown in Fig. 3.1b. It is a h-type cell that was used for controlled potential electrolysis of bulk electrolyte. Two compartments contain a WE electrode each. They are joined together by a glass tube that can be filled by gelled agar that serves as a salt bridge. Each single cell is purged by *Ar* gas as described above. One of the compartments houses a RE electrode holder to determine the potential of that half-cell. The salt bridge was prepared by mixing *5 %* agar with *3.5 M KCl* and heating the solution in a microwave. Then the gel-like product was poured into the connecting glass-tube to separate the two compartments while providing ionic conductivity [110].

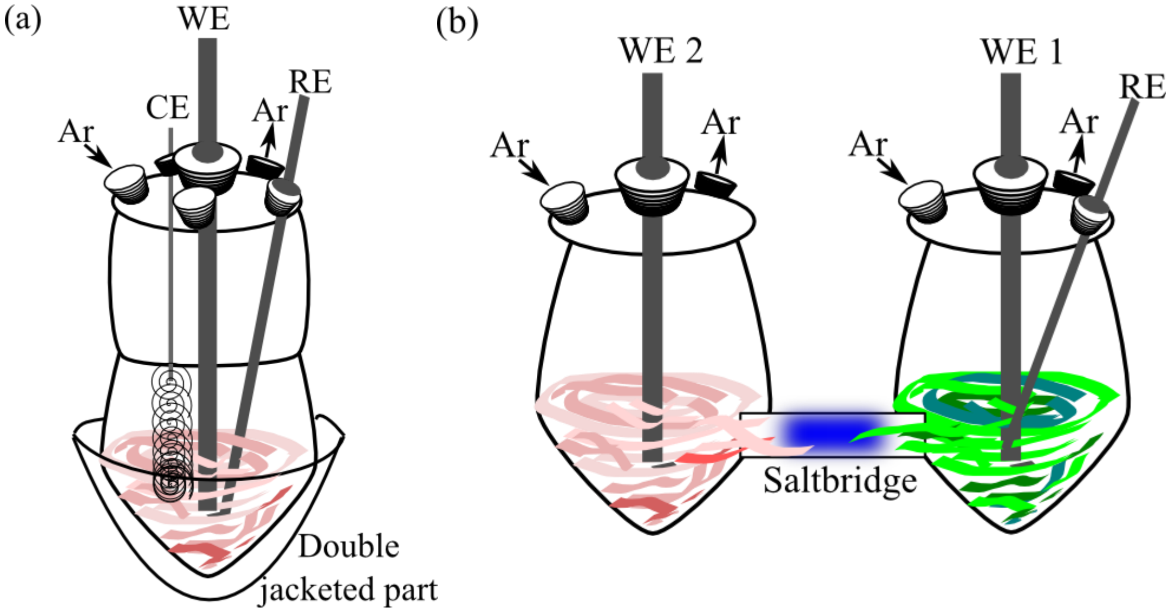

Figure 3.1 - *Schematic glass cells used in electrochemical experiments.* ***(a)*** *The double jacketed glass cell used for most of the electrochemical experiments.* ***(b)*** *The h-type glass cell used for bulk electrolysis of electrolytes. WE – working electrode, CE – counter electrode, RE – reference electrode, Ar – argon gas.*

3.2.2 Potentiostats and galvanostats

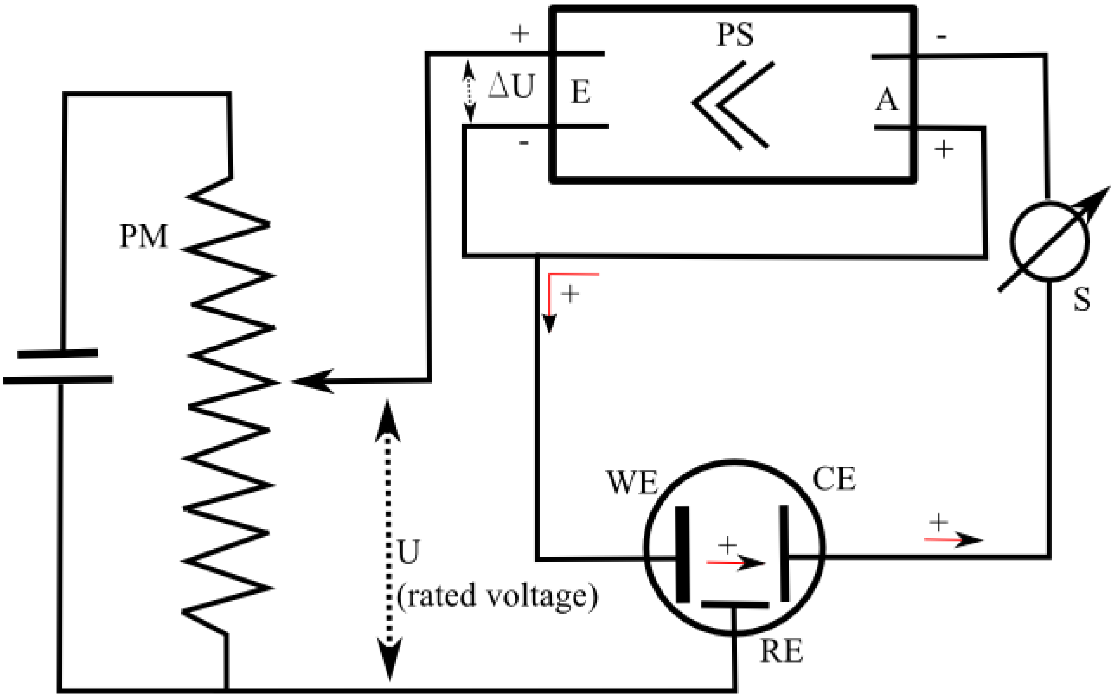

Figure 3.2 - *Method of operation of a potentiostat. PM – potentiometer, PS – potentiostat (power source). The graph is adapted from* [54].

Figure 3.2 demonstrates the method of operation of a potentiostat [54]. The WE is maintained at constant potential versus the RE, which can be adjusted via the potentiometer (PM). The polarization current is applied to the CE by the potentiostat (PS) which functions as a power source and current amplifier. It is important that the PS features an input impedance (E) that is high enough so that the current flowing through the input terminal is small compared to the polarization current. This ensures that the RE is not polarized. A galvanostat has a similar operating principle; it ensures that a fixed current flows between WE and CE by adjusting the potential at the WE.

For this work mostly a Bio-Logic SP 300 potentiostat was used. Control of the instrument and data acquisition was accomplished by the EC-Lab software (ver. 10.18). The SP 300 is also capable of galvanostatic operation and it can perform EIS.
In order to investigate the potentiostatic response time and to obtain the minimal sample time a dummy cell was put together. The dummy cell consisted of a resistance of $1000\ \Omega$ and a capacitance of $10^{-8}\ F$ in series. This circuit has a time-constant of $\tau = 10\ \mu s$. At $t = 0\ s$ a current pulse of $100\ mA$ was applied to the dummy cell; Figure 3.3 shows the resulting data points and a simulated response of the circuit.

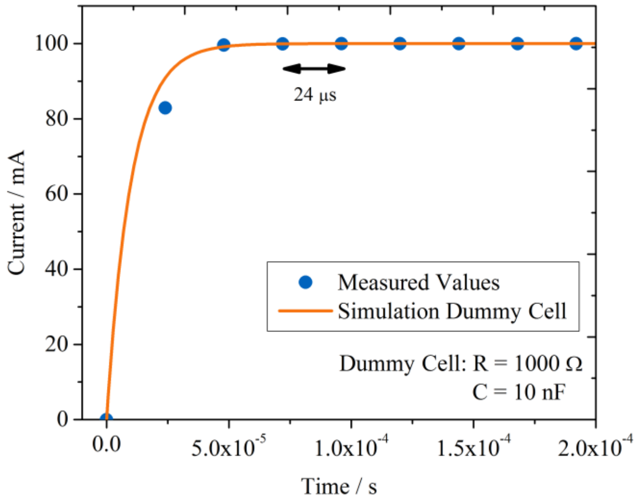

Figure 3.3 - *Response of the SP-300 to a current pulse of 100 mA commencing at t =0 s.*

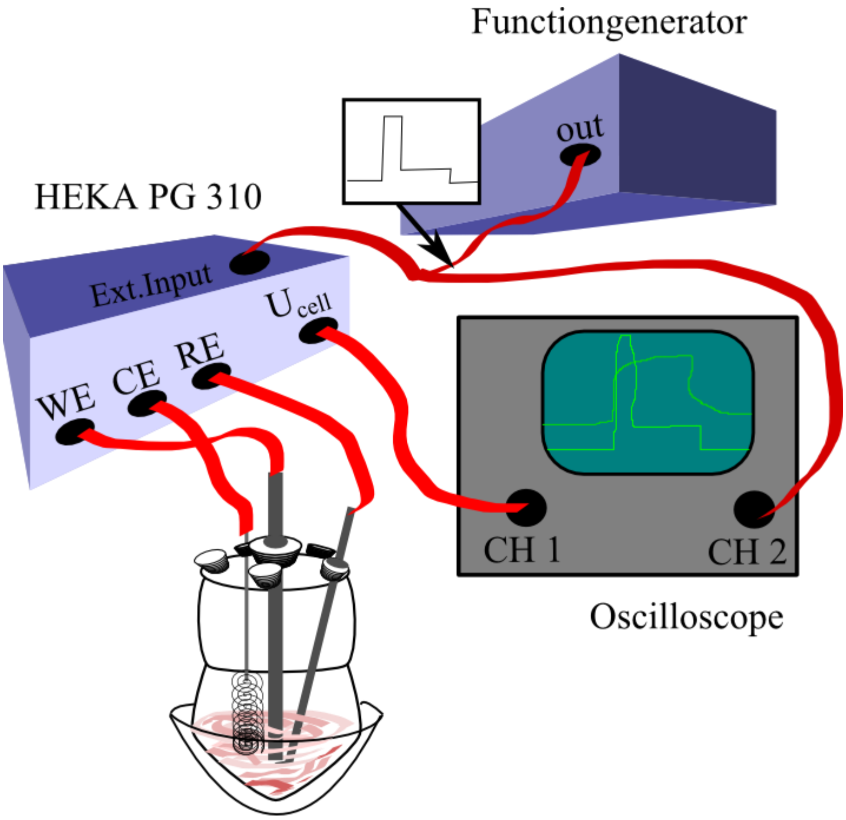

Figure 3.4 - *Connection-scheme to record double current pulses with a function generator, the HEKA PG 310 galvanostat and an oscilloscope.*

This result suggests that the SP-300 potentiostat reacts without delay and immediately applies the current. The charging of the RC element follows the expected exponential behavior; the charging is completed at 5 τ. Furthermore, it was shown that the minimal resolvable time-step is 24 μs.

For DCP measurements a HEKA PG 310 (HEKA Elektronik Dr. Schulze GmbH) in combination with a function generator (FG) and an oscilloscope was used. The FG triggered both the HEKA PG 310 and the oscilloscope with two overlaying rectangular pulses (compare Fig. 2.9). The cell was controlled by the HEKA PG 310 and cell voltage and applied current were transmitted to the oscilloscope for data acquisition. Fig. 3.4 shows the details on the connections that were made to record DCPs.

3.2.3 Electrolyte characterization

To assess the oxidation state of POMs in solution UV-Vis spectroscopy was employed. The electrolyte was collected either immediately after preparing the solutions or after controlled potential electrolysis in the h-type cell. The UV-Vis spectra were recorded on a Cary 5000 spectrophotometer from Agilent Technologies. For conclusions about the oxidation state of the investigated POMs the spectra were compared with spectra reported in the literature for similar molecules [183–186]. The electrolytes were re-measured after *24* hours to assert possible changes due to slow processes.

3.2.4 Atomic force microscopy

For studies on the adsorption behavior of POMs a HOPG electrode was employed as WE. Prior to measurement, a clean surface was prepared with adhesive tape. After the electrochemical experiments the HOPG was emmersed from the electrolyte and dried at room temperature. AFM was conducted with a Bruker Multimode 8 in Scan-Assist mode.

3.3 Multi-walled carbon nanotube electrode preparation

MWCNTs with different amount and varying type of surface functional group were prepared in order to investigate the influence of the carbon surface chemistry on redox-couples [14]. Starting from Nanocyl 3100 MWCNTs (NC 3100) chemical means were chosen to increase the coverage with oxygen containing surface functional groups. In addition, surface functional groups were removed from NC 3100 by a temperature treatment in inert atmosphere. This section deals with the functionalization process, the characterization methods and the electrode preparation.

3.3.1 Functionalization of pristine multi-walled carbon nanotubes

Covalent chemical strategies were chosen for the functionalization of MWCNT surfaces. The end caps of nanotubes are usually composed of highly curved fullerene-like hemispheres, which are much more reactive than the sidewalls, due to their curvature [187–189]. The sidewalls contain defect sites, like Stone-Wales defects (pentagon-heptagon pairs) or sp^3-hybridizations [188]. Oxidizing agents, such as strong acids, tend to attack the caps or defect sites which leaves holes terminated by oxygen containing functional groups, as shown in figure 2.12 [190].

Two different oxidizing agents were employed in this study. Either $3\ M\ HNO_3$ or conc. H_2SO_4 mixed with conc. HNO_3 mixed in a ratio of *3:1*. For a functionalization step *500 mg* of pristine NC 3100 were mixed with *200 ml* of oxidizing agent. The heat impact on the sample was reduced by external cooling with water. The suspension was stirred and sonicated to disperse the MWCNTs in the acids [116].

Exposure times followed values from the literature but were kept below *6* hours in the concentrated acid as tube shortening of about $130\ nm\ h^{-1}$ can be expected under these conditions [123,125,190,191].

After the treatment with the oxidizing agents the MWCNTs were filtrated and washed until the rinsing water had a neutral *pH*. The agglomeration of sample material on the filter paper was subjected to a heat treatment at *100 ˚C* and a pressure of *300 mbar* in a box furnace to remove excess water.

In a last step loose functional groups were removed at *150 ˚C* under constant flow of *Ar* ($100\ ml\ min^{-1}$) with subsequent dwelling time at *30 ˚C* for one hour. At this low temperature $5\ \%\ O_2$ were added to *Ar* to saturate the MWCNTs in a controlled way.

Thermal defunctionalization, removal of almost all surface functional groups, was carried out at *1000 ˚C* in an *Ar* atmosphere ($100\ ml\ min^{-1}$) for *3* hours. It was also followed by dwelling at *30 ˚C* in $5\ \%\ O_2$ for one hour.

A list of all the MWCNTs based on NC 3100 and their respective treatments is given in Table 3.2.

Sample name	Treatment	Exposure time
PRIST	Untreated, used as delivered	n.a.
DEFUNC	*1000 ˚C* in *Ar* atmosphere	*3 h*
NITRIC	$3\ M\ HNO_3$	*18 h*
NITSULF_3h	Conc. H_2SO_4 / conc. HNO_3	*3 h*
NITSULF_6h	Conc. H_2SO_4 / conc. HNO_3	*6 h*

Table 3.3 - MWCNT samples based on Nanocyl 3100 with their respective treatment methods and exposure times.

3.3.2 Characterization of multi-walled carbon nanotubes

The decomposition temperature of functional groups was studied with a TGA-MS setup consisting of a “STARe TGA” from Mettler Toledo connected to a “Thermostar GSD3200” from Pfeiffer Vacuum. The samples were heated from room temperature to $1000\ ^\circ C$ by applying a constant temperature ramp of $10\ K\ min^{-1}$ after dwelling at $100\ ^\circ C$ for two hours. The furnace was purged with $100\ ml\ min^{-1}\ Ar$. For the measurement the samples were contained in 70 μl Al_2O_3 crucibles.
The MS was set to detect ions CO^+ ($28\ amu$), CO_2^+ ($44\ amu$) and CO^{++} ($14\ amu$). Doubly charged ions appear at half of the mass of their parent ion.

With a FTIR spectrometer “Spectrum GC” form Perkin Elmer the degree and type of surface functional groups on the MWCNTs was determined [14]. To obtain sufficient transmission the carbon samples were mixed with KBr (1:20) and pressed into a pellet. A background spectrum of pure KBr was recorded and subtracted. As further data manipulation a baseline subtraction was performed.

Raman spectroscopy was performed using a WITec “alpha 300SR” with an excitation wavelength of $\lambda = 632.8\ nm$ emitted from a HeNe-Laser driven at a power of $60\ mW$. Acquisition time was set to $30\ s$. The measurement was performed at room temperature in laboratory atmosphere. To ensure accurate data acquisition a Si reference peak was detected at $522\ cm^{-1}$. The recorded spectrum ranges from $600\ cm^{-1}$ to $3000\ cm^{-1}$ and displays the Stokes line of the Raman scattering.
A baseline subtraction was performed and the spectra were normalized to the intensity of the G-band I_G. To determine the ratio I_D/I_G Lorentz curve fitting was performed.

The morphology of the MWCNT samples coated onto the GC samples was imaged using a JEOL “7600F” field emission SEM. The images were taken on actual electrode surfaces instead of MWCNT powder in order to determine electrode topology.

3.3.3 Electrode coating process

Goal of the coating process was to deploy a well-controlled mass of sample onto the GC substrate; therefore the drop-casting method was used. Prior to the coating process the GC facets were polished as described. Variable amounts of MWCNTs were suspended in Hexane and ultrasonically dispersed. Then 20 μl of this suspension were drop-cast onto the GC facets with a pipette. The decorated substrates were then heated in a Memmert oven at $55\ ^\circ C$ until the solvent was evaporated. Other solvents (like water and isopropanol) were examined but did not give reproducible results when investigated with an SEM. As the density of MWCNTs in Hexane is known, the mass of sample that was coated onto the substrates can be calculated. This coating process we repeated in order to obtain the desired mass of MWCNTs as electrode. Four exemplary SEM micrographs of GC surface decorated with variable amounts of sample PRIST are shown in Figure 3.5. The pictures confirm that well-dispersed tubes were coated onto the substrate. In Fig. 3.5a and b, which are recorded with 1 μg and 2 μg of sample respectively, the blank GC substrate can still be seen, as the coverage with PRIST is not sufficient to cover the entire surface. Fig. 3.5c and d on the other hand show porous electrodes with a dense network of MWCNTs.

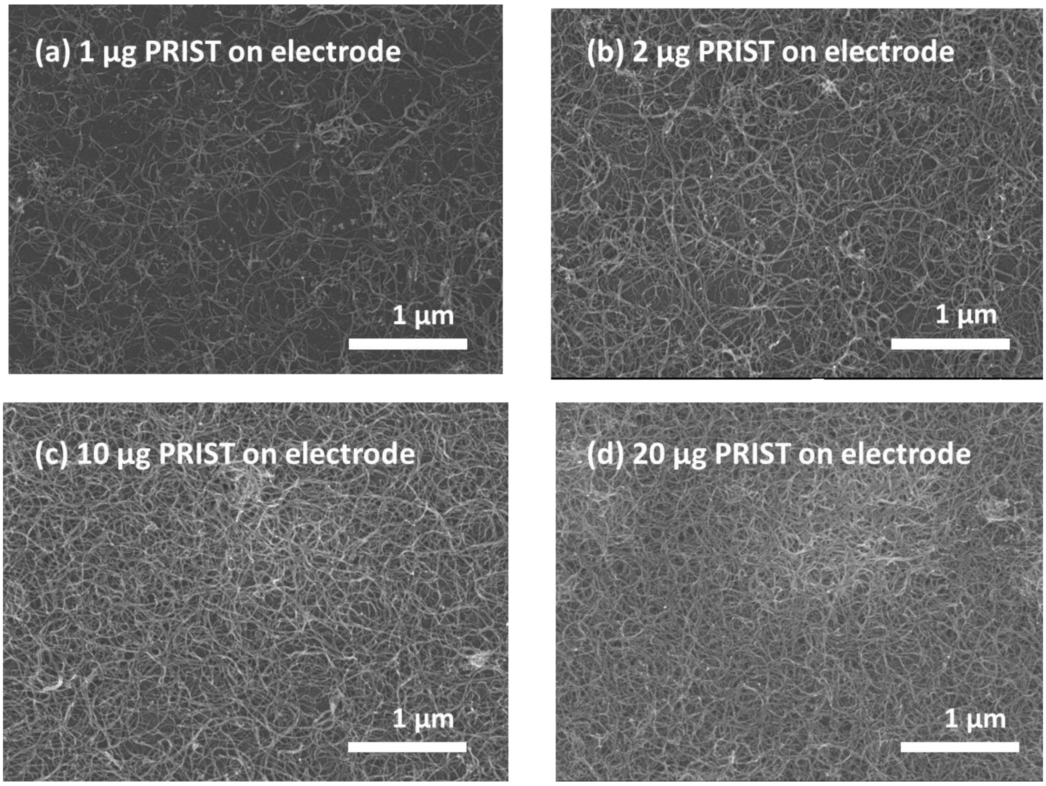

Figure 3.5 - *SEM micrographs of the glassy carbon surface coated with variable amounts of sample PRIST. The magnification was x 30000. The mass of MWCNTs is given in each subfigure. The graph is taken from* [14].

Chapter 4
Extracting kinetic information from redox systems

Electron transfer can be described by the empirical model of Butler and Volmer, if no bonds are broken [192]. Within this framework there are four kinetic parameters: Standard heterogeneous electron transfer constant k_0, equilibrium potential U_0 and transfer coefficients α_a and α_c. This set of parameters $\{k_0; U_0; \alpha_a; \alpha_c\}$ is well suited for the comparison of redox reactions and there is an extensive database of these, see for example the chapter “Experimental results of electrochemical kinetics” in ref. [54]. Evidence was presented that the Butler-Volmer model is not universally applicable. As early as 1975, Savéant and Tessier found a potential-dependent transfer coefficient for the reduction of tert-nitrobutane [193], which cannot be explained with Butler-Volmer kinetics. However, the model is ubiquitous and well suited for comparison of different redox-reactions and this is why we will employ it in this work.

In this chapter different experimental methods to extract $\{k_0; U_0; \alpha_a; \alpha_c\}$ are evaluated. Aim of this study was to find a suitable experimental technique which can be employed to characterize the more complicated electrode-electrolyte systems encountered in later chapters. In chapter 5 the influence of surface functional groups attached to MWCNTs on the VO^{2+}/VO_2^+ and the Fe^{2+}/Fe^{3+} redox systems will be investigated. In chapter 6 the multi-electron transfer of POMs, which is often coupled to proton- or cation-transfer, will be analyzed.

The model system for this comparison of experimental techniques used in this chapter is a redox-reaction that was often considered to be a prototype of a simple redox electrode, the ferric/ferrous electrode [54]. However, it was shown later that this reaction is not as simple as assumed and that it is catalyzed by Cl^- and other anions [194].

First the ferric/ferrous couple is investigated on a platinum disk electrode. With the fundamentals established the more complicated situation on a porous carbon electrode will be tackled [195].

4.1 Ferrous/Ferric redox couple on a platinum disk-electrode

The electron transfer reaction of the ferrous/ferric redox couple in non-interacting aqueous systems reads:

$$[Fe(H_2O)_6]^{2+} \rightleftharpoons [Fe(H_2O)_6]^{3+} + e^- \tag{4.1}$$

The reaction was studied in $1\,M\,HClO_4$ as supporting electrolyte and with $50\,mM$ of each Fe^{2+} and Fe^{3+}. The working electrode was a small Pt disk sealed in glass.

4.1.1 Cyclic voltammetry

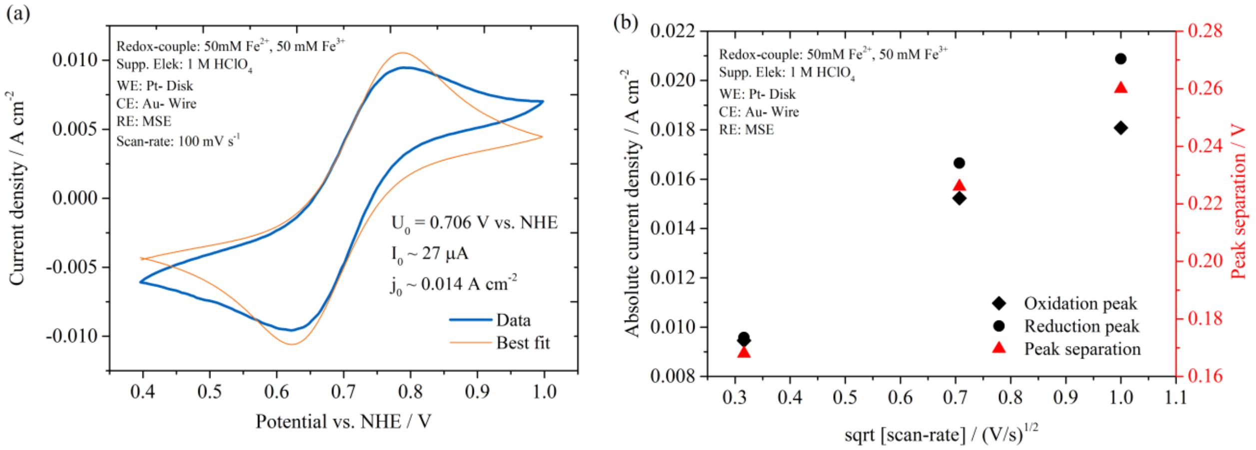

***Figure 4.1** - **(a)** Cyclic voltammogram of the ferrous/ferric redox couple in 1 M $HClO_4$ on Pt at a scan-rate of 100 mV s^{-1}. The experimental details are given in the graph. The orange curve shows the best obtained fit. **(b)** Evaluation of cyclic voltammograms at three different scan-rates. Absolute values for current densities at the peaks (black symbols) and the potential difference of the two peaks (red triangle) are given.*

To get an overview of the reaction a CV was recorded with a scan-rate of $100\ mV\ s^{-1}$, it is shown in Fig. 4.1a. In addition to the experimental data (blue curve), a current response was simulated with the EC-Lab software (orange curve). The diffusion coefficients $D_{ox} = 6.1\ 10^{-6}\ cm^2\ s^{-1}$ and $D_{red} = 5.5\ 10^{-6}\ cm^2\ s^{-1}$ of the oxidized and reduced species respectively were obtained from the literature [196]. Obviously, the agreement between the two curves is not too good. The equilibrium potential was obtained as the arithmetic mean of the peak potential of the oxidation and the reduction wave. The set of kinetic parameters that was evaluated is: $\{k_0 = 2.9\ 10^{-3}\ cm\ s^{-1};\ U_0 = 0.706\ V\ vs.\ NHE;\ \alpha_a = 0.50;\ \alpha_c = 0.5\}_{\mathrm{CV}}$. While there is some confidence in the value for U_0, the other parameters are rough estimations at best. Therefore, CVs will be only employed to determine U_0 and to get a semi-quantitative overview. In Fig. 4b the characteristics of the oxidation and the reduction wave are evaluated. The almost linear increase of the absolute current densities of anodic and cathodic wave over the square-root of scan-speed is typically interpreted as evidence of a diffusion-limited, pure electrochemical reaction [67]. Qualitatively, the difference in potential position of the oxidation and the reduction peak, the peak-separation ΔU^{peak}, is a measure for the kinetics of a redox-reaction on non-porous electrodes. The fastest one-electron redox-reactions exhibit a peak-separation as small as 59 mV, independent of the scan-rate. However, very sluggish redox-reactions can show peak separation of 1 V or more [14]. Therefore, Fig. 4.1b reveals that the ferrous/ ferric redox couple on Pt is a pure electrochemical reaction with intermediate reaction rate.

4.1.2 Electrochemical impedance spectroscopy

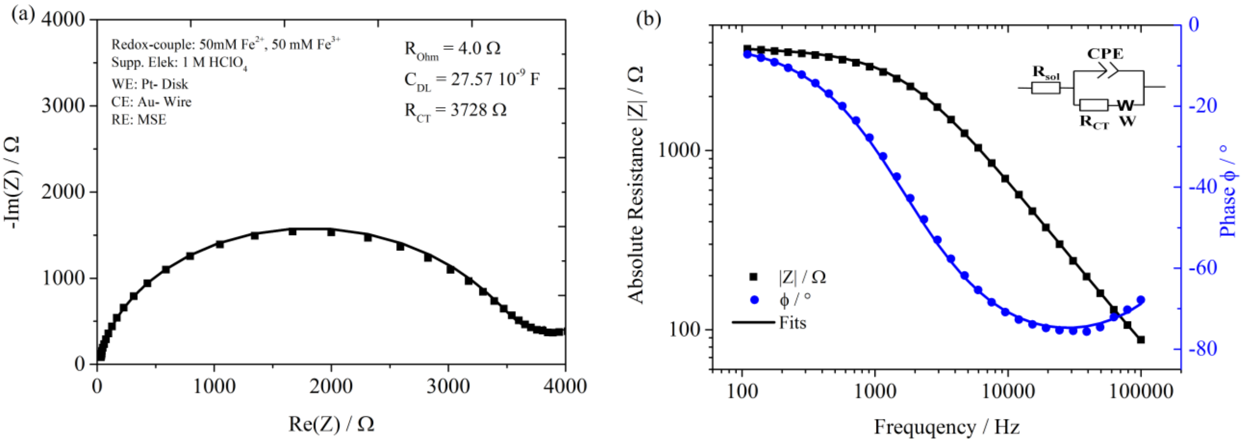

***Figure 4.2** - Electrochemical impedance spectroscopy measurements of the ferrous/ferric redox couple in 1 M $HClO_4$ on Pt. **(a)** Nyquist- and **(b)** Bode representation. The data points were fitted to the Randles-circuit given in the upper right.*

EIS studies are a reliable and swift tool to determine k_0. They are unable to discriminate α_a and α_c, however. Also U_0 is only indirectly obtainable; if the activities of the two redox-species are equal the resting potential of the cell U_{OCV} should be equal to U_0. Therefore, it is useful to record CVs prior to EIS measurements to compare U_{OCV} and U_0.

EIS provides additional information about the time constant of the cell via C_{DL} and R_{Ohm}. This is of use in the determination in the contribution of I_{NF} in other experiments such as PS, SCP and DCP. A Nyquist- (Fig. 4.2a) and Bode-representation (Fig. 4.2b) of an EIS experiment for frequencies from $10^5\ Hz$ to $1\ Hz$ with an amplitude of $10\ mV$ are shown. From the trend of the phase in Fig. 4.2b it is obvious that higher frequencies should have been included in the measurement. Nevertheless, the performed fit to the Randles-circuit shows only minimal deviation from the experimental data. Values for R_{Ohm}, C_{DL} and R_{CT} are given in Fig 4.2a. With the area of the electrode we can calculate a specific double layer capacitance of $c_{DL} = 14\ 10^{-6}\ F\ cm^{-2}$. This value corresponds well with the value given for metal electrodes in the literature [15]. The determined time-constant τ is less than 1 μs, a merit of the very small surface area of the WE $(r = 0.025\ cm)$.

With eq. 2.23 the kinetic parameter k_0 is obtained from R_{CT}: $\{k_0 = 7.2\ 10^{-4}\ cm\ s^{-1}$; $U_0 = n.a.$; $\alpha_a = n.a.$; $\alpha_c = n.a.\}_{\text{EIS}}$

4.1.3 Potential steps

For the evaluation of PSs, see section 2.5.1, there are two approaches possible. One is to employ the approximation introduced in eq. 2.28 that relies on linear extrapolation of the current transient over square-root of time back to $t \longrightarrow 0\ s$. The other method is to fit every current response to a potential step following eq. 2.26. Here, both methods will be conducted and compared.

For the approximation method the current transients are plotted over the square-root of time as can be seen in Fig. 4.3a for the oxidation (positive overpotentials) and in Fig. 4.3b for the reduction (negative overpotentials).

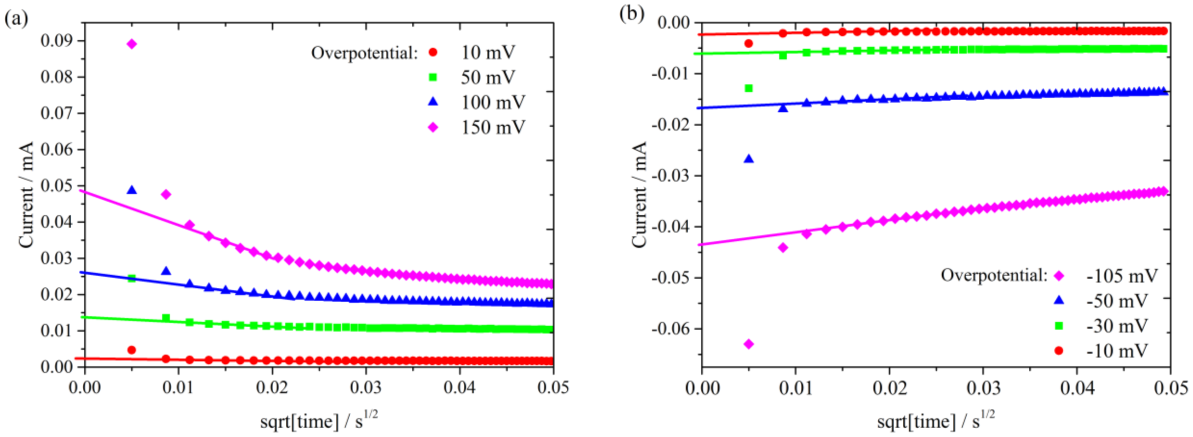

***Figure 4.3** - Evaluation of potential step measurements of the ferrous/ferric redox couple in 1 M $HClO_4$ on Pt. **(a)** Oxidation and **(b)** reduction. The curves were linearly extrapolated back to $t = 0$ s to obtain $I(t = 0$ s$)$.*

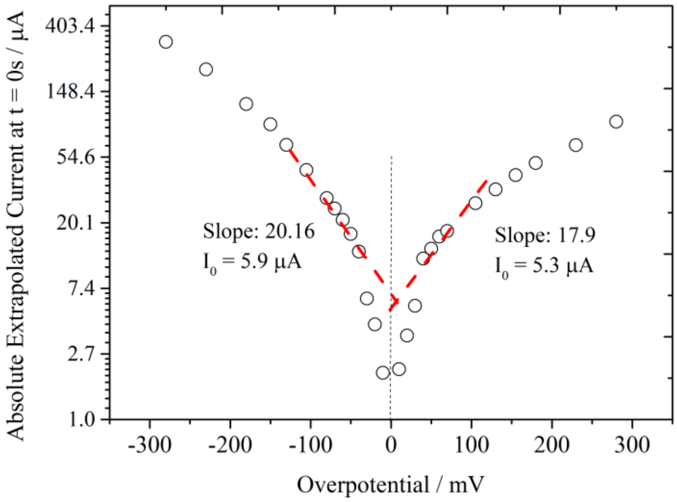

***Figure 4.4** - Values for the absolute current transients extrapolated to $t = 0$ s for the overpotentials for the ferrous/ferric redox couple in 1 M $HClO_4$ on Pt. The left data points represent the cathodic branch with $\alpha_c = 0.52$ and the right side corresponds to the anodic branch with $\alpha_a = 0.44$.*

For each transient the first two data-points are omitted, as they contain a contribution from I_{NF} and also the potential set by the potentiostat might not be perfectly stable for the initial phase of the potential step. It is assumed that immediately afterwards these initial data points the faradaic current I_F is measured that decays due to depleting concentration of active species according to eq. 2.26. Especially for higher overpotentials, for example the data recorded for $\eta = 150\ mV$ in Fig. 4.3a, a notable kink in the transient is visible. This is the transition from the behavior governed by eq. 2.26 to mass-transport controlled current, as stated by H. Gerischer [99,197]. The extrapolated $I(t=0\ s)$ values are then employed to reconstruct the Bulter-Volmer equation (eq. 2.21). As can be seen in Fig. 4.4, the anodic and cathodic branch can be investigated separately. As the current values are plotted on an exponential scale, the slopes of the linear approximations (red lines) are given by $\alpha_{a/c}nF/(RT)$ which can easily be realized when looking at eq. 2.21. The current at zero overpotential is I_0. At overpotentials higher than $100\ mV$ the current does not grow exponentially with applied overpotential anymore, the line-fit cannot be extended past these initial data points. From this graph the kinetic parameter can be determined. As there are no “cathodic exchange currents” or “anodic exchange currents” we take the arithmetic mean for I_0: $\{k_0 = 6.0\ 10^{-4}\ cm\ s^{-1};\ U_0 = n.a..;\ \alpha_a = 0.44;\ \alpha_c = 0.52\}_{\text{PS 1}}$.

The current response to the PSs was also fitted to eq. 2.26 with independent variables η and t, dependent variable current density j_0 and fitting parameters $D = D_{ox} = D_{red}$. Equal diffusion coefficients were chosen because the system should not be over-parameterized and the literature values only deviate little $D_{red}/D_{ox} = 0.9$. For the same reason $\alpha_c = \alpha_a = 0.5$. The fitting was done using a Levenberg-Marquardt algorithm [198].

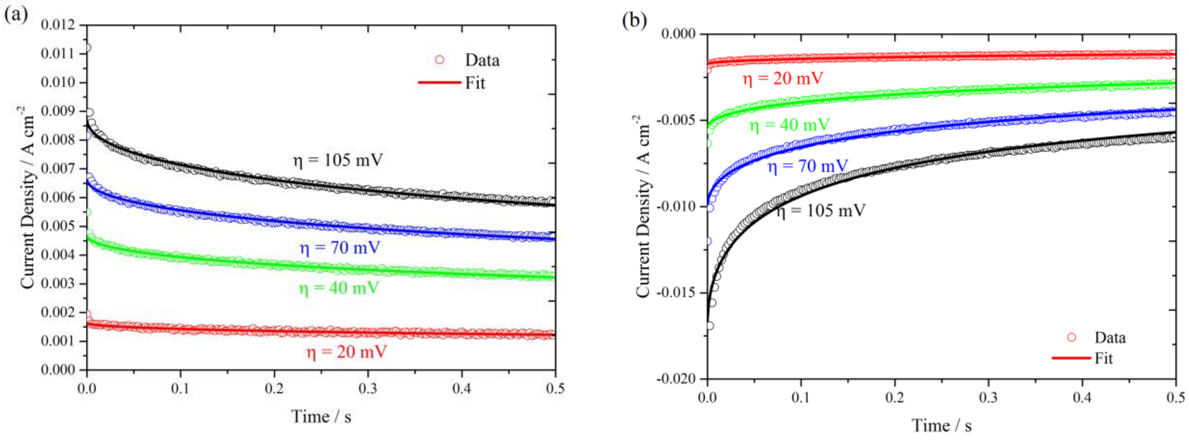

***Figure 4.5** - Evaluation of potential step measurements of the ferrous/ferric redox couple in 1 M $HClO_4$ on Pt. **(a)** Oxidation and **(b)** reduction. The curves were fitted to eq. 2.26 and the overpotentials η at which the current transients were recorded is given in the graph.*

Exemplary results for fitted current transients can be seen in Fig 4.5. The calculated curves match the experimentally obtained trajectories well. For each applied overpotential one value for the exchange current density j_0 and one value for D are obtained. These values are given in Fig. 4.6 and it is apparent that their deviation is quite significant. The diffusion coefficient for high anodic overpotentials ($100\ mV < \eta < 155\ mV$) is three times higher than for cathodic overpotentials. On the other hand, j_0 seems to decline with increasing absolute overpotential. As it should be a constant this has to be an artifact of the evaluation. For both values, D and j_0, the mean and the standard deviation was calculated and they are given in the graph. From this value, $\bar{j}_0 = (2.02 \pm 0.87)\ 10^{-3} A\ cm^{-2}$, the electron transfer constant k_0 was calculated: $\{k_0 = 4.2\ 10^{-4}\ cm\ s^{-1};\ U_0 = n.a..;\ \alpha_a = n.a.;\ \alpha_c = n.a.\}_{\text{PS 2}}$.

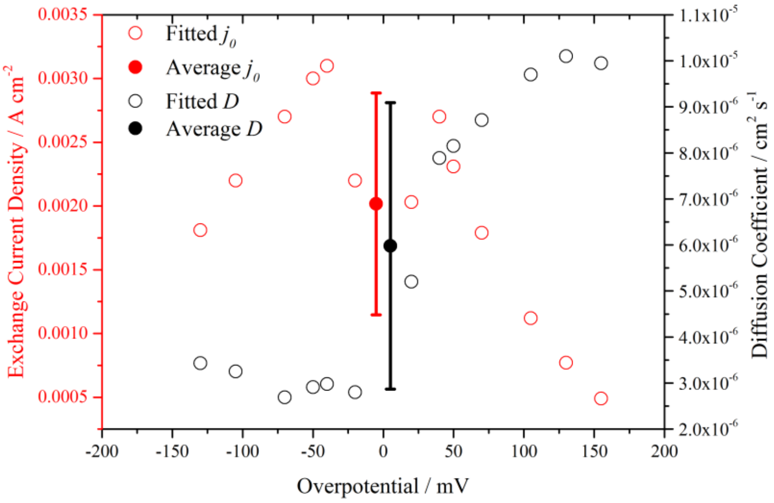

***Figure 4.6** - Values for the exchange current density (left ordinate) and the diffusion coefficient (right ordinate) for various overpotentials for the ferrous/ferric redox couple in 1 M HClO$_4$ on Pt. The empty markers were obtained from fitting curves as seen in Fig.4.5; the full markers are the mean values with standard deviation.*

4.1.4 Single current pulse and double current pulses

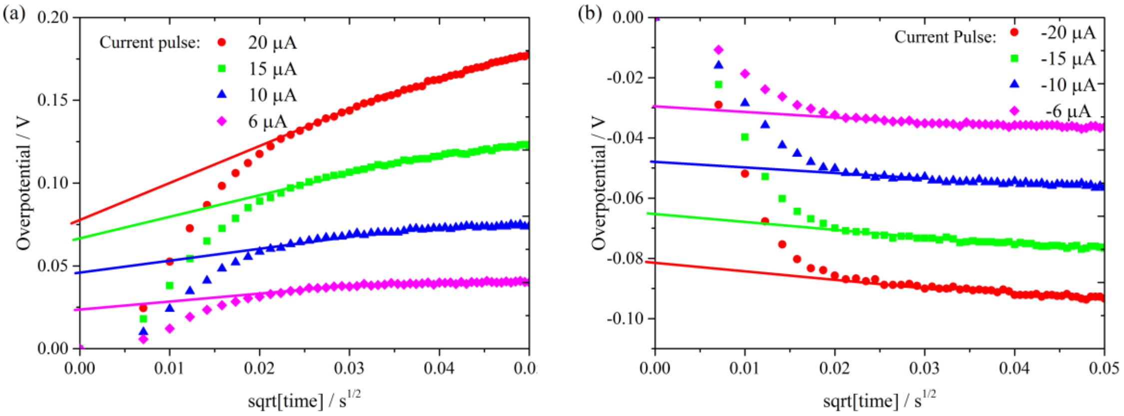

***Figure 4.7** - Evaluation of current step measurements of the ferrous/ferric redox couple in 1 M HClO$_4$ on Pt. **(a)** Oxidation and **(b)** reduction. The curves were linearly extrapolated back to $t^{1/2} \rightarrow 0\ s^{1/2}$ to obtain $\eta(t = 0\ s)$.*

SCPs and DCPs were performed to extract kinetic information from the ferrous/ferric redox couple. Fig. 4.7a shows exemplary potential transients for three applied currents. In the initial phase the potential rises slowly as the ECDL is charged. At approximately *0.02* $s^{1/2}$ ($\widehat{=}\ 4\ 10^{-4} s$) I_{NF} subsides and the overpotential rises linearly due to the developing concentration gradient at the electrode.

Looking at eq. 2.30 one realizes that extrapolation to $\sqrt{t} \rightarrow 0\ s^{1/2}$ does not yield only the overpotential but also the contribution from the term:

$$-\frac{R\,T}{n\,F}\left(\frac{L}{n\,F}\right)^2 C_{DL} \tag{4.2}$$

However, with $C_{DL} = 27.57\ 10^{-9}\ F$ (determined from EIS) and the relatively high concentration of redox-species ($0.1\ M\ L^{-1}$) the term is on the order of $10^{-8}\ cm^2\ A^{-1}$. Therefore, it is negligible in comparison with the expected inverse exchange current density. The extrapolated values were plotted on the abscissa with the applied currents on the ordinate, as seen in Fig. 4.8.

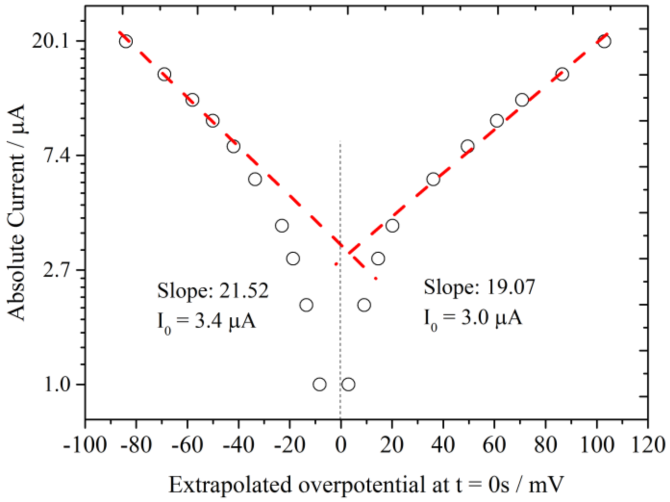

***Figure 4.8** - Values for the overpotentials extrapolated to t = 0 s for the ferrous/ferric redox couple in 1 M $HClO_4$ on Pt. The left data points represent the cathodic branch with α_c =0.55 and the right side corresponds to the anodic branch with α_a = 0.48.*

In comparison to Fig. 4.4 a smaller range of overpotentials was evaluated; the data points at the highest recorded overpotential do not deviate from the exponential behavior of the Butler-Volmer kinetics yet. At smaller overpotentials ($|\eta| < 50\ mV$) the linear character of the Butler-Volmer equation dominates and therefore the linear fit in the logarithmic representation starts at $|\eta| > 50\ mV$. Again, cathodic and anodic branch can be investigated separately which gives α_a and α_c. The exchange current I_0 is again taken as the mean of the anodic and cathodic result. This yields following set of kinetic parameters: $\{k_0 = 3.4\ 10^{-4}\ cm\ s^{-1}$; *n.a.*.; $\alpha_a = 0.49$; $\alpha_c = 0.55\}_{\mathrm{SCP}}$

The non-faradaic contribution to charge the ECDL is very obvious in Fig. 4.7. Therefore, the logical evolution of SCPs is to add a second current pulse that transfers the required charge ($Q_{DL} = C_{DL}\Delta U$) in a very short time. As presented in 2.5.2, the slope ($d\eta/dt$) should be equal to zero after the first current pulse. This was achieved in the case of the exemplary potential profile given in Fig. 4.9a. While the first pulse lasted only for $t_1 = 6\ 10^{-3}\ s$, it transferred a charge of $Q = 2.5\ 10^{-8}\ C$. This was apparently the right amount of charge to charge the ECDL and the overpotential transient (blue curve) starts out flat after $t = t_1$. A number of measurements were taken in that fashion and the extrapolated overpotentials with their corresponding currents are shown in Fig. 4.9b. Unfortunately, after recording the cathodic branch the galvanostat (HEKA PG 310) had a short-circuit and was beyond repair. Therefore, the anodic branch could not be recorded. The set of kinetic parameters obtained reads: $\{k_0 = 1.2\ 10^{-4}\ cm\ s^{-1};\ U_0 = n.a.;\ \alpha_a = n.a.;\ \alpha_c = 0.52\}_{\mathrm{DCP}}$

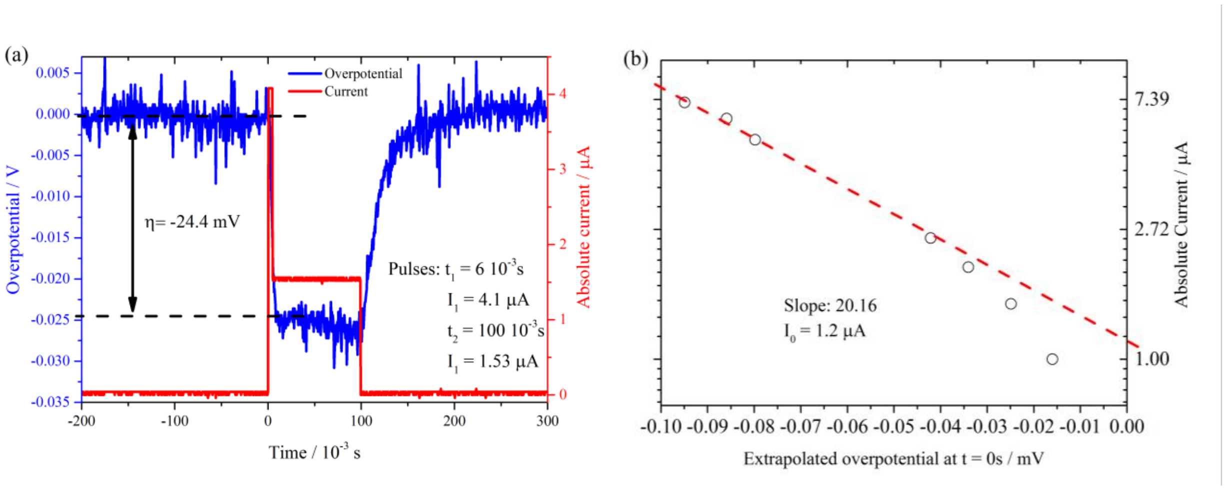

***Figure 4.9 - (a)** Evaluation of a double current pulse measurement of the ferrous/ferric redox couple in $1\ M\ HClO_4$ on Pt. The duration and magnitude of the two pulses are given in the graph. **(b)** Values for the overpotentials extrapolated to $t = 0$ s for the ferrous/ferric redox couple in $1\ M\ HClO_4$ on Pt. Only the cathodic branch was recorded due to instrument malfunction. The slope corresponds to $\alpha_c = 0.52$.*

4.1.5 Comparison and discussion

As a preface to comparing and discussing the obtained results the literature is consulted for kinetic parameters of the ferric/ferrous couple on Pt.
An early review on the topic was given by Klaus Vetter [54]. Gerischer found a value of $k_0 = 3.2\ 10^{-3}\ cm\ s^{-1}$ on a Pt electrode in $1\ M\ HClO_4$ [199]. The value was established via the changing polarization of the electrode at U_0 when the concentrations of Fe^{2+} and Fe^{3+} were changed. Gerischer mentioned that the addition of Cl^- increases k_0. However, his reference electrode was saturated $Ag/AgCl$ and therefore the used solution was certainly not free of Cl^- ions. Randles and Somerton determined a value in agreement with the former one ($k_0 = 5\ 10^{-3}\ cm\ s^{-1}$ on a Pt electrode in $1\ M\ HClO_4$) [200]. Weber et al. scrutinized the dependency of the redox-reaction on Cl^-, Br^- and SO_4^{2-} anions [201]. They discovered that a typical supporting electrolyte ($1\ M\ HClO_4$ prepared from “suprapur” grade conc. $HClO_4$ and triply distilled water) contains $5\ 10^{-7}$ to $8\ 10^{-7}\ M\ L^{-1}$ of chlorides. Therefore, the solution was then meticulously purified and the minimum rate constant the authors found on a Pt electrode was $k_0 = 10^{-5}\ cm^{-1}$. This value increased up to one hundred times upon addition of chlorides and up to ten times upon addition of sulfates.
Ultimately, Hung and Nagy listed 13 studies on the topic of kinetic data for the Fe^{2+}/Fe^{3+} redox reaction in $HClO_4$ with rate constants in the range of $k_0 = 1.3\ 10^{-4}$ to $k_0 = 2.3\ 10^{-2}\ cm\ s^{-1}$ [194]. Extrapolating over different Cl^- coverages they obtained a “chloride free” rate constant of $k_0 = 2.5\ 10^{-5}\ cm\ s^{-1}$ which corresponds well with the rate found by Weber et al. For an explanation of this catalytic effect of the anions there are two possibilities [194]:

- An electrostatic effect of the adsorbed ions perturbs the interfacial potential distribution of the transition complex and faster electron transfer is possible;
- A bridge-activated charge transfer mechanism during which the anion is incorporated into the first coordination shell of the reactant. The charge transfer then proceeds via the bridging, adsorbed anion. This is then an inner-sphere reaction mechanism and therefore faster than the non-catalyzed electron transfer.

For the transfer coefficient the literature values are relatively unanimous. Gerischer and also Hung and Nagy give the anodic transfer coefficient as $\alpha_a = 0.48$ and the cathodic counterpart as $\alpha_c = 0.52$ [194,199]. The transfer coefficient is stated to be independent of the Cl^- ion concentration [194].
The obtained kinetic parameters of the presented experiments are summarized in Table 4.1.

	CV	**EIS**	**PS 1**	**PS 2**	**SCP**	**DCP**
k_0 / cm s^{-1}	$2.9\ 10^{-3}$	$7.2\ 10^{-4}$	$6.0\ 10^{-4}$	$4.2\ 10^{-4}$	$3.4\ 10^{-4}$	$1.2\ 10^{-4}$
U_0 / V vs. NHE	*0.706*	*n.a.*	*n.a.*	*n.a.*	*n.a.*	*n.a.*
α_a	*0.5*	*n.a.*	*0.44*	*n.a.*	*0.49*	*malfunction*
α_c	*0.5*	*n.a.*	*0.52*	*n.a.*	*0.55*	*0.52*

***Table 4.1** - Kinetic parameters for the ferrous/ferric redox couple in 1 M $HClO_4$ on Pt extracted from the various performed experiments. CV – cyclic voltammetry, EIS – electrochemical impedance spectroscopy, PS 1 – potential steps extrapolated to $t \rightarrow 0$ s, PS 2 – potential steps fitted to equation, SCP – single current pulse, DCP – double current pulse. The DCP-method does not have a result for α_a because of instrument malfunction.*

Immediately apparent when looking at Table 4.1 is the fact that out of the applied techniques CVs are the only reliable method to determine U_0. While all the other techniques are performed in potential ranges around U_0, only with CVs it is possible to calculate U_0 with some degree of confidence. Therefore, in this thesis CVs will always be used to obtain a first impression of a redox reaction and to determine U_0. However, the fit for the CV, for the determination of k_0, is poor and therefore this method can be disregarded for the evaluation of the electron transfer rate. In addition, porous electrode structures, like MWCNT decorated glassy carbon, lead to apparent electrocatalytic effects [14,24,202]. Also, multiple redox-reactions and adsorption onto the electrode, as for the redox-reactions of POMs, render CVs too complicated to be modelled [39,42].
EIS as a method has two big advantages. One is that it provides additional information about the electrochemical cell, like C_{DL} and R_{Ohm}. Another benefit is the ease of operation. A suitable potentiostat, one that is equipped with a frequency response analysis board, is able to automatically perform the measurement within a few minutes. The other techniques, PSs, SCPs, DCPs, require an operator to constantly monitor and manipulate both electrochemical cell and potentiostat/galvanostat. Also, data evaluation for the latter techniques is more time-consuming.
The extrapolation of the current response to a PS provided results for the electron transfer constant k_0 and the transfer coefficients. Yeager and Kuta claimed that this method is the

most suitable to analyze fast redox-reactions, especially when the contribution of the non-faradaic currents is known [94]. A problem related to this method is certainly that it requires two line-fits. First, the “kinetic current” has to be selected in the raw data (see. Fig. 4.3). Second, the exponential part of the extrapolated current values $I(t = 0\ s)$ over the overpotential has to be found and fitted (see Fig. 4.4). This introduces two slightly arbitrary elements into the analysis. However, we gauge this source of error to be a minor one. Therefore, this method will be employed to obtain kinetic parameters from POMs in chapter 6. Additional numerical subtraction of the non-faradaic currents will be employed to enhance the accuracy.

While the numerical fits matched the experimental curves for PS quite well (see. Fig. 4.5), the obtained exchange current densities scatter too much, as seen in Fig. 4.6. It might be possible to enhance this method with a more sophisticated analysis, to employ more parameters and then get more consistent values. However, the analysis that uses extrapolation is deemed superior and will therefore be employed for the kinetic analysis.

The two current pulse methods, SCP and DCP, resemble the PSs in most aspects. However, as it was pointed out by Yeager and Kuta, there is the additional complication of the term that accounts for the fact that the concentrations at the electrode change less than otherwise expected due to the non-faradaic currents [94]. While this contribution is negligible in the case of the relatively high concentrations of Fe^{2+}/Fe^{3+} and the small C_{DL} of the Pt-disk electrode, this is not the case for the POM studies ($C_{DL} \approx 1\mu F$ and $c_{POM} = 0.5\ 10^{-3}\ mol\ L^{-1}$) . Therefore, SCPs and DCPs were omitted in favor of PSs.

All the quantitative values for k_0 lie in between the limiting value for “chloride-free” supporting electrolytes, $k_0 = 2.5\ 10^{-5}\ cm\ s^{-1}$, and non-purified electrolytes, $k_0 = 5\ 10^{-3}\ cm\ s^{-1}$ [194,201]. In fact, the values, except for the one obtained from CV, correspond quite well with the mentioned ten-fold increase of kinetics in the presence of SO_4^{2-}, the order of magnitude for k_0 is $10^{-4}\ cm\ s^{-1}$ [201]. A possible explanation is that the de-ionized water that was obtained for this work contains less Cl^- ions than the “triply-distilled” water used by Weber et al. Also, it seems possible that SO_4^{2-}- ions from the reference electrode compartment saturated the electrode; therefore the catalysis is predominantly performed by these anions.

The shift in U_0 from the characteristic standard potential $U^{\theta} = 0.77\ V\ vs.\ NHE$ is another indication for the presence of SO_4^{2-} ions, as this effect was attributed to sulfate-ions in the literature [14,47,67].

All the performed measurements that are sensitive to transfer coefficients α_c and α_a agree with the literature that the cathodic coefficient is slightly larger than α_a [54,199]. The PS and DCP technique even reproduced the same α_c= 0.52.

4.2 Ferrous/Ferric redox couple on a porous carbonaceous electrode

The measurement techniques described in the previous subsection were designed to extract electron transfer kinetics of a redox couple on an ideal, flat electrode. However, most commercial electrodes for RFBs are high surface-area, porous electrodes [166]. Also, the advent of nanostructured electrodes complicated the discourse, as these nanostructures often feature an intricate electrode geometry that has to be taken into account if one wants to evaluate its activity towards a certain redox reaction. Examples for such nanostructures for the application in RFBs are discussed in the recent review by Chakrabarti et al. [13].

4.2.1. Cyclic voltammetry

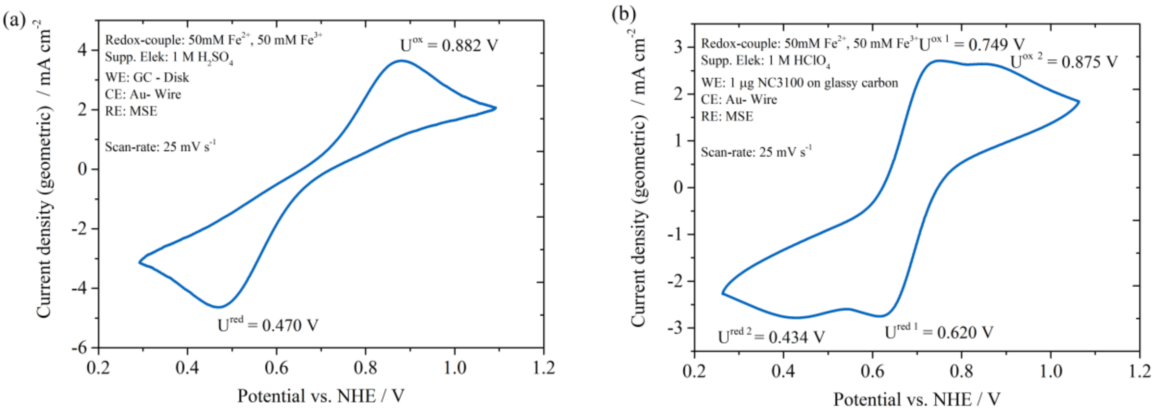

***Figure 4.10** - Cyclic voltammogram of the ferrous/ferric redox couple in 1 M H_2SO_4 with a scan-rate of 25 mV s^{-1} on **(a)** a polished glassy carbon disk electrode and **(b)** on a glassy carbon electrode decorated with 1 µg NC3100 multi-walled carbon nanotubes. The experimental details are given in the graph.*

In this section three experimental techniques, CVs, PSs and EIS, are compared and evaluated regarding their ability to obtain kinetic information on porous electrodes. Again, the investigated electrolyte contains *50 mM* Fe^{2+} and *50 mM* Fe^{3+}. However, perchloric acid was replaced with *1 M* H_2SO_4 because $HClO_4$ is not permitted in Singaporean laboratories due its explosive threat. The left graph, Fig. 4.10a, shows the ferrous/ferric redox couple on a glassy carbon electrode, the experimental details are given in the graph. The cathodic and the anodic peak exhibit a considerable peak separation of $\Delta U^{peak} = 412\ mV$ with $U_0 = 0.676\ V$ *vs. NHE.* Fig. 4.10b shows a CV of the same electrolyte on a GC electrode decorated with *1 µg* of untreated NC3100 MWCNTs. The structure of such an electrode was imaged with an SEM and the micrograph is shown in Fig. 3.5 (upper left micrograph). From the image it can be deducted that there are areas on the electrode that are extensively covered with bundles of nanotubes and that these form a porous network. On the other hand, plain GC surface is visible as well. The CV for the porous electrode, Fig, 4.10b, shows two oxidation and two reduction peaks. Their potential positions are marked in the graph. Analyzing the peak separation one obtains two values, $\Delta U^{peak\,1} = (U^{ox\,1} - U^{red\,1}) = 129\ mV$ and $\Delta U^{peak\,2} = (U^{ox\,2} - U^{red\,2}) = 441\ mV$. As the exact ECSA of the porous electrode is unknown both CVs were normalized to geometrical surface area of the glassy carbon electrode, which constitutes only a part of the electrode area in the case of Fig. 4.10b. Comparing the two CVs it is obvious, that the peaks $U^{ox\,2}$ and $U^{red\,2}$ resemble the peaks U^{ox} and U^{red} on plain GC in shape and peak separation.

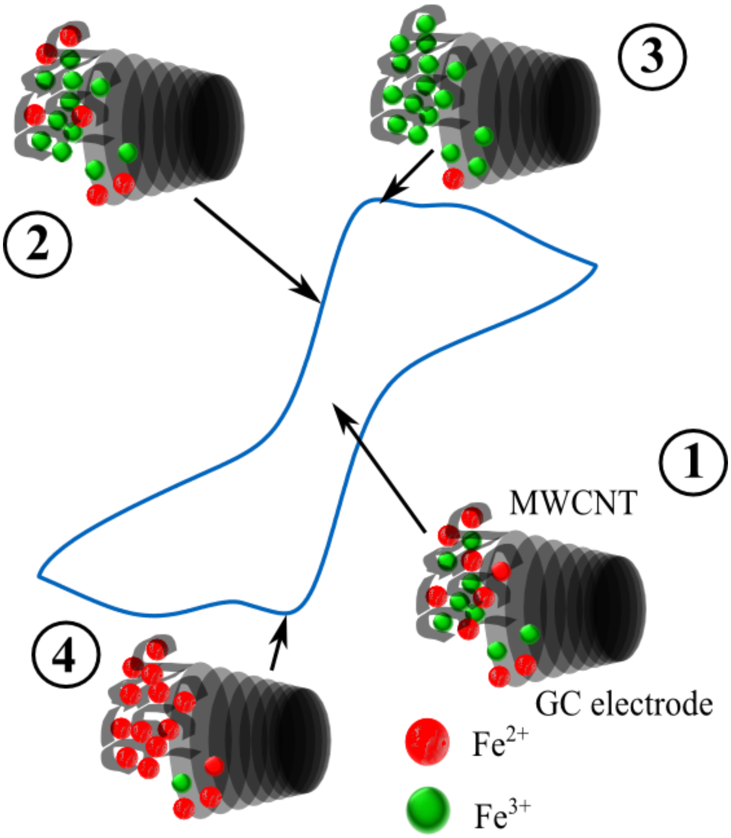

Figure 4.11 *- Schematic explanation for the occurrence of two oxidation and reduction peaks in Fig. 4.10b. A model for an electrode is shown that is partially covered with multi-walled carbon nanotubes that form a porous cavity that is filled with Fe^{2+} (red) and Fe^{3+} (green) cations.*

Thus, it is assumed, that the secondary peaks in Fig. 4.10b stem from the electron transfer of the Fe^{2+}/Fe^{3+} couple on the GC substrate, a notion that is supported by the fact that the substrate is visible in Fig. 3.5a. A CV measured on an electrode that was decorated with 4 μg of MWCNTs (not shown here, scan rate $25\ mV\ s^{-1}$) yielded no secondary peaks and a peak separation of $\Delta U^{peak\,1} = (U^{ox\,1} - U^{red\,1}) = 109\ mV$. If the substrate is sufficiently covered with MWCNTs there is no current signal from the GC anymore.

The primary peaks stem from the oxidation and reduction of the redox-species within the porous framework of the MWCNT network. It was reported that porous electrodes can exhibit faster apparent kinetics in CVs than their flat counterparts [14,24,202]. Faster apparent kinetics are attributed to such electrodes because the inverse peak separation is usually taken to be proportional to the electron transfer constant k_0 [67]. Fig. 4.11 schematically explains why two oxidation and reduction waves are observed. The drawn electrode is partially covered in MWCNTs. These tubes form a porous structure and its

voids are filled with Fe^{2+} and Fe^{3+} ions. State 1 represents the equilibrium potential. According to the Nernst equation (eq. 2.16), U_0 is characterized by equal activities of oxidized and reduced species. State 2 corresponds to a small anodic overpotential. As the ECSA of the porous structure is high and the redox-ions are in close proximity to the electrode there is a large oxidation current. In state 3 all the Fe^{2+} ions within the porous structure were oxidized to Fe^{3+}. As diffusion of Fe^{2+} ions from the bulk into the pores is hindered the current contribution from the MWCNTs decays. However, the second peak emerges as the flat GC oxidizes Fe^{2+} ions. Its peak potential is determined by the interplay of Butler-Volmer kinetics and mass-transport limitation. State 4 is similar to state 3. But its potential corresponds with total reduction of Fe^{3+} within the porous structure.
As peak position is a function of porosity and not of the kinetics of the redox couple on the electrode material, CVs are not a suitable technique to extract k_0 from high surface area, porous electrodes [14,24]. A similar splitting of the waves into two, one peak for depletion of material inside the porous structure and one peak for diffusion of species, was also reported for graphene electrodes very recently [17].

4.2.2 Electrochemical impedance spectroscopy

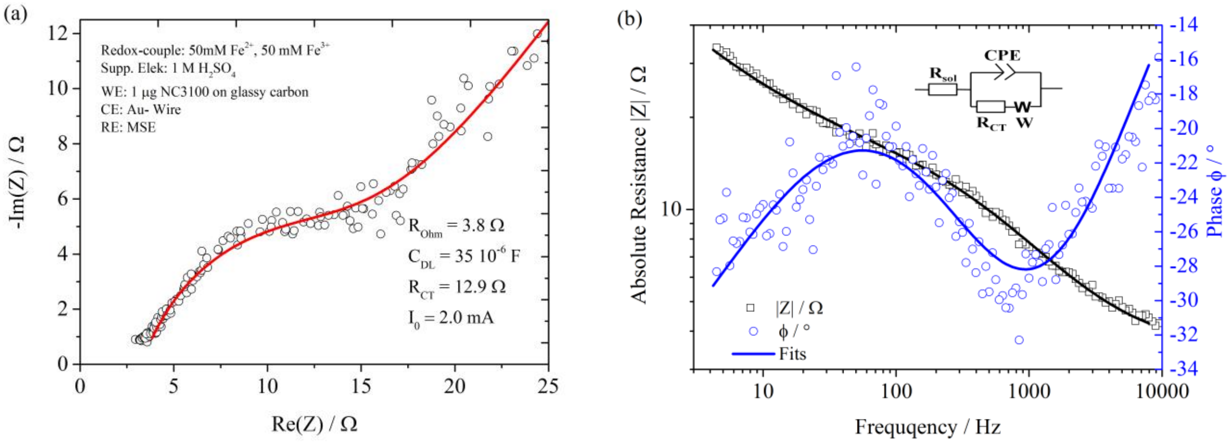

Figure 4.12 *- Electrochemical impedance spectroscopy measurements of the ferrous/ferric redox couple in 1 M H_2SO_4 on a glassy carbon electrode decorated with 1 µg NC3100 multi-walled carbon nanotubes.* ***(a)*** *Nyquist- and* ***(b)*** *Bode-representation. The data points were fitted to the Randles-circuit given in the upper right.*

The result from EIS for the electrode covered with *1 µg* of untreated NC3100 MWCNTs in the same electrolyte as above can be seen in Fig 4.12. The data points are fit to the Randles-circuit and the Nyquist- and Bode-representation are given. Interestingly, there is only one semicircle present, not two as one could expect from the respective CV (Fig. 4.10b). This might be due to the fact that for the small applied overpotentials, an amplitude of 10 mV was used for the sine wave, the contribution from the porous MWCNTs part of the electrode dominates the plain GC current response. If the obtained $C_{DL} = 35\ 10^{-6}\ F$ is normalized by the typical specific capacitance of carbonaceous material ($c_{DL} = 10\ 10^{-6}\ F\ cm^{-2}$ [15]), a value of $A^{ECSA} \approx 3.5\ cm^2$ is obtained for the ECSA. Since the geometric surface area is $A^{geo.} \approx 0.20\ cm^2$, the roughness factor caused by the addition of 1 μg of MWCNT can be estimated to $\approx$17.5. If this extended surface area is used together with the fitted exchange current $I_0 = 2.0\ mA$ the electron transfer constant $k_0 = 1.2\ 10^{-4}\ cm\ s^{-1}$ is obtained. The mass-transport limitations that rendered CVs an improper technique are intrinsically considered by EIS as the Warburg impedance accounts for it [107]. The additional information obtainable with EIS, C_{DL} and R_{Ohm}, can prove useful as demonstrated by obtaining a rough estimate for the ECSA.

4.2.3 Potential steps

The electrode decorated with $1\ \mu g$ *NC3100* MWCNTs was also subjected to PSs in $50\ mM\ Fe^{2+}$ and $50\ mM\ Fe^{3+}$ in $1\ M\ H_2SO_4$. Exemplary curves for the current over $\sqrt{t}$ for five overpotentials are shown in Fig. 4.13a. Taking C_{DL} and R_{Ohm} into account, the non-faradaic currents are expected to have decayed after $5\,\tau = 6.7\ 10^{-4}\ s \mathrel{\widehat{=}} 0.026\ \sqrt{s}$. Therefore, the linear extrapolation was initiated after this value. This indicates that the three regimes one can distinguish, for example for the blue data points ($\eta = 200\ mV$), can be assigned to three mixed regions. In the beginning, until approximately $0.02\ \sqrt{s}$, there is the mixed regime of faradic- and non-faradaic currents. Afterwards, until approximately $0.055\ \sqrt{s}$, the faradaic current decays due to the diminishing concentration of oxidizable species (Fe^{2+}). The adjacent kink in the curve marks the transition to purely mass-transport limited current. As before, the electron transfer constant is calculated by normalizing with the ECSA obtained by EIS: $\{k_0 = 8.7\ 10^{-5}\ cm\ s^{-1};\ U_0 = n.a.;\ \alpha_a = 0.50;\ \alpha_c = 0.46\}_{\mathrm{PS}}$.

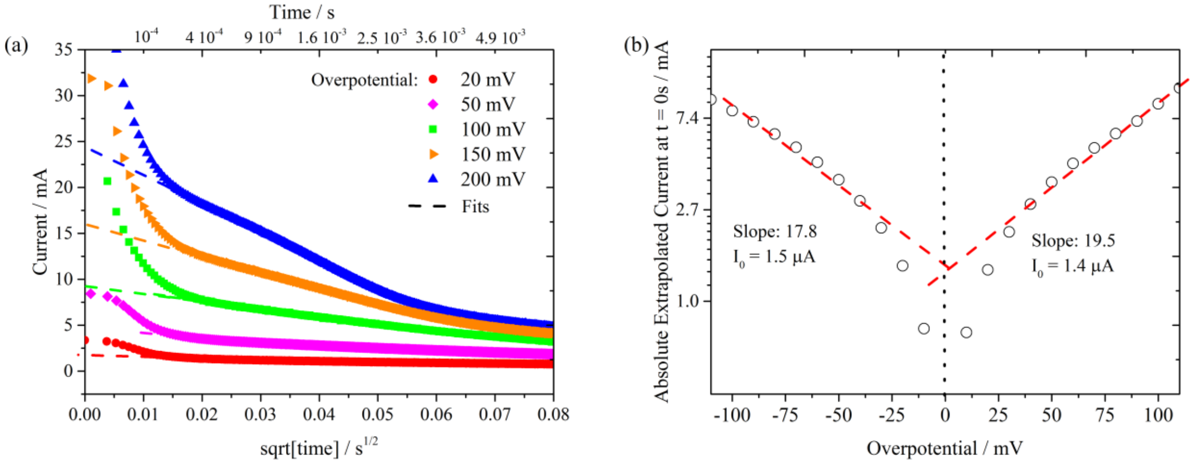

***Figure 4.13** - Results for the potential step experiment for the ferrous/ferric redox couple in 1 M H_2SO_4 on a glassy carbon electrode decorated with 1 µg NC3100 multi-walled carbon nanotubes.* ***(a)** Exemplary curves for the anodic reaction.* ***(b)** Extrapolated absolute current values at t=0.*

4.2.4 Comparison and discussion

General statements about the kinetics of the ferric/ferrous redox-reaction on carbon electrodes prove difficult because the reaction is highly sensitive to the presence of surface oxides, particularly carbonyl groups [15]. This fact will be scrutinized in the next chapter when the influence of surface functional groups on this reaction is investigated. Here, it was analyzed if certain methods are suitable to extract k_0 when a porous electrode is employed. Without a doubt it was shown that CVs are an unsuitable tool to extract kinetics of a redox reaction on high surface area, porous electrodes. The porous structure leads to an apparent catalytic effect and the peak potential position and therefore the peak separation becomes a function of porosity [14,24,202]. On the other hand, EIS and PSs produce a reasonable value for k_0. The fact that the onset of mass-transport limitation is clearly visible encourages confidence in these two methods, because obscure diffusion properties are the reason for the non-applicability of CVs. From the Bode-plot one can determine that EIS produces meaningful results for the investigated reaction in a time regime from $10^{-5}\ s$ to $10^{-3}\ s$. If the wavelength of the potential perturbation is longer, mass-transport limitation commences.

Analogous, for a PS with applied overpotential of $200\ mV$ mass transport limitation masks the kinetic current after approximately $3.5\ 10^{-3}\ s$.

Chapter 5
Catalysis on functionalized multi-walled carbon nanotubes

As highlighted in the introduction, a plethora of recent studies investigated the influence of novel electrode materials on the activity of the VO^{2+}/VO_2^{+}-redox reaction [18–23,203]. A catalytic effect was assigned to these structures. However, mostly CVs were used to investigate the electrochemical performance, and, as shown in the previous chapter, these are not a valid technique for porous electrodes. Therefore, a new technique is presented here. It is based on EIS that was shown to yield meaningful results in the previous chapter. The approach is to synthesize MWCNTs with a surface functional group content ranging from very low to very high and then to assess if the introduced method is able to detect differences in k_0. The investigated redox couples are the VO^{2+}/VO_2^{+} system because of its importance for RFBs, and the Fe^{2+}/Fe^{3+} redox couple because it is well studied and often used as model system. Furthermore, it is plausibly demonstrated in the literature that the Fe^{2+}/Fe^{3+} system is indeed catalyzed by surface oxides [15].
First, the characterization of the functionalized MWCNT samples will be presented. Second the electrochemical results for the MWCNT samples on GC will be shown and discussed. This chapter is based on a publication by Friedl et al. [14].

5.1 Characterization of electrode material

The as-received NC3100 MWCNT from the company Nanocyl were functionalized as described in chapter 3. Also, the descriptive names of the samples were introduced.

5.1.1 Thermogravimetric analysis coupled to mass spectroscopy

The TGA-MS measurements are shown in Fig. 5.1. After the temperature ramp was completed the samples lost some of their mass due to thermal removal of functional groups. The details are given in Table 5.1:

	PRIST	**DEFUNC**	**NITRIC**	**NITSULF_3h**	**NITSULF_6h**
Weight loss (%)	2.2	0.7	4.5	7.0	19.0

Table 5.1 *Weight loss due to thermal removal of functional groups during the temperature ramp described in section 3.3.2*

Fig. 5.1 and the extracted data indicate that the functionalization process had the intended effect on the carbon samples. Two samples with heavy functionalization were obtained, sample NITSULF_3h and NITSULF_6h.

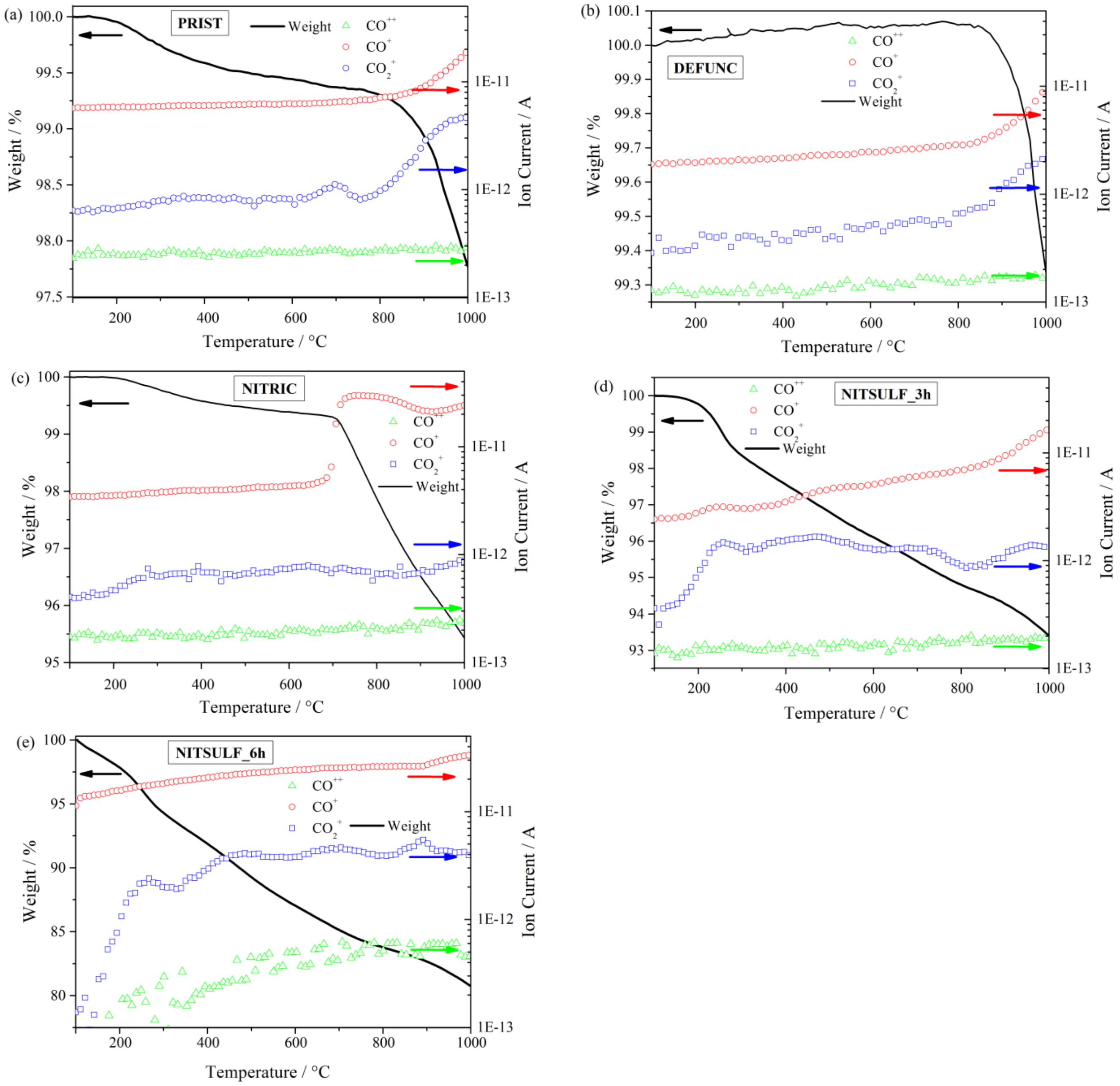

__Figure 5.1__ - TGA-MS spectra for the functionalized MWCNT samples. __(a)__ PRIST, __(b)__ DEFUNC, __(c)__ NITRIC, __(d)__ NITSULF_3h and __(e)__ NITSULF_6h.

Intermediate functionalization was achieved for sample NITRIC and the as-received MWCNTs, sample PRIST, exhibits a mild degree of functionalization as well. The de-functionalization process for sample DEFUNC was successful, as the initial amount of removable surface groups was decreased from 2.2% to 0.7%. The gain in weight of roughly

0.05 % for sample DEFUNC (Fig. 5.1b) during the temperature ramp can be explained by a slight mismatch between the crucible holding the sample and the empty reference crucible.

The desorption temperature reveals the type of functional group that was present on the carbon surface [112–116]. A list of desorption temperature ranges together with detectable gases and the responsible functional groups was given in Table 2.2. Sample PRIST (Fig 5.1a) shows distinct regions of mass loss above and below *800 ˚C*. The small peaks in CO_2^+ signal starting at *300 ˚C* most likely stem from carboxylic groups. The small bump in CO_2^+ signal at *700 ˚C* corresponds well with the reported signal from lactones. Carbonyls and quinones are most likely responsible for the CO and CO_2 evolution at temperatures higher than *800 ˚C*.

The same high-temperature trend can be observed for sample DEFUNC. Prior to that, at lower temperatures, no appreciable signal was recorded by the MS. Therefore it is possible to conclude that all functional groups except carbonyls and/or quinones were removed from sample DEFUNC.

At low temperatures, up until approximately *700 ˚C*, sample NITRIC shows a trend very similar to sample PRIST that indicates that some carboxylic groups are present. At *700 ˚C*, however, there is a steep increase in CO^+ signal. As this rise in signal is not reproduced for CO_2^+, the desorbing species must be phenols, carbonyls or quinones. The high temperature behavior is again very similar to PRIST.

The spectra of the highly functionalized samples NITSULF_3h (Fig. 5.1d) and NITSULF_6h (Fig. 5.1e) deviate considerably from the spectra of the other MWCNT samples. Both samples show a pronounced peak at *280 ˚C* that was not observed in that intensity for any other sample. The range of temperature as well as the evolution of CO_2^+ point towards the presence of large amounts of carboxylic groups. The presence of carboxyl is expected due to the functionalization process in the oxidizing acids H_2SO_4 and HNO_3 [115]. Until *800 ˚C* there are two more peaks in the CO_2^+ spectrum observable. While the position of the one at *700 ˚C* corresponds to the one assigned to lactones for sample PRIST, the one at *480 ˚C* might stem from desorption of anhydrides.

5.1.2 Fourier transform infrared spectroscopy

FTIR spectra for the five MWCNT samples under investigation are shown in Fig. 5.2. The absorption peak at $\bar{\nu} = 1716\ cm^{-1}$ indicates the presence of carboxylic surface groups [112,204]. This corresponds well with the TGA-MS results, as FTIR shows this dip in transmission only for samples NITSULF_3h and NITSULF_6h. Aromatic groups and quinones are the most likely candidates to cause absorption at $\bar{\nu} = 1558\ cm^{-1}$ [113,121]. This absorption peak is present on all samples but the signal is weakest on sample DEFUNC and strongest on NITSULF_6h, which indicates that the functionalization approach was successful. From $\bar{\nu} = 1169\ cm^{-1}$ to lower wavenumbers all the samples show absorption which can be attributed to a many different functional groups like lactones, anhydrides and phenols [113,122]. Again, there is a clear sequence in strengths of absorption that corresponds with the relative amount of functional groups shown in Table 5.1.

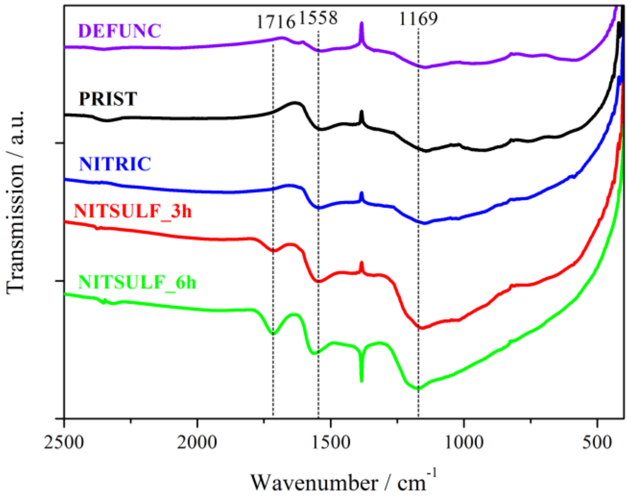

Figure 5.2 *- Fourier transform infrared spectra for the MWCNT samples. Three absorption lines are marked. The curves are normalized to their transmission at 400* cm^{-1} *and shifted for clarity. The graph is taken from* [14].

5.1.3 Raman spectroscopy

Raman spectroscopy was employed to monitor changes in the graphitic character of the MWCNTs induced by the functionalization process. As described earlier, the ratio of the D-band to G-band reflects the graphitic character of the sample [205,206]. The Raman spectra of the five samples are shown in Fig. 5.3. Lorentz curve-fitting was performed to determine the peak heights and the ratios are given in Fig. 5.3a. Comparison of the I_D/I_G ratios for PRIST and NITRIC indicates that the treatment in diluted HNO_3 had little effect on the graphitic character of the MWCNTs. On the other hand, exposure to concentrated H_2SO_4 and HNO_3 deteriorated the crystal structure and introduced defects. This is indicated by the higher ratios for samples NITSULF_3h and NITSULF_6h. Heat treatment, as performed for sample DEFUNC, increased the graphitic character of the MWCNTs as lattice defects were healed [207]. The literature value for Nanocyl 3100 is given as $I_D/I_G =1.8$ which corresponds well with the result shown here [179].

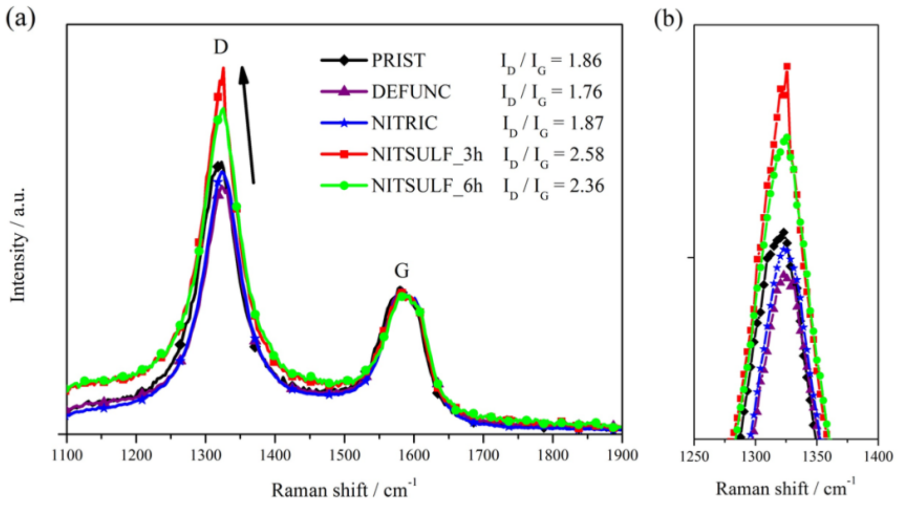

***Figure 5.3 - (a)** Comparison of the Raman spectra for the MWCNT samples. **(b)** Detail of the D-band peak. The graph is taken from* [14].

5.1.4 Discussion of MWCNT functionalization-process

The spectroscopic results clearly show that the functionalization process was successful and five MWCNT samples with varying amounts of surface functional groups were obtained. It is difficult, however, to create a narrow distribution of functional groups with oxidizing acids as the ongoing reactions are too manifold [208]. The MWCNTs are not decorated with a single, specific type of functional group, but samples with a wide range of different amounts of functional groups were created, as proven by the mass-loss detected by TGA (Table 5.1). NITSULF_3h and NITSULF_6h are decorated with significantly more carboxylic groups than the other samples, which were detected by TGA-MS and FTIR. This is important because a catalytic effect towards the VO^{2+}/VO_2^+ redox-reaction was specifically assigned to carboxylic groups [209].

It was suggested that x-ray photoelectron spectroscopy (XPS) should be used to detect and characterize the MWCNT samples, as it is a highly sensitive method to analyze surface oxygen groups [210]. This technique was omitted, however, because the methods of generation of functional groups were quite coarse and a wide spectrum of different functional groups was generated. The characterization methods, especially TGA-MS, were therefore selected to give a more quantitative than qualitative results. The wide array of surface functional groups would make XPS peak assignment rather complicated.

5.2 Dependence of double layer capacitance and electrochemical active surface area on mass of multi-walled nanotubes

As seen in Fig. 3.5, drop-casting of MWCNTs on GC substrates leads to the formation of a porous electrode. The determination of the ECSA of such an electrode is complicated. It is possible to employ the Brunauer-Emett-Teller (BET) method which determines the surface available for the adsorption of N_2, however, this technique has two flaws. First, the surface area of a powder sample is investigated, not of the actual electrode. Second, the surface area that is accessible to the N_2 molecules is certainly larger than the area accessible to hydrated ions, especially large ions such as VO^{2+} and VO_2^+ [25,211]. Tessonnier et al. investigated a number of commercial carbon nanostructures and give a BET surface area of $A^{BET} = 334\, m^2 g^{-1}$ for the Nanocyl 3100 tubes [179].

On the other hand, it was seen in section 4.2, that EIS is a valid tool to determine reaction kinetics on porous electrodes and that it also provides C_{DL}. If a single nanotube is considered as cylinder with length l and radius r, its capacitance is given by:

$$C_{DL} = 2\pi\, \varepsilon_r\, \varepsilon_0 \frac{l}{\ln(\frac{r+t_{DL}}{r})} \approx 2\pi\, \varepsilon_r\, \varepsilon_0 \frac{l}{\ln\left(\frac{t_{DL}}{r}\right)} = \varepsilon_r\, \varepsilon_0 \frac{A}{t_{DL}} \tag{5.1}$$

Above formula simplifies to that of a plate capacitor if one assumes that the thickness of the ECDL t_{DL} is much smaller than r. This simplification is certainly valid as t_{DL} is on the order of some Angstroms and the NC 3100 have an average external diameter of 9 nm [14,125]. Therefore, eq. 5.1 predicts that the true ECSA A is directly proportional to C_{DL}. This assumption was used earlier, in section 4.2 when the determined C_{DL} was divided by the specific double layer capacitance to obtain an estimate for A. In the former case the validity of this proportionality of C_{DL} and A was simply assumed without proof, this is now verified: For this purpose electrodes were coated with samples NITSULF_3h and PRIST. The mass of MWCNT sample mixed with organic solvent and also the volume drop-cast onto the electrodes were carefully controlled to obtain accurate values for the mass of nanotubes on the electrodes. The prepared electrodes were then tested in an electrolyte that consisted only of $1\ M\ H_2SO_4$ (blank) and electrolyte that comprised $1\ M\ H_2SO_4$ and $50\ mM\ VO^{2+}$ and $50\ mM\ VO_2^+$. The C_{DL} was determined for both types of electrodes in both electrolytes via two methods, CVs and EIS.

For CVs, the calculation of C_{DL} is done by:

$$C_{DL} = \frac{I^{ox} - I^{red}}{2} \left(\frac{dU}{\mathrm{dt}}\right)^{-1} \tag{5.2}$$

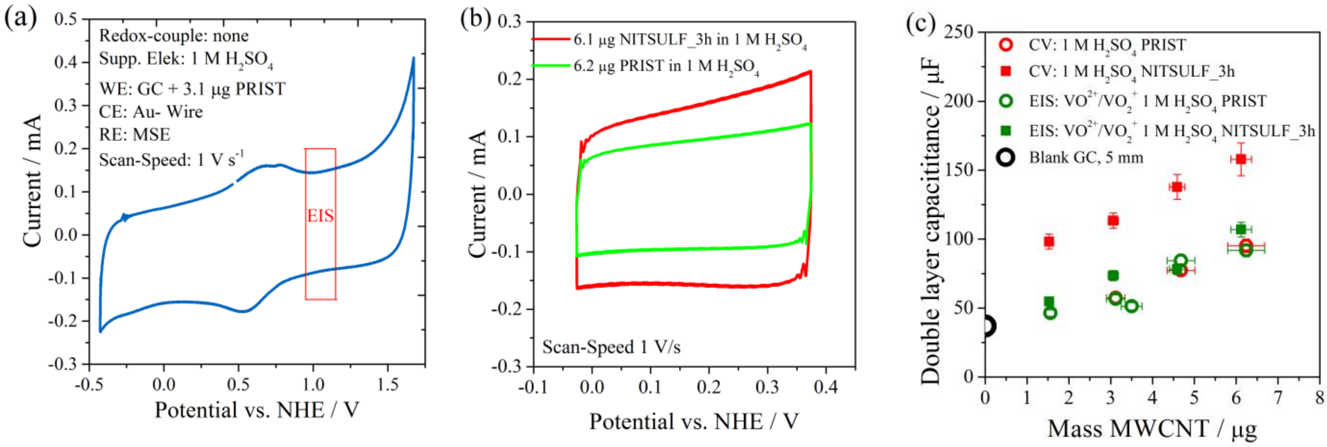

Figure 5.4 - (a) *A cyclic voltammogram of a glassy carbon electrode decorated with 3.1 µg PRIST measured in 1 M* H_2SO_4 *without a dissolved redox-couple. The potential region in which EIS is measured is marked.* ***(b)*** *Comparison of two CVs both recorded in 1 M* H_2SO_4*. The red curve stems from an electrode decorated with 6.1 µg NITSULF_3h while the green curve was recorded with 6.2 µg PRIST on the GC substrate. The scanned potential range was chosen to be smaller than in (a).* ***(c)*** *Compiled results for double layer capacitance* C_{DL} *over mass of MWCNTs for samples PRIST and NITSULF_3h, measured in both blank electrolyte and electrolyte containing 50 mM* VO^{2+} *and 50 mM* VO_2^+*.*C_{DL} *of the GC substrate is given as comparison at a mass of 0 µg MWCNT.*

As can be seen in Fig. 5.4a, which shows a CV for *3.1 µg* PRIST on GC at a scan-rate of $1\ V\ s^{-1}$, even in blank supporting electrolyte there are redox reactions taking place. While the anodic current at the higher vertex potential and the cathodic current at the lower vertex potential are expected due the stability limit of $1\ M\ H_2SO_4$, the oxidation peak at $U = 0.66\ V$ *vs. NHE* and the reduction peak at $U = 0.54\ V$ *vs. NHE* are contributions from the electrode, and not from the electrolyte. These faradaic currents from the functional groups lead to a deviation of the CV from the rectangular shape of an ideal capacitor. To employ eq. 5.2, a smaller scan-window was therefore chosen, as it can be seen in Fig. 5.4b. However, even in the range from $-0.02\ V$ *vs. NHE* $< U < 0.37\ V$ *vs. NHE* a faradaic contribution from functional groups is observable, which is more pronounced for the heavier functionalized NITSULF_3h. For the calculation of C_{DL} according to eq. 5.2 average values for I^{ox} and I^{red} were determined. Values for C_{DL} were determined for four electrodes with increasing mass of MWCNT, for both samples and in the two electrolytes. The results are presented in Fig. 5.4c. The trend of C_{DL} vs. mass is offset from the origin by the C_{DL} of the GC substrate, which contributes to the ECDL as well. It is given in the graph as black, empty data point. Values determined from EIS and from the CVs of the PRIST sample match quite well and yield a slope of roughly $10\ \mu F/\mu g$. The presence of vanadium ions does not change the behavior of C_{DL} vs. mass of MWCNT. Data points for sample

NITSULF_3h obtained from CVs show a considerably offset from the other data points at the same mass, a fact that can be attributed to the faradaic contribution of the functional groups. This adds a systematic error to the measurement. That this effect does not appear for the EIS measurements can be explained by the fact that these experiments were performed around $U_{eq} = 1.05\ V\ vs. NHE$ with an amplitude of $10\ mV$, and that at this potential the functional groups are not redox-active and therefore do not contribute pseudo-capacitance.

If one calculates a specific gravimetric double layer capacitance from the BET surface area of the Nanocyl 3100 ($334\ m^2 g^{-1}$) and the c_{DL} of carbonaceous materials ($10\ \mu F\ cm^{-2}$) [15,179], the obtained value is $33\ \mu F/\mu g$. While the order of magnitude is certainly similar to the value obtained for the slope in Fig. 5.4b, the fact that it is larger might indicate that the BET method yields an overestimation for the surface area accessible for hydrated ions, as speculated earlier.

Now, with the proportionality between mass, ECSA and C_{DL} established, the foundation for a new method to determine the kinetics of a redox-reaction is laid down. For porous structures the exchange current can be determined via PSs or EIS measurements, as shown in section 4.2. However, normalization to the electron transfer constant k_0 is difficult because the ECSA is unknown. EIS measurements yield R_{CT} and C_{DL}, which are both proportional, the former inversely the latter directly, to A (compare eq. 2.23 and eq. 5.1). Substitution of eq. 5.1 into eq. 2.23 yields:

$$R_{CT}^{-1} = \frac{n\ F\ t_{DL}}{\mathrm{R\ T}\ \varepsilon_r\ \varepsilon_0}\ j_0\ C_{DL} \tag{5.3}$$

This equation predicts that a plot of inverse R_{CT} versus C_{DL} is linear with a slope proportional to the kinetic information j_0. While t_{DL} and ε_r are unknown a priori, it can be assumed that they are constant for similar samples.
In the following sections the hypothesis of linearity is checked and this method is used to compare the activity of samples PRIST, DEFUNC, NITRIC, NITSULF_3h and NITSULF_6h for the VO^{2+}/VO_2^{+} and Fe^{2+}/Fe^{3+} redox-reaction. It will also be discussed if the constants t_{DL} and ε_r can be determined to obtain numerical values for j_0 and k_0.

5.3 The VO^{2+}/VO_2^{+} reaction on functionalized multi-walled carbon nanotubes

The electrochemistry of the VO^{2+}/VO_2^{+} redox reaction has been discussed widely in the literature especially due to its importance as high potential half-cell in the All-Vanadium RFB [25,26,212–214]. According to Gattrell et al. the $V(IV)$ cation exists as the blue oxovanadium ion $[VO(H_2O)_5]^{2+}$ in non-complexing acid solutions [25]. The structure is that of a tetragonal bipyramid. The $V(V)$ cation exists as yellow dioxovanadium ion, *cis*-

$[VO_2(H_2O)4]^+$ in strong acids [25]. In Fig. 5.5 a photograph *of 50 mM* of vanadium species in *1 M* H_2SO_4 is shown. From left to right: V^{2+} (purple), V^{3+} (green), VO^{2+} (blue) and VO_2^+ (yellow).

***Figure 5.5** - Photograph of 0.1 M vanadium species in 1 M* H_2SO_4 *prepared for this study*. From left to right: V^{2+} (purple), V^{3+} (green), VO^{2+} (blue) and VO_2^+ (yellow).

5.3.1 Cyclic voltammetry

In Fig. 5.6 four CVs for each MWCNT sample recorded at a scan-rate of $20\ mV\ s^{-1}$ are shown. The CVs are characterized by the pronounced VO^{2+}/VO_2^+ redox reaction which takes place around $U_0 = 1.05$ *V vs. NHE*. For samples with a large mass of MWCNT on the electrode, and therefore a high porosity, the V^{2+}/V^{3+} redox reaction is observable as well ($U_0 = -0.38$ *V vs. NHE*). The latter reaction is masked by the onset of the hydrogen evolution reaction.

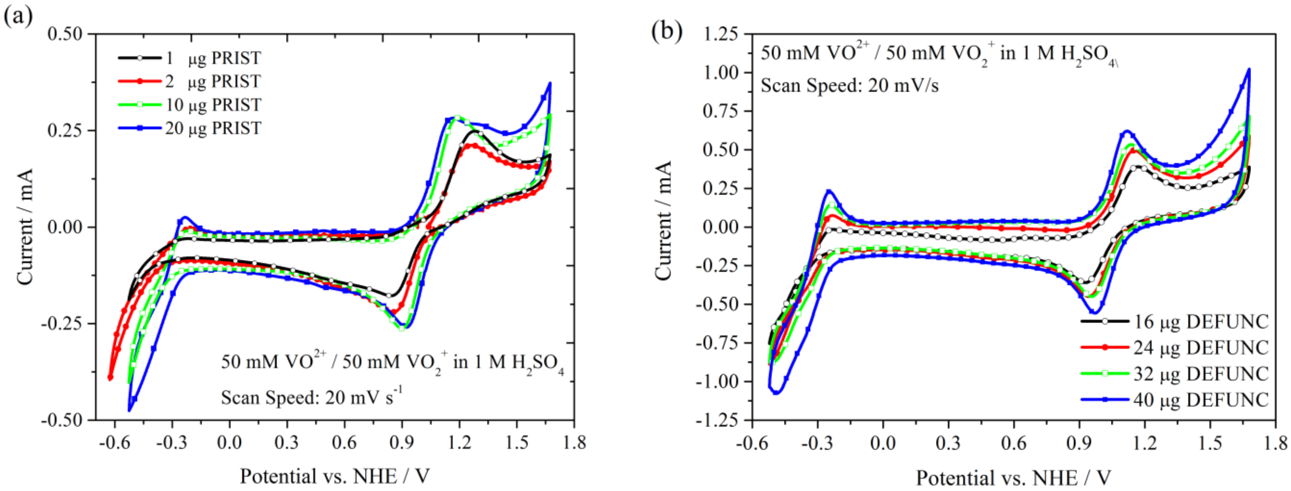

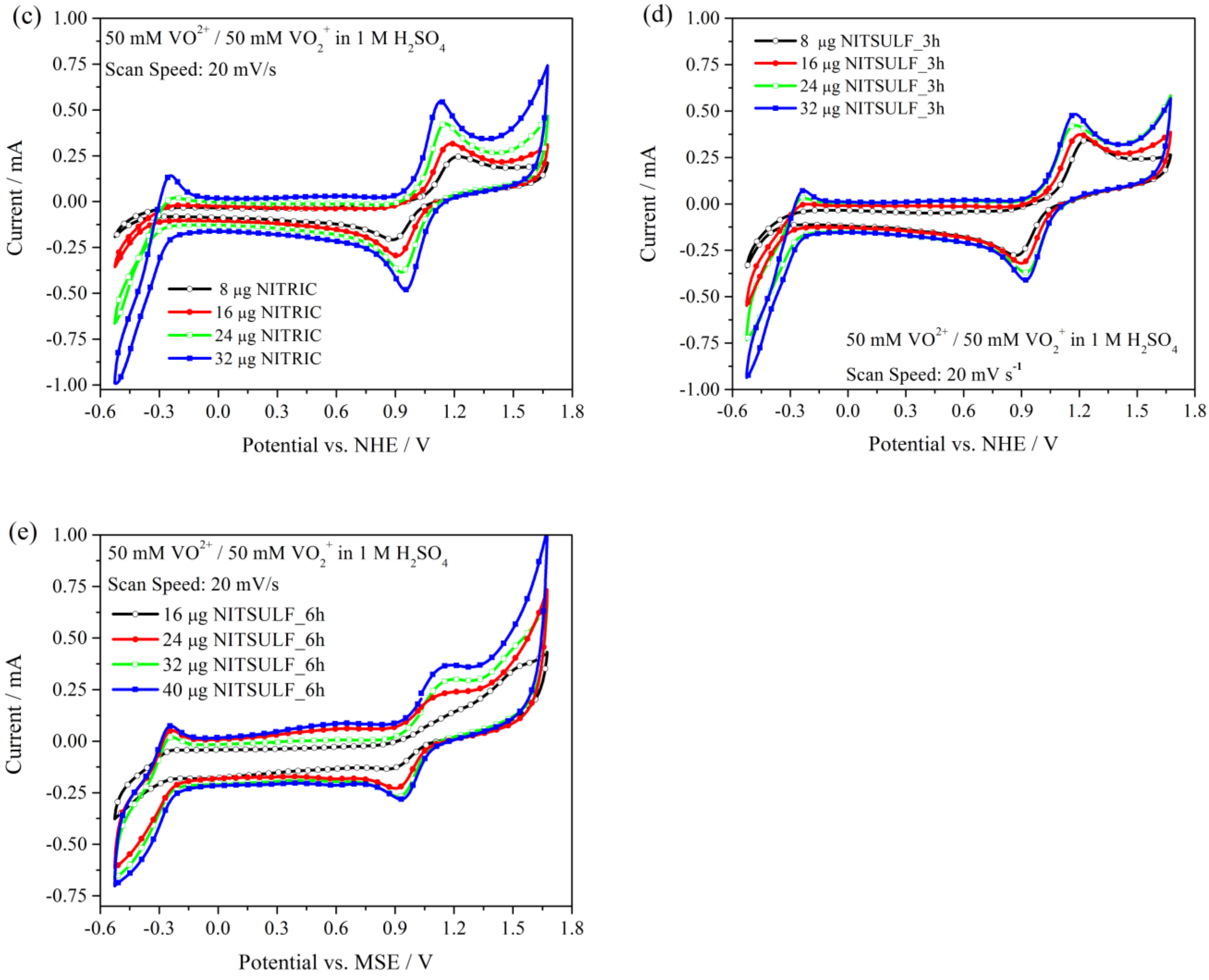

Figure 5.6 *- Cyclic voltammograms of the MWCNT samples in 50 mM* VO^{2+} *and 50 mM* VO_2^+ *in 1 M* H_2SO_4 *at a scan-rate of 20 mV* s^{-1}. ***(a)*** *PRIST,* ***(b)*** *DEFUNC,* ***(c)*** *NITRIC,* ***(d)*** *NITSULF_3h and* ***(e)*** *NITSULF_6h.*

The amount of MWCNTs on the sample has an influence on the shape of the CVs. With increasing coverage the peak separation for the VO^{2+}/VO_2^+ redox reaction decreases and the peak currents increase. The plotted CVs in Fig. 5.5 confirm what was shown in subsection 4.2, that this experimental method is not suitable to obtain information on the kinetics of a redox reaction on porous electrodes [14,24,202]. For the same system of redox couple and electrode material the apparent onsets of electron transfer and also the peak separation change with the amount of MWCNTs on the working electrode.

5.3.2 Electrochemical impedance spectroscopy

To utilize the relation given in eq. 5.3, four electrodes with variable mass of MWCNT were prepared per sample and measured in the vanadium-containing electrolyte. Also, one glassy carbon electrode without MWCNT coverage was measured as reference. This is necessary because the substrate constitutes an interface with the electrolyte in addition to the MWCNTs and therefore a double layer capacitance and also a faradaic current contribution are expected.

The Nyquist- and Bode representations are given in Fig. 5.7. The data was fitted to the Randles-circuit and the fits are also shown in the plots. For transparency, all the determined values for R_{CT} and C_{DL} are given in Table 5.2. In this list values for R_{Ohm} are omitted. It varied with electrode but was always smaller than $10\ \Omega$. The C_{DL} was calculated from CPE according to eq. 2.35. Values for the exponent σ are also omitted, it was around 0.9 for all the MWCNT – electrodes [14].

Porous structures, such as MWCNT modified GC electrodes investigated here, usually exhibit a pore size distribution which leads to a dispersed concentration of redox-active species [107]. This is often represented by an equivalent circuit with multiple serial and parallel impedances. In this case the simple Randles circuit was sufficient to fit the experimental data. This might be due to the fact that the VO^{2+}/VO_2^+ redox-reaction is considered very sluggish [25], which might slow down the concentration dispersion.

The value for the mass given throughout this section and also in Table 5.2 is prone to error, as for its calculation it was assumed that the MWCNT are evenly suspended in the organic solvent and that there is no spillage during the drop-casting process. However, this value should be regarded as a rough guideline for the fabrication process only, not as a numerically meaningful parameter. The normalization of R_{CT} is done via C_{DL} and not via the mass of MWCNT sample (see eq. 5.3).

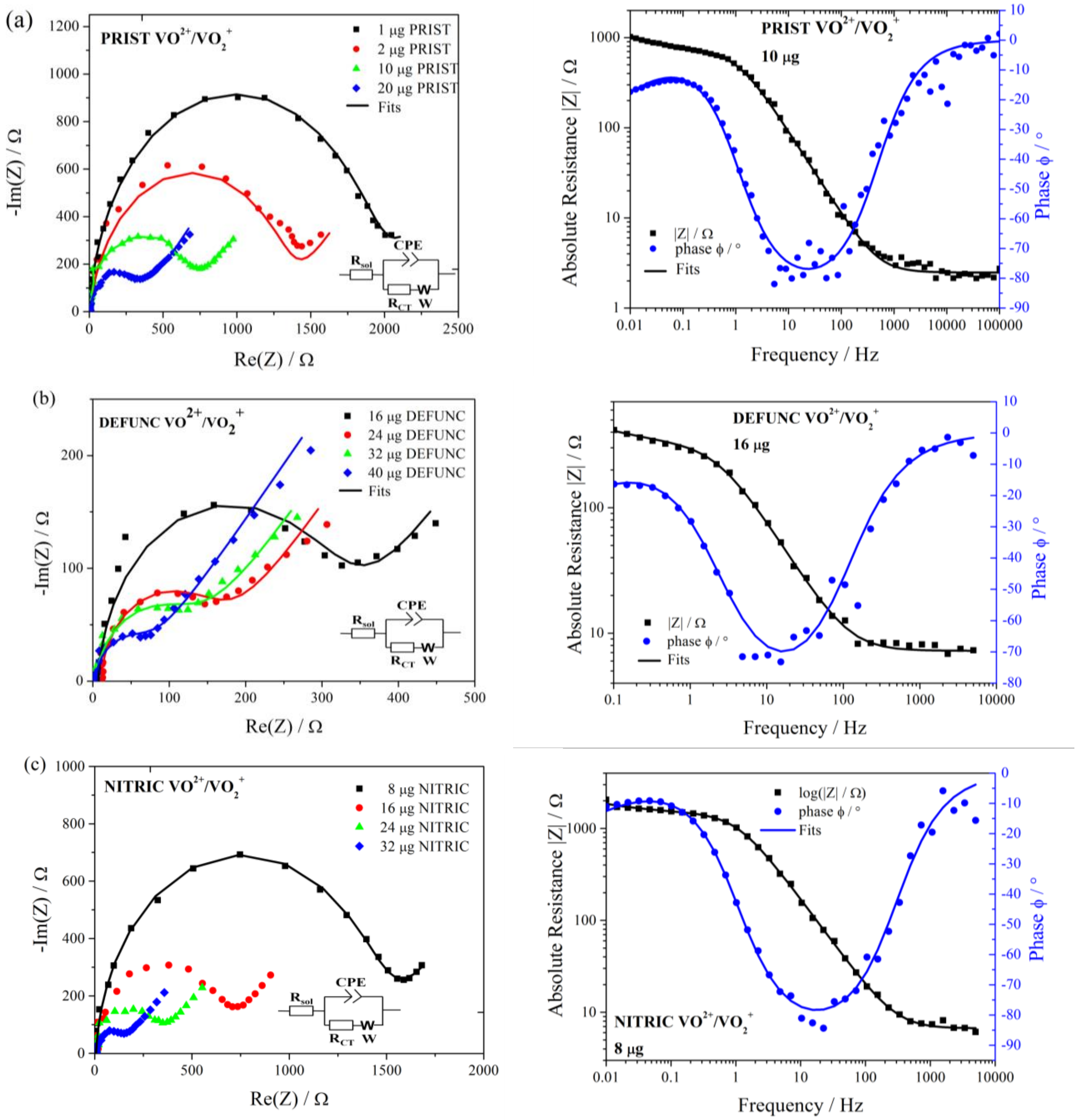
(a)
PRIST VO^{2+}/VO$_2^+$
1 µg PRIST
2 µg PRIST
10 µg PRIST
20 µg PRIST
Fits
R$_{sol}$
CPE
R$_{CT}$
W
-Im(Z) / Ω
Re(Z) / Ω
0
200
400
600
800
1000
1200
500
1000
1500
2000
2500
PRIST VO^{2+}/VO$_2^+$
10 µg
|Z| / Ω
phase ϕ / °
Fits
Absolute Resistance |Z| / Ω
Phase ϕ / °
Frequency / Hz
0.01
0.1
1
10
100
1000
10000
100000
(b)
DEFUNC VO^{2+}/VO$_2^+$
16 µg DEFUNC
24 µg DEFUNC
32 µg DEFUNC
40 µg DEFUNC
Fits
R$_{sol}$
CPE
R$_{CT}$
W
-Im(Z) / Ω
Re(Z) / Ω
0
100
200
300
400
500
DEFUNC VO^{2+}/VO$_2^+$
16 µg
|Z| / Ω
phase ϕ / °
Fits
Absolute Resistance |Z| / Ω
Phase ϕ / °
Frequency / Hz
(c)
NITRIC VO^{2+}/VO$_2^+$
8 µg NITRIC
16 µg NITRIC
24 µg NITRIC
32 µg NITRIC
R$_{sol}$
CPE
R$_{CT}$
W
-Im(Z) / Ω
Re(Z) / Ω
0
200
400
600
800
1000
500
1000
1500
2000
log(|Z| / Ω)
phase ϕ / °
Fits
NITRIC VO^{2+}/VO$_2^+$
8 µg
Absolute Resistance |Z| / Ω
Phase ϕ / °
Frequency / Hz

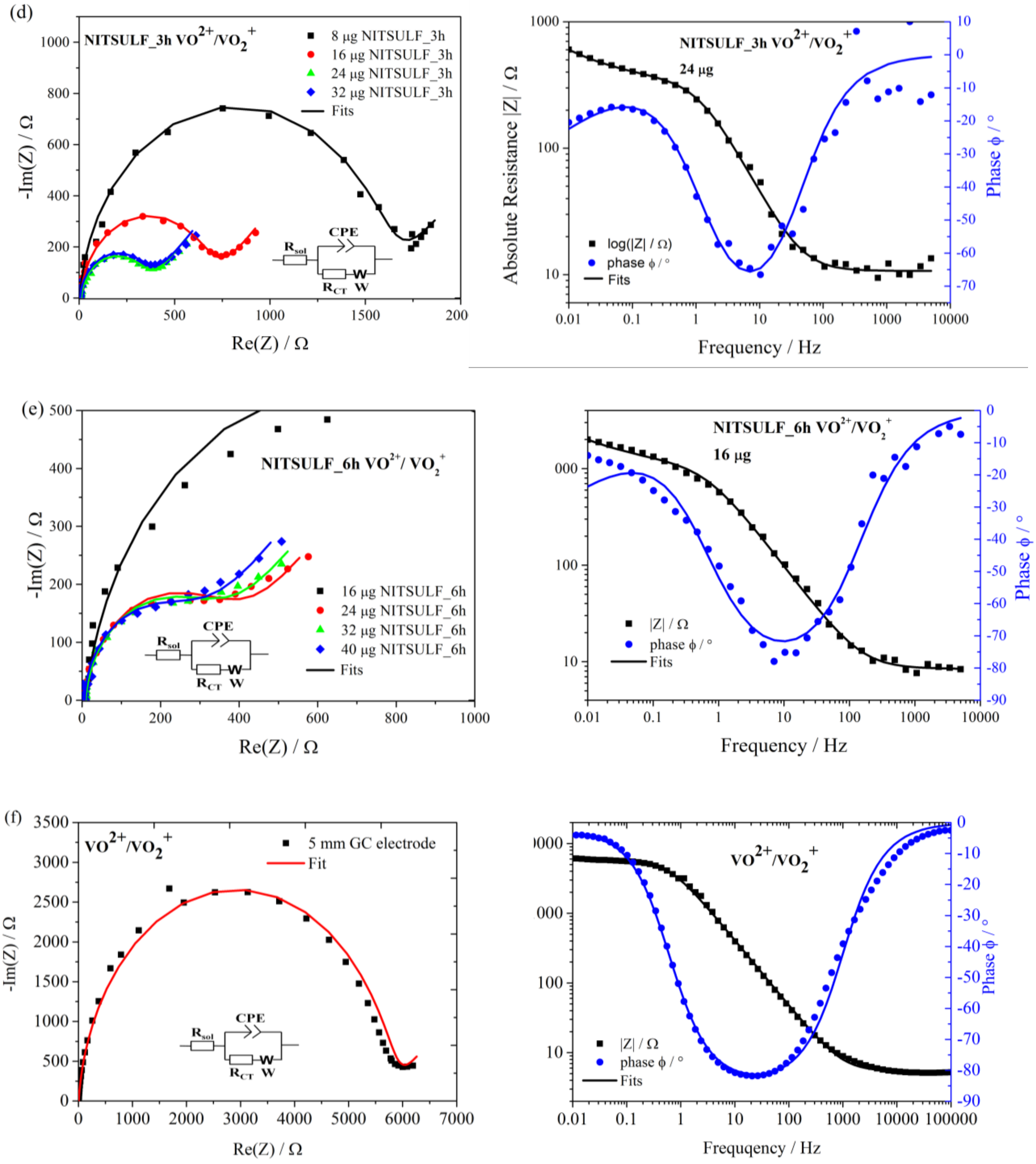

***Figure 5.7** - Electrochemical impedance spectroscopy studies of the carbon samples in 50 mM VO^{2+} and 50 mM VO$_2^+$ in 1 M H$_2$SO$_4$. Nyquist- and Bode-representation are given. **(a)** PRIST, **(b)** DEFUNC, **(c)** NITRIC, **(d)** NITSULF_3h, **(e)** NITSULF_6h and **(f)** polished glassy carbon electrode.*

Mass / μg	R_{CT} / Ω	C_{DL} / μF	Mass / μg	R_{CT} / Ω	C_{DL} / μF
	PRIST			**DEFUNC**	
1	1915	91	16	308	237
2	1330	119	24	144	467
10	692	230	32	120	674
20	319	387	40	63	935
	NITRIC			**NITSULF_3h**	
8	1424	109	8	1595	114
16	650	217	16	666	246
24	324	422	24	336	474
32	132	691	32	346	484
	NITSULF_6h			**Glassy Carbon**	
16	1134	264	n.a.	5471	37
24	364	559			
32	324	646			
40	267	987			

Table 5.2 *- Values for charge transfer resistance R_{CT} and double layer capacitance C_{DL} for the different MWCNT samples and the glassy carbon substrate in 50 mM VO^{2+} and 50 mM VO_2^+ in 1 M H_2SO_4.*

A glimpse at Table 5.2 indicates that R_{CT} decreases with increasing C_{DL}. A fact that corresponds to an increase in I_0 with increasing A. Errors were estimated to $\frac{\sigma C_{DL}}{C_{DL}} = \pm 0.2$ and $\frac{\sigma R_{CT}}{R_{CT}} = \pm 0.05$ [14]. The error in the capacitance is larger because for its determination three parameters have to be obtained from the fits (Q, σ, f_{max}), while R_{CT} is directly read out.

A plot of the inverse charge transfer resistance R_{CT}^{-1} vs. C_{DL} for the values listed in Table 5.2 is shown in Fig. 5.8. Several conclusions can be immediately drawn from the graph:

- With the exception of two data points (One for sample DEFUNC and one for sample NITRIC) the plot of R_{CT}^{-1} vs. C_{DL} exhibits linear behavior for the MWCNT samples. Eq. 5.3, normalization by C_{DL}, seems legitimate;
- The fitted lines are offset from the origin by the data point of the glassy carbon substrate (black empty marker). This is reasonable as the electrolyte penetrates the porous structure and there is contact with the polished GC substrate;
- The sequence of the determined slopes is DEFUNC > PRIST > NITRIC > NITSULF_3h > NITSULF_6h, numerical values are given in the graph and also in table 5.3. This is the reversed sequence of mass of surface functional groups on the sample, see table 5.1;
- As the slopes are proportional to j_0, the result indicates that the VO^{2+}/VO_2^+ reaction is fastest on the MWCNTs with the lowest amount of functional groups, DEFUNC. It also suggests that functional groups have a detrimental influence on the kinetics

of above redox reaction. This result is diametrical to previous studies that attested a catalytic effect to surface functional groups [19,20].

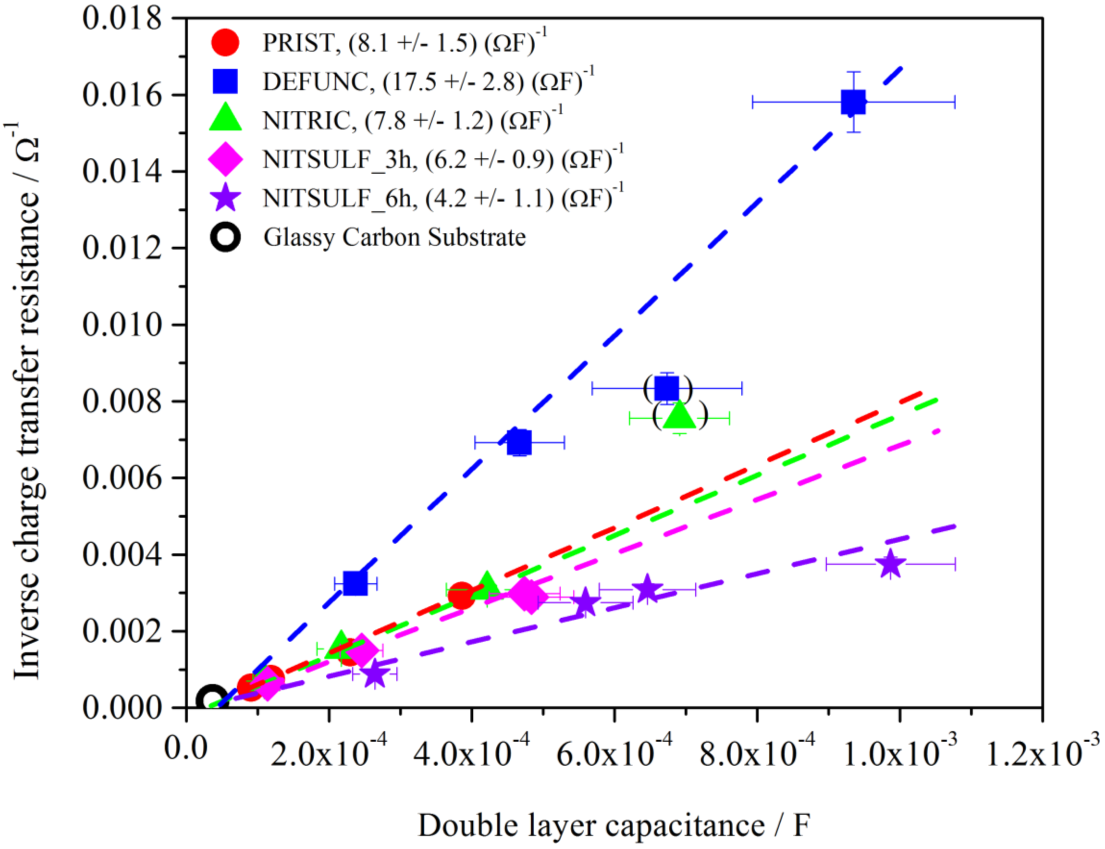

Figure 5.8 *- Data points obtained from Electrochemical impedance spectroscopy for the carbon samples in 50 mM VO^{2+} and 50 mM VO_2^+ in 1 M H_2SO_4. The slopes are proportional to j_0 and are given in the graph.*

	PRIST	**DEFUNC**	**NITRIC**	**NITSULF_3h**	**NITSULF_6h**
Slope / $(F\ \Omega)^{-1}$	8.1 ± 1.5	17.5 ± 2.8	7.8 ± 1.2	6.2 ± 1.2	4.2 ± 1.1
$k_0 \cdot 10^7$ / cm s^{-1}	17.6 ±3.3	38.0 ±6.1	17.0 ±2.6	13.6 ±2.0	9.1 ± 2.3

Table 5.3 *- Extracted slopes and calculated electron transfer rates for different MWCNT samples and the glassy carbon substrate in 50 mM VO^{2+} and 50 mM VO_2^+ in 1 M H_2SO_4.*

In order to convert the slopes from Fig. 5.8 into a physically meaningful parameter, the ratio of t_{DL}/ε_r from equ. 5.3 has to be estimated. This was done by plotting R_{CT}^{-1} vs. C_{DL} for two differently sized GC discs-electrodes in VO^{2+}/VO_2^+ and inserting the obtained slope of $1.4\ (\Omega F)^{-1}$ into eq. 5.3, assuming an electron transfer constant of $k_0^{GC} = 3\ 10^{-7}\ cm\ s^{-1}$ [14,25]. This calculation yields a value of t_{DL}/ε_r = 2.2 10^{-11} m. With this normalization via GC the electron transfer constants k_0 in Table 5.3 were calculated.

5.4 The Fe^{2+}/Fe^{3+} reaction on functionalized multi-walled carbon nanotubes

The intricacies of the Fe^{2+}/Fe^{3+} redox reaction were discussed in chapter 4. It was pointed out that the electron transfer is catalyzed in the presence of anions such as Cl^- and SO_4^{2-} [194]. Also, it was mentioned that the reaction is highly sensitive to the presence of surface oxides that facilitate the reaction [15].

Due to this property the Fe^{2+}/Fe^{3+} redox reaction was employed as a control to the VO^{2+}/VO_2^+ redox reaction. While the novel technique found impeded kinetics for functional groups for the latter redox-couple, it should be able to detect the opposite effect for the ferric/ferrous couple. These experiments are shown in this subsection. Only samples PRIST, DEFUNC and NITSULF_3h were tested, as this was deemed sufficient to establish the dependency on amount of functional groups.

5.4.1 Cyclic voltammetry

CVs of the Fe^{2+}/Fe^{3+} redox reaction are shown in Fig. 5.9. The investigated electrode materials were PRIST, DEFUNC and NITSULF_3h. With this selection one sample with heavy functionalization, one with intermediate functionalization and one that had almost no surface functional groups were investigated. The mass of sample on the glassy carbon was chosen to be smaller than for the VO^{2+}/VO_2^+ reaction. Reasoning was that the Fe^{2+}/Fe^{3+}reaction is expected to exhibit faster kinetics which could lead to a more severe concentration dispersion within extended porous networks.

The determined equilibrium potential was $U_{eq} = 0.679\ V\ vs. NHE$. Again, the mass of MWCNT sample on the electrode has an influence on the shape of the CVs. Qualitatively there is a bigger difference in the shapes of the CVs for Fe^{2+}/Fe^{3+} of the different electrode materials than it was observed for the VO^{2+}/VO_2^+.

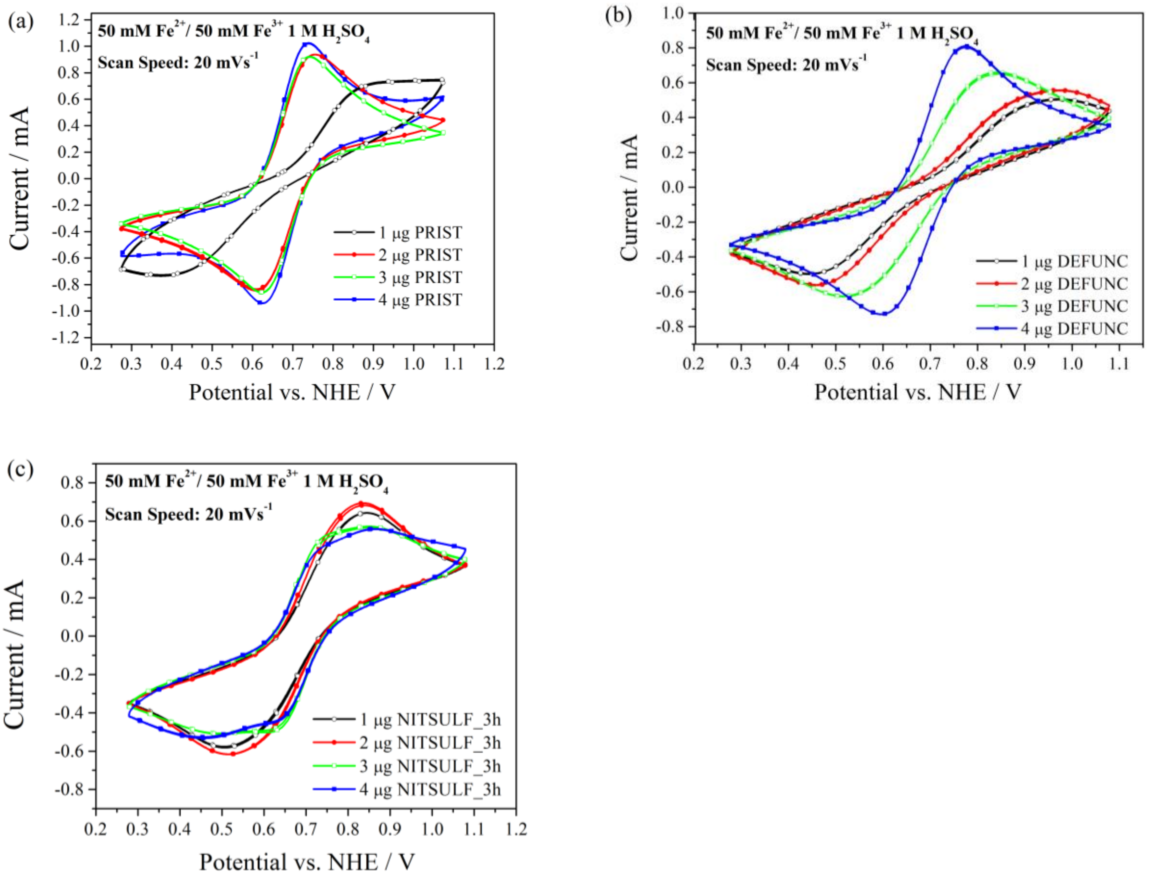

***Figure 5.9** - Cyclic voltammograms of the MWCNT samples in 50 mM Fe^{2+} and 50 mM Fe^{3+} in 1 M H_2SO_4 at a scan-rate of 20 mV s^{-1}. **(a)** PRIST, **(b)** DEFUNC and **(c)** NITSULF_3h.*

5.4.2 Electrochemical impedance spectroscopy

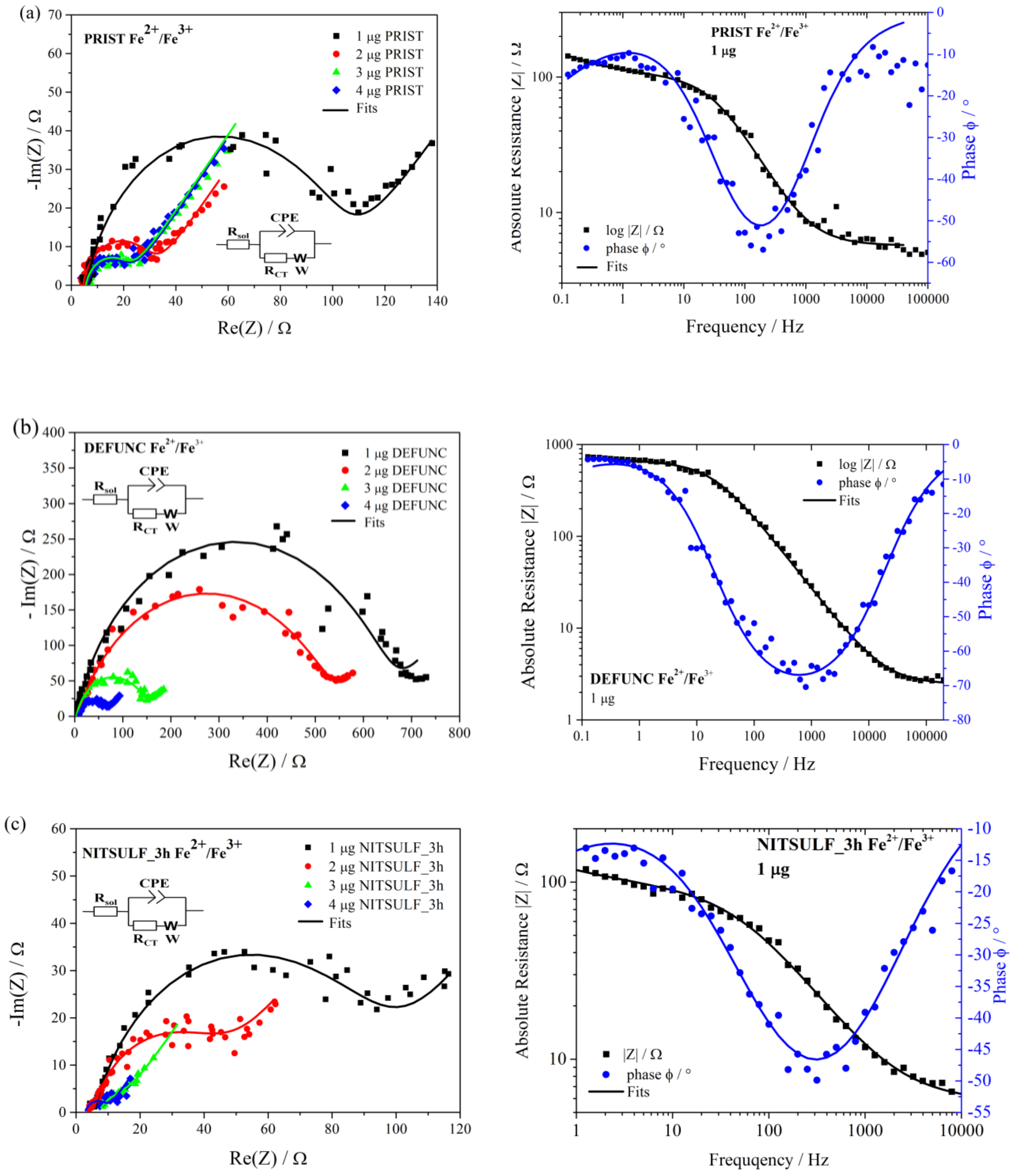

Figure 5.10 *- Electrochemical impedance spectroscopy studies of the carbon samples in 50 mM Fe^{2+} and 50 mM Fe^{3+} in 1 M H_2SO_4. Nyquist- and Bode-representation are given.* ***(a)*** *PRIST,* ***(b)*** *DEFUNC and* ***(c)*** *NITSULF_3h.*

EIS was performed with an amplitude of *10 mV* at $U_{eq} = 0.679\ V\ vs. NHE$. Fig. 5.10 shows Nyquist- and Bode-representations for the Fe^{2+}/Fe^{3+} redox reaction on samples PRIST (Fig. 5.10a), DEFUNC (Fig. 5.10b) and NITSULF_3h (Fig. 5.10c). As before, the data points were fitted to the Randles-circuit which is shown in the graphs. Comparison of the Bode-representations in Fig. 5.7 with the ones in Fig. 5.10 indicates that the former stems from redox-reactions that are slower than the latter, as the minimum in phase ϕ occurs at much higher frequencies for Fe^{2+}/Fe^{3+} than for VO^{2+}/VO_2^{+}.

The determined values for C_{DL} and R_{CT} are given in Table 5.4. Two of the values for electrodes prepared with sample DEFUNC exhibit a C_{DL} that is lower than that of the GC substrate. This can be explained by the hydrophobic character of those MWCNTs which reduces the effective surface area [14,116]. Immersion of the electrodes decorated with sample DEFUNC often led to a film of gas bubbles surrounding the electrode. This film had to be removed by directed purging with Argon gas.

Mass / μg	**R_{CT} / Ω**	**C_{DL} / μF**	**Mass / μg**	**R_{CT} / Ω**	**C_{DL} / μF**
	PRIST			**DEFUNC**	
1	95	50	1	652	9
2	25	90	2	532	23
3	16	108	3	61	112
4	17	133	4	146	49
	NITSULF_3h			**Glassy Carbon**	
1	90	34	n.a.	348	31
2	41	45			
3	8	101			
4	6	132			

Table 5.4 *- Values for charge transfer resistance* R_{CT} *and double layer capacitance* C_{DL} *for three MWCNT samples and the glassy carbon substrate in 50 mM* Fe^{2+} *and 50 mM* Fe^{3+} *in 1 M* H_2SO_4.

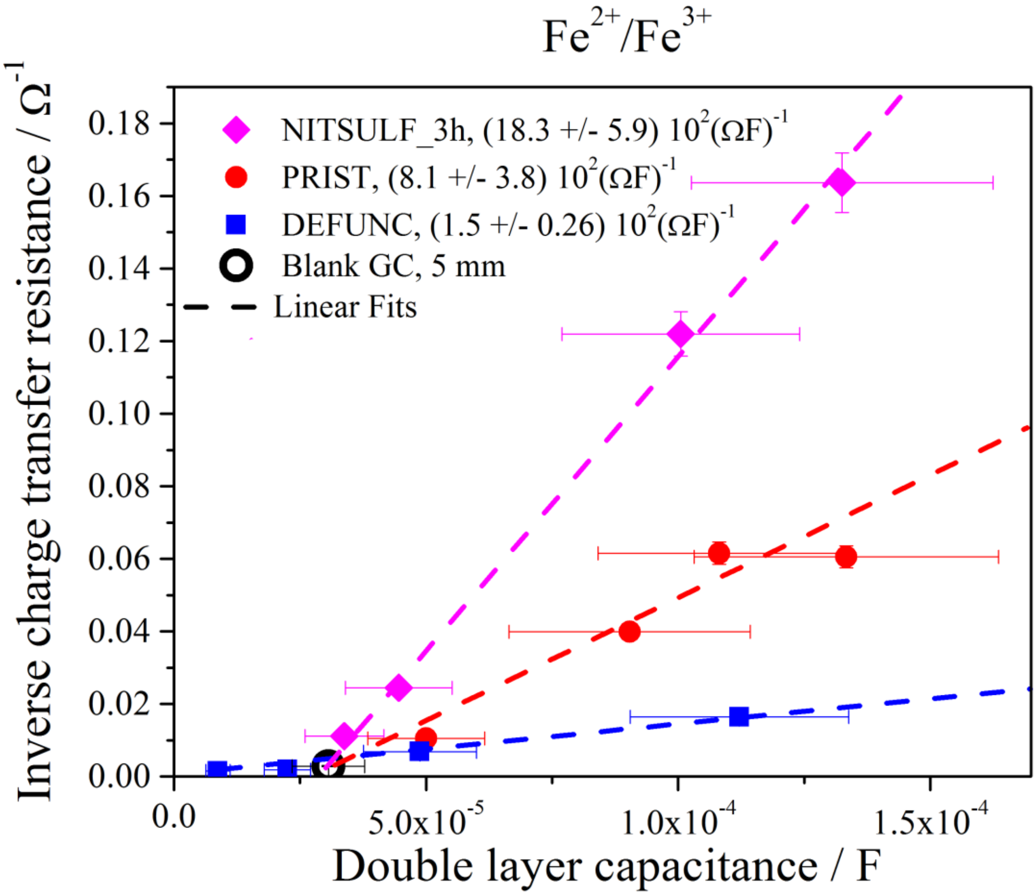

Figure 5.11 *- Data points obtained from Electrochemical impedance spectroscopy for the carbon samples in 50 mM* Fe^{2+} *and 50 mM* Fe^{3+} *in 1 M* H_2SO_4*. The slopes are proportional to* j_0 *and are given in the graph.*

A plot of the values R_{CT}^{-1} vs C_{DL} from Table 5.4 is shown in Fig. 5.11. From the graph and by comparison with the analogous plot for the VO^{2+}/VO_2+ redox reaction (Fig. 5.8) a number of conclusions can be drawn:

- The plot of R_{CT}^{-1} vs. C_{DL} exhibits linear behavior for the MWCNT samples. Eq. 5.3, normalization by C_{DL} seems legitimate;
- The fitted lines are offset from the origin by the data point of the glassy carbon substrate (black empty marker). Two data-points for sample DEFUNC exhibit a lower C_{DL} than the substrate due to the reduced wetting of the electrode because of the hydrophobicity of the sample;
- The sequence of the determined slopes is NITSULF_3h > PRIST > DEFUNC, numerical values are given in the graph and also in Table 5.5. This sequence is the reversed sequence determined for the VO^{2+}/VO_2^{+}-redox reaction. It follows the sequence of amount of functional groups as given in Table 5.1;

- As the slopes are proportional to j_0, the result indicates that the Fe^{2+}/Fe^{3+}-redox reaction is fastest on the MWCNTs with the highest amount of functional groups, NITSULF_3h. It also suggests that surface oxides catalyze the redox-reaction as predicted by the literature [15];
- The determined slopes are significantly larger than for the previously studied VO^{2+}/VO_2^+- redox reaction. This indicates faster kinetics for the Fe^{2+}/Fe^{3+}- redox reaction, which is also suggested by the literature [15,25,194].

	PRIST	**DEFUNC**	**NITSULF_3h**
Slope · 10^{-2} / $(F\ \Omega)^{-1}$	8.1 ± 3.8	1.50 ± 0.26	18.3 ± 5.9
k_0/ cm s^{-1}	$(17.8 \pm 8.4) \cdot 10^{-5}$	$(32.3 \pm 5.6) \cdot 10^{-6}$	$(4.0 \pm 1.3) \cdot 10^{-4}$

***Table 5.5** - Extracted slopes and calculated electron transfer rates for different MWCNT samples and the glassy carbon substrate in 50 mM Fe^{2+} and 50 mM Fe^{3+} in 1 M H_2SO_4.*

In above Table 5.5, the extracted slopes are listed and also the calculated values for the electron transfer constant k_0 are given. For the calculation of this parameter it was again assumed that $t_{DL}/\varepsilon_r = 2.2\ 10^{-11}\ m$.

5.5 Summary and conclusions

5.5.1. Kinetics and reaction mechanism

Looking at the VO^{2+}/VO_2^+-redox reaction and comparing the values for k_0 for the MWCNT samples with those for GC the highest increase of k_0^{DEFUNC} / k_0^{GC} = 12.7 is shown by sample DEFUNC, while the lowest increase is exhibited by NITSULF_6h, $k_0^{NITSULF\_6h}$ / k_0^{GC} = 3.0. It is interesting to note that for the slightly vague expression of a “Carbon” electrode a value of $k_0 = 1\text{-}3\ 10^{-6}\ cm\ s^{-1}$ was given which corresponds well with the values determined here [7,14].

Comparing the values for the Fe^{2+}/Fe^{3+}-redox reaction on the three MWCNTs samples with the values determined in the previous section reveals that sample NITSULF_3h yields an electron transfer constant that is very similar to the k_0 determined on platinum. On sample DEFUNC, however, the value for k_0 is very close to what was given for the non-catalyzing, chloride free electrolyte, k_0^{DEFUNC} / $k_0^{Pt,no\ Cl-}$ = 1.3 [14,194].

Fig. 5.12 clearly shows that diametrical effects are taking place for the two redox-reactions under investigation when the number of functional groups on MWCNTs is increased. While the electron transfer constant increases when the mass of functional groups is increased for Fe^{2+}/Fe^{3+}, the opposite is true for VO^{2+}/VO_2^+.

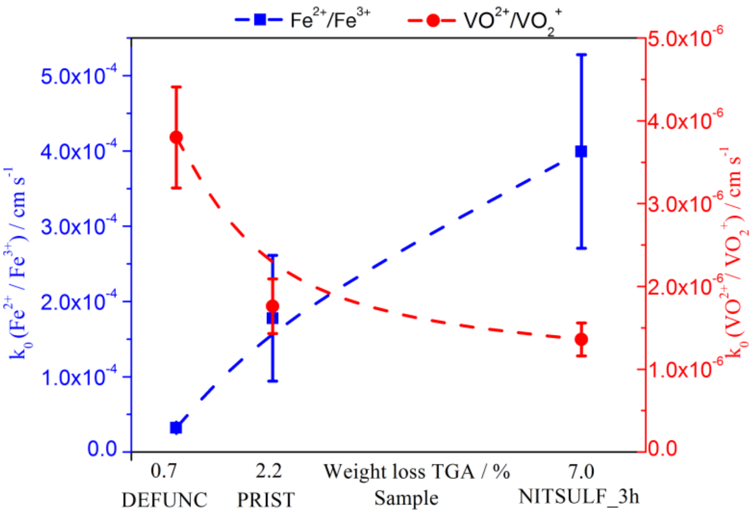

Figure 5.12 *- Electron transfer constants for the two redox systems under investigation versus the weight recorded for the three MWCNT samples DEFUNC, PRIST and NITSULF_3h. Dashed lines are a guide to the eye to demonstrate the principal dependence. The graph is taken from* [14].

The electrocatalysis of ferric/ferrous redox-couple by oxygen containing functional groups does not come as a surprise and can be explained by one of the two mechanisms discussed in chapter 4 for the interaction with anions such as Cl^- and SO_4^{2-}. Either an electrostatic effect or a bridge-activated charge transfer mechanism takes place [194].

The impediment of the redox kinetics for the VO^{2+}/VO_2^+-redox reaction by functional groups has not been discussed in the literature; in fact, a catalytic effect was assigned to functional groups earlier.

One reason why other studies concluded that electrocatalysis takes place is certainly the wetting behavior of the carbon samples. The heavily functionalized samples (NITSULF_3h and NITSULF_6h) feature a large amount of polar groups on their surface. These polar groups interact with the polar molecules of the electrolyte which results in a very hydrophilic sample. On the other hand, sample DEFUNC was almost devoid of polar surface groups and therefore the electrode was hydrophobic. As seen in Table 5.4, this resulted in a double layer capacitance sometimes even smaller than that of the GC substrate. The ECSA of hydrophilic carbon samples is larger than that of hydrophobic sample, as the electrolyte penetrates deeply into the porous structure in the former case. Therefore, higher exchange currents are expected for functionalized samples, as the wetting effect is larger than the difference in kinetics. In addition, the apparent catalytic effect of CVs added to the misinterpretation of the data. The merit of the proposed method is certainly that it normalizes the exchange current I_0 with the C_{DL}, a value that utilizes the same electrode/electrolyte interface area as R_{CT}. Therefore, it is suggested that the plethora of reports assigning catalytic effects to carbon nanomaterials, as given in the introduction , need to be revisited and the effects of electrode geometry and hydrophilicity have to be considered.

Two possible explanations can be given why surface functional groups impede electron transfer in the case of the VO^{2+}/VO_2^+ reaction:

- In the strong acid employed in this study the functional groups are certainly protonated, therefore positively charged. As both VO^{2+} and VO_2^+ are positively charged as well there might be electrostatic repulsion which hinders the approach of the cations to the carbon surface of the electrode. Unfortunately, the chemistry of vanadium-ions in solution is complex and other species than the dioxovanadium and the oxovanadium ion exist at other pH values [25]. In addition, V_2O_5 is only soluble in strong acids. Therefore, it was not possible to repeat the experiments in a neutral or less acidic electrolyte in which the surface functional groups are not protonated to test this hypothesis;
- Another plausible explanation can be derived from a recently published study by Melke et al. [27]. In this publication the sp^2 carbon content and amount and kind of surface functional groups was determined with Near Edge X-Ray Absorption Fine-Structure (NEXAFS). It was stated that the sp^2 carbon content determines the conductivity of the sample as electrons are transported along the delocalized π-orbitals. This suggests that the electron transfer does in fact not depend on the surface functional groups, but on the graphitic character of the samples. As the sequence of k_0 follows the trend in I_D/I_G ratio determined from RAMAN spectroscopy (see Fig. 5.3), this is plausible. This would indicate that the electron transfer is not limited by the redox reaction but by the solid state electron transfer. This hypothesis could be tested by investigating the interaction of a surface-insensitive redox-couple with facile electron transfer kinetics like $Ru(NH_3)_6^{2+}/Ru(NH_3)_6^{3+}$ with the MWCNTs [15]. If the solid-state electron transport is the limiting factor the observed trend should be the same as for VO^{2+}/VO_2^+. Most likely it would be even aggravated due to the higher exchange current.

5.5.2 Validity of method

The calculation of k_0 from the slope of R_{CT}^{-1} vs. C_{DL} was performed by determining the ratio of t_{DL}/ε_r for a known electron transfer constant. The so obtained ratio was $2.2\ 10^{-11}\ m$. This ratio is fairly large when assuming that t_{DL} is the size of the HP extending for some Angstroms and the relative permittivity being that of water $\varepsilon_r \approx 80$ [14]. However, Bockris et al. stated that the dielectric constant within the first water-layer is much smaller, approximately $\varepsilon_r^{HP} \approx 7$ [55]. This value was supported by other findings [62,63]. With this smaller value for ε_r the thickness of the innermost water layer is $t_{DL} \approx$ 2 Å, which seems to be a valid estimation for MWCNTs in $1\ M\ H_2SO_4$.

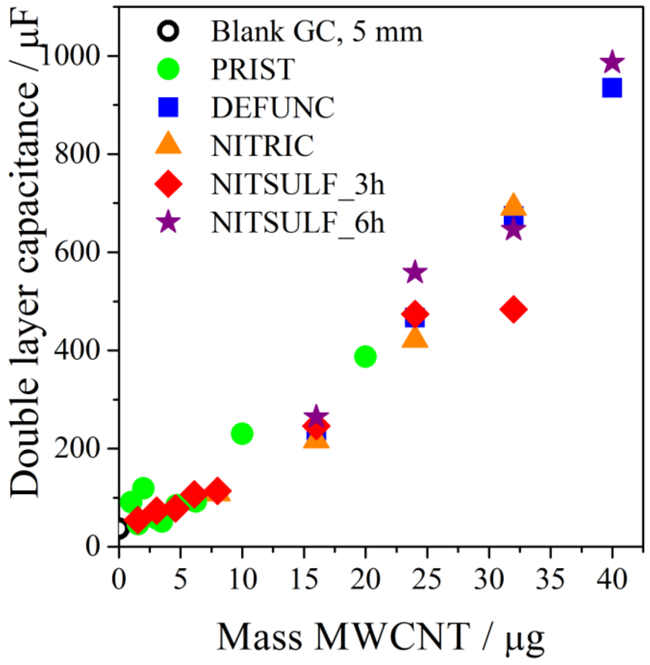

Figure 5.13 *- Double layer capacitance over mass of MWCNTs on the glassy carbon electrode for all samples in 50 mM* VO^{2+} and *50 mM* VO_2^+ in $1\ M\ H_2SO_4$*. The graph is adapted from* [14].

The method is based on the fact that the specific double layer capacitance for the different samples is similar. The general dependence of C_{DL} on mass of carbon nanotubes was discussed in Fig 5.4. The pseudo-capacitive contribution of carbonyl and carboxyl groups can be neglected, because their $U_{eq} \approx 0.24\ V$ vs. *NHE* and they therefore do not transfer electrons in the potential ranges where EIS took place [215].

Also, the increased wetting and therefore larger ECSA for functionalized samples does not refute the measurements because the additional area which contributes to the ECDL also participates in the redox reaction [14].

Figure 5.13 concludes above statements by showing the trend of C_{DL} over mass of MWCNTs for all measurements performed in *50 mM* VO^{2+} and *50 mM* VO_2^+ in $1\ M\ H_2SO_4$. While the values scatter, there is no sample-type that systematically exceeds the others in terms of gravimetric specific capacitance. The scattering is most likely due to the inaccurate determination of mass of MWCNTs, as discussed earlier.

Therefore, we conclude that the employed method is suitable to compare the kinetics of redox-reactions on porous, high surface area electrodes. This method has the distinct advantage that the typically inaccessible value for the ECSA does not have to be known.

Chapter 6
Electrochemical studies of tri-manganese substituted Keggin polyoxoanions

This chapter presents in-depth electrochemical investigations of two POMs, tri-manganese substituted Keggin-ions. It was investigated whether they can be employed as catholyte in a novel RFB.
The properties that were investigated due to their importance for that application were the number of transferred electrons per molecule, the potential at which these electron transfers take place, the kinetics of the reaction, the adsorption behavior of the POMs on carbon electrodes and the stability in all oxidation states.

While the concept of POMs for RFBs was presented by us first [35], the first paper on the topic was published by Pratt et al. [36]. This chapter is based on two recent publications [39,42].

6.1 Synthesis and characterization of the polyoxometalates

For this work a number of POMs were synthesized in the workgroup of Prof. Ulrich Kortz at the Jacobs University, Bremen, Germany. Hydrated potassium salts of the Keggin-type tungstosillicate $K_4[SiW_{12}O_{40}]\ 17\ H_2O$ (**K-SiW$_{12}$**) and its monolacunary derivative $K_8[SiW_{11}O_{39}]\ 13\ H_2O$ (**K-SiW$_{11}$**) were synthesized following published procedures [216]. The same is true for the mono-substituted manganese-containing Keggin-based salt $K_6[Mn^{II}(H_2O)SiW_{11}O_{39}]\ 21\ H_2O$ (**K-Mn^{II}SiW$_{11}$**) [217,218]. The trilacunary derivative was synthesized in alpha, $K_{10}[\alpha\text{-}SiW_9O_{34}]\ 14\ H_2O$ (**K-α-SiW$_9$**), and beta, $K_9[\beta\text{-}SiW_9O_{34}H]\ 23\ H_2O$ (**K-β-SiW$_9$**), configuration [216,219]. Beta designates a rotation of the lower triad of WO_6-units by 60° (for a representation see [39]).
The synthesis of the tri-manganese containing Keggin-based tungstosilicate salts $NaK_{4.5}H_{1.5}[Mn^{II}_3(OH)_3(H_2O)_3(A\text{-}\alpha\text{-}SiW_9O_{34})]\ 18\ H_2O$ (**K-Mn$^{II}_3$SiW$_9$**) and $K_4[Mn^{III}_3(OH)_3(H_2O)_3(A\text{-}\alpha\text{-}SiW_9O_{34})]\ 10\ H_2O$ (**K-Mn$^{III}_3$SiW$_9$**) was carried out according to procedures published by Al-Oweini et al. [39].

All identities were confirmed in the solid by infrared spectroscopy and TGA, and single-crystal X-ray diffraction for **K-Mn$^{II}_3$SiW$_9$** and **K-Mn$^{III}_3$SiW$_9$** [39]. Combined polyhedral/ball-and-stick representations of the anions $[Mn^{II}_3(OH)_3(H_2O)_3(A\text{-}\alpha\text{-}SiW_9O_{34})]^{7-}$ (**Mn$^{II}_3$SiW$_9$**) and $[Mn^{III}_3(OH)_3(H_2O)_3(A\text{-}\alpha\text{-}SiW_9O_{34})]^{4-}$ (**Mn$^{III}_3$SiW$_9$**) are shown in Fig. 6.1. For details on ion paring of the Keggin-type POMs with cations of the supporting electrolyte please see references [220,221].

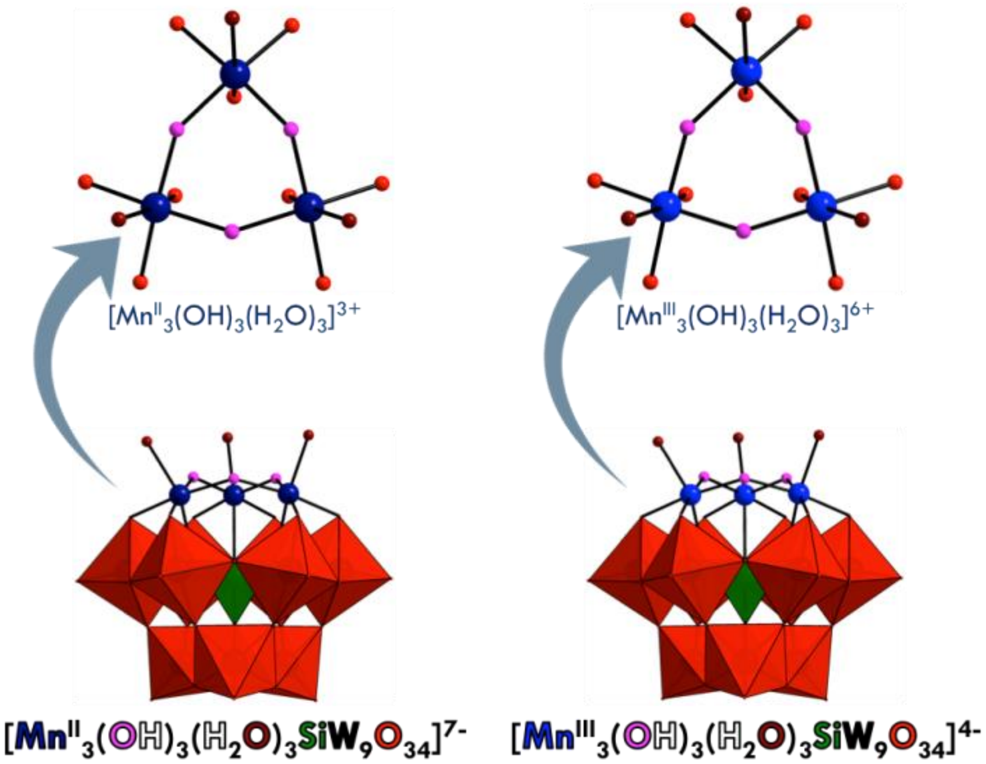

Figure 6.1 – *Combined polyhedral/ball-and-stick representations of* $\mathbf{Mn^{II}_3SiW_9}$ *(left) and* $\mathbf{Mn^{III}_3SiW_9}$ *(right). Color code: Balls:* Mn^{II} *dark-blue,* Mn^{III} *blue,* OH^- *pink, terminal* H_2O *dark-red. Polyhedra:* SiO_4 *green,* WO_6 *red. The graph is adapted from* [39].

6.2 Evolution of cyclic voltammograms of lacunary Keggin polyoxoanions

In Fig. 6.1 it is indicated that the polyoxoanions $\mathbf{Mn^{II}_3SiW_9}$ and $\mathbf{Mn^{III}_3SiW_9}$ can be seen as a combination of the three lacunary polyoxoanion $[\alpha\text{-}SiW_9O_{34}]^{10-}$ ($\boldsymbol{\alpha}$-$\mathbf{SiW_9}$) with an active group, namely $[Mn^{II}_3(OH)_3(H_2O)_3]^{3+}$ or $[Mn^{III}_3(OH)_3(H_2O)_3]^{6+}$. While there is increased interest in the electrochemistry of active site, the tungsten-ions of the lacunary polyanion are also electrochemically active. To identify their contribution to the electron transfers of $\mathbf{Mn^{II}_3SiW_9}$ and $\mathbf{Mn^{III}_3SiW_9}$ the evolution of CVs with successive removal of WO_6 will be monitored, starting from $[SiW_{12}O_{40}]^{4-}$ ($\mathbf{SiW_{12}}$) via $[SiW_{11}O_{39}]^{8-}$ ($\mathbf{SiW_{11}}$) to $\boldsymbol{\alpha}$-$\mathbf{SiW_9}$**.** The CVs were recorded in a *20 mM* sodium-acetate buffer ($NaCH_3COO^-/CH_3COOH$, NaAC) with addition of *0.5 M* Li_2SO_4 at *pH 5.4*. That particular pH was chosen because both $\mathbf{Mn^{II}_3SiW_9}$ and $\mathbf{Mn^{III}_3SiW_9}$ are stable at that value [42] and a previous study on $[Mn^{II}(H_2O)SiW_{11}O_{39}]^{6-}$ ($\mathbf{Mn^{II}SiW_{11}}$) was performed at the same value which allows for simple comparison [222]. Li_2SO_4 was added as supporting electrolyte to enhance the conductivity of the electrolyte.

The alpha rotational isomer of the Keggin-type tungstosilicate **SiW$_{12}$** is among the most studied polyanions in the POM literature [148,223–226]. The **SiW$_{12}$** polyanion possesses a T$_d$ point-group symmetry and contains twelve equivalent W^{VI}-ions, so-called addenda atoms, at external or peripheral positions [227,228]. The Keggin-structure **SiW$_{12}$** was referred to as an electron reservoir and it easily accepts electrons by *W*-ion reduction [228,229]. This manifests itself in the curves shown in Fig. 6.2. The orange curve gives the experimental data for *1 mM* **SiW$_{12}$** and the thick blue curve represents the same curve with the signal of the supporting electrolyte subtracted. Multiple one- or two electron redox waves can be seen, they are discussed extensively in the literature. From ^{17}O and ^{183}W NMR spectra is it known that any electrons added beyond two are fully delocalized and generate ring currents [148]. Therefore, there are only modest changes in electronic and molecular structure of the **SiW$_{12}$** and the reductions are fully reversible.

The large reduction wave that can be seen at $U = -0.86$ *V vs. NHE* is only seen for **SiW$_{12}$** and not for the blank electrolyte. This fact, as well as CVs with a lower vertex potential, indicate that this current does not stem from a HER but from an irreversible decomposition of the molecule.

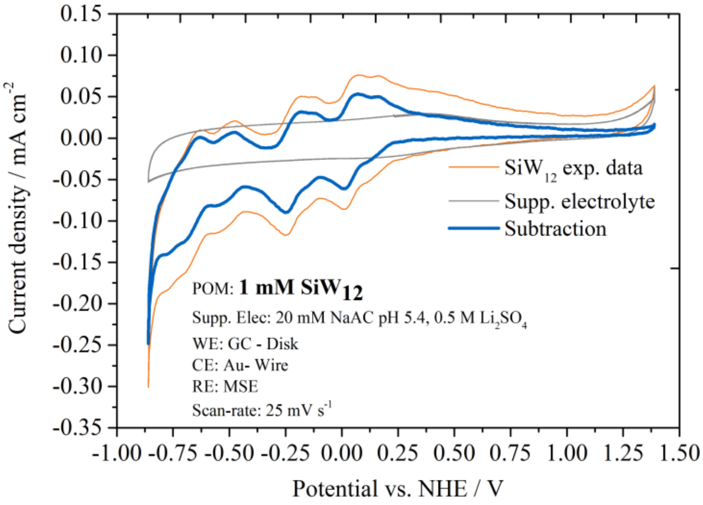

Figure 6.2 – *Cyclic voltammograms for 1 mM* **SiW$_{12}$** *and blank supporting electrolyte in 20 mM NaAC buffer at pH 5.4. The scan-rate is 25 mV* s^{-1}**.**

The mono-lacunary **SiW$_{11}$**, that is generated by the formal removal of one $[W^{VI}O]^{4+}$ from the **SiW$_{12}$** precursor, has a high charge of negative *8* [230]. The redox-processes in aqueous media are described as being coupled to acid-base chemistry which indicates that electron transfer is accompanied by proton transfer [218,231]. Guo et al. verified with acetonitrile as electrolyte that in fact all redox reactions for **SiW$_{11}$** are proton coupled electron transfers (PCETs) [230]. Typically in acidic aqueous solutions ($pH \leq 4.6$), two two-electron processes are given for the reduction and successive oxidation of the W-ions [230].

However, with increasing pH value these two waves become more distorted. This can also be seen in Fig. 6.3a that was recorded at *pH 5.4*.

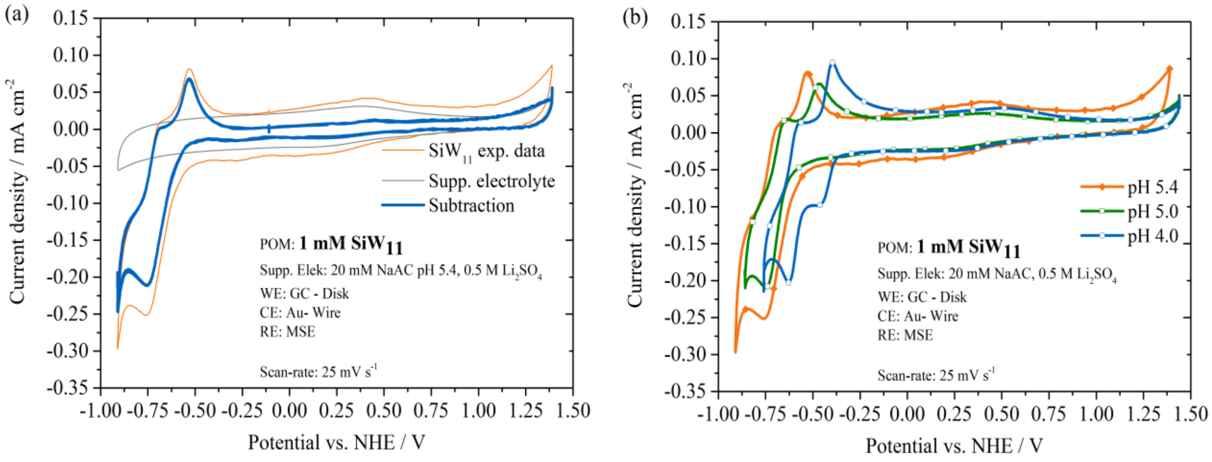

Figure 6.3 – (a) *Cyclic voltammograms for 1 mM* **SiW_{11}** *and blank supporting electrolyte in 20 mM NaAC buffer at pH 5.4. The scan-rate is 25 mV s^{-1}*. **(b)** *Cyclic voltammograms of 1 mM* **SiW_{11}** *at three different pH values.*

As before, the contribution of the blank supporting electrolyte was subtracted. The evolution of the redox reaction with decreasing pH is shown in Fig. 6.3b. Only for the CV taken in pH 4.0 there are two clearly observable two-electron oxidation and reduction waves. For lower proton concentrations the first reduction takes place at a more negative potential. This can be rationalized because protons are required for the PCET mechanism, according to:

$$[W^{VI}]^{6+} + H^{+} + e^{-} \rightleftharpoons [HW^{V}]^{6+} \tag{6.1}$$

The difference between Fig. 6.3a and Fig. 6.2 is striking. Due to the loss in symmetry the W-ions accept electrons at much more negative potentials for **SiW_{11}** than they do for **SiW_{12}**.

The two molecules **α-SiW_9** and **β-SiW_9** contain only nine W-ions. As a consequence their electron transfer properties are further reduced compared to **SiW_{11}** and **SiW_{12}**. The alpha configuration exhibits a two-electron reduction peaking at *U = - 0.72 V vs. NHE* and a slightly split re-oxidation centered around *U = - 0.50 V vs. NHE*. The beta configuration does not show a reversible redox behavior, the reduction wave and successive oxidation at *U = -0.43 V vs. NHE* resembles the irreversible decomposition observed for **SiW_{12}** for low potentials.

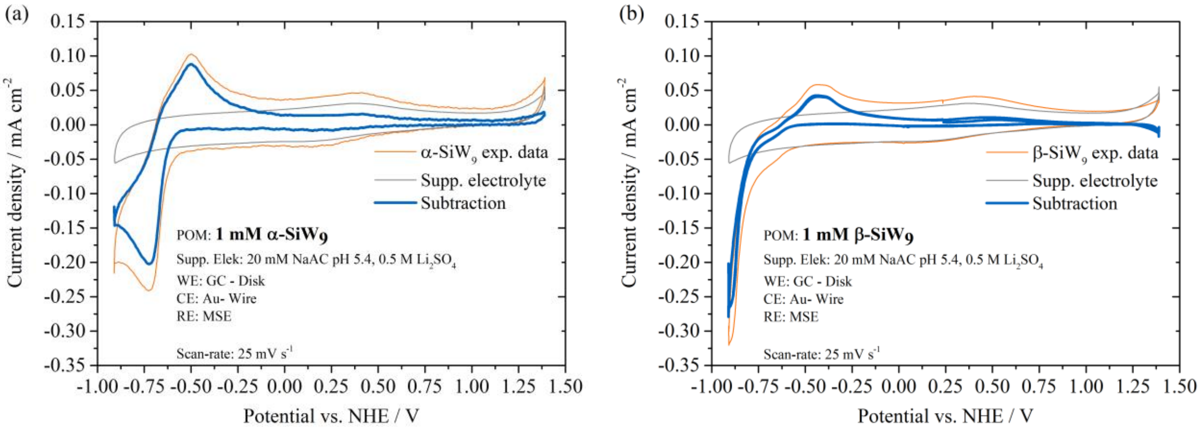

Figure 6.4 – *Cyclic voltammograms for 1 mM* ***(a)*** **α-SiW$_9$** *and* ***(b)*** **β-SiW$_9$** *and blank supporting electrolyte in 20 mM NaAC buffer at pH 5.4. The scan-rate is 25 mV s^{-1}*.

The CVs in Fig. 6.2 to 6.4 exemplify that the electrochemical behavior of the tungstosilicates investigated here changes with step-wise removal of tungsten ions. While the **SiW$_{12}$** anion shows a fairly rich redox-behavior, **SiW$_{11}$** and **α-SiW$_9$** exhibit two-two electron or one two-electron transfer respectively. The molecule with the rotated WO_6 triad, **β-SiW$_9$**, did not show any reversible redox-reaction at all.

6.3 Redox properties of the mono-Mn substituted Keggin ion Mn^{II}SiW$_{11}$

The mono-manganese substituted alpha-Keggin polyoxoanion **Mn^{II}SiW$_{11}$** was intensively investigated by Sadakane et al. [183,222]. Therefore, this section will treat in detail only the new findings on the redox properties of this anion. Figure 6.5 shows a CV of *0.5 mM* **Mn^{II}SiW$_{11}$** in a *20 mM* NaAC buffer at *pH 6*. Comparison with the CVs of **SiW$_{11}$** (Fig. 6.3) and the publications by Sadakane et al. [183,222] makes identification of the observed redox-reactions possible.

Starting from low potentials, the first peaks, after the one corresponding to water reduction, are the waves associated with *W*-ion reduction and re-oxidation, they are marked with **W^{V}/W^{VI}**. The shape is very similar to the signal of the *W*-ions of **SiW$_{11}$** at high pH. At higher potentials, the inserted *Mn*-ion has its electron transfers. At U_0 = *0.713 V vs. NHE* the Mn^{II}/Mn^{III} redox-reaction takes place. According to the literature the equation reads [183]:

$$C_6[Mn^{II}SiW_{11}O_{39}(H_2O)]^{6-} \rightleftharpoons C_5[Mn^{III}SiW_{11}O_{39}(H_2O)]^{5-} + e^- + C^+ \qquad (6.2)$$

As the nature of the counter-ion, whether it's Li^+ or K^+ is unknown, it was designated C^+.

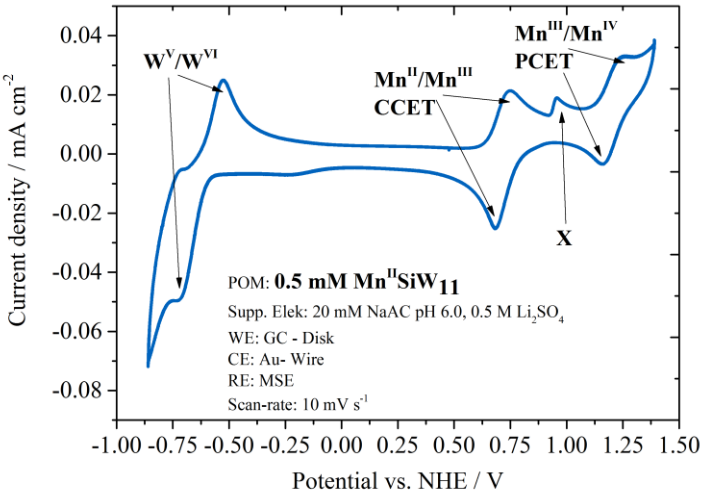

Figure 6.5 – *Cyclic voltammograms for 0.5 mM* **Mn^{II}SiW$_{11}$** *20 mM NaAC buffer at pH 6.0. The scan-rate is 10 mV s^{-1}*. *The redox transitions are marked. The oxidation wave designated with X is previously unrecorded in the literature.*

Since the redox-waves have no equivalent in CVs of **SiW$_{11}$**, it is very plausible that the current stems from the *Mn*-ion. It was shown, that the redox-reaction is indeed a CCET by varying the concentration of the cations in the supporting electrolyte [220,222]. Also, the U_0 of this reaction is independent of the pH, as can be seen in Fig. 6.6a. A ligand exchange of the aquo ligand in acetate or phosphate containing electrolytes was reported [183]. It takes place when the Mn-ion is in oxidation state Mn^{II}. Therefore, in the acetic acid buffer that was employed, above CCET reads:

$$\begin{gathered} C_6[Mn^{II}SiW_{11}O_{39}(CH_3COOH)]^{6-} \rightleftharpoons \\ C_5[Mn^{III}SiW_{11}O_{39}(CH_3COOH)]^{5-} + e^- + C^+ \end{gathered} \tag{6.3}$$

At *0.95 V vs. NHE* an oxidation wave was observed which is marked with X. This peak has not been reported before. Its shape resembles the oxidation of adsorbed species. The hypothesis, that the peak X stems from adsorbed species was tested by increasing the scan-speed, as can be seen in Fig. 6.6b. According to the Randles-Sevcik equation, the current in a CV increases with the square-root of the scan-rate [67]. To eliminate this effect the currents in Fig. 6.6b were normalized with their respective scan-rate. A higher scan-rate leads to disappearance of the formerly unidentified peak X. For $\nu \geq 50\ mV\ s^{-1}$ it is almost not visible anymore. A reasonable explanation is that $[Mn^{III}SiW_{11}O_{39}(CH_3COOH)]^{5-}$ slowly adsorbs on the surface of the glassy carbon working electrode. Increased scan-rates result in a shorter time between oxidation of **Mn^{II}SiW$_{11}$** to the formal charge of negative five and the potential at which the adsorbed species $[Mn^{III}SiW_{11}O_{39}(CH_3COOH)]^{5-}_{ads}$ can be oxidized which means that less of the molecule will have adsorbed. A similar behavior was described by Keita et al. for the oxidation of $[(Mn^{III}(H_2O)_3(SbW_9O_{33})_2]^{9-}$[184]. In their study the CV showed characteristics of adsorbed species for scan-rates smaller than 20 mV s^{-1}. However, they did not observe a splitting of the peak into one adsorption and one diffusion part, as we did.

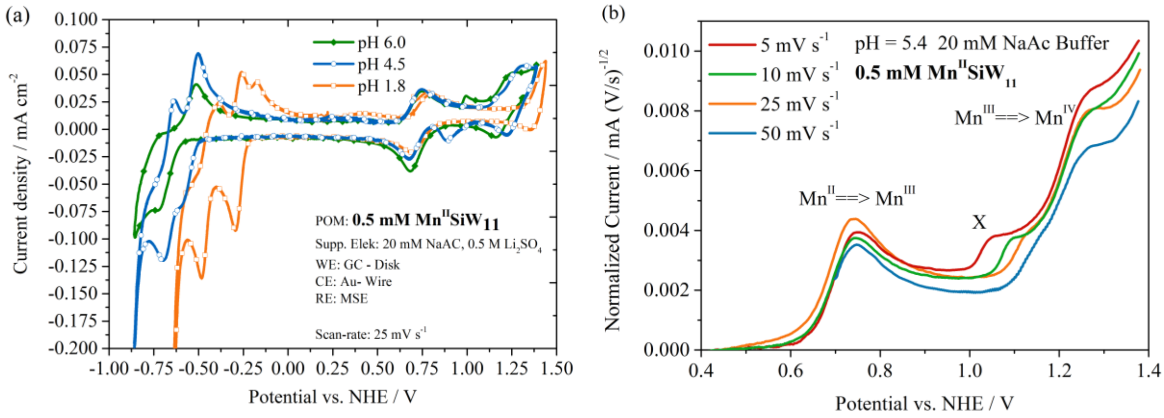

Figure 6.6 – (a) *Cyclic voltammograms for 0.5 mM* $\mathbf{Mn^{II}SiW_{11}}$ *in 20 mM NaAC at different pH values at a scan-rate of 25 mV* s^{-1}. **(b)** *Partial CV for the oxidation of 0.5 mM* $\mathbf{Mn^{II}SiW_{11}}$ *at different scan-rates. The current is normalized to eliminate the effect of a faster change in concentration of redox-species for higher scan-rates.*

The pair of peaks at $U_0 = 1.21\ V\ vs.\ NHE$ in Fig. 6.5 is the Mn^{III}/Mn^{IV} redox reaction. Its dependence on the proton concentration can clearly be observed in Fig. 6.6a. Analyzing four equilibrium potentials from *pH 1.8* to *pH 6.0*, the obtained shift in U_0 is $-0.047\ V\ pH^{-1}$ [42]. This is lower than the value determined by Sadakane and Steckhan for the same reaction, $-\ 0.057\ V\ pH^{-1}$ [183]. The theoretically expected shift for a one-electron-one proton PCET is $-\ 0.059\ V\ pH^{-1}$ [232]. The reaction that takes place is [183]:

$$C_5[Mn^{III}SiW_{11}O_{39}(CH_3COOH)]^{5-} \rightleftharpoons \\ C_5[Mn^{IV}SiW_{11}O_{39}(CH_3COO)]^{5-} + e^- + H^+ \tag{6.4}$$

As the oxidation (reduction) is accompanied by a proton release (uptake) by the incorporated acetic acid group, the charge of the polyanion does not change. The produced polyanion $[Mn^{IV}SiW_{11}O_{39}(CH_3COO)]^{5-}$ was investigated with UV-Vis by Sadakane and Steckhan and they showed that the complex is able to oxidize alcohols [232]. Notably, a reduction peak X* can be observed in Fig 6.6a that could correspond to the oxidation peak X. Also this reduction wave was not reported before.

With the reaction-mechanism established, the question remains why the peak X and its possible reduction wave X*, both are highlighted in Fig. 6.7, were not described previously? When investigating $\mathbf{Mn^{II}SiW_{11}}$ Sadakane and Steckhan chose a supporting electrolyte that consisted of $0.5\ M\ KH_2PO_4$ and stated that results with "…other anions of the supporting electrolyte like perchlorate and acetate." were similar [232]. Also, the proton concentration was in a comparable range with measurements performed from *pH 4.2* to *6.0*. Therefore, the concentration of the supporting electrolyte was increased from *0.02 M* to *1.0 M* NaAC to investigate the influence of this parameter. As can be seen in Fig. 6.7 the concentration of the buffer has an effect. While the reduction wave at low potentials (~ *-0.25 V vs. NHE*) for the blue curve stems from residual oxygen in the electrolyte, the other significant difference between the curves is the absence of peaks X and X* in *1.0 M* NaAc-Buffer [42]. This indicates that a larger amount of ions in the supporting electrolyte enhances the solubility of **$Mn^{II}SiW_9$** in higher oxidation states. According to the Born solvation model, the solvation free energy is proportional to q^2/a with the total charge of the anion q and the radius of the molecule a [233]. As GC is hydrophobic, a decrease in q^2/a will increase the interaction between the molecule and the electrode [234]. Therefore, as the charge of the anion is reduced from 6- to 5-, according to eq. 6.3, adsorption on GC is more likely than before.

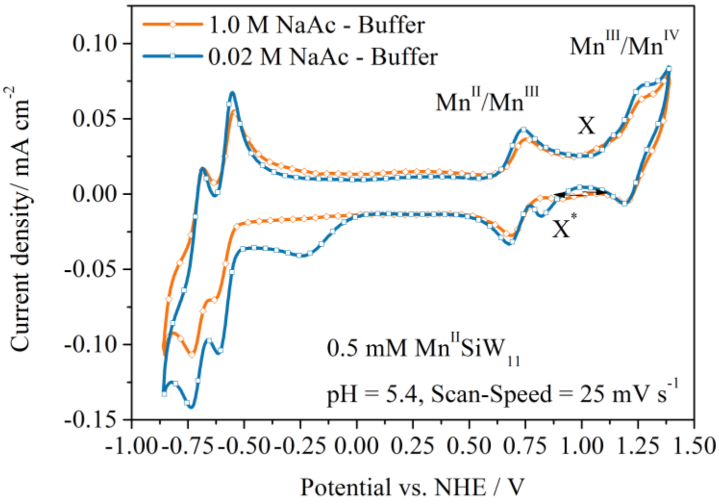

Figure 6.7 – (a) *Cyclic voltammogram for 0.5 mM* **$Mn^{II}SiW_{11}$** *in 20 mM and 1.0 M NaAc at pH 5.4 at a scan-rate of 25 mV s^{-1}. The peaks marked with X and X* are more prominent for the lower concentration.*

6.4 Redox properties of the tri-Mn substituted Keggin ion $Mn^{II}_3SiW_9$ and $Mn^{III}_3SiW_9$

Analogous to **$Mn^{II}SiW_{11}$,** the two Keggin polyoxoanions **$Mn^{II}_3SiW_9$** and **$Mn^{III}_3SiW_9$** were investigated. The results were published in two papers [39,42]. The special merit of the studies was that for the first time the influence of the initial oxidation state on the redox reactions of two isostructural POMs was elucidated.

6.4.1 Proposed reaction mechanism for $\mathbf{Mn^{II}{}_3SiW_9}$ and $\mathbf{Mn^{III}{}_3SiW_9}$

The CVs of both polyoxoanions are shown in Fig. 6.8. The redox-signal can be interpreted as a combination of the electron transfer of $\boldsymbol{\alpha}$**-SiW₉** and the electrochemical properties of the included $[Mn^{II}{}_3(OH)_3(H_2O)_3]^{3+}$ (for $\mathbf{Mn^{II}{}_3SiW_9}$) or $[Mn^{III}{}_3(OH)_3(H_2O)_3]^{6+}$ (for $\mathbf{Mn^{III}{}_3SiW_9}$) active site. Both molecules exhibit a reduction and re-oxidation of W^{VI} ions at a very similar U_0. It is slightly lower than that of $\boldsymbol{\alpha}$**-SiW₉**. The potentials are given in Table 6.1. The potential positions of the *W*-ion reaction is dependent on the concentration of protons. For $\mathbf{Mn^{III}{}_3SiW_9}$ a shift of $-0.127\ V\ pH^{-1}$ was determined when six data points from $pH = 6.0$ to $pH = 4.0$ were measured. This shift is close to the theoretical $-0.118\ V\ pH^{-1}$ expected for a $1e^-/2\ H^+$ PCET [235].

	$\boldsymbol{\alpha}$**-SiW₉**	$\mathbf{Mn^{II}{}_3SiW_9}$	$\mathbf{Mn^{III}{}_3SiW_9}$
$W^{VI}/W^{V}\ U_0$ *vs. NHE / V*	-0.61	-0.69	-0.68

Table 6.1 – *Equilibrium potential positions of the W-ion for three polyanions at pH 5.4 extracted from cyclic voltammograms***.**

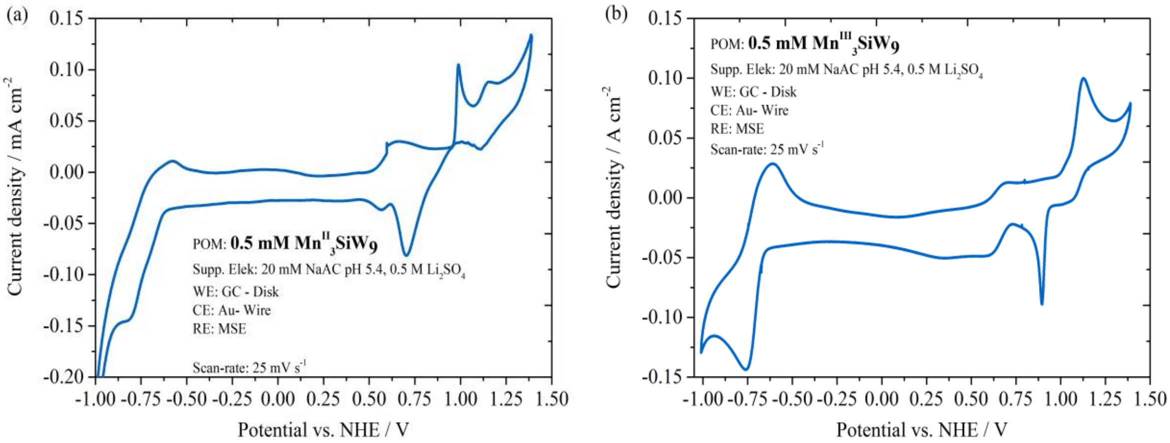

Figure 6.8 – *Cyclic voltammograms for 0.5 mM* ***(a)*** $\mathbf{Mn^{II}{}_3SiW_9}$ *and* ***(b)*** $\mathbf{Mn^{III}{}_3SiW_9}$ *in 20 mM NaAC buffer at pH 5.4. The scan-rate was 25 mV* s^{-1}**.**

At potentials higher than $U = 0.3\ V$ *vs. NHE* the electron transfer reactions of the inserted *Mn*-ions take place. Identification of the single peaks is less straight-forward than for $\mathbf{Mn^{II}SiW_{11}}$ (Fig. 6.5). In addition, the CVs in Fig. 6.8 a and b differ from each other, which is not expected as the two polyanions are isostructural. A CV restricted to the potential range in which only the *Mn*-ions are active for both molecules, $\mathbf{Mn^{II}{}_3SiW_9}$ and $\mathbf{Mn^{III}{}_3SiW_9}$, is shown in Fig. 6.9

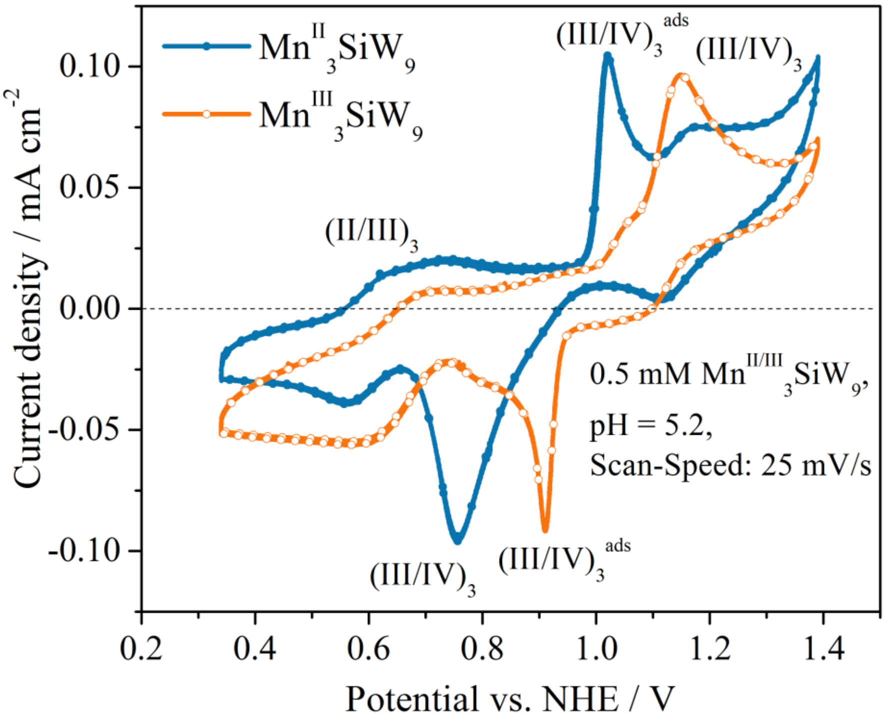

.

Figure 6.9 – *Cyclic voltammograms for 0.5 mM* $\mathbf{Mn^{II}{}_3SiW_9}$ *and* $\mathbf{Mn^{III}{}_3SiW_9}$ *in 20 mM NaAC buffer at pH 5.2. The scan-rate is 25 mV s*$^{-1}$ *and the potential is restricted to a range in which only the Mn-ions are redox active.*

In analogy to the work of Sadakane and Steckhan, we propose a reaction mechanism that can explain the observed CV. Experimental evidence for these formulas will be presented subsequently.

For the $Mn^{II}{}_3/Mn^{III}{}_3$ redox-reaction, which is marked with (II/III)$_3$ in Fig. 6.9, we assume a three electron, three cation CCET:

$$C_7[Mn_3^{II}(OH)_3SiW_9O_{34}(L)_3]^{7-} \rightleftharpoons \\ C_4[Mn_3^{III}(OH)_3SiW_9O_{34}(L)_3]^{4-} + 3e^- + 3C^+ \tag{6.5}$$

L designates a ligand. In the case of $\mathbf{Mn^{III}{}_3SiW_9}$ this ligand is water, as can be seen in the ball-and stick representation in Fig. 6.1. For $\mathbf{Mn^{II}{}_3SiW_9}$, as it is in oxidation state Mn^{II}, we propose that CH_3COOH replaces the terminal water, as it does for $\mathbf{Mn^{II}SiW_{11}}$. The CCET in the graph is very similar for the two polyanions [42]. For the $Mn^{III}{}_3/Mn^{IV}{}_3$ redox-reaction the deviation between the two molecules is significant. The electron transfer is assumed to be coupled to protons that are released or taken up by *L*:

$$C_4[Mn_3^{III}(OH)_3SiW_9O_{34}(CH_3COOH)_3]^{4-} \rightleftharpoons \\ C_4[Mn_3^{IV}(OH)_3SiW_9O_{34}(CH_3COO)_3]^{4-} + 3e^- + 3H^+ \tag{6.6}$$

And:

$$C_4[Mn_3^{III}(OH)_3SiW_9O_{34}(H_2O)_3]^{4-} \rightleftharpoons \\ C_4[Mn_3^{IV}(OH)_6SiW_9O_{34}]^{4-} + 3e^- + 3H^+ \tag{6.7}$$

In Fig. 6.9 one oxidation peak and one reduction peak show the characteristic shape of adsorbed species, they are marked with $(III/IV)_3^{ads}$. Both polyanions exhibit one of these, for **$Mn^{II}_3SiW_9$** it is an anodic wave at *1.02 V vs. NHE*, for **$Mn^{III}_3SiW_9$** it is a cathodic current at *0.91 V vs. NHE.* At the same time, each CV contains one peak marked with $(III/IV)_3$ and their shape indicates that the correspond to oxidation or reduction of freely diffusing species. The $(III/IV)_3$ peak potential is always at more extreme potentials than the $(III/IV)_3^{ads}$ peak potentials; the oxidation current peaks at *1.15 V vs. NHE* for **$Mn^{II}_3SiW_9$**, the reduction current has its maximum at *0.76 V vs. NHE* for **$Mn^{II}_3SiW_9$**. For the chosen parameters of the CV in Fig. 6.9, each polyanion shows a smaller bump at potentials for which the other molecule undergoes its characteristic redox wave. For example, at the potential of the $(III/IV)_3^{ads}$ oxidation wave of **$Mn^{II}_3SiW_9$** the CV of the other POM, **$Mn^{III}_3SiW_9$**, shows a small redox wave. This indicates that each of the species has at least a small concentration in the configuration of the other.

The shape and number of peaks can be analyzed further which is done in Fig. 6.10. Aim was to answer the question whether eq. 6.6 takes place as a simultaneous transfer of three electrons or if the peaks are a superposition of three single electron transfer. Fig. 6.10a shows **$Mn^{III}_3SiW_9$** subjected to a potential scan at a scan-rate of *100 mV s^{-1}*. It is possible to distinguish three single reduction peaks that are marked with U^1_{red}, U^2_{red} and U^3_{red}. However, the center reduction peak (U^2_{red}) is not very pronounced and not observable in most CVs. Therefore, it is assumed that the reduction process of eq. 6.6 is a stepwise reduction and not a simultaneous three electron process [42].

The oxidation proceeds in one broad wave, marked with $U^{1,2,3}_{ox}$. The dotted orange line in Fig. 6.10b shows this process recorded at a scan-rate of *10 mV s^{-1}*. For comparison, oxidation waves were calculated with the software EC-Lab. The simulation parameters electrode area, scan-rate, temperature and concentration of active species were chosen to match the experimental details. The diffusion constant was assumed to be $D = 2.56\ 10^{-6}\ cm^2\ s^{-1}$, as reported for the Keggin ion [226]. The electron transfer constant was assumed to be $k_0 = 0.01\ cm\ s^{-1}$. The red curve was simulated with $n = 3$, concerted transfer of three electrons. Its shape and peak current differ greatly from the experimental data, also the onset of the current takes place at higher potential. Three curves for $n = 1$ were simulated as well, they are shown as light blue lines. Their equilibrium potentials vary slightly; the addition of the three lines is given by the thick blue line. While the match of this data with the experimental curve is not perfect, it agrees much better with the orange scatter data than the red lines does. This indicates that the oxidation wave also proceeds via three single-electron transfer. However, their split in potential is much smaller than for the reduction and therefore their signals overlap in the CVs that were recorded. Bard and Faulkner comment on consecutive electron transfer [67]. They state that if the difference between the U_0 of two redox-reactions is $\Delta U_0 \leq 100\ mV$, their individual waves will merge into one broad wave independent of scan rate.

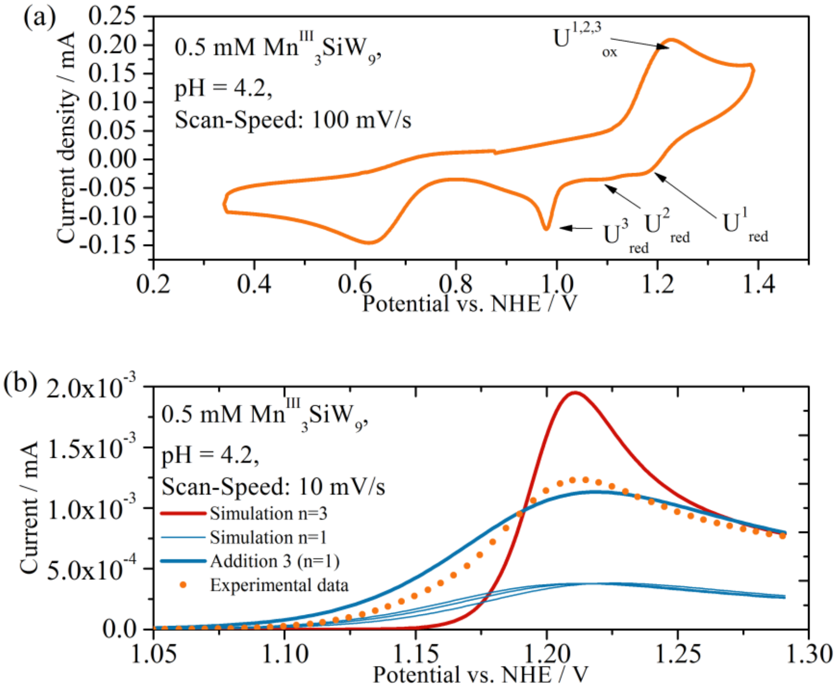

Figure 6.10 – *Cyclic voltammograms of 0.5 mM* **$Mn^{III}_3SiW_9$** *20 mM NaAC buffer at pH 4.2.* ***(a)*** *The scan-rate is 100 mV s^{-1} and a splitting of the reduction wave into three single peaks U^1_{red}, U^2_{red} and U^3_{red} is observed.* ***(b)*** *The oxidation reaction for eq. 6.6 at a scan-rate of 10mV s^{-1} is compared to two simulated anodic waves. One wave for concerted three electron oxidation (red curve) and one for a superposition of three single electron transfers (blue curve).*

6.4.2 Dependence on pH and supporting electrolyte

A first evaluation of the proposed reaction mechanism can be conducted by varying the proton concentration in the supporting electrolyte and by replacing the acetate-ions in the buffer by other species. The former because the CCETs are independent and PCET are dependent of pH value, the latter because a ligand exchange was proposed. Incorporation of other molecules than CH_3COOH should have an effect on the CVs.

A Pourbaix diagram gives U_{eq} over pH value for a redox reaction [235]. The dependency arises because protons, which are transferred during a PCET, enter the Nernst equation together with the concentrations of the redox-couple. Equilibrium potentials for the redox reactions that involve *Mn*-ions were determined for $\mathbf{Mn^{II}SiW_{11}}$, $\mathbf{Mn^{II}{}_3SiW_9}$ and $\mathbf{Mn^{III}{}_3SiW_9}$. They are displayed in Fig. 6.11. The peaks marked (III/IV)$_3^{ads}$ and (III/IV)$_3$ in Fig. 4.9 were combined across the two polyanions to form one U_0 respectively.
In general, it can be stated that the redox-reactions of $\mathbf{Mn^{II}SiW_{11}}$ take place at a higher potentials than the *Mn*-ion electron transfer of the tri-*Mn* substituted Keggin polyanions. The pH range is restricted to the values shown here because it was observed that the stability range of $\mathbf{Mn^{II}{}_3SiW_9}$ and $\mathbf{Mn^{III}{}_3SiW_9}$ is relatively small and that they decompose at $pH < 3.5$ [39,42].

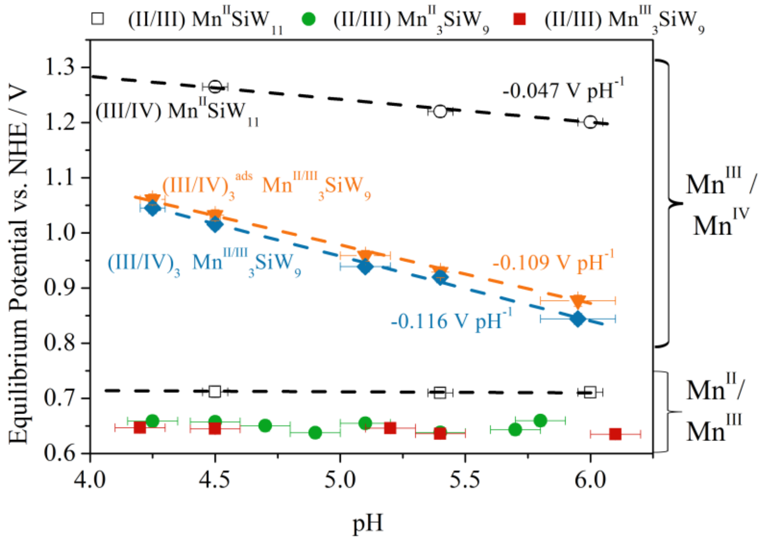

Figure 6.11 – *Equilibrium potentials over pH value for the Mn-ion redox reactions of* $\mathbf{Mn^{II}SiW_{11}}$, $\mathbf{Mn^{II}{}_3SiW_9}$ *and* $\mathbf{Mn^{III}{}_3SiW_9}$ *with the slopes of linear fits given.*

U_0 for the Mn^{II}/Mn^{III} reactions does not exhibit a dependence on the proton concentration for any of the three species, which indicates that is indeed a pure electron transfer or CCET. As CCETs are reported for multiple transition metal-substituted Keggin-ions, including $\mathbf{Mn^{II}SiW_{11}}$, it is assumed that the Mn^{II}/Mn^{III} redox-reactions are coupled to cation transfer.

This mechanism can be explained by ion-pairing of the cations of the electrolyte with the negatively charged polyoxoanions [183,220,221,231].

On the other hand, the Mn^{III}/Mn^{IV} redox-reactions show a clear dependence on *pH* value. The slope of $-0.047\ V\ pH^{-1}$ for $\mathbf{Mn^{II}SiW_{11}}$ was discussed in a previous subsection. The adsorbed $(III/IV)_3^{ads}$ and the freely diffusing $(III/IV)_3$ markers show a very similar slope of $-0.109\ V\ pH^{-1}$ for the former and $-0.116\ V\ pH^{-1}$ for the latter. This result shows that the Mn^{III}/Mn^{IV} redox-reactions are indeed PCET reactions, as indicated in eq. 6.5 and 6.6. It can be suspected that two protons are involved per electron as the experimental values are close to the theoretical $-0.118\ V\ pH^{-1}$ [42].

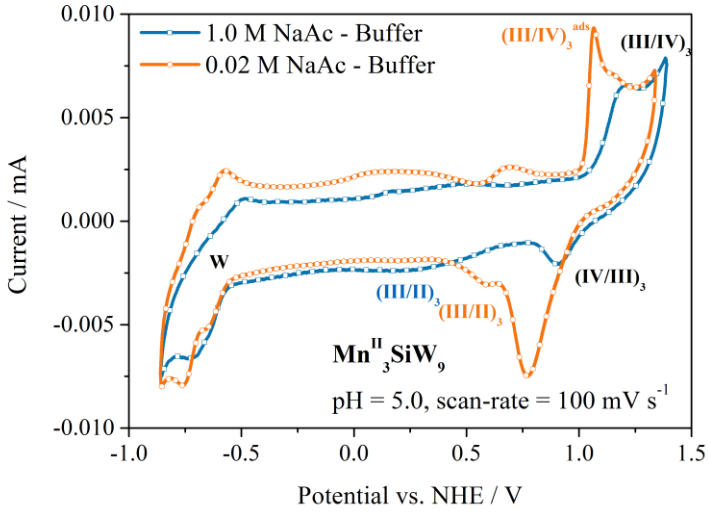

Figure 6.12 – *Cyclic voltammograms of 0.5 mM* $\mathbf{Mn^{II}_3SiW_9}$ *at pH 5.0 with a scan-rate of* $100\ mV\ s^{-1}$. *The blue curve was recorded in 1.0 M* $NaCH_3COO/CH_3COOH$ *buffer while the orange curve was recorded in an electrolyte with a concentration of 0.02 M of same buffer. Some of the peaks are labelled. The graph is adapted from* [42].

Besides cations and protons, also anions influence the POMs under investigation. It was shown for $\mathbf{Mn^{II}SiW_{11}}$ that a change in concentration of the buffer has an immediate effect on the CV (Fig. 6.7). While the electrochemistry of $\mathbf{Mn^{II}_3SiW_9}$ and $\mathbf{Mn^{III}_3SiW_9}$ in low buffer concentrations (20 *mM*) was extensively described in ref. [42], CVs in *1 M* $LiCH_3COOH/CH_3COOH$ were treated in ref. [39]. The direct comparison of two CVs recorded at $100\ mV\ s^{-1}$ for $\mathbf{Mn^{II}_3SiW_9}$, one in *0.02 M* and one in *1.0 M* $NaCH_3COO/CH_3COOH$ buffer is shown in Fig. 6.12. The effect of increased buffer concentration is even more pronounced than for $\mathbf{Mn^{II}SiW_{11}}$. Notable differences and similarities include:

- The peak designated $(III/IV)_3^{ads}$ for the oxidation of adsorbed species (at *1.07 V vs. NHE*) is present only in *20 mM* buffer;

- The peak designated $(III/IV)_3$ for the oxidation of freely diffusing species (at *1.21 V vs. NHE*) is visible in both buffer concentrations;
- The reduction wave designated $(IV/III)_3$ (at *0.91 V* and *0.77 V vs. NHE*) is much bigger in the lower buffer concentration;
- The reduction wave $(III/II)_3$ takes place at much lower potential in the higher buffer concentration;
- The W-redox waves are smaller and not as clearly resolved in high buffer concentrations.

The lack of the oxidation current related to adsorbed species $(III/IV)_3^{ads}$ in *1.0 M* $NaCH_3COO/CH_3COOH$ buffer suggest that the species either does not adsorb, or that the adsorbed species is not redox-active. Also, it has to be noted that the reduction wave $(IV/III)_3$ is smaller than the corresponding oxidation wave, if *1.0 M* of buffer is used. This indicates the existence of an irreversible reaction.

To investigate this irreversible reaction, the development of CVs in *1 M* $NaCH_3COO/CH_3COOH$ over multiple cycles was examined. This study is shown in Fig. 6.13. As it can be seen in the left graph, Fig. 6.13a, the CV changes with continued cycling. Most notable is a shift of the W^{VI}-ion reduction to lower potentials and a decreasing current density for the oxidation of the Mn^{III}-ions (peak $(III/IV)_3$). These changes are quantitatively presented in the right graph, Fig. 6.13b, for the first ten cycles. The shift of the reduction potential to lower values indicates a kinetic hindrance of the otherwise facile reduction. A similar deleterious effect on *W*-ion reduction was reported by Ammam et al. for $[Mn^{II}_4(H_2O)(H_4AsW_{15}O_{56})_2]^{18-}$ [236]. With energy dispersive X-ray spectroscopy (EDX) they found that the decomposition product on the electrode might be *MnOOH*, as suggested previously [237].

The decreasing intensity of the $(III/IV)_3$ wave indicates that either less concentration of $\mathbf{Mn^{II}_3SiW_9}$ is available for oxidation or that the ECSA became smaller [39]. Both phenomena can be explained by non-redox-active decomposition products depositing onto the electrode.

While decomposition and deposition of POMs is not uncommon, typically the carbon electrode is activated for POM related reactions and often also for reactions such as oxygen reduction [184,236,238,239]. Interestingly, continuous cycling of $\mathbf{Mn^{III}_3SiW_9}$ in *1.0 M* $NaCH_3COO/CH_3COOH$ buffer also led to increased currents, a behavior diametrical to the one observed for $\mathbf{Mn^{II}_3SiW_9}$ [39]. The process of deposition and the difference in deposit composition for $\mathbf{Mn^{III}_3SiW_9}$ and $\mathbf{Mn^{II}_3SiW_9}$ is interesting and should be investigated in the future. The observation indicates that the two polyoxoanions have a different chemical composition in the electrolyte which supports the theory that ligand exchange takes place in oxidation state Mn^{II}.

In low buffer concentrations the CVs are stable and do not show alteration for extended periods of time. The reason for this striking deviation of redox behavior in different concentrations (see Fig. 6.12) is unknown. As one of the major differences between CVs of $\mathbf{Mn^{II}_3SiW_9}$ in *0.02 M* and *1.0 M* $NaCH_3COO/CH_3COOH$ buffer is the missing $(III/IV)_3^{ads}$ peak in the CV of the latter, the next section will deal with the adsorption behavior of the polyoxoanion on carbon electrodes.

Another indirect evidence for ligand exchange was found when replacing the *0.02 M* $NaCH_3COO/CH_3COOH$ buffer with the same concentration of citrate ($Na_3C_6H_5O_7/C_6H_8O_7$) or phosphate (NaH_2PO_4/H_3PO_4) buffer. As it is hypothetically prone to ligand exchange, $\mathbf{Mn^{II}_3SiW_9}$ was investigated with CVs in above buffers to assert any effect that uptake of $C_6H_7O_7^{-1}$ or $H_2OPO_4^{-1}$ might have. The results are shown in Fig. 6.14.

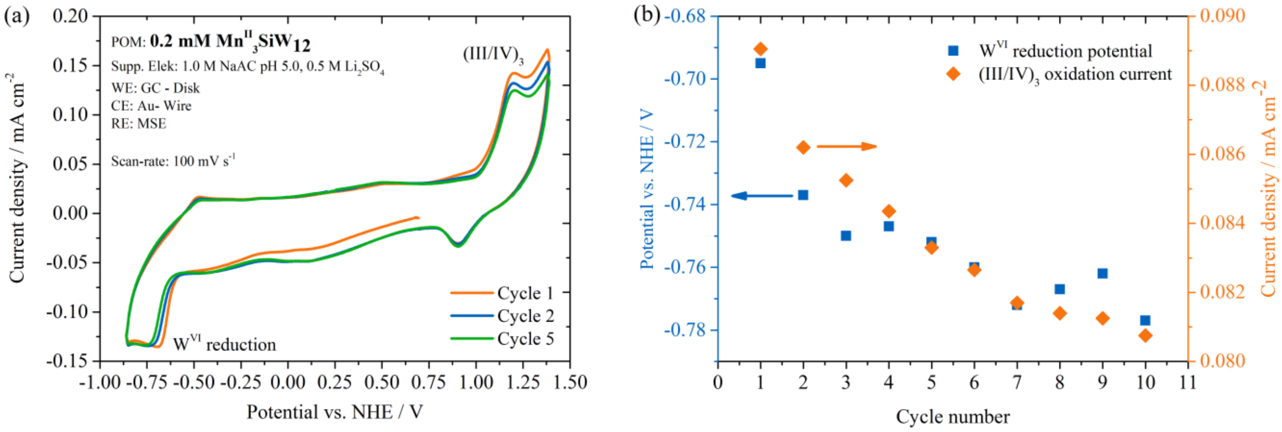

Figure 6.13 – (a) *Cyclic voltammograms of 0.2 mM* $\mathbf{Mn^{II}_3SiW_9}$ *at pH 5.0 with a scan-rate of 100 mV* s^{-1} *recorded in 1.0 M* $NaCH_3COO/CH_3COOH$ *buffer*. *Three cycles are shown, the first, second and fifth scan.* **(b)** *Changes in the CVs with continued cycling. The left ordinate gives the peak potential of* W^{VI}*-ions reduction, the right ordinate gives the peak current density* $(III/IV)_3$. *These points of interest are marked in (a). The graphs are adapted from* [39].

The blue curve in Fig. 6.14a was recorded in *0.02 M* acetic acid buffer and was discussed previously, it is given for comparison.

The green curve shows a CV of $\mathbf{Mn^{II}_3SiW_9}$ in phosphoric acid buffer at a $pH = 5.0$. The peaks assigned to the CCET Mn^{II}/Mn^{III} are quite similar to the feature in acetic acid. According to eq. 6.5 the electron transfer is accompanied by cation exchange, the phosphoric acid group, if it has replaced the terminal water, does not participate in the reaction. However, the exchanged ligand participates in the Mn^{III}/Mn^{IV} redox reaction which is a PCET, see eq. 6.6. The oxidation current (release of proton from ligand) resembles the anodic peak $(III/IV)_3$. The reduction, however, is significantly smaller and less defined which indicates an irreversible reaction.

$\mathbf{Mn^{II}_3SiW_9}$ in citric acid buffer (orange curve) shows even further reduced redox properties.

The only noticeable peak is a broad anodic wave around *1.05 V vs. NHE.* At the applied scan-rate there is no cathodic waver corresponding to the oxidation. It is possible to record a reduction wave at increased scan-rates, which are shown in Fig. 6.14b. The green and red curve, recorded at $500\ mV\ s^{-1}$ and $1000\ mV\ s^{-1}$ respectively, show a reduction wave. This indicates that by oxidation an unstable compound is formed that decays in less than one second ($0.2\ V / 1\ V\ s^{-1} = 0.2\ s$).

Therefore the study in different buffer solutions indicates that indeed the anion of the supporting electrolyte is of big importance for the redox behavior of the polyoxoanion $\mathbf{Mn^{II}_{3}SiW_{9}}$. It was found that anions larger than the acetate ion lead to a reduced redox behavior and that addition of citrate forms an unstable molecule upon oxidation to Mn^{IV}. This finding is another evidence for the existence of ligand exchange at oxidation state Mn^{II}.

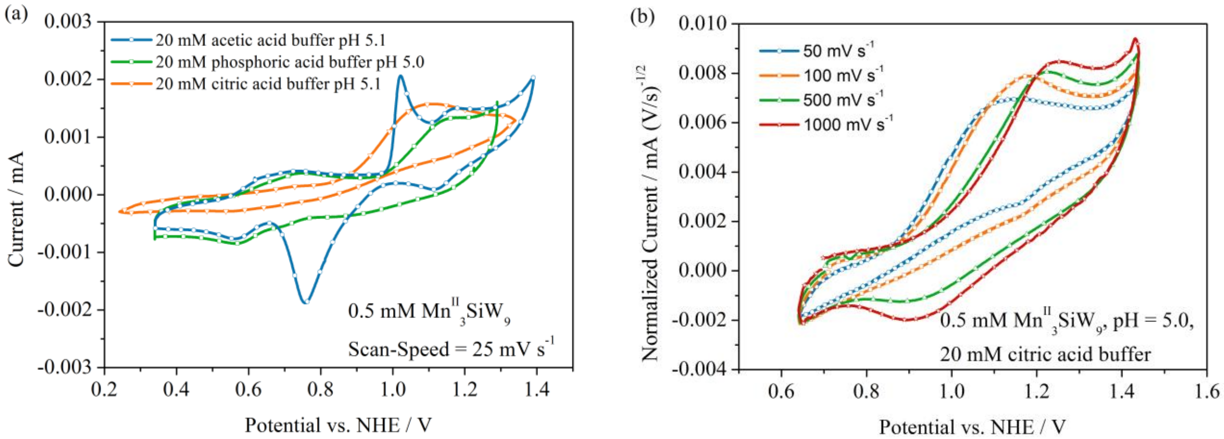

Figure 6.14 – (a) *Cyclic voltammograms of 0.5 mM* $\mathbf{Mn^{II}_{3}SiW_{9}}$ *with a scan-rate of 25* mV s^{-1} *recorded in three different buffer solutions. The potential is restricted to potentials at which the Mn-ions undergo redox-reactions.* **(b)** *CVs* of *0.5 mM* $\mathbf{Mn^{II}_{3}SiW_{9}}$ in citric acid *buffer with various scan speeds. The ordinate is the normalized current to adjust for variations that stem from a faster scan-rate. The graphs are adapted from* [42].

6.4.3 Adsorption behavior

Study of the adsorption behavior is of importance as it seems to be one of the major differences between the redox properties of $\mathbf{Mn^{II}_{3}SiW_{9}}$ and $\mathbf{Mn^{III}_{3}SiW_{9}}$. In addition, it was observed that $\mathbf{Mn^{II}_{3}SiW_{9}}$ behaves fully reversible when cycled continuously in $0.02\ M\ NaCH_3COO/CH_3COOH$ buffer, while it seemed to permanently deposit on the carbon electrode in $1.0\ M\ NaCH_3COO/CH_3COOH$ buffer. It was analyzed if adsorption takes place, and if the polyoxoanion desorbs again in low buffer concentrations. A two-pronged approach was chosen, CVs on the one hand and imaging with an AFM on the other hand.

One of the hypothesis was that **$Mn^{II}_3SiW_9$** adsorbs at the electrode prior to oxidation to Mn^{IV} while **$Mn^{III}_3SiW_9$** does not, and that this difference is caused by the ligand exchange. In Fig. 6.15 linear sweeps of *0.5 mM* **$Mn^{II}_3SiW_9$** in $0.02\ M\ NaCH_3COO/CH_3COOH$ at various scan rates are shown, the current given on the ordinate was again normalized to eliminate the effect of the variable change of the concentration gradient. The redox-reaction monitored in this potential range is the oxidation from $[Mn_3^{III}(OH)_3SiW_9O_{34}(CH_3COOH)_3]^{4-}$ to $[Mn_3^{IV}(OH)_3SiW_9O_{34}(CH_3COO)_3]^{4-}$.

It is important to realize that slower scan-rates result in passing of more time before reaching the onset of oxidation. For example, while a potential ramp of *100 mV* takes *10 s* at $10\ mV\ s^{-1}$ (blue curve), the same potential ramp is completed in *0.1 s* at $1000\ mV\ s^{-1}$ (teal curve).

There are two peaks observable in Fig. 6.15. One is located at *1.01 V vs. NHE* for $10\ mV\ s^{-1}$ and was previously labelled $(III/IV)_3^{ads}$, the other one can be seen at *1.15 V vs. NHE* for $10\ mV\ s^{-1}$ and was assigned to freely diffusing species $(III/IV)_3$. The evolution of the current responses with increased scan-rates sees a continuous decay of $(III/IV)_3^{ads}$ which is accompanied by simultaneous growth of $(III/IV)_3$. For scan-rates of $250\ mV\ s^{-1}$ and higher, $(III/IV)_3^{ads}$ has vanished, while $(III/IV)_3$ grew by an increment that is far larger than the slight change witnessed for the evolution for scan rates $10\ mV\ s^{-1} \leq \nu \leq\ 100\ mV\ s^{-1}$. Once $\nu \geq\ 250\ mV\ s^{-1}$, the current of the $(III/IV)_3$ stays approximately constant. The small decrease in peak current and shift to higher potentials is attributed to a kinetic limitation.

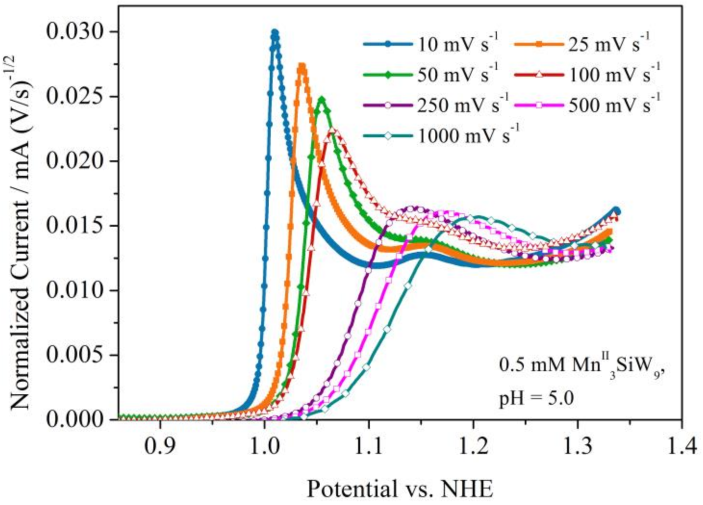

Figure 6.15 – *Partial CV for the oxidation of 0.5 mM* **$Mn^{II}_3SiW_9$** *at different scan-rates. The current is normalized to eliminate the effect of a faster change in concentration of redox-species for higher scan-rates. The graph is taken from* [42].

From these observations two conclusions can be drawn:

- First, the two peaks stem from the same redox-reaction, the oxidation of the *Mn*-ions from Mn^{III} to Mn^{IV}, but represent parallel reaction pathways. As the first peak shrinks, the second one grows, which indicates that all the species, that was not oxidized in $(III/IV)_3^{ads}$ is oxidized in $(III/IV)_3$;
- Second, the existence of the first peak $(III/IV)_3^{ads}$ is dependent on the time that elapses between some event during the CV and reaching the potential at which pathway $(III/IV)_3^{ads}$ takes place. However, this event cannot take place at the resting potential of the cell, during which $\mathbf{Mn^{II}_3SiW_9}$ is in oxidation state Mn^{II}, because otherwise the resting time would influence the existence and size first peak and not the scan rate.

An hypothesis that complies with above observations is that $\mathbf{Mn^{II}_3SiW_9}$ adsorbs on the GC electrode while in oxidation state $[Mn_3^{III}(OH)_3SiW_9O_{34}(CH_3COOH)_3]^{4-}$. Therefore, the scan-rate is important as higher speeds leave less time for the adsorption of the generated Mn^{III} species.

Above hypothesis assumes a potential dependent adsorption, as potential of the working electrode translates into oxidation state of $\mathbf{Mn^{II}_3SiW_9}$ at the electrode. To test this assumption the coverage of an HOPG electrode with the polyoxoanion at different potentials was imaged with an AFM. For this purpose $1\ cm^2$ of HOPG was immersed into an electrolyte containing $0.02\ M$ NaAC buffer, $0.5\ M\ Li_2SO_4$ and $50\ 10^{-6}\ M$ $\mathbf{Mn^{II}_3SiW_9}$. After performing electrochemical conditioning, as described below, the electrode was dipped into ultrapure water and investigated with the AFM [42].
Three different HOPG surface were imaged, these are shown in Fig. 6.16:

- *60 s* at OCV (*0.442 V vs. NHE*), shown in Fig. 6.16b. The polyoxoanion is in oxidation state $[Mn_3^{II}(OH)_3SiW_9O_{34}(CH_3COOH)_3]^{7-}$ and some agglomerated clusters cover the edge plane of HOPG. There are no molecules on the basal plane, apparently the interaction of the POMs with the basal plane is too weak for them to withstand the drag of the AFM tip and therefore they agglomerate on the HOPG edges;
- CV to *1.29 V vs. NHE* with $10\ mV\ s^{-1}$. This equals an immersion time of *84.8 s*. The micrograph is shown in Fig. 6.16c. The polyoxoanion is in oxidation state $[Mn_3^{IV}(OH)_3SiW_9O_{34}(CH_3COO)_3]^{4-}$ and its coverage on HOPG is much higher than for Fig. 6.16b. Some of the clusters are stable on the basal plane. An inset shows a magnification of an edge with particles attached to it;
- CV to *1.29 V vs. NHE* and back to OCV which equals an immersion time of *169.6 s*. The polyoxoanion is in oxidation state $[Mn_3^{II}(OH)_3SiW_9O_{34}(CH_3COOH)_3]^{7-}$. The

HOPG is almost entirely free of molecular clusters. This indicates that the adsorption process in *0.02 M* $NaCH_3COO/CH_3COOH$ buffer is fully reversible.

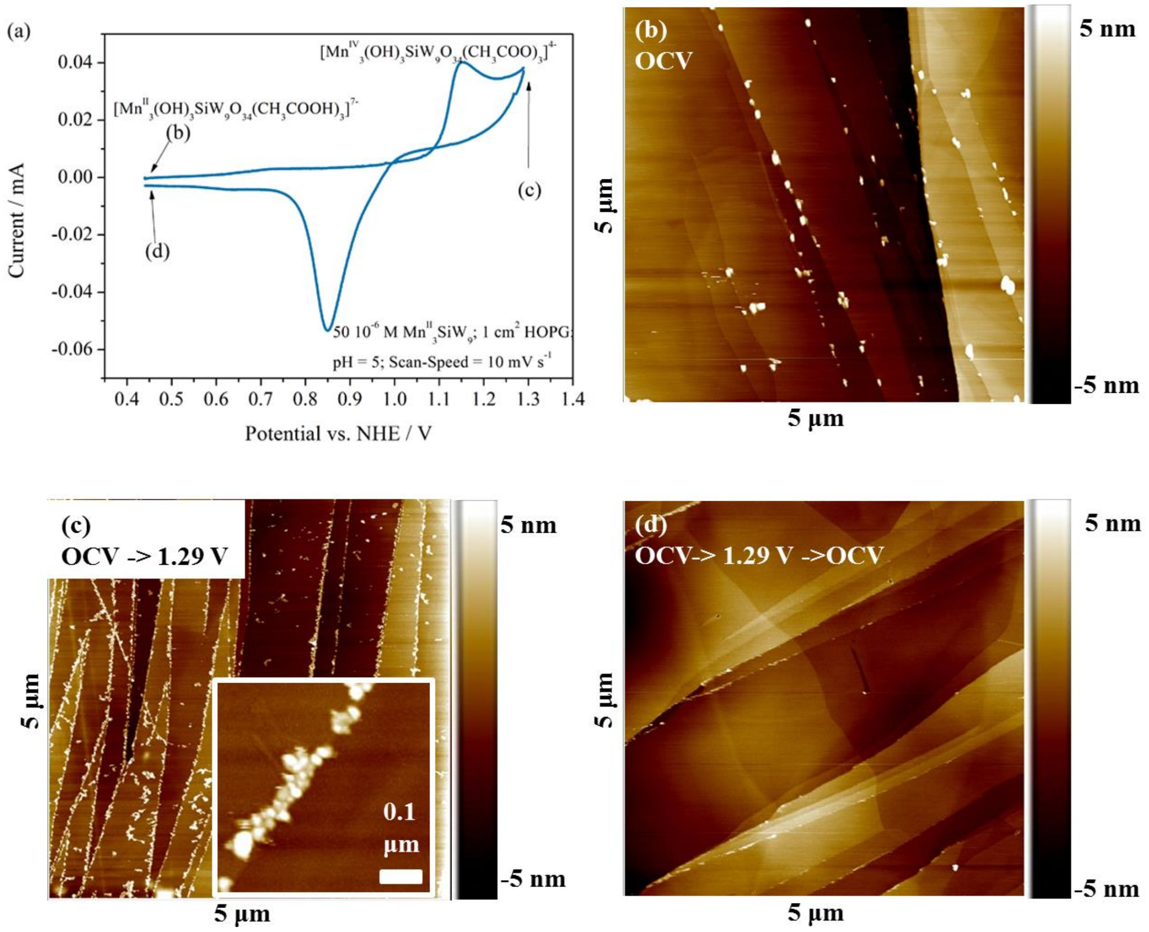

Figure 6.16 – (*a*) *CV of 50 µM* $\mathbf{Mn^{II}_3SiW_9}$ *on 1* cm^2 *HOPG.* ***(b)*** *5 µm x 5 µm micrograph recorded after immersing the HOPG at U = 0.442 V vs. NHE (OCV) for 60 s.* ***(c)*** *5 µm x 5 µm micrograph recorded after performing a linear potential sweep from OCV to 1.29 V vs. NHE with 10 mV* s^{-1}*. The inset shows a magnification of an edge plane with attached clusters of POM.* ***(d)*** *5 µm x 5 µm micrograph recorded after performing a CV from OCV to 1.29 V vs. NHE and back to OCV at 10 mV* s^{-1}*. The graph is taken from* [42].

The corresponding CV with HOPG as working electrode is shown in Fig. 6.16a. Potential dependent adsorption of POMs was confirmed for $[(Mn^{III}(H_2O))_3(SbW_9O_{33})_2]^{9-}$ with an electrochemical quartz crystal microbalance (EQCM) setup [184]. As early as 1993, Keita and Nadjo were able to employ in-situ scanning probe microscopy to show potential dependent adsorption of POMs [240]. Later it was shown that in- and ex-situ patterns for $[P_2Mo_{18}O_{62}]^{6-}$ are comparable [241]. Despite their significant negative charge and the resulting electrostatic repulsive forces POMs are known to interact with each other forming dimers or higher oligomers in aqueous electrolytes [234]. This can be understood as an effect of ion-pairing [220,221,242]. Molecular dynamics studies also predicted interaction with hydrophobic materials like ionic liquids or graphite [233].

The Born energy of solvation ΔG_{Born} is given as [243]:

$$\Delta G_{Born} = \frac{z^2 e^2}{8 \pi \varepsilon_0 a} (1 - \frac{1}{\varepsilon_r}) \tag{6.8}$$

With charge of a molecule z and ionic radius a. ΔG_{Born} becomes smaller with decreasing absolute, formal charge of a molecule and increasing radius. Further it is important to note that for hydrophilic substances, such as HOPG or GC, the interaction becomes larger when ΔG_{Born} decreases [234].

Utilizing eq. 6.8 it is possible to explain the potential dependent adsorption behavior of **$Mn^{II}_3SiW_9$** and **$Mn^{III}_3SiW_9$** in agreement with the observations from CV- and AFM-studies. At OCV the formal charge of **$Mn^{II}_3SiW_9$** is negative *7* and the polyoxoanion replaces its terminal water with CH_3COOH according to the model of ligand exchange. The absolute charge is large and prevents adsorption on hydrophilic GC. This explains the time-dependence in Fig. 6.15, there has to occur an event that triggers adsorption. This event is the oxidation via a cation coupled electron transfer to $[Mn_3^{III}(OH)_3SiW_9O_{34}(CH_3COOH)_3]^{4-}$ which changes the formal charge to negative *4*. The reduced absolute charge and the increased ionic radius, due to the incorporated CH_3COOH – groups, render ΔG_{Born} sufficiently small for adsorption to take place. This species is then oxidized in $(III/IV)_3^{ads}$. Remaining freely diffusing species is oxidized in $(III/IV)_3$. Once the polyoxoanion is again reduced to its original form **$Mn^{II}_3SiW_9$** it will desorb due to the limited interaction. The same scheme holds true for **$Mn^{III}_3SiW_9$** with the difference that this polyoxoanion does not undergo ligand exchange. Therefore, its size *a* will be smaller than that of **$Mn^{II}_3SiW_9$** and that difference seems to be enough to keep ΔG_{Born} above a critical value for adsorption [42].

This reaction scheme is able to explain the found difference in redox behavior for the isostructural **$Mn^{II}_3SiW_9$** and **$Mn^{III}_3SiW_9$** (see Fig. 6.9). It is visualized in Fig. 6.17 with **$Mn^{II}_3SiW_9$** on top and **$Mn^{III}_3SiW_9$** at the bottom.

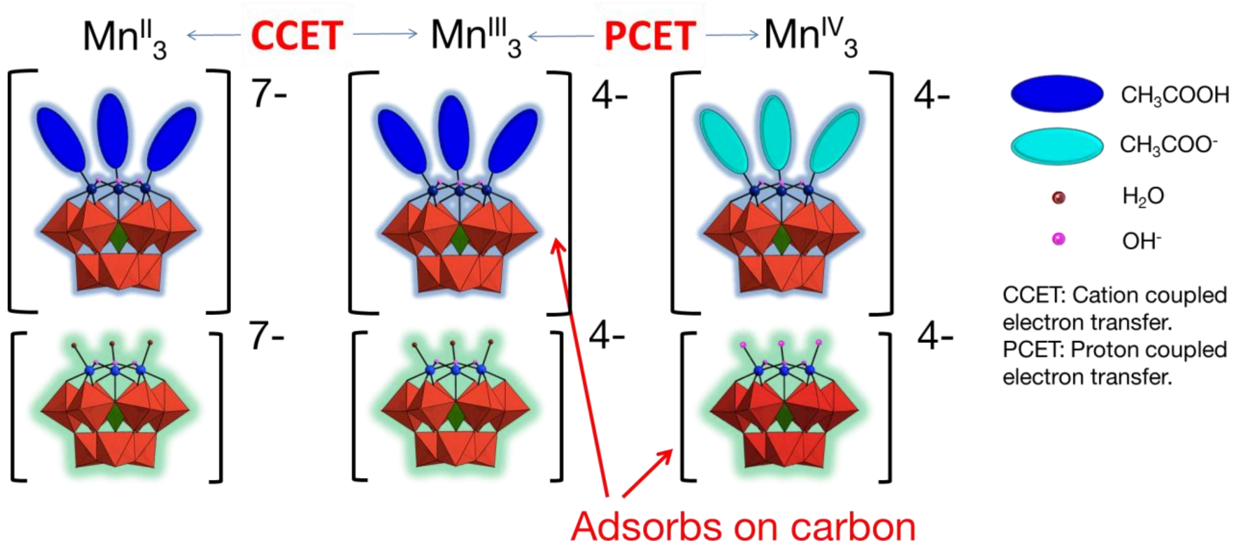

Figure 6.17 – *Reaction scheme for* **Mn$^{II}_3$SiW$_9$** *(above, after ligand exchange) and* **Mn$^{III}_3$SiW$_9$** *(below, no ligand exchange). As described in the text, the CCET lowers the formal charge of the polyanion* **Mn$^{II}_3$SiW$_9$** *sufficiently so that the PCET takes place for partially adsorbed species.*

6.4.4 Number of transferred electrons

In Fig. 6.10b CV-simulation was employed to obtain a qualitative idea of how many electrons are transferred during the oxidation of **Mn$^{III}_3$SiW$_9$**. In this section two methods will be used to obtain quantitative numbers for *n*. One is based on the Randles-Sevcik equation, another one uses coulomb-counting during bulk electrolysis. The latter method is complimented by UV-Vis spectroscopy in order to compare the spectrum of chemically generated **Mn$^{II}_3$SiW$_9$** with reduced **Mn$^{III}_3$SiW$_9$** and evaluate the stability of electrochemically generated species.

The Randles-Sevcik equation predicts a linear dependence of the peak current on the square-root of scan-rate [67]. This relation was used in previous figures to eliminate the influence of a variable scan-speed on the current. There are certain caveats, as the equation only holds for infinitely fast redox-reactions and the ECSA of the electrode, despite being polished, might be larger than the geometric surface area. Curves for the oxidation of *0.5 mM* **Mn$^{III}_3$SiW$_9$** in pH 5.2 are shown for four different scan-rates in Fig. 6.18.

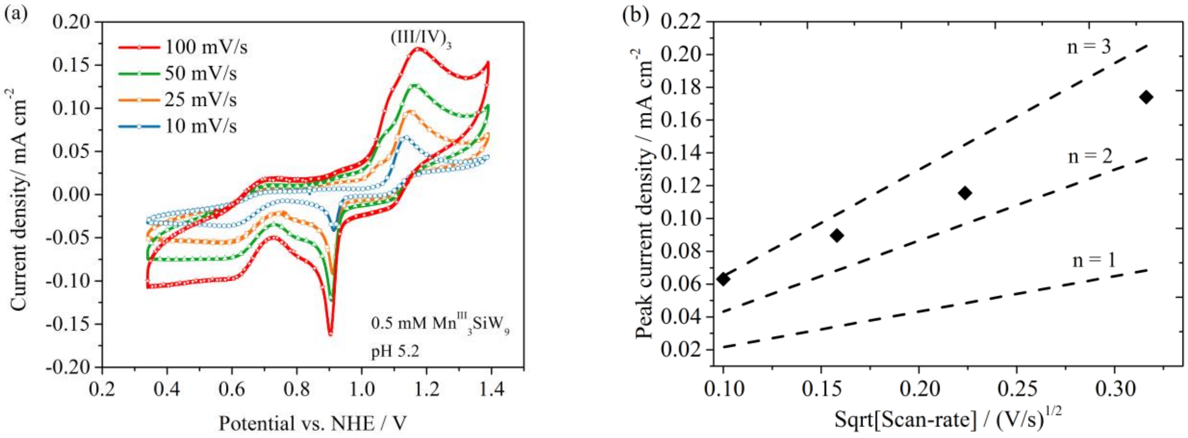

Figure 6.18 – (a) *Cyclic voltammograms of 0.5 mM* $\mathbf{Mn^{III}_3SiW_9}$ *with variable scan-rate. The potential is restricted to potentials at which the Mn-ions undergo redox-reactions.* **(b)** *Values for peak current density over square-root of scan-rate. For ease of comparison the theoretical curves for 1, 2 and 3 electron transfer are given. The graphs are adapted from* [42].

Fig. 6.18a clearly shows that the current density of the oxidation peak $(III/IV)_3$ increases with faster scan-rates. The visible shoulder at potentials slightly lower than the main anodic peak might stem from the oxidation of adsorbed species, as it was already commented that each species ($\mathbf{Mn^{II}_3SiW_9}$ and $\mathbf{Mn^{III}_3SiW_9}$) shows some limited current at potentials at which the other one undergoes it characteristic reactions. For ease of comparison Fig. 6.18b shows the extracted peak current density (diamonds) together with calculated curves for different values of n. The experimental data are located in between $n = 2$ and $n = 3$. Especially for $\nu = 10\ mV\ s^{-1}$ the experimental and theoretical result for $n = 3$ correspond well.

A possible explanation for the experimentally found electron transfer number n lying in between 3 and 2 is that three electrons are transferred during the oxidation of $\mathbf{Mn^{III}_3SiW_9}$, however, the missing electrons to $n = 3$ are transferred via a parallel pathway, the oxidation of adsorbed species [42]. This is very likely as the $(III/IV)_3^{ads}$ can be seen in Fig. 6.18a and because Fig. 6.15 shows that the parallel reaction pathways draw electrons from the same species.

This result was confirmed by coulomb counting in an h-type cell. A volume of *7 ml* of *0.5 mM* $\mathbf{Mn^{III}_3SiW_9}$ was oxidized while simultaneously reducing $\mathbf{Mn^{III}_3SiW_9}$ in the second half-cell. Supporting electrolyte was *0.02 M* $NaCH_3COO/CH_3COOH$ at *pH 5.0*. The potential in compartment with the anode was set to *1.29 V vs. NHE*. The current recorded between anode and cathode is shown in Fig. 6.19a. The theoretical capacity, product of concentration of active species, number of transferred electrons per molecule and volume, was calculated to $Q = 1.05\ C$, assuming $n = 3$. During the measurement both compartments were stirred and purged with argon gas. After passage of the theoretical capacity there was still a small current registered, which most likely stemmed from water oxidation to form O_2 [42]. A pronounced change in color was noted for both compartments.

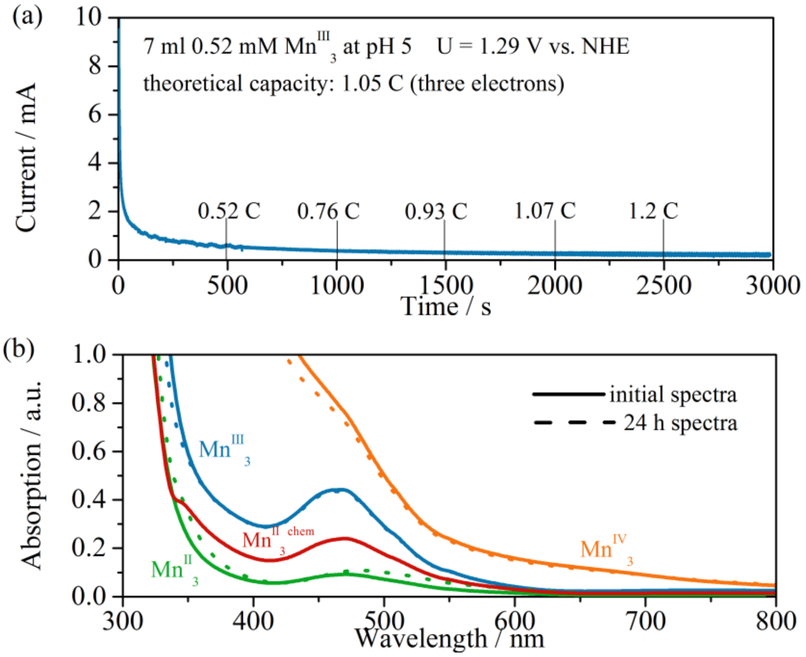

Figure 6.19 – *(a) Chronoaperometric curve for 0.5 mM* $\mathbf{Mn^{III}_3SiW_9}$ *as anolyte in a bulk electrolysis cell* **(b)** *UV-Vis spectra of electrochemically generated and synthesized polyoxoanion in oxidation states* Mn^{II}_3, Mn^{III}_3, *and* Mn^{IV}_3. *The graphs are adapted from* [42].

UV-Vis measurements were performed on extracted solutions from the two compartments; these are shown in Fig. 6.19b. The solution from the anode compartment is the orange curve, designated Mn^{IV}_3. Polyoxoanions in solution that had been reduced in the lower potential half-cell, Mn^{II}_3 showed the green line absorption spectrum. For comparison spectra of the precursor $\mathbf{Mn^{III}_3SiW_9}$ in solution (Mn^{III}_3, blue line) and as-received $\mathbf{Mn^{II}_3SiW_9}$ ($Mn^{II}_3{}^{chem}$, red line) were recorded as well and are given in Fig. 6.19b. All measurements were repeated after exposing the samples to lab environment for *24 h*. These control-measurements are shown as dashed lines. A number of observations can be made:

- The electrochemically generated species (Mn^{II}_3 and Mn^{IV}_3) both deviate from their parent Mn^{III}_3. Mn^{IV}_3 shows generally much higher absorption while the absorption of Mn^{II}_3 is quite low;
- The solutions seem to be stable on the timescale investigated;
- Spectra Mn^{II}_3 and $Mn^{II}_3{}^{chem}$ are similar, but do not overlap. A possible explanation is that Mn^{II}_3 was overly reduced as more than *1.05 C* worth of electrons was transferred to Mn^{III}_3 [42].

Glass et al. stated that the strong UV absorption, starting from $\lambda \leq 350$ nm, is arising from $O_{2p} \rightarrow W_{5d}$ charge transfer reactions, common to all polyoxotungstates [244].
For $[Mn^{III}_3(SiO_4)W_{10}O_{36}H_6]^{4-}$ Pope et. al reported an absorption peak at *460 nm* with a shoulder at higher wavelengths [186]. Shevchenko et al. published a peak at *492 nm* with a shoulder at higher wavelength for a Mn^{III}_3 substituted Keggin tungstosilicate in lutidine buffer [245]. Both studies correspond well with the shown spectrum of $\mathbf{Mn^{III}_3SiW_9}$ with a peak at 466 nm and a shoulder at *508 nm*.
Sadakane and Steckhan oxidized $\mathbf{Mn^{II}SiW_{11}}$ and reported the UV-Vis spectrum of $[Mn^{IV}(OH)SiW_{11}O_{39}]^{5-}$ [183]. Its spectrum looks very similar to the absorption profile of $\mathrm{Mn}^{\mathrm{IV}}_3$ in Fig. 6.19b. In both spectra there is a peak around *500 nm* recognizable which smoothly transitions into a strong rise in absorption at lower wavelengths. References [185,186], both showing absorption spectra for Mn^{IV}-containing polyoxoanions, support that the notion that above mentioned attributes are characteristic for oxidation state Mn^{IV}.
For Mn^{II}-containing POMs typically quite featureless spectra are reported [185,186]. These spectra are quite similar to the green curve in Fig. 6.19b which was assigned to electrochemically generated $\mathbf{Mn^{II}_3SiW_9}$.

As a conclusion, bulk electrolysis was able to prepare polyanions whose UV-Vis absorption spectra suggest that the initial oxidation state Mn^{III} was changed to Mn^{IV} and Mn^{II}. The produced molecules were stable in air on a time-scale of *24* hours. It can be speculated that the stability is an effect of the PCET and CCET taking place. These processes tend to avoid high energy intermediates which enhances stability, e.g. in biological systems [232].
Slightly more than three electrons were added or removed, which indicates that a side reaction (likely oxygen evolution) took place and that all three *Mn*-ions are redox active, in agreement with CV-studies.
Controlled potential electrolysis in *1.0 M* $NaCH_3COO/CH_3COOH$ at *pH 5.0* at *-0.160 V vs. NHE* resulted in a charge transferred equal to *3.0* electrons and UV-Vis spectra that were very similar to Fig. 6.19b [42].

6.4.5 Charge transfer kinetics

Due to the wealth of redox-reactions taking place in the potential range that corresponds to *Mn*-ion oxidation or reduction, many of them overlapping, it was difficult to select one reaction that takes pace in a potential range that is free from other reactions. The reaction deemed to be most suitable is the oxidation of $\mathbf{Mn^{III}_3SiW_9}$ from Mn^{III} to Mn^{IV}. As it can be seen Fig. 6.18, the main reaction pathway is $(\mathrm{III/IV})_3$. The rationale behind this choice was that the reaction had to involve dissolved species, as for electrons transfer of adsorbed species the techniques presented in chapter 4 are not applicable [67], and that there is only the $(\mathrm{III/IV})_3^{\mathrm{ads}}$ pathway as competing reaction.

The selected technique for kinetic characterization is potential steps due to the reasons named in chapter 4. With EIS the cell parameters were determined prior to the measurement. Although the luggin-capillary of the RE was placed in direct vicinity to the working electrode, the ohmic drop was relatively high, $R_{Ohm} = 43.6\ \Omega$. One reason is the small surface area of the WE, another one is the composition of the supporting electrolyte. The almost neutral, buffered solution has a lower conductivity than the diluted acids employed in chapters 4 and 5. This problem is often encountered when using small WE electrodes and the issue aggravates if microelectrodes are employed [110]. However, as upside, a small surface area entails a small double layer capacitance. The EIS measurement gave $C_{DL} = 0.654\ 10^{-6}\ F$ $(\approx 33\ 10^{-6}\ F\ cm^{-2})$. For comparison, $C_{DL} = 0.542\ 10^{-6}\ F$ $(\approx 27\ 10^{-6}\ F\ cm^{-2})$ was determined from fast CVs in plain supporting electrolyte [42]. Both values correspond well with the literature value for the specific C_{DL} of GC, $c_{DL} = (24 - 36)\ 10^{-6}\ F\ cm^{-2}$[15]. With the value obtained from EIS the time constant of the cell was determined to $\tau = R_{Ohm} \cdot C_{DL} = 28.5\ \mu s$ and therefore all non-faradaic current should have decayed after $5\,\tau = 142.5\ \mu s$.

For the PSs the potential was initially held at $U = 0.89\ V\ vs. NHE$, a potential at which no net current is measured and $\mathbf{Mn^{III}{}_3SiW_9}$ is in oxidation state Mn^{III}. At $t = 0\ s$ the potential was stepped to the desired value. Fig. 6.20a shows the current response to an exemplary PS as blue curve. The potential program is given in the inset. To improve the evaluation the non-faradaic current was determined. For that purpose the first datapoints of the current transient were fitted to an exponential decay, as the current required to charge the double layer is certainly dominant in the time regime immediately after changing the potential. This curve is given in orange. It initially overlaps with the experimental blue curve but decays faster and vanishes after approximately 400 μs. The time constant that was obtained from fitting is larger than the one that was determined experimentally, $\tau^{fit} = 57\ \mu s$. The difference between the experimental curve and the simulated non-faradaic current is expected to give the faradaic current and is plotted as red curve. Extrapolation of this curve back to t = 0 s yields the current which corresponds to the respective overpotential without mass-transport effects or non-faradaic currents.

Temperature / K	$\boldsymbol{I_0 / \mu A}$	$\boldsymbol{k_0 / cm\ s^{-1}}$
298	9.2	0.0032
293	7.6	0.0026
288	6.6	0.0023

Table 6.2 – *Values for exchange currents I_0 and electron transfer constants k_0 for the oxidation of* $\mathbf{Mn^{III}{}_3SiW_9}$ *at three different temperatures.*

These values for the current *I(t = 0 s)* were determined for potentials from *0.9 V vs. NHE* to *1.15 V vs. NHE* at three different temperatures, *298 K*, *293 K* and *288 K*. These curves are given in Fig. 6.20b. Linear extrapolation of these values back to the equilibrium potential yields exchange currents I_0 for the respective temperatures. These values are given in Fig. 6.20b and also in Table 6.2.

These exchange currents were converted to fundamental electron transfer constants k_0 according to the formula given in eq. 2.12. It was assumed that three electrons are transferred. There are several sources of error: The contribution via the adsorbed species pathway $(III/IV)_3^{ads}$, as discussed in section 6.4.4, and the unknown fraction of the three electrons transferred in each reaction [42].Thus, the order of magnitude for k_0 might be more interesting than its actual value.

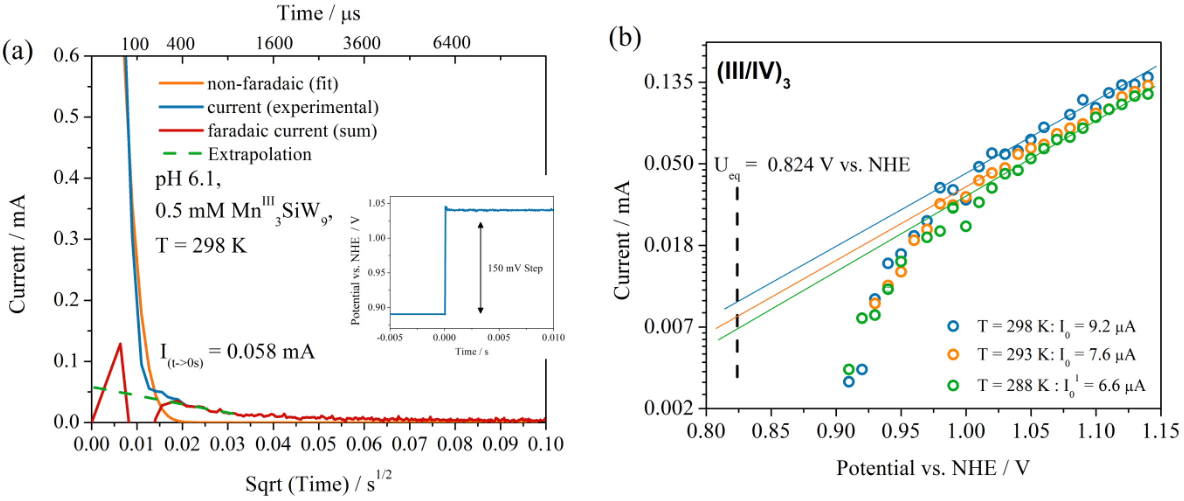

Figure 6.20 – (a) *Potentiostatic single pulse experiment for the oxidation of* **$Mn^{III}_3SiW_9$.** *The bottom ordinate shows the square-root of time while the top ordinate shows linear time. The applied potential program is shown in the inset.* **(b)** *Extrapolated faradaic currents at t ⟶ 0 s over the potential they were recorded at. Three temperatures were investigated. The graphs are taken from* [42].

The electron transfer constant k_0 is temperature dependent as can be seen in eqs. 2.39 and 2.40. The experimental results are able to reproduce the general dependence of k_0 on T, as seen in Table 6.2. This is also confirmed by a plot of the logarithmic electron transfer constant over inverse temperature which is shown in Fig. 6.21. The slope of the datapoints gives, according to eqs. 6.9 and 6.10, ΔG^* and therefore the reorganization energy λ.

The obtained slope can be converted to $\Delta G^* = 0.244\ eV$ which yields $\lambda \approx\ 0.976\ eV$. For comparison an extract of a table published by N. Hush will be given together with the result for **$Mn^{III}_3SiW_9$** in Table 6.3 [133]

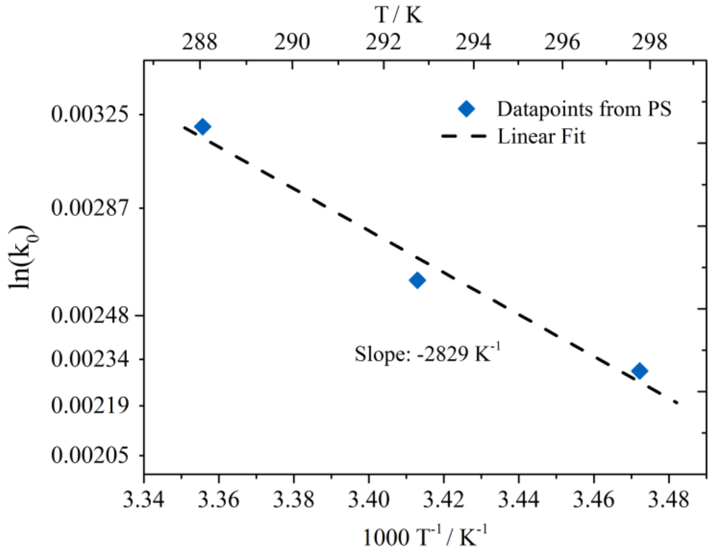

Figure 6.21 – *Logarithmic electron transfer constant* k_0 *over inverse temperature time times 1000. The data points were fitted linearly.*

Redox Couple	ΔG^***/ eV**	$k_0 / \, cm \, s^{-1}$
V^{3+}/V^{2+} *on Hg*	*0.377*	$4 \; 10^{-3}$
Cr^{3+}/Cr^{2+} *on Hg*	*0.542*	$1.4 \; 10^{-5}$
Mn^{3+}/Mn^{2+} *on Pt*	*0.425*	$6 \; 10^{-4}$
Fe^{3+}/Fe^{2+} *on Pt*	*0.373*	$5 \; 10^{-3}$
$Mn^{IV}{}_3/Mn^{III}{}_3$ *on GC*	*0.244*	$3 \; 10^{-3}$

Table 6.3 – *Experimental values for free energy barrier* ΔG^* *at 298 K. The upper four datasets are taken from* [133].

Looking at Table 6.3 it is apparent that the value determined for the Gibbs free energy of activation is on the correct order of magnitude. While ΔG^* for $\mathbf{Mn^{III}{}_3SiW_9}$ is slightly lower than for the fastest redox-couple in the list, Fe^{3+}/Fe^{2+}, its k_0 is slightly smaller. However, the former was also measured on a carbon electrode and not on a metal electrode and it was seen that Pt electrodes typically exhibit faster heterogeneous kinetics due to its metallic character, see chapter 4. N. Hush acknowledges that a non-catalyzed rate constant for the ferric/ferrous redox reaction should be slower than the one given in Table 6.3 [133].

While above comparison and discussion indicates that the determined ΔG^* is reasonable, it remains dubious whether the measurement is reliable. The chosen temperature range of *10 K* for the different three measurements is small. Larger temperature variations are however not practicable with the laboratory setup at hand. While higher temperatures are easily reached by the double jacketed glass cell, evaporation of supporting electrolyte increases the concentration of the polyoxoanion in solution, which leads to a systematic error. Also the linear fit performed in Fig. 6.21 seems arbitrary; certainly other functions could be used to fit the datapoints.

6.5 Summary and conclusions

In this chapter the electrochemistry of two tri-Mn substituted Keggin polyoxoanions, $\mathbf{Mn^{II}_3SiW_9}$ and $\mathbf{Mn^{III}_3SiW_9}$, was investigated. The dependence of the redox behavior of the two molecules on the composition of the supporting electrolyte, e.g. *pH* value, concentration of buffer and species of the buffer, was elucidated.

While a dependence on electrolyte is not uncommon for POMs, this study was the first to show that the bulk oxidation state has an influence on the redox behavior, too [37,236,246–250]. A plausible explanation for this previously unreported phenomenon is schematically shown in Fig. 6.17. As ligand exchange takes place in oxidation state Mn^{II}, $\mathbf{Mn^{II}_3SiW_9}$ releases its terminal water groups and replaces them with acetic acid groups. This changes the hydrodynamic radius of the polyoxoanion and after oxidation to Mn^{III} the interaction of the molecule with hydrophobic carbon is strong enough to allow for adsorption of $\mathbf{Mn^{II}_3SiW_9}$ on the electrode [42]. This hypothesis was supported by CV studies (Fig. 6.15) and potential dependent AFM micrographs (Fig. 6.16).

The number of transferred electrons between the different oxidation states Mn^{II}, Mn^{III} and Mn^{IV} was investigated with a two-pronged approach, combining electrochemistry and spectroscopy. CVs with variable scan-rate indicated that more than two electrons are released when $\mathbf{Mn^{III}_3SiW_9}$ is oxidized (Fig. 6.18). The missing current to three transferred electrons was attributed to a parallel pathway via adsorbed species. As an alternative experiment $\mathbf{Mn^{III}_3SiW_9}$ was simultaneously oxidized and reduced in two ionically connected half-cells (Fig. 6.19a). The electrons needed for reduction to Mn^{II} were provided by oxidation to Mn^{IV}. Coulomb counting revealed that more than three electrons per molecule were transferred, which can be explained by a small contribution of water oxidation. Recorded UV-Vis spectra confirmed that two new species were produced which had features clearly attributable to either Mn^{IV} or Mn^{II} polyoxoanions. Re-measuring the solutions after storing them for 24 hours in laboratory atmosphere yielded UV-Vis absorption spectra that were almost unchanged, which proofed the stability of the generated species.

Whether the (proton coupled) electron transfer associated with the oxidation of $\mathbf{Mn^{III}_3SiW_9}$ is a facile process or kinetically hindered was investigated with potential steps (Fig. 6.20). At $T = 298\ K$ an electron transfer constant of $k_0 = 3.3\ 10^{-3}\ cm\ s^{-1}$ was determined. This value is on the same order of magnitude as some facile transition metal redox couples like the ferrous/ferric couple on platinum (Table 6.3). Also, the reorganization energy was obtained via the temperature dependence of k_0. As the range of experimental temperatures was quite small ($10\ K$), the value of $\lambda \approx 0.976\ eV$ is not very reliable.

Chapter 7
Discussion

The previous chapters dealt with fundamental, electrochemical studies.
In chapter 5 the VO^{2+}/VO_2^+ redox reaction was investigated and the possibility of electrocatalysis by functional groups on MWCNTs was examined. Employing a novel characterization method, we were the first group to show conclusively that the exchange current density j_0 can't be increased by addition of surface functional groups.
In chapter 6 the reaction mechanism of two tri-manganese substituted polyoxoanions was explored. That study was the first study to elucidate the influence of the oxidation state of the active group on the redox behavior of POMs.

The aim of this concluding discussion is to consider the inferences that these electrochemical studies might have on future RFB systems.

The disproval of a catalytic effect for the slower half-cell reaction does not condemn future VRB system to remain low-power systems. However, remedies, e.g. increased electrode surface area, might entail other negative effects such as increased capital cost. In the first part of this discussion metrics for the VRB as archetype for all RFBs will be analyzed. The metrics are cost and performance. Of special interest are how these macroscopic, economic parameters depend on microscopic, electrochemical properties such as k_0 or U_0.
In a second part it will be discussed if the investigated POMs can be used as anolyte and catholyte for an All-POM RFB.
The third part will examine this hypothetical All-POM RFB, using the found physical and chemical properties of the polyoxoanions, by applying the metrics found for the VRB in terms of cost and performance.

7. 1 Metrics for Vanadium Redox Flow Batteries

Primary application for RFBs is large-scale electrical grid storage [31]. Peak-shaving, storing energy during periods of low demand and supplying electricity during periods of high demand, is one of the intended areas of operation. Also, RFBs could facilitate the grid integration of renewables such as wind and solar by improving their service reliability. Despite the lack of other large scale electricity storage systems and considerable research efforts, the practical implementation of RFBs is still hampered by cost and performance issues [251]. As RFBs are stationary systems, capital cost is arguably more critical than the performance metrics such as energy- and power density or efficiency. However, we will see how these performance parameters influence capital cost.
As a benchmark, the Advanced Research Projects Agency – Energy (ARPA-e) of the U.S. Department of Energy has announced $US\$ \ 100 \ kWh^{-1}$ installed as target for the VRB system [31].
A recent analysis by Zhang et al. showed that electrolyte (*37 %*) and cell stack (*31 %*) contribute most to the capital cost of a base case VRB [31]. The base case VRB stores $E = 12 \ MWh$ at an electrical power of $P = 1000 \ kW$. Other contributions to the total capital costs

of the base case VRB were [31]:

- Heat exchangers and pumps: *3 %*;
- Electrolyte tank costs: *8 %*;
- Power conditioning system and balance of plant : *21 %*.

Cell stack costs are dominated by membrane costs which were given as *US\$ 500* m^{-2}. The costs will drop in larger productions but will still represent a considerable percentage [252]. Electrolyte costs are mostly due to the costs for the vanadium, *US\$ 21* kg^{-1} of V_2O_5. The supporting electrolyte should not contribute to chemical costs, it was recently stated that aqueous electrolytes must be almost for free the achieve low-cost electrochemical energy storage [253].

Therefore, we would like to obtain values for the total area of cell surface A_{Total} as well as the required amount of redox active species as these are the two values that influence capital cost the most. This approach also illustrates one of the major advantages of RFBs in general: Power and energy are independently scalable which allows for flexibility. The cost of the former is represented by A_{Total} times the membrane costs, the cost of the latter by V_{Total} times the electrolyte concentration and the costs for the chemical species.

The power P of the RFB is:

$$P = N_C \, I \, \Delta U \, \eta \, (SOC^{max} - SOC^{min}) \tag{7.1}$$

With number of cells N_C, current I, cell potential ΔU, efficiency η and the operating range of the battery, which is given as the difference between the maximum state of charge (SOC) SOC^{max} and the minimum SOC^{min}.
Similarly one can define the energy content E via P and discharge time t_D:

$$E = P \, t_D = \frac{1}{2} n \, c \, F \, \Delta U \, \eta \left(SOC^{max} - SOC^{min}\right) V_{Total} \tag{7.2}$$

The current I, with surface roughness of electrodes ϑ, is defined as:

$$I = k_0 \, n \, F \, c \, A_{Cell} \, \vartheta \tag{7.3}$$

The total area A_{Total} is the product of N_C and A_{Cell}.

Therefore, once P and t_D are decided, A_{Total} and V_{Total} can be determined from physical and chemical parameters of the cell. As stated previously, A_{Total} and V_{Total} are responsible for most of the cost in a VRB and therefore we focus on them here.
The physical parameters for equations 7.1 – 7.3 were determined in previous chapters or are given in the literature.
The cell potential varies with SOC but an average value of $\Delta U = 1.3\ V$ for discharge can be assumed [254].
Overall efficiency for the VRB was given as $\eta = 0.91$ [31].

The upper limit for the SOC was given as $SOC^{max} = 0.8$ because higher cell voltages lead to an increased parasitic current due to the HER [255]. The HER has a higher U_0 than the V^{2+}/V^{3+} redox reaction but is kinetically hindered on carbon electrodes. The combination of high surface area electrodes and cathodic overpotentials can lead to a significant water reduction current which then reduces cell efficiency η and leads to an imbalance in the *SOC* of anolyte and catholyte.

The lower limit is usually assumed as $SOC^{min} = 0.2$, although no reason for this is given [31]. In a presentation held on 18th of November 2014 at the Nanyang Technological University, Singapore, Dr. Adam Whitehead, head of core component development of the Cellstrom GmbH acknowledged the problem of HER influencing the SOC^{max} but also stated that “the battery likes to be deep-discharged” [256]. Therefore, we will assume $SOC^{min} = 0.1$.

As both processes, V^{2+}/V^{3+} and VO^{2+}/VO_2^{+} are one-electron redox reactions, $n = 1$.

The concentration of vanadium ions, both in anolyte and catholyte is $c = 1.6\ mol\ L^{-1}$ [7,8].

As the slower half-cell reaction limits overall cell performance the effective activity is that of VO^{2+}/VO_2^{+} . The value for PRIST Nanocyl 3100 MWCNT is assumed as this sample combined good wetting behavior with the second highest activity of the analyzed samples. Therefore $k_0 = 1.7\ 10^{-6}\ cm\ s^{-1}$ [25].

For the roughness of the electrodes we assume $\vartheta = 50$.

These parameters, together with the results of equations 7.1 – 7.3 are given in Table 7.1:

Parameters All Vanadium RFB		
Specifications base case	**Physical parameters**	**Output**
$P = 1\ MW$	$\Delta U = 1.3\ V$	$A_{Total} = 9777\ m^2$
$t_D = 12\ h$	$\eta = 0.91$	$V_{Total} = 675.8\ m^3$
$N_C = 10$	$SOC^{max} = 0.8$	
	$SOC^{min} = 0.1$	
	$c = 1.6\ mol\ dm^{-3}$	
	$k_0 = 1.7\ 10^{-6}\ cm\ s^{-1}$	
	$\vartheta = 50$	

Table 7.1 – *List of variables and constants for the All Vanadium RFB system.*

The capital cost for vanadium and membrane can then be converted from A_{Total} and V_{Total}:

	Total capital cost / *US$*	**Normalized capital cost / *US$ kWh^{-1}***
Membrane:	$4.9\ 10^6$	*407.4*
Redox species (V_2O_5):	$4.1\ 10^6$	344.2

Table 7.2 – *Calculated costs for membrane and redox species of a 1000 kW VRB system. Prices of 500 US\$ m^{-2} and 21 US\$ kg^{-1} were assumed* [31].

From Table 7.2 it is obvious that with the assumed parameters the total capital costs for the base case *1000 kW* VRB system are much higher than the targeted *100 US* kWh^{-1}. While the set goal might be very ambitious [31], the membrane and redox species costs certainly have to be reduced significantly. Also, it has to be kept in mind that the costs for power converter and chemicals only amount to *68 %* of the total capital costs in the base case scenario. And

furthermore, that the membrane costs represent the majority of the power converter costs, but not all of it. Therefore, the normalized costs for the VRB can be estimated at roughly *1000 US$* kWh^{-1}.
Alternative electrochemical energy storage systems include Lead-acid batteries (*200-400 US$* kWh^{-1}) or *Li*-ion batteries (*600 - 2500 US$* kWh^{-1}) [257].

In our chapters 4 – 6 it was shown that electron transfer constants vary over several orders of magnitude, with the VO^{2+}/VO_2^+ system being one of the more sluggish redox couples. In Figure 7.1 it is evaluated how the capital cost for the membrane in the base case VRB changes with the electron transfer constant of the employed redox couple. An increase of activity by two orders of magnitude would make a significant reduction of power converter size and therefore membrane size viable.

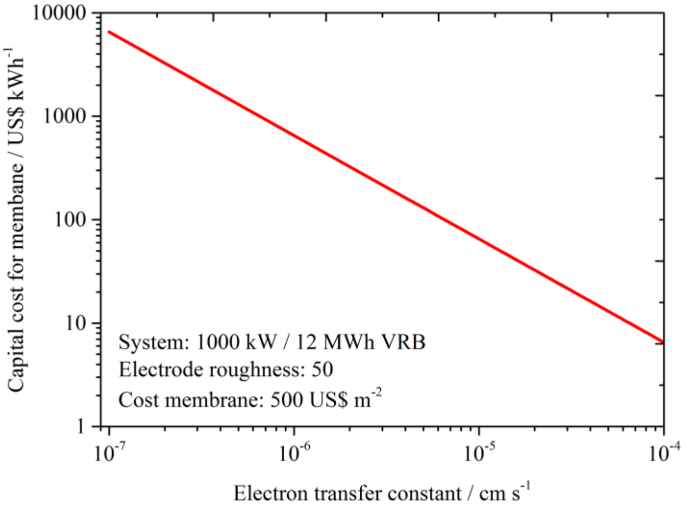

Figure 7.1 – *Calculated capital cost for the membrane of a vanadium RFB in dependence on the electron transfer constant of redox species. All other parameters as given in Table 7.1.*

As a conclusion to this rough capital cost analysis of VRBs it can be said that by changing one parameter the goal of ARPA-e cannot be reached, which is in agreement with the more detailed study by Zhang et al. [31]. Many of the parameters in Table 7.1 are already at a very competitive value, e.g. an efficiency of $\eta = 0.91$ can be considered as satisfying. It is dubious if the chemical costs, one of the two big contributions to total costs, can be reduced much further. This weak point of the VRB was earlier identified by the group of Michael J. Aziz who favored replacement of vanadium with much cheaper quinones [30].
The electron transfer kinetics of the catholyte were identified as the most promising parameter to lower capital costs as k_0 ranges over several orders of magnitude and it has direct influence on the required size of the power converter.

7.2 Tri-Manganese substituted polyoxoanions for Redox Flow Batteries

As seen in the previous section the VRB will be hard pressed to reach the capital costs goal set by ARPA-e. One possible way to potentially reach this target for future RFBs is to replace the vanadium ions altogether, in the light of the non-catalyzable VO^{2+}/VO_2^+ redox reaction that was detected in chapter 5 of this work [14].
From the power-cost point of view the substituting electron-shuttles should be chosen for their fast electron transfer kinetics, as demonstrated in Fig. 7.1. From an energy-cost perspective the new molecules should consist of abundant and inexpensive elements and should be soluble in aqueous electrolytes [253]. Multiple redox-reactions per molecule are also be beneficial, as it increases *n*.
From these requirements, it can be deducted that POMs can be a good candidate as electron shuttle for a future RFB. In this section we will first investigate whether the polyoxoanions that were thoroughly investigated in chapter 6 exhibit the required properties to be employed in an All-POM RFB. Afterwards, it will be analyzed how the introduction of POMs could alter the total capital costs of a system, using the metrics developed in section 7.1.

A possible design for such an All-POM RFB is shown in Fig. 7.2. Catholyte and anolyte will be analyzed in the next sections. Assuming a concentration of *1 M* of POM and six electrons per molecule, as well a cell voltage of *1.3 V*, the energy density of the electrolyte would be *210 Wh L*$^{-1}$.

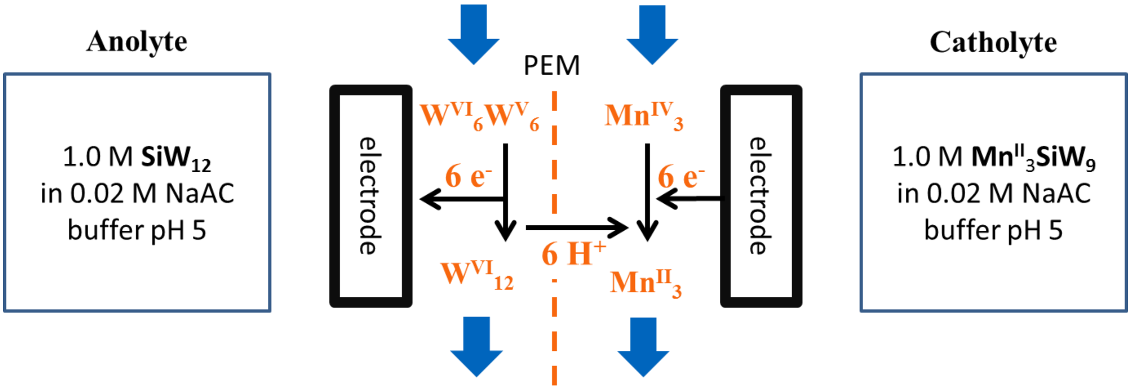

Figure 7.2 – *Schematic of an All-POM RFB employing the Keggin-type polyoxoanions presented in chapter 6. The drawn reactions represent the discharge of the battery.*

7.2.1 Suitability of tri-Manganese substituted polyoxoanions as catholyte

Before a new redox-molecule can be employed as electrolyte in a RFB, its behavior has to be fully understood. This fundamental understanding for $\mathbf{Mn^{II}_3SiW_9}$ and $\mathbf{Mn^{III}_3SiW_9}$ has been acquired in chapter 6. Aim of this section is to investigate whether tri-Mn substituted Keggin polyoxoanions are suitable as catholyte for operation in a RFB.

There are some prerequisites for a redox-couple to be applied in real-life application as RFB electrolyte:

- Stability of the molecule in all oxidation states;
- Suitability for high power density;
- Suitability for high energy density.

The first item on the list, stability of the molecule in all oxidation states, is certainly very important. A redox-ion that spontaneously changes its oxidation state has a detrimental effect on the overall efficiency. This is especially important for the *Mn*-ion substituted POMs as a disproportion reaction for Mn^{III} ions is a common phenomenon [258].
In contrast to that, the stability of $\mathbf{Mn^{II}{}_3SiW_9}$ and $\mathbf{Mn^{III}{}_3SiW_9}$ in all oxidation states seems to be excellent. The UV-Vis spectra (Fig. 6.19b) showed only minimal changes after storing the electrolytes containing species in oxidation states $Mn^{II}{}_3$, $Mn^{III}{}_3$ and $Mn^{IV}{}_3$ in laboratory atmosphere for 24 hours. It can be speculated that this is a direct consequence of the encountered PCET and CCET mechanisms, because coupled proton (cation)-electron transfer "…provides reaction pathways in which electrons and protons are transferred simultaneously avoiding high energy intermediates" [235]. Thus, PCET and CCET are of utmost importance for successful energy conversion strategies in biological systems. However, above statement is only valid in low concentrations of buffer (~ *0.02 M*). It was seen that in higher concentrations of buffer (*1.0 M*) the CVs change and irreversible adsorption and probably decomposition of the polyoxoanions at the working electrode take place. Also, investigated concentrations of $\mathbf{Mn^{II}{}_3SiW_9}$ and $\mathbf{Mn^{III}{}_3SiW_9}$ were always below *1 mM*. Nevertheless, it can be stated that the found stability of the polyoxoanions qualifies them for the application in RFBs. This is especially true if one remembers that also the benchmark system, the VRB, has stability issues: At elevated temperatures (T > 40 ℃) V_2O_5 precipitates while low temperatures (T > 5 ℃) entail a low solubility of VO^{2+}[259]. To mitigate this effect mixed acid solutions, containing $2.5\ M\ H_2SO_4$ and *6 M HCl,* can be employed, however, they might lead to corrosion issues [172].

A point related to efficiency is the cross-over of molecules through the membrane. One of the advantages of VRBs is that penetration of the separating membrane by ions does not lead to a chemical contamination. Since the investigated POMs are significantly larger than *V*-ions, they might not as easily cross through the separator which would increase efficiency.

In Section 7.1 it was stated that one of the main problems of the VRB is the sluggish $VO^{2+}/VO_2{}^+$-reaction with an electron transfer constant of $k_0 = 3\ 10^{-7}\ cm\ s^{-1}$ on GC [14]. The electron transfer constant that was obtained for the oxidation of $\mathbf{Mn^{III}{}_3SiW_9}$ was 10^4 times higher than above value. This makes an All-POM RFB suitable for high-power applications, without the need for a catalyst as discussed for VRBs. Facile kinetics have numerous advantages for RFBs, besides the possibility to charge or discharge with high currents. Fast reaction kinetics reduce overpotentials which in turn promotes high voltage efficiency. Furthermore, electrode areas can be designed smaller and therefore smaller, cheaper power converters can be designed, as shown in Fig. 7.1.

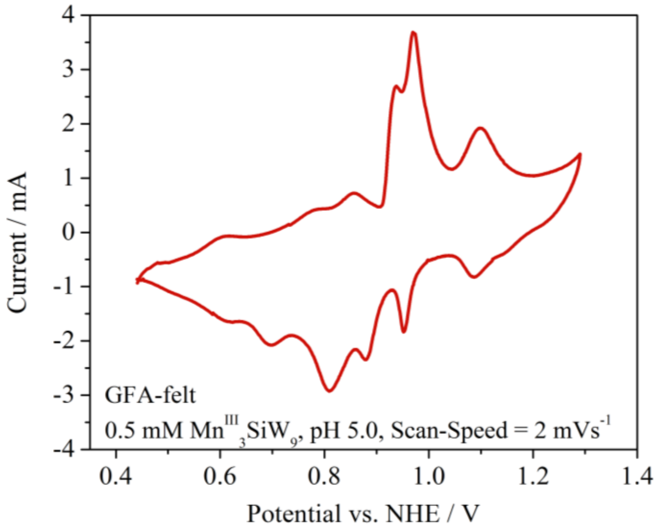

Figure 7.3 – *CV of* $\mathbf{Mn^{III}_3SiW_9}$ *recorded in the h-type cell on a high surface area, porous carbon felt electrode. The graph is taken from* [42].

As seen in eq. 7.2, suitability for high energy density can be estimated from several physical parameters. For tri-*Mn* substituted polyoxoanions it was established that they transfer six electrons per molecule, therefore $n = 6$. This is six times higher than for the *V*-ion.
As the cell-potential enters eqs. 7.1 and 7.2 the potential of electron transfer should be as high as possible for a catholyte. $\mathbf{Mn^{III}_3SiW_9}$ transfers its six electrons at various potentials, as shown by a CV of $\mathbf{Mn^{III}_3SiW_9}$ on a porous, high surface-area carbon felt GFA electrode, Fig. 7.3. The features of the CV can be explained by a combination of the reaction pathways for $\mathbf{Mn^{II}_3SiW_9}$ and $\mathbf{Mn^{III}_3SiW_9}$ [42]. While these electron transfers are partly pH dependent, at pH 5 an average equilibrium potential $\overline{U}_0 = 0.9\ V\ vs.\ NHE$ can be assumed. The maximum concentration of $\mathbf{Mn^{II}_3SiW_9}$ or $\mathbf{Mn^{III}_3SiW_9}$ could not be determined yet due to the limited amount of species obtained for electrochemical testing. However, for Keggin ions a concentration of $1\ mol\ L^{-1}$ was mentioned [36].

Therefore, it can be concluded that tri-Mn substituted Keggin polyoxoanions possess all the fundamental properties to function as redox-molecule in a RFB. They are stable, exhibit fast reaction kinetics and transfer six electrons per molecules.

7.2.2 Suitability of Keggin-type ions as anolyte

It seems much easier to find molecules that transfer electrons at a low potential and are therefore suitable for an anolyte, than identifying candidates for catholytes.
There are many Keggin-type ions to choose from. The heteroatom can be *Si, P, As, Ge,* with *W* or *Mo* as addenda ions [225]. These variations lead to altered redox properties which can be utilized to adjust parameters such as SOC^{min} or ΔU. As seen in chapter 6, the standard Keggin ions employed in our studies, $\mathbf{SiW_{12}}$, transfers six electrons at a suitably low potential. From Fig. 6.2 $\overline{U}_0$ can be determined to $-\ 0.3\ V\ vs.\ NHE$ at *pH 5.4*. With the solubility of $1\ mol\ L^{-1}$ given in the literature the usage of $\mathbf{SiW_{12}}$ from an energy point of view is viable [36].
While we did not study the kinetics of the electron transfer reactions of $\mathbf{SiW_{12}}$ in detail, from CVs and also from the proposed mechanism, delocalization of electrons on *W*-ions, it is clear that k_0 is high. Peak separation close to the theoretical limit of *59 mV* was observed at a scan-rate of $25\ mV\ s^{-1}$ [67].
Stability of reduced species is of some concern. Just like the V^{2+}-ion, the reduced forms are prone to oxidation in air [12]. However, as in the VRB, this can be solved by blanketing with inert gases.

Therefore, it can be concluded that Keggin-type ions possess all the required properties to be employed as anolyte in a RFB.

7.2.3 Costs analysis for an All-POM RFB

While the VRB has not reached full maturity yet, there are a lot of demonstrator projects and even some commercial systems in place [256]. In order to replace the VRB, the All-POM RFB has to be superior to the former, in performance as well as in capital cost. This section estimates the costs for an All-POM RFB based on the physical parameters found in chapter 6 and the metrics developed in section 7.1.
Again, a hypothetical energy storage system with $P = 1\ MW$ and $E = 12\ MWh$ is taken as scenario. The list of parameters together with the output of eq. 7.1 – 7.3 is given in table 7.3:

Parameters All-POM RFB		
Specifications base case	**Physical parameters**	**Output**
$P = 1\ MW$	$\Delta U = 1.3\ V$	$A_{Total} = 1.26\ m^2$
$t_D = 12\ h$	$\eta = 0.91$	$V_{Total} = 180.2\ m^3$
$N_C = 10$	$SOC^{max} = 0.8$	
	$SOC^{min} = 0.1$	
	$c = 1.0\ mol\ dm^{-3}$	
	$k_0 = 3.3\ 10^{-3}\ cm\ s^{-1}$	
	$\vartheta = 50$	

Table 7.3 – *List of variables and constants for the All-POM RFB system.*

The cell potential is assumed as $\Delta U = 1.3\ V$. While the subtraction of the two $\overline{U}_0$ yields 1.4 V, we took ΔU to be slightly smaller because overpotentials might diminish the useable voltage during discharge. Also there might be losses when converting the voltage, as discharge takes place at different plateaus due to the various electron transfer steps.
As the electrolyte is less acidic and therefore the HER takes place at lower potential, SOC^{max} might actually be larger. However, the estimation was chosen to be conservative.
As rate determining electron constant the value found for the oxidation of $\mathbf{Mn^{III}{}_3SiW_9}$ $k_0 = 3.3\ 10^{-3}\ cm\ s^{-1}$ was assumed [42]
As predicted in Fig. 7.1, the swift redox reaction makes a much smaller power converter design viable and A_{Total} is almost *5* orders of magnitude smaller than in the VRB case which also reduces the capital costs for this component.
The reduction in electrolyte volume V_{Total} is much smaller. In the case of the All-POM RFB as envisioned here, the tanks can be *3.8* times smaller than for a VRB with the same specifications.

	Total capital cost / *US$*	**Normalized capital cost / *US$ kWh^{-1}***
Membrane:	*632.1*	*0.053*
Redox species (*MnO_2, WO_3*):	*$5.7\ 10^6$*	477.6

Table 7.4 – *Calculated costs for membrane and redox species of a 1000 kW All-POM RFB. Prices of 500 US\$ m^{-2} and 31.8 US\$ mol^{-1} of* $\mathbf{Mn^{II}{}_3SiW_9}$ *were assumed* [31].

For a total capital cost calculation similar to the one performed for the VRB, the chemical costs need to be estimated. As neither $\mathbf{Mn^{II}{}_3SiW_9}$ nor $\mathbf{Mn^{III}{}_3SiW_9}$ can be purchased, a price in *US\$ kg^{-1}* based on the single components was estimated. A similar method is applied for electrolyte production for VRBs, which sees procurement of the low cost V_2O_5 and its subsequent conversion to V^{2+},V^{3+}, VO^{2+} and VO_2^{+}.
Battery grade manganese dioxide can be purchased for *US\$ 1800 – 1950 (1000 kg)$^{-1}$* [260]. The price for tungsten trioxide was roughly *US\$ 15 kg^{-1}* in *2012* [261]. In comparison to the other two components the contribution of *Si* can be neglected. With these values a rough molar price for $\mathbf{Mn^{II}{}_3SiW_9}$ can be estimated at *31.8 US\$ mol^{-1}*. Of course this optimistic scenario assumes that the synthesis of $\mathbf{Mn^{II}{}_3SiW_9}$ from raw materials can be performed for free. As many POM synthesis processes are one-pot synthesis, this assumption is valid for the moment [262].
The results for total capital cost and normalized capital cost for membrane and redox species are given in Table 7.4. It can be seen that due to the fast electron transfer kinetics the cost for the membrane diminished to less than *1 US\$* per *kWh*. However, the chemical costs increased slightly by *39 %* compared to the VRB. This increase stems from the relatively high cost for the heavy WO_3.

As a final conclusion it can be said that an All-POM RFB with $\mathbf{SiW_{12}}$ as anolyte and $\mathbf{Mn^{II}{}_3SiW_9}$ as catholyte is viable from an electrochemical point of view. From an economical perspective, the All-POM RFB as envisioned might be less expensive than the VRB, due to the higher electron transfer rates that can be achieved by the POMs. However, the difference in capital cost might not be significant enough to warrant replacement of the established VRB system. The employed chemicals for the novel RFB are too expensive at the moment.

Chapter 8

Outlook

In the previous chapter the capital cost of VRBs and a hypothetical All-POM RFB were analyzed.

For the VRB it was shown that the capital cost is higher than targeted by the ARPA-e, and that sluggish electron transfer kinetics are at least partly responsible for the high price. We showed in chapter 5 that the redox-reaction cannot be catalyzed by a strategy that was commonly suggested in previous studies: addition of functional groups [14]. Supported by other studies [27,263], this means that the VRB will have to work around the sluggish kinetics, by large power converter area, until a working catalyst is found.

Using the number of publications and patents as measure, the scientific interest in VRBs is continuously growing. Figure 8.1 shows the results of a Google scholar query for the keywords "vanadium", "redox" and "flow" listed by year of publication.

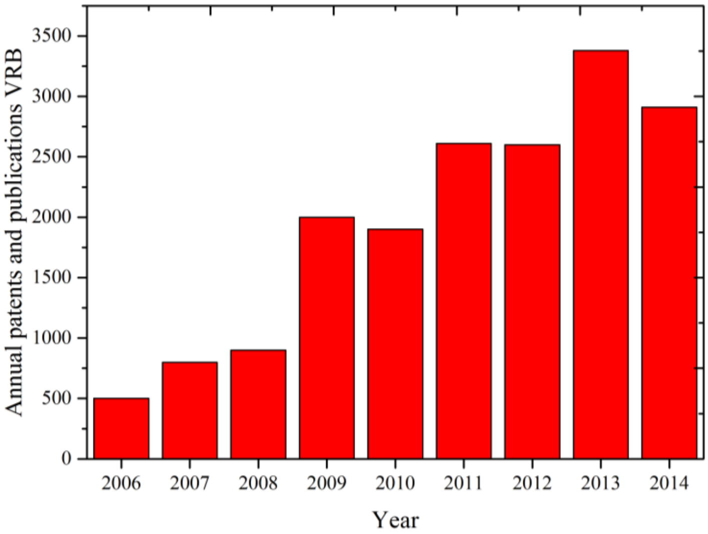

Figure 8.1 – *Results of a Google scholar search for keywords "vanadium", "redox" and "flow" accessed on 10th December 2014.*

At the same time development of energy storage plants based on the VRB technology is well under way [256]. It was said that RFBs are a technology of the 21st century and until there is a more suitable redox system found, the VRB will be the system that is being mostly explored and built. A number of examples for new approaches were mentioned in the introduction [29,30,32,34,264]. In chapter 7 of this work, using electrochemical information obtained in chapter 6, it was investigated if an All-POM RFB using $\mathbf{SiW_{12}}$ as anolyte and $\mathbf{Mn^{II}{}_3SiW_9}$ could be such a more suitable system.

While the investigated POMs possess the required properties for an electron shuttle, stability, multiple electrons per molecules and fast electron transfer kinetics, they cannot compete with the *V*-ion from a cost perspective. However, as POMs offer intrinsic advantages for energy storage applications, high electron transfer rates and multiple redox reactions per molecule, research in this area should be continued. $\mathbf{Mn^{II}{}_3SiW_9}$ and $\mathbf{Mn^{III}{}_3SiW_9}$ were first trials that turned out to show interesting electrochemical behavior [42].

To find a more suitable POM for the application in a RFB, a wide range of molecules should be examined. Also it seems desirable to use computational means to create new, rational synthesis procedures [154]. As high k_0 can be expected for most POMs due to their small solvent reorganization energy, the two parameters that should be optimized are cost and number of transferred electrons n.

For example, MoO_3 costs $20\ US\$\ kg^{-1}$, which is comparable to $15\ US\$\ kg^{-1}$ for WO_3 [261,265]. Due to the lower weight of the former transition metal, however, the price per mole for a $[Mn^{II}_3(OH)_3(H_2O)_3SiMo_9O_{34}]^{7-}$, provided it can be synthesized, would drop to 20.25 $US\$\ mol^{-1}$. This is only *63 %* of the molar cost for $\mathbf{Mn^{II}_3SiW_9}$, as estimated in section 7.2.3.

Besides *Mo* and *W*, also *V*, *Nb*, *U* and *Pd* can be used as building block for the synthesis of POMs [262]. Vanadium, much cheaper and lighter than *W* or *Mo*, might indeed be the future of RFBs, albeit not in the existing VRB but as major component in a novel All-POM RFB that utilizes the superior kinetics of POMs to its advantage.

A relatively small molecule that can transfer many electrons is the heteropolyoxopalladate $[Pd^{II}_{13}As^{V}_8O_{34}(OH)_6]^{8-}$ [266]. This nanocube, with an edge length of *1 nm* can be reduced at GC electrodes, converting almost all Pd^{2+} to Pd^0. While this reduction is irreversible, and Palladium is of course much too expensive for RFBs, it shows that the heterpolyoxopalladate can shuttle close to *26* electrons. A similar molecule, consisting of a another metal and undergoing a reversible redox-reaction, could be a very good electron shuttle for RFBs.

The POMs investigated in this work were not initially designed to function as electron shuttle. Target-oriented, rational synthesis and screening of the vast library of existing POMs should be started to find suitable candidates for anolyte and catholyte.

Chapter 9
Bibliography

[1] International Energy Agency. MEDIUM-TERM Oil Market Report. 4th ed. Paris: 2009.

[2] International Energy Agency. Tracking Clean Energy Progress. Paris: 2012.

[3] Friedl J, Stimming U. The Importance of Electrochemistry for the Development of Sustainable Mobility. In: Bruhns H, editor. Energ. Forsch. und Konzepte, Arbeitskreis Energie (AKE) in der Deutschen Physikalischen Gesellschaft; 2014.

[4] International Energy Agency. World Energy Outlook. 2011.

[5] Chu S. Meeting the energy and Climate Change Challenge. In: Bruhns H, editor. Energ. Technol. und Energiewirtschaft, Arbeitskreis Energie (AKE) in der Deutschen Physikalischen Gesellschaft; 2014.

[6] Chu S, Majumdar A. Opportunities and challenges for a sustainable energy future. Nature 2012;488:294–303.

[7] Weber AZ, Mench MM, Meyers JP, Ross PN, Gostick JT, Liu Q. Redox flow batteries: a review. J Appl Electrochem 2011;41:1137–64.

[8] Ponce de Leon C, Friasferrer A, Gonzalezgarcia J, Szanto D, Walsh F. Redox flow cells for energy conversion. J Power Sources 2006;160:716–32.

[9] Skyllas-Kazacos M, Chakrabarti MH, Hajimolana SA, Mjalli FS, Saleem M. Progress in Flow Battery Research and Development. J Electrochem Soc 2011;158:R55–79.

[10] Skyllas-Kazacos M, Rychcik M, Robins RG, Fane AG. New All-Vaadium Redox Flow Cell. J Electrochem Soc 1986:1057–8.

[11] Skyllas-Kazacos M, Grossmith F. Efficient vanadium redox flow cell. J Electrochem Soc 1987;134:2950–4.

[12] Weber AZ, Mench MM, Meyers JP, Ross PN, Gostick JT, Liu Q. Redox flow batteries: a review. J Appl Electrochem 2011;41:1137–64.

[13] Chakrabarti MH, Brandon NP, Hajimolana S a., Tariq F, Yufit V, Hashim M a., et al. Application of carbon materials in redox flow batteries. J Power Sources 2014;253:150–66.

[14] Friedl J, Bauer CM, Rinaldi A, Stimming U. Electron transfer kinetics of the VO2+/VO2+ Reaction on multi-walled carbon nanotubes. Carbon N Y 2013;63:228–39.

[15] McCreery RL. Advanced Carbon Electrode Materials for Molecular Electrochemistry. Chem Rev 2008;108:2646–87.

[16] Pumera M. Voltammetry of carbon nanotubes and graphenes: excitement, disappointment, and reality. Chem Rec 2012;12:201–13.

[17] Punckt C, Pope M, Aksay I. High Selectivity of Porous Graphene Electrodes Solely due to Transport and Pore Depletion Effects. J Phys Chem C 2014.

[18] Zhu HQ, Zhang YM, Yue L, Li WS, Li GL, Shu D, et al. Graphite–carbon nanotube composite electrodes for all vanadium redox flow battery. J Power Sources 2008;184:637–40.

[19] Yue L, Li W, Sun F, Zhao L, Xing L. Highly hydroxylated carbon fibres as electrode materials of all-vanadium redox flow battery. Carbon N Y 2010;48:3079–90.

[20] Li W, Liu J, Yan C. Multi-walled carbon nanotubes used as an electrode reaction catalyst for /VO2+ for a vanadium redox flow battery. Carbon N Y 2011;49:3463–70.

[21] Gao C, Wang N, Peng S, Liu S, Lei Y, Liang X, et al. Influence of Fenton's reagent treatment on electrochemical properties of graphite felt for all vanadium redox flow battery. Electrochim Acta 2013;88:193–202.

[22] González Z, Botas C, Blanco C, Santamaría R, Granda M, Álvarez P, et al. Thermally reduced graphite and graphene oxides in VRFBs. Nano Energy 2013;2:1322–8.

[23] Li W, Liu J, Yan C. Graphite–graphite oxide composite electrode for vanadium redox flow battery. Electrochim Acta 2011;56:5290–4.

[24] Punckt C, Pope MA, Aksay IA. On the Electrochemical Response of Porous Functionalized Graphene Electrodes. J Phys Chem C 2013;117:16076–86.

[25] Gattrell M, Park J, MacDougall B, Apte J, McCarthy S, Wu CW. Study of the Mechanism of the Vanadium 4+/5+ Redox Reaction in Acidic Solutions. J Electrochem Soc 2004;151:A1–25.

[26] Bourke A, Lynch RP, Buckley DN. Effect of Electrode Pretreatment on the Cyclic Voltammetry of VO2+/VO2+ at a Glassy Carbon Electrode. ECS Trans 2013;53:59–67.

[27] Melke J, Jakes P, Langner J, Riekehr L, Kunz U, Zhao-Karger Z, et al. Carbon Materials for the positive electrode in all-Vanadium Redox Flow Batteries. Carbon N Y 2014.

[28] Gao S, Cao R, Li X. Self-assembly of Keggin-type tungstoborate-based multilayer films and their electrochemical behavior. Thin Solid Films 2006;500:283–8.

[29] Pratt HD, Rose AJ, Staiger CL, Ingersoll D, Anderson TM. Synthesis and characterization of ionic liquids containing copper, manganese, or zinc coordination cations. Dalton Trans 2011;40:11396–401.

[30] Huskinson B, Marshak MP, Suh C, Er S, Gerhardt MR, Galvin CJ, et al. A metal-free organic-inorganic aqueous flow battery. Nature 2014;505:195–8.

[31] Zhang M, Moore M, Watson JS, Zawodzinski T a., Counce RM. Capital Cost Sensitivity Analysis of an All-Vanadium Redox-Flow Battery. J Electrochem Soc 2012;159:A1183–8.

[32] Yang B, Hoober-Burkhardt L, Wang F, Surya Prakash GK, Narayanan SR. An Inexpensive Aqueous Flow Battery for Large-Scale Electrical Energy Storage Based on Water-Soluble Organic Redox Couples. J Electrochem Soc 2014;161:A1371–80.

[33] Duduta M, Ho B, Wood VC, Limthongkul P, Brunini VE, Carter WC, et al. Semi-Solid Lithium Rechargeable Flow Battery. Adv Energy Mater 2011;1:511–6.

[34] Huang Q, Li H, Grätzel M, Wang Q. Reversible chemical delithiation/lithiation of LiFePO4: towards a redox flow lithium-ion battery. Phys Chem Chem Phys 2013;15:1793–7.

[35] Friedl J, Bauer C, Al-Oweini R, Yu D, Kortz U, Hoster H, et al. Investigation on Polyoxometalates for the Application in Redox Flow Batteries. 222nd Meet. ECS, 2012.

[36] Pratt HD, Hudak NS, Fang X, Anderson TM. A polyoxometalate flow battery. J Power Sources 2013;236:259–64.

[37] Bi L-H, Kortz U, Nellutla S, Stowe AC, van Tol J, Dalal NS, et al. Structure, Electrochemistry, and Magnetism of the Iron(III)-Substituted Keggin Dimer, [Fe 6 (OH) 3 (A- α - GeW 9 O 34 (OH) 3) 2] 11-. Inorg Chem 2005;44:896–903.

[38] Proust A, Matt B, Villanneau R, Guillemot G, Gouzerh P, Izzet G. Functionalization and post-functionalization: a step towards polyoxometalate-based materials. Chem Soc Rev 2012;41:7605–22.

[39] Al-Oweini R, Bassil BS, Friedl J, Kottisch V, Ibrahim M, Asano M, et al. Synthesis and characterization of multinuclear manganese-containing tungstosilicates. Inorg Chem 2014;53:5663–73.

[40] Wang H, Hamanaka S, Nishimoto Y, Irle S, Yokoyama T, Yoshikawa H, et al. In operando X-ray absorption fine structure studies of polyoxometalate molecular cluster batteries: polyoxometalates as electron sponges. J Am Chem Soc 2012;134:4918–24.

[41] Marcus RA. Elektronentransferreaktionen in der Chemie - Theorie und Experiment (Nobel-Vortrag). Angew Chemie 1993;8:1161–72.

[42] Friedl J, Al-Oweini R, Herpich M, Keita B, Kortz U, Stimming U. Electrochemical studies of tri-manganese substituted Keggin Polyoxoanions. Electrochim Acta 2014;141:357–66.

[43] Trasatti S. The concept and physical meaning of absolute electrode potential: A reassessment. J Electroanal Chem 1982;139:1–13.

[44] Gerischer H, Ekardt W. Fermi levels in electrolytes and the absolute scale of redox potentials. Appl Phys Lett 1983;3:393–5.

[45] Lang N, Kohn W. Theory of metal surfaces: work function. Phys Rev B 1971;3:1215–23.

[46] Lang N. The density-functional formalism and the electronic structure of metal surfaces. Solid State Phys 1974;28:225–96.

[47] International Union of pure and applied Chemistry. Standard Potentials in Aqueous Solution. New York: CRC Press; 1985.

[48] Zwolinski BJ, Marcus RJ, Eyring H. Inorganic oxidation-reduction reactions in solution. Chem Rev 1955;55:157–80.

[49] Trasatti S. Surface science and electrochemistry: concepts and problems. Surf Sci 1995;335:1–9.

[50] Trasatti S. Systematic trends in the crystal face specificity of interfacial parameters: The cases of Ag and Au. J Electroanal Chem 1992;329:237–46.

[51] Hurth CM. Scanning Probe Microscopy Studies of Active Enzymes at Solid Surfaces, Dissertation. The University of Texas at Austin, 2005.

[52] Gouy M. Sur la constitution de la charge electrique a la surface d’un electrolyte. J Phys Theor Appl 1910;9:457.

[53] Chapman D. A contribution to the theory of electrocapillarity. Philos Mag 1913;25:475.

[54] Vetter KJ. Electrochemical Kinetics - Theoretical and Experimental Aspects. English Ed. New York/London: Academic Press Inc.; 1967.

[55] Bockris JO, Devanathan MAV, Mueller K. On the structure of charged interfaces. Proc R Soc Lond A Math Phys Sci 1963;274:55–79.

[56] Leese H, Mattia D. Electroosmotic flow in nanoporous membranes in the region of electric double layer overlap. Microfluid Nanofluidics 2013;16:711–9.

[57] Stern-Hamburg O. Zur Theorie der elektrolytischen Doppelschicht. Zeitschrift Fuer Elektrochemie 1924;30:508.

[58] Freise V. Zur Theorie der diffusen Doppelschicht. Zeitschrift Für Elektrochemie 1952;41:822–7.

[59] Grahame DC. The Electrical Double Layer and the Theory of Elecrocapillarity. Chem Rev 1947;41:441–501.

[60] Grahame DC. Diffuse Double Layer Theory for Electrolytes of Unsymmetrical Valence Types. J Chem Phys 1953;21:1054.

[61] Macdonald JR, Barlow C a. Theory of Double-Layer Differential Capacitance in Electrolytes. J Chem Phys 1962;36:3062.

[62] Parsons R. The rate of electrolytic Hydrogen evolution and the heat of adsorption of Hydrogen. Trans Faraday Soc 1958;54:1053–63.

[63] Rampolla RW, Miller RC, Smyth CP. Microwave Absorption and Molecular Structure in Liquids. XXV. Measurements of Dielectric Constant and Loss at 3.1-mm Wavelength by an Interferometric Method. J Chem Phys 1959;30:566–73.

[64] Stillinger FH, Kirkwood JG. Theory of the Diffuse Double Layer. J Chem Phys 1960;33:1282.

[65] Bazant MZ, Storey BD, Kornyshev A a. Double Layer in Ionic Liquids: Overscreening versus Crowding. Phys Rev Lett 2011;106:046102.

[66] Kornyshev AA. Double-layer in ionic liquids: paradigm change? J Phys Chem B 2007;111:5545–57.

[67] Bard A, Faulkner L. Electrochemical methods: Fundamentals and Applications. Second. New York: John Wiley and Sons; 2001.

[68] Ramette R. Outmoded terminology: The normal hydrogen electrode. J Chem Educ 1987;64:55057.

[69] Butler J. The mechanism of overvoltage and its relation to the combination of hydrogen atoms at metal electrodes. Trans Faraday Soc 1932;1428:379–82.

[70] Butler JA. Studies in heterogeneous equilibria. Trans Faraday Soc 1924;19:734.

[71] Erdey-Gruz T, Volmer M. The theory of hydrogen overvoltage. Zeitschrift Für Phys Chemie 1930;150 A:203.

[72] Schmickler W, Vielstich W. Electron transfer rates in the levich and dogonadze theory of redox reactions. Electrochim Acta 1973;18:883–8.

[73] Gurney RW. The Quantum Mechanics of Electrolysis. Proc R Soc A Math Phys Eng Sci 1931;134:137–54.

[74] Gerischer H. Über den Ablauf von Redoxreaktionen an Metallen und an Halbleitern. Zeitschrift Für Phys Chemie 1960;26:223–47.

[75] Marcus RA. Exchange reactions and electron transfer reactions including isotopic exchange. Theory of oxidation-reduction reactions involving electron transfer. Part 4.-A statistical-mechanical basis for treating contributions from solvent, ligands, and inert salt. Discuss Faraday Soc 1960;29:21–31.

[76] Wilkinson A, McNaught A. IUPAC Compendium of Chemical Terminology, (the“Gold Book”). International Union of Pure and Applied Chemistry; 1997.

[77] Marder MP. Condensed Matter Physics. 2nd ed. Hoboken: John Wiley & Sons, Inc.; 2010.

[78] Koval CA, Howard JN. Electron transfer at semiconductor electrode-liquid electrolyte interfaces. Chem Rev 1992;92:411–33.

[79] Bockris JO, Reddy AKN. Modern electrochemistry. 2nd ed. New York, Boston, Dordrecht, London, Moscow: Kluwer Academic Publishers; 2002.

[80] Anderson TN, Eyring H. Principles of Electrode Kinetics. In: Eyring H, editor. Phys. Chem. An Adv. Treatise. Vol. IXA Electrochem., New York/London: Academic Press; 1970, p. 247–340.

[81] Friedl J, Stimming U. Model catalyst studies on hydrogen and ethanol oxidation for fuel cells. Electrochim Acta 2013;101:41–58.

[82] Conway BE, Bockris JO. Electrolytic hydrogen evolution kinetics and its relation to the electronic and adsorptive properties of the metal. J Chem Phys 1957;26:532.

[83] Dahms H, Bockris JO. The Relative Electrocatalytic Activity of Noble Metals in the Oxidation of Ethylene. J Electrochem Soc 1964;111:728.

[84] Friedrich K., Henglein F, Stimming U, Unkauf W. Size dependence of the CO monolayer oxidation on nanosized Pt particles supported on gold. Electrochim Acta 2000;45:3283–93.

[85] Maillard F, Eikerling M, Cherstiouk O V., Schreier S, Savinova E, Stimming U. Size effects on reactivity of Pt nanoparticles in CO monolayer oxidation: The role of surface mobility. Faraday Discuss 2004;125:357.

[86] Maillard F, Savinova ER, Stimming U. CO monolayer oxidation on Pt nanoparticles: Further insights into the particle size effects. J Electroanal Chem 2007;599:221–32.

[87] Gasteiger HA, Panels JE, Yan SG. Dependence of PEM fuel cell performance on catalyst loading. J Power Sources 2004;127:162–71.

[88] Neyerlin KC, Gu W, Jorne J, Gasteiger HAA. Study of the Exchange Current Density for the Hydrogen Oxidation and Evolution Reactions. J Electrochem Soc 2007;154:B631.

[89] Zhou Y, Pasquarelli R, Holme T, Berry J, Ginley D, O’Hayre R. Improving PEM fuel cell catalyst activity and durability using nitrogen-doped carbon supports: observations from model Pt/HOPG systems. J Mater Chem 2009;19:7830.

[90] Roudgar A, Groß A. Local reactivity of thin Pd overlayers on Au single crystals. J Electroanal Chem 2003;548:121–30.

[91] Wolfschmidt H, Weingarth D, Stimming U. Enhanced reactivity for hydrogen reactions at Pt nanoislands on Au(111). Chemphyschem 2010;11:1533–41.

[92] Brülle T, Denisenko A, Sternschulte H, Stimming U. Catalytic activity of platinum nanoparticles on highly boron-doped and 100-oriented epitaxial diamond towards HER and HOR. Phys Chem Chem Phys 2011;13:12883–91.

[93] Brülle T, Stimming U. Platinum nanostructured HOPG – Preparation, characterization and reactivity. J Electroanal Chem 2009;636:10–7.

[94] Yaeger E, Kuta J. Techniques for the Study of Electrode Processes. In: Eyring H, editor. Phys. Chem. An Adv. Treatise. Vol. IXA Electrochem., New York/London: Academic Press; 1970, p. 346–451.

[95] Delahay P. Double Layer Studies. J Electrochem Soc 1966;113:967.

[96] Delahay P. Charge separation and recombination without external current at nonideal polarized electrodes. J Phys Chem 1966;70:2067–8.

[97] Delahay P. Electrode processes without a priori separation of double-layer charging. J Phys Chem 1966;70:2373–9.

[98] Delahay P, Holub K. Coupling of charging and faradaic processes: Electrode admittance for reversible processes. J Electroanal Chem 1968;16:131–6.

[99] Gerischer H. Eine Einführung in die Methoden zur Untersuchung der Kinetik von Elektrodenprozessen. Zeitschrift Für Elektrochemie 1955;50:604–12.

[100] Gerischer H, Vielstich W. Zur Elektrolyse bei konstantem Elektrodenpotential. Zeitschrift Für Phys Chemie 1955;3:16–33.

[101] Laitinen H, Tischer R, Roe D. Exchange Current Measurements in KCl-LiCl Eutectic Melt. J Electrochem Soc 1960;107:546–55.

[102] Paunovic M. Chronopotentiometry. J Electroanal Chem 1967;14:447.

[103] Gerischer H, Krause M. Eine Doppelimpuls-Methode zur Untersuchung sehr schneller Elektrodenreaktionen. Zeitschrift Für Phys Chemie 1957;10:264–9.

[104] Matsuda H, Delahay P, Kleinerman M. Kinetics of Discharge of Metal Ion Complexes with Preceding Chemical Reaction. J Am Chem Soc 1959;81:6379–81.

[105] Kooijman D, Sluyters J. Reconsideration of the galvanostatic double-pulse method. J Electroanal Chem 1967;13:1–5.

[106] Perone SP, Kretlow WJ. Application of Controlled Potential Techniques to Study of Rapid Succeeding Chemical Reaction Coupled to Electro-Oxidation of Ascorbic Acid. Anal Chem 1966;38:1760–3.

[107] Orazem M, Tribollet B. Electrochemical Impedance Spectroscopy. Hoboken: John Wiley and Sons; 2008.

[108] Jorcin J-B, Orazem ME, Pébère N, Tribollet B. CPE analysis by local electrochemical impedance spectroscopy. Electrochim Acta 2006;51:1473–9.

[109] Hsu C, Mansfeld F. Technical note: concerning the conversion of the constant phase element parameter Y0 into a capacitance. Corrosion 2001;57:747.

[110] Zoski CG, editor. Handbook of Electrochemistry. Amsterdam: Elsevier B.V.; 2007.

[111] Wagner M, editor. Thermal Analysis in Practice. METTLER TOLEDO Collected Applications; 2009.

[112] Ros TG, van Dillen AJ, Geus JW, Koningsberger DC. Surface oxidation of carbon nanofibres. Chem a Eur J 2002;8:1151–62.

[113] Figueiredo J, Pereira M, Freitas M, Orfao J. Modification of the surface chemistry of activated carbons. Carbon N Y 1999;37:1379–89.

[114] Gorgulho HF, Mesquita JP, Gonçalves F, Pereira MFR, Figueiredo JL. Characterization of the surface chemistry of carbon materials by potentiometric titrations and temperature-programmed desorption. Carbon N Y 2008;46:1544–55.

[115] Hu C, Su J, Wen T. Modification of multi-walled carbon nanotubes for electric double-layer capacitors: Tube opening and surface functionalization. J Phys Chem Solids 2007;68:2353–62.

[116] Bauer CM. Investigations of the electron transfer kinetics on advanced carbon electrodes for the all-vanadium redox-flow battery. Technische Universität München, Diploma Thesis, 2012.

[117] Kaufmann EN, editor. Characterization of Materials. Hoboken: John Wiley & Sons, Inc.; 2003.

[118] Niemantsverdriet J. Spectroscopy in Catalysis. Third Edit. Wiley-VCH Verlag GmbH & Co. KGaA; 2007.

[119] Ardenne M v. Das Elektronen-Rastermikroskop, Theoretische Grundlagen. Zeitschrift Für Phys 1938;109:553–72.

[120] Fuchs P, Semmel J, Friedl J, Höfling S, Koeth J, Worschech L, et al. Distributed feedback quantum cascade lasers at 13.8 μm on indium phosphide. Appl Phys Lett 2011;98:211118.

[121] Zielke U, Hüttinger KJ, Hoffman WP. Surface oxidized Carbon Fibers: I. Surface Structure and Chemistry. Carbon N Y 1996;34:983–98.

[122] Yang D-Q, Rochette J-F, Sacher E. Functionalization of multiwalled carbon nanotubes by mild aqueous sonication. J Phys Chem B 2005;109:7788–94.

[123] Zhang J, Zou H, Qing Q, Yang Y, Li Q. Effect of chemical oxidation on the structure of single-walled carbon nanotubes. J Phys Chem B 2003;107:3712–8.

[124] Kugler E, Boudart M. Ligand and ensemble effects in the adsorption of carbon monoxide on supported palladium-gold alloys. J Catal 1979;59:201–10.

[125] Rinaldi A. Synthesis of Carbon Nanotubes on Carbon Supports and the Purification of Carbon Nanotubes. Technische Universität Berlin, PhD Thesis, 2010.

[126] Tuinstra F, Koenig J. Raman Spectrum of Graphite. J Chem Phys 1970;53:1126.

[127] Vohler O, von Sturm F, Wege E, von Kienle H, Voll M, Kleinschmit P. Carbon. Ullmann's Encycl. Ind. Chem., Weinheim: VCH Verlagsgesellschaft; 1986, p. 95–163.

[128] Schlögl R. Graphite - A unique lattice host. In: Mueller-Warmuth W, Schoellhorn R, editors. Prog. Intercalation Res., Kluwer Academic Publishers; 1994, p. 83–176.

[129] Gerischer H, McIntyre R, Scherson D, Storck W. Density of the electronic states of graphite: derivation from differential capacitance measurements. J Phys Chem 1987;91:1930–5.

[130] Rice RJ, McCreery RL. Quantitative relationship between electron transfer rate and surface microstructure of laser-modified graphite electrodes. Anal Chem 1989;61:1637–41.

[131] Chen P, Fryling M, McCreery R. Electron transfer kinetics at modified carbon electrode surfaces: the role of specific surface sites. Anal Chem 1995;67:3115–22.

[132] Chen P, McCreery R. Control of electron transfer kinetics at glassy carbon electrodes by specific surface modification. Anal Chem 1996;68:3958–65.

[133] Hush N. Electron transfer in retrospect and prospect 1: Adiabatic electrode processes. J Electroanal Chem 1999;460:5–29.

[134] Taube H. Electron Transfer between Metal Complexes - A Retrospective View (Nobel Lecture). Angew Chemie Int Ed 1984;23:329–39.

[135] Peter LM, Dürr W, Bindra P, Gerischer H. The influence of alkali metal cations on the rate of the Fe(CN)64-/Fe(CN)63-electrode process. J Electroanal Chem 1976;71:31–50.

[136] Kneten K, McCreery R. Effects of redox system structure on electron-transfer kinetics at ordered graphite and glassy carbon electrodes. Anal Chem 1992:2518–24.

[137] Birkin PR, Silva-Martinez S. Determination of heterogeneous electron transfer kinetics in the presence of ultrasound at microelectrodes employing sampled voltammetry. Anal Chem 1997;69:2055–62.

[138] Iwasita T, Schmickler W, Schultze J. The influence of the metal on the kinetics of outer sphere redox reactions. Berichte Der Bunsengesellschaft Für Phys Chemie 1985;308:138–42.

[139] McDermott M, McDermott CA, McCreery RL. Scanning tunneling microscopy of carbon surfaces: relationships between electrode kinetics, capacitance, and morphology for glassy carbon electrodes. Anal Chem 1993;65:937–44.

[140] Valota AT, Toth PS, Kim Y-J, Hong BH, Kinloch I a., Novoselov KS, et al. Electrochemical investigation of chemical vapour deposition monolayer and bilayer graphene on the microscale. Electrochim Acta 2013;110:9–15.

[141] Tan C, Rodríguez-López J, Parks JJ, Ritzert NL, Ralph DC, Abruña HD. Reactivity of monolayer chemical vapor deposited graphene imperfections studied using scanning electrochemical microscopy. ACS Nano 2012;6:3070–9.

[142] Güell AG, Ebejer N, Snowden ME, Macpherson J V, Unwin PR. Structural correlations in heterogeneous electron transfer at monolayer and multilayer graphene electrodes. J Am Chem Soc 2012;134:7258–61.

[143] Rice RJ, Pontikos NM, McCreery RL. Quantitative correlations of heterogeneous electron-transfer kinetics with surface properties of glassy carbon electrodes. J Am Chem Soc 1990;112:4617–22.

[144] Valcárcel M, Cárdenas S, Simonet BM. Role of carbon nanotubes in analytical science. Anal Chem 2007;79:4788–97.

[145] Heller I, Kong J, Williams K a, Dekker C, Lemay SG. Electrochemistry at single-walled carbon nanotubes: the role of band structure and quantum capacitance. J Am Chem Soc 2006;128:7353–9.

[146] Bai P, Bazant MZ. Charge transfer kinetics at the solid–solid interface in porous electrodes. Nat Commun 2014;5:1–7.

[147] Pope M, Müller A. Polyoxometalate chemistry: from topology via self-assembly to applications. New York, Boston, Dordrecht, London, Moscow: Kluwer Academic Publishers; 2001.

[148] Pope MT, Müller A. Polyoxometalate chemistry: an old field with new dimensions in several disciplines. Angew Chemie Int Ed 1991;30:34–48.

[149] Keggin J. Structure of the Molecule of 12-Phosphotungstic Acid. Nature 1933;13:908–9.

[150] Pope MT. Heteropoly and Isopoly Oxometalates. Berlin, Heidelberg: Springer Berlin Heidelberg; 1983.

[151] Kortz U. Polyoxometalates. Eur J Inorg Chem 2009;2009:5056.

[152] Mitchell SG, Boyd T, Miras HN, Long D-L, Cronin L. Extended polyoxometalate framework solids: two Mn(II)-linked {P8W48} network arrays. Inorg Chem 2011;50:136–43.

[153] Bardin BB, Bordawekar S V., Neurock M, Davis RJ. Acidity of Keggin-Type Heteropolycompounds Evaluated by Catalytic Probe Reactions, Sorption Microcalorimetry, and Density Functional Quantum Chemical Calculations. J Phys Chem B 1998;102:10817–25.

[154] Errington RJ. Rational Approaches to Polyoxometalate Synthesis. In: Pope MT, Mueller A, editors. Polyoxometalate Chem. From Topol. via Self-Assembly to Appl., New York, Boston, Dordrecht, London, Moscow: Kluwer Academic Publishers; 2001, p. 7–22.

[155] Vilà-Nadal L, Mitchell SG, Rodríguez-Fortea A, Miras HN, Cronin L, Poblet JM. Connecting theory with experiment to understand the initial nucleation steps of heteropolyoxometalate clusters. Phys Chem Chem Phys 2011;13:20136–45.

[156] Yan L, López X, Carbó JJ, Sniatynsky R, Duncan DC, Poblet JM. On the origin of alternating bond distortions and the emergence of chirality in polyoxometalate anions. J Am Chem Soc 2008;130:8223–33.

[157] Duclusaud H, Borshch S a. Electron delocalization and magnetic state of doubly-reduced polyoxometalates. J Am Chem Soc 2001;123:2825–9.

[158] Strong JB, Yap GPA, Ostrander R, Liable-sands LM, Rheingold AL, Gouzerh P, et al. A New Class of Functionalized Polyoxometalates : Synthetic , Structural , Spectroscopic , and Electrochemical Studies of Organoimido Derivatives of [Mo 6 O 19] 2 - 2000:639–49.

[159] Yan J, Long D-L, Wilson EF, Cronin L. Discovery of heteroatom-“embedded” Te {W18O54} nanofunctional polyoxometalates by use of cryospray mass spectrometry. Angew Chem Int Ed Engl 2009;48:4376–80.

[160] Bagno A, Bini R. NMR spectra of terminal oxo gold and platinum complexes: relativistic DFT predictions. Angew Chem Int Ed Engl 2010;49:1083–6.

[161] Marcus R. On the theory of electron-transfer reactions. VI. Unified treatment for homogeneous and electrode reactions. J Chem Phys 1965;43:679–700.

[162] Weaver MJ. Redox reactions at metal–solution interfaces. In: Compton RG, editor. Electrode Kinet. React., vol. 27, Amsterdam: Elsevier; 1987, p. 1–60.

[163] Hupp JT, Weaver MJ. Experimental estimate of the electron-tunneling distance for some outer-sphere electrochemical reactions. J Phys Chem 1984;88:1463–7.

[164] Kortz U, Müller A, van Slageren J, Schnack J, Dalal NS, Dressel M. Polyoxometalates: Fascinating structures, unique magnetic properties. Coord Chem Rev 2009;253:2315–27.

[165] Winpenny REP. Quantum information processing using molecular nanomagnets as qubits. Angew Chem Int Ed Engl 2008;47:7992–4.

[166] Chalamala BR, Soundappan T, Fisher GR, Anstey MR, Viswanathan V V., Perry ML. Redox Flow Batteries: An Engineering Perspective. Proc IEEE 2014;102:976–99.

[167] Wen YH, Zhang HM, Qian P, Zhou HT, Zhao P, Yi BL, et al. Studies on Iron (Fe[sup 3+]∕Fe[sup 2+])-Complex/Bromine (Br[sub 2]∕Br[sup −]) Redox Flow Cell in Sodium Acetate Solution. J Electrochem Soc 2006;153:A929.

[168] Wang W, Kim S, Chen B, Nie Z, Zhang J, Xia G-G, et al. A new redox flow battery using Fe/V redox couples in chloride supporting electrolyte. Energy Environ Sci 2011;4:4068.

[169] Johnson DA, Reid MA. Chemical and Electrochemical Behavior of the Cr(lll)/Cr(ll) Half-Cell in the Iron-Chromium Redox Eenrgy System. J Electrochem Soc 1985;132:1058–62.

[170] Sum E, Skyllas-Kazacos M. A study of the V (II)/V (III) redox couple for redox flow cell applications. J Power Sources 1985;15:179–90.

[171] Yamamura T, Watanabe N, Yano T, Shiokawa Y. Electron-Transfer Kinetics of Np[sup 3+]∕Np[sup 4+], NpO[sub 2][sup +]∕NpO[sub 2][sup 2+], V[sup 2+]∕V[sup 3+], and VO[sup 2+]∕VO[sub 2][sup +] at Carbon Electrodes. J Electrochem Soc 2005;152:A830.

[172] Li L, Kim S, Wang W, Vijayakumar M, Nie Z, Chen B, et al. A Stable Vanadium Redox-Flow Battery with High Energy Density for Large-Scale Energy Storage. Adv Energy Mater 2011;1:394–400.

[173] Ding C, Zhang H, Li X, Liu T, Xing F. Vanadium Flow Battery for Energy Storage: Prospects and Challenges. J Phys Chem Lett 2013;4:1281–94.

[174] Skyllas-Kazacos M. Novel vanadium chloride/polyhalide redox flow battery. J Power Sources 2003;124:299–302.

[175] Armand M, Tarascon J-M. Building better batteries. Nature 2008;451:652–7.

[176] Chang F, Hu C, Liu X, Liu L, Zhang J. Coulter dispersant as positive electrolyte additive for the vanadium redox flow battery. Electrochim Acta 2012;60:334–8.

[177] Tsai H-M, Yang S-J, Ma C-CM, Xie X. Preparation and electrochemical activities of iridium-decorated graphene as the electrode for all-vanadium redox flow batteries. Electrochim Acta 2012;77:232–6.

[178] Li W, Liu J, Yan C. Reduced graphene oxide with tunable C/O ratio and its activity towards vanadium redox pairs for an all vanadium redox flow battery. Carbon N Y 2013;55:313–20.

[179] Tessonnier J-P, Rosenthal D, Hansen TW, Hess C, Schuster ME, Blume R, et al. Analysis of the structure and chemical properties of some commercial carbon nanostructures. Carbon N Y 2009;47:1779–98.

[180] Bassil BS, Ibrahim M, Al-Oweini R, Asano M, Wang Z, van Tol J, et al. A planar {Mn19(OH)12}26+ unit incorporated in a 60-tungsto-6-silicate polyanion. Angew Chem Int Ed Engl 2011;50:5961–4.

[181] Al-Oweini R, Bassil BS, Palden T, Keita B, Lan Y, Powell AK, et al. The manganese(III)-containing tungstophosphate [MnIII3(H2O)5(A-α-PW9O34)2]9−. Polyhedron 2013;52:461–6.

[182] Wolfschmidt HH. Interfaces and Energy Conversion Substrate Effects in Electrocatalysis. Technische Universitaet Muenchen, PhD Thesis, 2012.

[183] Sadakane M, Steckhan E. Investigation of the manganese-substituted alpha-Keggin-heteropolyanion K6SiW11O39Mn(H2O) by cyclic voltammetry and its application as oxidation catalyst. J Mol Catal A Chem 1996;114:221–8.

[184] Keita B, Mialane P, Sécheresse F, de Oliveira P, Nadjo L. Electrochemical generation of high-valent manganese catalysts in aqueous solutions from the sandwich-type polyoxoanion [(MnIII(H2O))3(SbW9O33)2]9−. Electrochem Commun 2007;9:164–72.

[185] Zhang X-Y, O'Connor CJ, Jameson GB, Pope MT. High-Valent Manganese in Polyoxotungstates. 3. Dimanganese Complexes of gamma-Keggin Anions. Inorg Chem 1996;35:30–4.

[186] Zhang X-Y, Jameson GB, O'Connor CJ, Pope MT. High-valent manganese in polyoxotungstates—II. Oxidation of the tetramanganese heteropolyanion [Mn4(H2O)2(PW9O34)2]10−. Polyhedron 1996;15:917–22.

[187] Banerjee S, Hemraj-Benny T, Wong SS. Covalent Surface Chemistry of Single-Walled Carbon Nanotubes. Adv Mater 2005;17:17–29.

[188] Hirsch A. Functionalization of single-walled carbon nanotubes. Angew Chemie Int Ed 2002:1853–9.

[189] Bahr JL, Tour JM. Covalent chemistry of single-wall carbon nanotubes. J Mater Chem 2002;12:1952–8.

[190] Chen J, Haman M, Hu H, Chen Y, Rao AM, Eklund PC, et al. Solution Properties of Single-Walled Carbon Nanotubes. Science (80-) 1998;282:95–8.

[191] Liu J, Rinzler A, Dai H, Hafner J, Bradley R, Boul P, et al. Fullerene pipes. Science 1998;280:1253–6.

[192] Laborda E, Henstridge MC, Batchelor-McAuley C, Compton RG. Asymmetric Marcus-Hush theory for voltammetry. Chem Soc Rev 2013;42:4894–905.

[193] Savéant J, Tessier D. Convolution potential sweep voltammetry V. Determination of charge transfer kinetics deviating from the Butler-Volmer behaviour. J Electroanal Chem 1975;65:57–66.

[194] Hung NG, Nagy Z. Kinetics of the Ferrous/Ferric Electrode Reaction in the Absence of Chloride Catalysis. J Electrochem Soc 1987;134:2215–20.

[195] Friedl J, Stimming U. Investigation of the electron transfer kinetics in complex systems. XIII. Int. Conf. Electrified Interfaces (ICEI 2013), 2013.

[196] Angell DH, Dickinson T. The kinetics of the Ferrous/Ferric and ferro/ferricyanide reactions at platinum and gold electrodes. J Electroanal Chem 1972;35:55–72.

[197] 1960.Gerischer.Die Erfassung schneller chemischer Reaktionen im potentiostatischen Ablauf einer Elektrodenreaktion.pdf n.d.

[198] Marquardt D. An algorithm for least-squares estimation of nonlinear parameters. J Soc Ind Appl Math 1963;11.

[199] Gerischer H. Messungen der Austauschstromdichte beim Gleichgewichtspotential an einer Platinelektrode in Fe2+/Fe3+-Lösungen. Zeitschrift Für Elektrochemie Und Angew Phys Chemie 1950;51:366–9.

[200] Randles JEB, Somerton KW. Kinetics of rapid electrode reactions. Part 3.?Electron exchange reactions. Trans Faraday Soc 1952;48:937.

[201] Weber J, Samec Z, Marecek V. The Effect of Anion Adsorption on the Kinetics of the Fe3+/Fe2+ Reacion on Pt and Au Electrodes in HClO4. J Electroanal Chem 1978;89:271–88.

[202] Punckt C, Pope MA, Liu J, Lin Y, Aksay IA. Electrochemical Performance of Graphene as Effected by Electrode Porosity and Graphene Functionalization. Electroanalysis 2010;22:2834–41.

[203] Flox C, Rubio-Garcia J, Nafria R, Zamani R, Skoumal M, Andreu T, et al. Active nano-CuPt3 electrocatalyst supported on graphene for enhancing reactions at the cathode in all-vanadium redox flow batteries. Carbon N Y 2012;50:2372–4.

[204] Kouklin N, Tzolov M, Straus D, Yin A, Xu JM. Infrared absorption properties of carbon nanotubes synthesized by chemical vapor deposition. Appl Phys Lett 2004;85:4463–5.

[205] Al-Jishi R, Dresselhaus G. Lattice-dynamical model for alkali-metal—graphite intercalation compounds. Phys Rev B 1982;26:4523–38.

[206] Wang Y, Alsmeyer DC, Mccreery RL. Raman spectroscopy of carbon materials: structural basis of observed spectra. Chem Mater 1990;2:557–63.

[207] Jin R, Zhou ZX, Mandrus D, Ivanov IN, Eres G, Howe JY, et al. The effect of annealing on the electrical and thermal transport properties of macroscopic bundles of long multi-wall carbon nanotubes. Phys B Condens Matter 2007;388:326–30.

[208] Wepasnick KA, Smith BA, Schrote KE, Wilson HK, Diegelmann SR, Fairbrother DH. Surface and structural characterization of multi-walled carbon nanotubes following different oxidative treatments. Carbon N Y 2011;49:24–36.

[209] Li W, Liu J, Yan C. Multi-walled carbon nanotubes used as an electrode reaction catalyst for VO2+/VO2+ for a vanadium redox flow battery. Carbon N Y 2011;49:3463–70.

[210] Rinaldi A. Synthesis of Carbon Nanotubes on Carbon Supports and the Purification of Carbon Nanotubes. Technische Universitaet Berlin, 2010.

[211] Lehman JH, Terrones M, Mansfield E, Hurst KE, Meunier V. Evaluating the characteristics of multiwall carbon nanotubes. Carbon N Y 2011;49:2581–602.

[212] ORIJI G. Investigation on V(IV)/V(V) species in a vanadium redox flow battery. Electrochim Acta 2004;49:3091–5.

[213] Rychcik M, Skyllas-Kazacos M. Characteristics of a new all-vanadium redox flow battery. J Power Sources 1988;22:59–67.

[214] Zhong S, Skyllas-Kazacos M. Electrochemical behaviour of vanadium (V)/vanadium (IV) redox couple at graphite electrodes. J Power Sources 1992;39:1–9.

[215] LI L, LI F. The effect of carbonyl, carboxyl and hydroxyl groups on the capacitance of carbon nanotubes. New Carbon Mater 2011;26:224–8.

[216] Laronze N, Marrot J, Hervé G. Cation-Directed Synthesis of Tungstosilicates. 1. Syntheses and Structures of K10A-r-[SiW9O34],24H2O, of the Sandwich-Type Complex K10.75[Co(H2O)6]0.5[Co(H2O)4Cl]0.25A-r-[K2{Co(H2O)2}3(SiW9O34)2],32H2O and of Cs15[K(SiW11O39)2],39H2O. Inorg Chem 2003;42:5857–62.

[217] Zonnevijlle F, Tourne CM, Tourne GF. Preparation and characterization of heteropolytungstates containing group 3a elements. Inorg Chem 1982;21:2742–50.

[218] Tézé A, Hervé G. Formation et isomerisation des undeca et dodeca tungstosilicates et germanates isomeres. J Inorg Nucl Chem 1977;39:999–1002.

[219] Ginsberg AP, editor. Inorganic Syntheses. Hoboken, NJ, USA: John Wiley & Sons, Inc.; 1990.

[220] Marcus Y, Hefter G. Ion pairing. Chem Rev 2006;106:4585–621.

[221] Leroy F, Miró P, Poblet JM, Bo C, Bonet Avalos J. Keggin polyoxoanions in aqueous solution: ion pairing and its effect on dynamic properties by molecular dynamics simulations. J Phys Chem Bchemistry B 2008;112:8591–9.

[222] Sadakane M, Steckhan E, Dory Y, Chapuzet JM, Lessard J, Tallec A, et al. Co-solvent Effects on the Redox Potentials of Manganese-substituted alpha-Keggin-type Silicon Polyoxotungstate K6SiW11O39Mn(H2O): First Electrochemical Generation of the Manganese(V) Redox System in an Aqueous Environment. Acta Chem Scand 1999;53:837–41.

[223] Maestre JM, Lopez X, Bo C, Poblet JM, Casañ-Pastor N. Electronic and magnetic properties of alpha-Keggin anions: A DFT study of [XM12O40](n-), (M = W, Mo; X = Al(III), Si(IV), P(V), Fe(III), Co(II), Co(III)) and [SiM11VO40] (m- (M = Mo and W). J Am Chem Soc 2001;123:3749–58.

[224] Himeno S, Takamoto M, Santo R, Ichimura A. Redox Properties and Basicity of Keggin-Type Polyoxometalate Complexes. Bull Chem Soc Jpn 2005;78:95–100.

[225] Himeno S, Takamoto M. Difference in voltammetric properties between the Keggin-type [XW12O40]n- and [XMo12O40]n- complexes. J Electroanal Chem 2002;528:170–4.

[226] Pope M, Varga GM. Heteropoly blues. I. Reduction stoichiometries and reduction potentials of some 12-tungstates. Inorg Chem 1966;5:3–8.

[227] Aparicio PA, Poblet JM, López X. Tungsten Redox Waves in [XMW 11 O 40] n- (X = P, Si, Al and M = W, Mo, V, Nb, Ti) Keggin Compounds - Effect of Localised/Delocalised Charges. Eur J Inorg Chem 2013;2013:1910–6.

[228] Varga GM, Papaconstantinou E, Pope MT. Heteropoly blues. IV. Spectroscopic and magnetic properties of some reduced polytungstates. Inorg Chem 1970;9:662–7.

[229] Prados RA, Meiklejohn PT, Pope MT. The Nature of Electron Delocalization in a Heteropoly “Blue” Anion. J Am Chem Soc 1974;96:1261.

[230] Guo S-X, Mariotti AW a, Schlipf C, Bond AM, Wedd AG. Investigation of the pronounced medium effects observed in the voltammetry of the highly charged lacunary anions [alpha-SiW11O39]8- and [alpha-PW11O39]7-. Inorg Chem 2006;45:8563–74.

[231] Toth J, Anson F. Electrochemical properties of iron (III)-substituted heteropolytungstate anions. J Electroanal Chem 1988;256:361–70.

[232] Huynh MH V, Meyer TJ. Proton-coupled electron transfer. Chem Rev 2007;107:5004–64.

[233] Chaumont A, Wipff G. Interactions between Keggin Anions in Water: The Higher Their Charge, the Higher Their Condensation? A Simulation Study. Eur J Inorg Chem 2013;2013:1835–53.

[234] Chaumont A, Wipff G. Polyoxometalate Keggin Anions at Aqueous Interfaces with Organic Solvents, Ionic Liquids, and Graphite: a Molecular Dynamics Study. J Phys Chem C 2009;113:18233–43.

[235] Weinberg DR, Gagliardi CJ, Hull JF, Murphy CF, Kent CA, Westlake BC, et al. Proton-coupled electron transfer. Chem Rev 2012;112:4016–93.

[236] Ammam M, Keita B, Nadjo L, Mbomekalle I-M, Ritorto MD, Anderson TM, et al. Cyclic Voltammetry Study of the Mn-Substituted Polyoxoanions [MnII4(H2O)2(H4AsW15O56)2]18− and [((MnIIOH2)MnII2PW9O34)2(PW6O26)]17−: Electrodeposition of Manganese Oxides Electrocatalysts for Dioxygen Reduction. Electroanalysis 2011;23:1427–34.

[237] Mao L, Zhang D, Sotomura T, Kenichi N, Kashiba N, Ohsaka T. Mechanistic study of the reduction of oxygen in air electrode with manganese oxides as electrocatalysts. Electrochim Acta 2003;48:1015–21.

[238] Bassil BS, Dickman MH, Reicke M, Kortz U, Keita B, Nadjo L. Transition metal containing decatungstosilicate dimer [M(H(2)O)(2)(gamma-SiW(10)O(35))(2)](10-) (M = Mn(2+), Co(2+), Ni(2+)). Dalt Trans 2006:4253–9.

[239] Bassil BS, Ibrahim M, Mal SS, Suchopar A, Biboum RN, Keita B, et al. Cobalt, manganese, nickel, and vanadium derivatives of the cyclic 48-tungsto-8-phosphate [H(7)P(8)W(48)O(184)](33-). Inorg Chem 2010;49:4949–59.

[240] Keita B, Nadjo L. Scanning tunnelling microscope monitoring of the surface morphology of the basal plane of highly oriented pyrolytic graphite during the cyclic voltammetry. J Electroanal Chem 1993;354:295–304.

[241] Abdeljalil E, Keita B, Nadjo L, Contant R. STM and AFM characterization of thin metal oxide films electrodeposited from [O2M18O62]6-. J Solid State Chem 2001;5:94–106.

[242] López X, Nieto-Draghi C, Bo C, Avalos JB, Poblet JM. Polyoxometalates in solution: Molecular dynamics simulations on the alpha-PW12O40^3- Keggin anion in aqueous media. J Phys Chem A 2005;109:1216–22.

[243] Born M. Volumen und Hydratationswaerme der Ionen. Zeitschrift Für Phys 1920;1:45–8.

[244] Glass EN, Fielden J, Kaledin AL, Musaev DG, Lian T, Hill CL. Extending metal-to-polyoxometalate charge transfer lifetimes: the effect of heterometal location. Chemistry 2014;20:4297–307.

[245] Shevchenko D, Huang P, Bon V V, Anderlund MF, Kokozay VN, Styring S, et al. Synthesis, crystal structure, mass spectrometry, electrochemistry and magnetism of a Mn(III)-substituted trilacunary Keggin tungstosilicate. Dalton Trans 2013;42:5130–9.

[246] Bi L-H, Al-Kadamany G, Chubarova E V, Dickman MH, Chen L, Gopala DS, et al. Organo-ruthenium supported heteropolytungstates: synthesis, structure, electrochemistry, and oxidation catalysis. Inorg Chem 2009;48:10068–77.

[247] Bi L, Kortz U, Keita B, Nadjo L. The ruthenium(II)-supported heteropolytungstates [Ru(dmso)3(H2O)-XW11O39]6- (X = Ge, Si). Dalton Trans 2004;3:3184–90.

[248] Keita B, Abdeljalil E, Nadjo L, Avisse B, Contant R, Canny J, et al. Ligand and electrolyte effects in the electroreduction of copper-substituted heteropolyanions. Electrochem Commun 2000;2:145–9.

[249] Keita B, Mbomekalle I-M, Nadjo L. Redox behaviours and electrocatalytic properties of copper within Dawson structure-derived sandwich heteropolyanions [Cu4(H2O)2(X2W15O56)2]16− (X=P or As). Electrochem Commun 2003;5:830–7.

[250] Keita B, Mbomekalle IM, Nadjo L, Anderson TM, Hill CL. Multi-iron wells-Dawson heteropolytungstates. Electrochemical probing of siderophoric behavior in sandwich-type complexes. Inorg Chem 2004;43:3257–63.

[251] Moore MA. A Base Case Design and Capital Cost Analysis of an All Vanadium Redox-Flow Battery. University of Tennessee, Knoxville, 2013.

[252] Taleb A, Kjeang E, Maine E. Cost analysis for durable proton exchange membrane in PEM fuel cells. PICMET ’12 Technol Manag Emerg Technol 2012;1:2943–50.

[253] Darling R, Gallagher KG, Kowalski J a, Ha S, Brushett FR. Pathways to low-cost electrochemical energy storage: a comparison of aqueous and nonaqueous flow batteries. Energy Environ Sci 2014:3459–77.

[254] You D, Zhang H, Chen J. A simple model for the vanadium redox battery. Electrochim Acta 2009;54:6827–36.

[255] Shah AA, Al-Fetlawi H, Walsh FC. Dynamic modelling of hydrogen evolution effects in the all-vanadium redox flow battery. Electrochim Acta 2010;55:1125–39.

[256] Whitehead AH. The vanadium redox flow battery: from laboratory to market. Present. NTU, 2014.

[257] Chen H, Cong TN, Yang W, Tan C, Li Y, Ding Y. Progress in electrical energy storage system: A critical review. Prog Nat Sci 2009;19:291–312.

[258] Xue F-Q, Wang Y-L, Wang W-H, Wang X-D. Investigation on the electrode process of the Mn(II)/Mn(III) couple in redox flow battery. Electrochim Acta 2008;53:6636–42.

[259] Rahman F, Skyllas-Kazacos M. Solubility of vanadyl sulfate in concentrated sulfuric acid solutions. J Power Sources 1998;72:105–10.

[260] http://www.alibaba.com/showroom/manganese-dioxide-price.html accessed on the 4th of Dec 2014. Manganese Dioxide Price n.d.

[261] http://www.itia.info/tungsten-prices.html accessed on the 4th of December 2014 n.d.

[262] Miras HN, Yan J, Long D-L, Cronin L. Engineering polyoxometalates with emergent properties. Chem Soc Rev 2012;41:7403–30.

[263] Bourke A, Quill N, Lynch RP, Buckley DN. Effect of Pretreatment on the Rate of the VO2+/VO2+ and V2+/V3+ Reactions at a Carbon Electrode. ECS Trans 2014;61:15–26.

[264] Duduta M, Ho B, Wood VC, Limthongkul P, Brunini VE, Craig Carter W, et al. Semi-Solid Lithium Rechargeable Flow Battery. Adv Energy Mater 2011;1:511–46.

[265] http://www.infomine.com/investment/metal-prices/molybdenum-oxide/ accessed on the 4th of December 2014 n.d.

[266] Chubarova E V, Dickman MH, Keita B, Nadjo L, Miserque F, Mifsud M, et al. Self-assembly of a heteropolyoxopalladate nanocube: [Pd(II)13As(V)8O34(OH)6]8-. Angew Chem Int Ed Engl 2008;47:9542–6.

Appendix

A1 Abbreviations and Symbols

α_a, α_c	Anodic, cathodic transfer coefficient
$\Gamma_{Ox}, \Gamma_{Red}$	Excess surface species [$mol\ cm^{-2}$]
ΔG^0	Change in Gibbs free energy [eV]
ΔG^*	Free energy barrier [eV]
ΔG_{Born}	Free Born energy of adsorption [eV]
ΔU^{peak}	Potential separation between anodic and cathodic peak [V]
ΔU	Volta potential difference [V]
ε_{op}	Optical dielectric constant
ε_r	Dielectric constant
ε_s	Static dielectric constant
ε	Absorptivity coefficient [$L\ mol^{-1}\ cm^{-1}$]
ϵ	Energy density [$Wh\ L^{-1}$]
η	Overpotential [V]
λ_D	Debye length [m]
λ_{in}	Inner reorganization energy [eV]
λ_{out}	Outer shell reorganization energy [eV]
λ	Wavelength [μm]
λ	Total reorganization energy [eV]
$\overline{\mu_e}$	Electrochemical potential [eV]
$\tilde{\nu}$	Wavenumber [cm^{-1}]
ν_j	Stoichiometric factor of species j
ξ	Inverse Debye length (λ_D^{-1})[m^{-1}]
ϑ	Roughness factor electrode
ϱ	Charge density [$C\ cm^{-3}$]
P	Probability
τ_{pot}	Potentiostat response time [s]
τ	Time constant of an electrochemical cell [s]
σ	Constant phase element parameter
φ	Phase angle [°]
$\varphi(z)$	Galvani potential at distance z [V]
χ_s	Surface potential of an electrolyte [V]
χ	Dipole layer contribution to workfunction [eV]
AQDS	9,10-anthraquinone-2,7-disuplhonic acid
A	Electrochemically active surface area [cm^2]
A	Height of (tunneling) barrier [m]
A_{Total}	Area of power converter [m^2]
a	Effective radius of reactant [m]
A^{BET}	Surface Area determined from the Brunauer-Emett-Teller method [m^2]
Abs	Absorbance
AFM	Atomic force microscopy

a_j	Activity of species j [$mol\ dm^{-3}$]
amu	Atomic mass unit ($amu = 1/12\ m(^{12}C)$)
ARPA-e	Advanced research projects agency - Energy
b	Path length [cm]
BET	Brunauer-Emett-Teller
CCET	Cation coupled electron transfer
C_d	Diffuse double layer capacitance [F]
C_{DL}	Double layer capacitance [F]
c_{DL}	Specific double layer capacitance [$F\ cm^{-2}$]
CE	Counter electrode
C_H	Differential capacitance [F]
c_j	Concentration of species j [$mol\ dm^{-3}$]
CNT	Carbon nanotube
CPE	Constant phase element [$F\ s^{1-\sigma}$]
CV	Cyclic voltammetry
DCP	Double current pulse
DEFUNC	Defunctionalized Nancyl 3100 multi-walled carbon nanotubes
DFT	Density functional theory
DI	De-ionised
DME	1,2-dimethoxy ethane
DOS	Density of states (units depend on dimensions)
D_{ox} , D_{red}	Diffusion coefficient [$m^2\ s^{-1}$]
e	Electron Charge ($e = 1.602\ 10^{-19}\ C$)
E	Input Impedance [Ω]
E	Energy content [MWh]
E_0	Energy of (tunneling) barrier [eV]
E_a	Activation energy [eV]
ECDL	Electrochemical double layer
ECSA	Electrochemically active surface area
E_F	Fermi Energy [eV]
EIS	Electrochemical impedance spectroscopy
EQCM	Electrochemical quartz crystal microbalance
F	Faraday constant ($F = 96485\ C\ mol^{-1}$)
f	Frequency [$Hz = s^{-1}$]
FTIR	Fourier transform infrared spectroscopy
GC	Glassy carbon
h	Planck constant ($h = 4.136\ 10\text{-}15\ eV\ s$)
HER	Hydrogen evolution reaction
HOPG	Highly oriented pyrolytic graphite
HP	Helmholtz plane
I	Ionization energy [eV]
I	Current [A]
i	Imaginary number ($i = \sqrt{-1}$).
I_0	Exchange current [A]
I_D	Intensity of D-band
I_F	Faradaic current

I_G	Intensity of G-band
IEA	International Energy Agency
IL	Ionic liquid
I_{NF}	Non-faradaic current [A]
IR	Infrared
j_0	Exchange current density [$A\ cm^{-2}$]
k_0	Electron transfer constant [$cm\ s^{-1}$]
k_B	Boltzmann constant ($k_B = 8.617\ eV\ K^{-1}$)
L	Liter [dm^3]
l	Length of a carbon nanotube [m]
LV	Linear voltammetry
m	Mass [g]
mol, M	Mole
MS	Mass spectroscopy
MSE	Mercury/Mercourus sulfate electrode
MWCNTS	Multi-walled carbon nanotube
n	Number of transferred electrons
N	Number of particles
N_C	Number of cells
NEXAFS	Near Edge X-Ray Absorption Fine-Structure
NHE	Normal Hydrogen Electrode
NITRIC	Mildly functionalized Nancyl 3100 multi-walled carbon nanotubes
NITSULF_3h	Heavily functionalized Nancyl 3100 multi-walled carbon nanotubes
NITSULF_6h	Very heavily functionalized Nancyl 3100 multi-walled carbon nanotubes
NMR	Nuclear magnetic resonance
P	Power [kW]
PCET	Proton coupled electron transfer
PEEK	Polyether ether ketone
PM	Potentiometer
POM	Polyoxometalate
PRIST	As-received Nancyl 3100 multi-walled carbon nanotubes
PS	Potential step
Q	Charge [C]
q	Specific capacity [$C\ L^{-1}$]
Q_e	Excess charge [C]
R	Gas constant ($R = 8.314\ J\ mol^{-1}\ K^{-1}$)
r	Radius of a carbon nanotube [m]
R_{CT}	Charge transfer resistance [Ω]
R_e	Distance molecule to its image in metal [m]
RE	Reference electrode
RFB	Redox Flow Battery
R_{Ohm}	Ohmic resistance [Ω]
RTIL	Room temperature ionic liquid
S	Free energy of solvation [eV]
SCP	Single current pulse
SE	Secondary electron

SEM	Scanning electron microscopy
SHE	Standard Hydrogen Electrode
$S_{ox/red}$	Redox species in electrolyte
SOC	State of charge
SOC^{max}	Maximum state of charge
SOC^{min}	Minimum state of charge
SWCNT	Single-walled carbon nanotube
T	(Absolute) temperature [K]
t_{DL}	Thickness of the electrochemical double layer [m]
t_D	Discharge time [s]
TGA	Thermogravimetric analysis
TGA-MS	Thermogravimetric analysis coupled to mass spectroscopy
U	Electrode potential [V]
U_0	Equilibrium potential [V]
$\bar{U}_0$	Average equilibrium potential [V]
U^{θ}	Characteristic standard potential [V]
UHV	Ultra-high vacuum
U_{OCV}	Open circuit potential [V]
UV-Vis	Ultraviolet –visible light spectroscopy
VRB	All-vanadium redox flow battery
V_{Total}	Total volume electrolyte [dm^3]
W	Workfunction [eV]
WE	Working electrode
XPS	X-ray photoelectron spectroscopy
z	Distance from an interface [m]
Z	Complex resistance [Ω]

In some cases there are two meanings for one symbol. This is because the conventions for symbols were followed and another, unambiguous assignment would have been awkward. In those cases, the meaning in the text is always clear.

A2 Publications

1. J. Friedl, U. Stimming “Model Catalyst Studies on Hydrogen and Ethanol Oxidation for Fuel Cells”, *Electrochim. Acta* **101** (2013) 41-58.

2. J. Friedl, C. Bauer, A. Rinaldi, U. Stimming „Investigation of the Electron Transfer Kinetics of the VO^{2+}/VO_2^+-Reaction on Multi-Walled Carbon Nanotubes”, *Carbon* **63** (2013) 228 – 239.

3. H-Y. Chen, G. Wee, R. Al-Oweini, J. Friedl, K.S. Tan, Y. Wang, C.L. Wong, U. Kortz, U. Stimming, M. Srinivasan „Polyoxovanadate as Advanced Electrode Material for Supercapacitors”, *ChemPhysChem* **15** (2014) 2162 – 2169.

4. R. Al-Oweini, B.S. Bassem, J. Friedl, V. Kottisch, M. Ibrahim, M. Asano, B. Keita, G. Novitchi, Y. Lan, A. Powell, U. Stimming, U. Kortz „Synthesis and Characterization of Multinuclear Manganese-Containing Tungstosilicates”, *Inorganic Chemistry* **53** (2014) 5663 – 5673.

5. J. Friedl, U. Stimming „The Importance of Electrochemistry for the Development of Sustainable Mobility” in: H. Bruhns (editor) *“Energie: Forschung und Konzepte”, Arbeitskreis Energie (AKE) in der Deutschen Physikalischen Gesellschaft*, 2014.

6. M. Herpich, J. Friedl, U. Stimming „Scanning Electrochemical Potential Microscopy (SECPM) and electrochemical STM (EC-STM)” in “Characterization Tools for Nanoscience & Nanotechnology, Springer, *in press*.

7. J. Friedl, R. Al-Oweini, M. Herpich, B. Keita, U. Kortz, U. Stimming „Electrochemical studies of tri-manganese substituted Keggin Ions“, *Electrochim. Acta* **141** (2014) 357 -366.

8. H-Y. Chen, R. Al-Oweini, J. Friedl, C. Lee, G. Wee, L. Li, U. Kortz, U. Stimming, M. Srinivasan „A Novel SWCNT-Polyoxometalate Nanohybrid Material as Electrode for Electrochemical Supercapacitors“, *submitted*.

A3 Conference Contributions, Seminars

1. J. Friedl, C. Bauer, R. Al-Oweini, D. Yu, U. Kortz, H. Hoster, U. Stimming „Investigation on Polyoxometalates for the Application in Redox Flow Batteries“ PRIME, Pacific Rim Meeting on electrochemical and solid-state science, 222nd ECS Meeting, October 2012, Honolulu, Hawaii, USA.

2. J. Friedl, C. Bauer, A. Rinaldi, U. Stimming „Investigation of the Electron Transfer Kinetics of the VO^{2+}/VO_2^{+}-Reaction on Multi-Walled Carbon Nanotubes”, 223rd ECS Meeting, May 2013, Toronto, Ontario, Canada.

3. J. Friedl, U. Stimming „Advanced Materials for Redox Flow Batteries”, Department of Chemistry, University of Guelph, May 2013, Guelph, Ontario, Canada.

4. J. Friedl, U. Stimming „Advanced Materials for Redox Flow Batteries”, Chemistry Department, Queen’s University, May 2013, Kingston, Ontario, Canada.

5. J. Friedl, U. Stimming „Advanced Materials for Redox Flow Batteries”, Department of Chemistry, University of Calgary, May 2013, Calgary, Alberta, Canada.

6. J. Friedl, U. Stimming „Advanced Materials for Redox Flow Batteries”, Eikerling Research Group, Simon Fraser University, May 2013, Vancouver, British Columbia, Canada.

7. J. Friedl, U. Stimming „Investigation of the electron transfer in complex systems”, 13th International Conference on Electrified Interfaces (ICEI 2013), June 2013, Chateau Liblice, Czech Republic (invited).

8. J. Friedl, U. Stimming „Vanadium Electron Transfer Kinetics on Multi-Walled Carbon Nanotubes”, 7th Asian Conference on Electrochemical Power Sources (ACEPS 7), November 2013, Osaka, Japan.

9. J. Friedl, U. Stimming „Advanced Materials for Redox Flow Batteries”, Department of Inorganic Chemistry, Fritz-Haber-Institut der Max-Planck-Gesellschaft, December 2013, Berlin, Germany.

10. J. Friedl, U. Stimming „Determining charge transfer kinetics on carbon nanotubes", ChemOnTubes 2014, March 2014, Riva del Garda, Italy.

11. J. Friedl, H. Chen, U. Stimming „Electrochemistry of Polyoxometalates for Energy Storage", 15th ISE Topological Meeting, April 2014, Niagara Falls, Canada.

12. J. Friedl, U. Stimming „The Importance of Electrochemistry for the Development of Sustainable Mobility", Verhandlungen der Deutschen Physikalischen Gesellschaft, April 2014, Berlin, Germany (invited).

13. J. Friedl, U. Stimming „Electrochemistry of Polyoxometalates", Roesch Research Group, Institute of High Performance Computing, August 2014, A*STAR, Singapore.

A4 Posters

1. “Singapore, a ‘Living Lab’ and ideal testbed for Electric Vehicles”, jDPG-Kongress, July 2012, Wolfsburg, Germany.

2. J. Friedl, R. Al-Oweini, M. Herpich, U. Kortz, U. Stimming „Electrochemistry of tri-Manganese substituted Keggin Ions” , 15th ISE Topological Meeting, April 2014, Niagara Falls, Canada.

3. H. Chen, J. Friedl, R. Al-Oweini, U. Kortz, M. Srinivasan, U. Stimming “Polyoxometalates as Electrode Materials for Molecular”, 15th ISE Topological Meeting, April 2014, Niagara Falls, Canada.

4. J. Friedl, H. Chen, U. Stimming „ Polyoxometalates for energy storage applications”, 3rd International Seminar on Green Energy Conversion, August 2014, Yamanashi, Japan.

A5 Summer Schools

1. ETH Sustainability Summer School: “Future Cities – Networks and Grammars”, July 2013, Singapore.

2. 3rd International Seminar on Green Energy Conversion, August 2014, Yamanashi, Japan.

A6 Acknowledgment

At the end of this endeavor it is right to give thanks and praise, because it would not have been possible alone.

First and foremost I would like to thank my supervisor Prof. Dr. Ulrich Stimming for accepting me as his doctoral student, introducing me to the field of electrochemical energy storage and his continuous support during the course of this work. I am deeply grateful for all the possibilities he provided for me. I was able to share results and engage in scientific discussions because he introduced me to his network and arranged visits at many universities and institutes abroad. Also, through him, I obtained the chance to contribute to review articles and invited presentations.

I would like to thank Prof. Dr. Ulrich Kortz for his hospitality during my two visits at his workgroup at the Jacobs University Bremen and the open mind with which he embraced our ideas for his POMs. Without his molecules and his expertise this thesis would not have been possible.

Also very important for the daily life in office and laboratory were the (co-) principal investigators of RP 1 of TUM CREATE: Prof. Dr. Harry E. Hoster, Prof. Dr. Madhavi Srinivasan and Dr. Guenther Scherer. Their friendliness and valuable suggestions during office hours, group meetings and retreats are highly appreciated.

A very warm Thank You goes to Prof. Dr. Rami Al-Oweini who I first met in Bremen when he was still a PhD candidate and who made it to become an Assistant Professor at record speed through creative, hard work. I am grateful for the supply of POM samples, the chance to be his co-author and his friendship. I hope the future has much more fruitful collaboration in store for us.

Terimah kasih to Dr. Ali Rinaldi for his expert’s advice on carbon materials and also for providing and characterizing same material. Frequent scientific discussions, insights into a foreign culture, cheerful chats, too-rare guitar play, halal camping in Canada and his friendship are also highly appreciated.

I would like to thank Dr. Bassil Bassem and Dr. Bineta Keita for their assistance and advice with the POMs. It is a complex and rich field and they helped to avoid pitfalls, or to climb out of them.

I am very grateful to the members of our small work group Ms. Han-Yi Chen and Mr. Max Herpich. Especially for the fun atmosphere and their friendship, but also for their permanent willingness to help in the lab. Especially Han-Yi’s tireless efforts to help her colleagues are admirable.

Also very important for the success of my work was the help of the couple Bucher. To Nicolas, for his advice as a true expert chemists and lab worker and for the many ventures into the wilderness of Asia. To Ramona for her amazing skills in the workshop.

Terimah kasih to Ms. Heryani Ahmad for running a tight ship in the labs and her constant support.

Many thanks to my former students, Mr. Christoph Bauer, Mr. Tobias Greese, Mr. Swapnil Parkhe and Mr. Alexander Wieczorek for the valuable work they performed with and for me. I hope I always acknowledged their work appropriately and that they learned something, I certainly did.

The help of Mr. Holger Fink in the construction of a prototype redox flow cell is highly appreciated as well as his insights into stacks and the industrial perspectives of vanadium redox flow batteries.

Hvala lepa to Mr. Jan Geder for his help with the TGA-MS setup. And for the Babi Guling. Twice.

All members of E19, RP 1, RP 7 and TUM CREATE in general are gratefully acknowledged for their assistance, encouragements, motivations and examples.

From the bottom of my heart I would like to thank my family for their love, encouragement and always believing in me. My parents and my brother always supported me, even if I planned to move far away.
Also many thanks to my newly acquired family for welcoming me in their midst and always being there for me.

Lastly and most importantly, I would like to thank my newly-wed wife Sara for encouraging and loving me and for embracing the idea of travelling the world together . I am very much looking forward to our shared future journey.